

**Identification of Operating Conditions and Steady
State Performance Enhancement of
Microgrid Systems**

Thesis submitted by

Yadala Pavankumar

Doctor of Philosophy in Engineering

Department of Electrical Engineering

Faculty Council of Engineering & Technology

Jadavpur University

Kolkata, India

2023

INDEX NO. 245/20/E

Identification of Operating Conditions and Steady State Performance Enhancement of Microgrid Systems

Under the guidance of

S. Debnath
13/10/2023
Professor
Electrical Engineering Department
Jadavpur University
Kolkata-700032

Dr. Sudipta Debnath

Professor
Department of
Electrical Engineering
Jadavpur University
Kolkata 700032
India

Subrata Paul
13/10/2023
Professor
Electrical Engineering Department
Jadavpur University
Kolkata-700032

Dr. Subrata Paul

Professor
Department of
Electrical Engineering
Jadavpur University
Kolkata 700032
India

List of Publications

A. Journal

Published

- I. **Y. Pavankumar**, R. Kollu, and S. Debnath, “Multi-objective optimization of photovoltaic/ wind/ biomass/ battery-based grid-integrated hybrid renewable energy system,” *IET Renewable Power Generation*, Pp. 1528-1541, March 2021, DOI: 10.1049/rpg2.12131.
- II. **Y. Pavankumar**, S. Debnath and S. Paul, “Microgrid fault detection technique using phase change of positive sequence current,” *International Journal of Modelling and Simulation*, Volume 43, Issue 3, Pp. 171-184, 2023, DOI: 10.1080/02286203.2022. 2059613.
- III. **Y. Pavankumar**, S. Debnath, and S. Paul, “Multi-objective pareto optimal unbalance voltage compensation in the microgrid,” *Electric Power Systems Research*, 217 (2023) 109104, DOI: 10.1016/j.epsr.2022.109104.
- IV. **Y. Pavankumar**, S. Debnath, and S. Paul, “A New Lissajous-Based Technique for Islanding Detection in Microgrid,” *IEEE Transactions on Smart Grid*, DOI: 10.1109/TSG.2023.3322435.

Communicated

- Y. Pavankumar**, S. Debnath, and S. Paul, “An optimization based flexible multi-objective control strategy for grid integrated microgrid system,” *Electrical Engineering*, Springer.

B. Conference

- I. **Y. Pavankumar**, R. Kollu, S. Debnath, and S. Paul, “A multi objective approach for optimal design of solar/ wind/ biomass/ battery-based grid connected microgrid system,” *2022 International Conference on Intelligent Controller and Computing for Smart Power (ICICCSP), Hyderabad, India, 2022, pp. 1-6, doi: 10.1109/ICICCSP53532.2022.9862483.*
- II. **Y. Pavankumar**, S. Debnath, and S. Paul, “Optimization based voltage unbalance compensation in the microgrid,” *2023 9th International Conference on Electrical Energy Systems (ICEES), Chennai, India, 2023, pp. 630-634, doi: 10.1109/ICEES57979.2023.10110127.*

Statement of Originality

I, Yadala Pavankumar registered on 18.02.2020, do hereby declare that this thesis entitled “**Identification of Operating Conditions and Steady State Performance Enhancement of Microgrid Systems**” contains literature survey and original research work done by the under signed candidate as part of Doctoral studies.

All information in this thesis have been obtained and presented in accordance with existing academic rules and ethical conduct. I declare that, as required by these rules and conduct, I have fully cited and referred all materials and results that are not original to this work.

I also declare that I have checked this thesis as per the “Policy on Anti Plagiarism, Jadavpur University, 2019”, and the level of similarity as checked by iThenticate software is 4%.

Signature of the Candidate:

Y. Pavankumar
13/10/23.

Date: 13-10-2023.

Certified by Supervisors

S. Debnath
13/10/2023
Professor
Electrical Engineering Department
Jadavpur University
Kolkata-700032

Dr. Sudipta Debnath

Professor
Department of
Electrical Engineering
Jadavpur University
Kolkata 700032
India

Subrata Paul
13/10/2023
Professor
Electrical Engineering Department
Jadavpur University
Kolkata-700032

Dr. Subrata Paul

Professor
Department of
Electrical Engineering
Jadavpur University
Kolkata 700032
India

CERTIFICATE FROM THE SUPERVISOR

This is to certify that the thesis entitled “Identification of Operating Conditions and Steady State Performance Enhancement of Microgrid Systems” submitted by Mr.Yadala Pavankumar, who got his name registered on February 18, 2020 for the award of Ph. D. (Engineering) degree of Jadavpur University is absolutely based upon his own work under the supervision of Prof. Sudipta Debnath and Prof. Subrata Paul, and that neither his thesis nor any part of the thesis has been submitted for any degree/diploma or any other academic award anywhere before.

S. Debnath
13/10/2023
Professor
Electrical Engineering Department
Jadavpur University
Kolkata-700032

(Prof. Sudipta Debnath)

Professor
Department of Electrical Engineering
Jadavpur University

Subrata Paul
13/10/2023
Professor
Electrical Engineering Department
Jadavpur University
Kolkata-700032

(Prof. Subrata Paul)

Professor
Department of Electrical Engineering
Jadavpur University

Acknowledgement

First and foremost, praises and thanks to the God, the Almighty, for His showers of blessings throughout my research work to complete the research successfully.

I would like to express my deep and sincere gratitude to my research supervisor, Prof. Sudipta Debnath, without whom, I would not have completed this research work. Her patience and guidance, motivation and relentless encouragement helped me to make a walk towards the target. Her thorough review process has helped me a lot to improve the quality and scientific vision of research papers and the thesis.

Secondly, I would like to express my sincere thanks and the deepest gratitude to my other supervisor Prof. Subrata Paul for his passionate guidance, continuous support, useful advices and encouragement throughout my Ph.D. study.

I am extremely grateful to my parents, Mr. Yadala Rattaiah and Mrs. Dhanalakshmi for their love, prayers, caring and sacrifices for educating and preparing me for my future. I consider myself nothing without them. They gave me enough moral support and inspiration to accomplish my objectives. I am very much thankful to my sister Lavanya for her love, prayers and continuing support during my research work. I would like to extend my gratitude towards some of my dear friends Pranita Yonzone, Rohith Marumulla, Yudha David, Naveen Bandela and Patibandla Anil Kumar for their encouragement and moral support throughout this journey.

Apart from my supervisors, I would like to thank the members of my thesis committee for their informative suggestions, which helped me to improve my research. I am also grateful to Dr. Ravindra Kollu for his unwavering support, encouragement, and helpful advice. They have all helped me to improve my research abilities. Their constant counsel has stayed with me throughout my research work tenure.

I would also want to thank the Head of the Department and renowned academic members of the Electrical Engineering Department of Jadavpur University for their unconditional support.

CONTENTS

Chapter 1: Introduction	1-19
1.1. Microgrid and the Challenges	1
1.2. Research Objectives	2
1.3. Literature Survey	3
1.4. Outcome of the Reported Research	16
1.5. Outline of the Thesis	18
Chapter 2: A Probabilistic Optimal Design of a Grid Connected Microgrid System	20-51
2.1. Introduction	20
2.2. Modelling of Grid Integrated Hybrid System	22
2.2.1. Modelling of Solar PV System	23
2.2.2. Modelling of Wind Energy System	26
2.2.3. Modelling of Biomass Gasifier	29
2.2.4. Load Modelling	29
2.2.5. Battery Energy System Modelling	31
2.2.5.1. State of Charge	31
2.3. Problem Formulation	33
2.3.1. Annual Life Cycle Costing	33
2.3.1.1. Annualized Capital Cost	33
2.3.1.2. Maintenance cost	34
2.3.1.3. Annualized Salvage Cost	34
2.3.1.4. Annualized Replacement Cost	34
2.3.1.5. Energy Purchased from the Grid and Energy Sold to the Grid	34
2.3.2. Loss of Power Supply Probability	35
2.3.3. Operational Strategy	35

2.3.4.	Multi-Objective Formation	36
2.4.	ACS Algorithm	38
2.4.1.	Artificial Cooperative Search Algorithm	38
2.4.2.	Multi-Objective Artificial Cooperative Search Algorithm	39
2.4.3.	Proposed Probabilistic Approach	41
2.5.	Simulation Results	42
2.5.1.	Grid Integrated Hybrid Renewable Energy System	43
2.5.1.1.	Scenario I (Without Biomass Gasifier)	44
2.5.1.2.	Scenario II (With Biomass Gasifier)	44
2.5.1.3.	Comparison of MOACS with IMOHS and NSGA-II	45
2.6.	Conclusion	51

Chapter 3: A Deterministic Approach for Optimal Design of Grid Connected Microgrid System 52-63

3.1.	Introduction	52
3.2.	Modelling of the Microgrid System	53
3.2.1.	Wind Energy System Modelling	53
3.2.2.	Solar Energy System Modelling	54
3.2.3.	Biomass Energy System Modelling	54
3.2.4.	Battery Energy System Modelling	55
3.3.	Data Collection	56
3.4.	Power Dispatch Strategy	56
3.5.	Problem Formulation	57
3.5.1.	Annual Life Cycle Costing	57
3.5.2.	Loss of Power Supply Probability	58
3.6.	Optimization Algorithm	58
3.7.	Simulation Results	59
3.7.1.	Scenario I (Off- Grid Mode)	60

3.7.2.	Scenario II (Grid Connected Mode)	60
3.7.3.	Comparison of the Proposed approach with WSA	61
3.8.	Conclusion	63

Chapter 4: Microgrid Fault Detection Technique Using Phase Change of Positive Sequence Current 64-82

4.1.	Introduction	64
4.2.	Control Strategy of Inverter-Interfaced Distributed Generators	66
4.3.	Proposed Fault Detection Scheme	68
4.3.1.	Test System	68
4.3.2.	Fault Detection Scheme for both DG Voltages Greater than 0.9	68
4.3.3.	Fault Detection Scheme for both DG Voltages Less than 0.9	72
4.3.4.	Fault Detection Scheme for one DG Voltage Greater than 0.9 and another DG Voltage less than 0.9	74
4.4.	Simulation Results	75
4.4.1.	Simulation Results for both DG Voltages Greater than 0.9	76
4.4.2.	Simulation Results for both DG Voltages less than 0.9	78
4.4.3.	Simulation Results for one DG Voltage Greater than 0.9 and another DG Voltage less than 0.9	80
4.5.	Comparative Assessment	81
4.6.	Conclusion	82

Chapter 5: A New Lissajous-Based Technique for Islanding Detection in Microgrid 83-102

5.1.	Introduction	83
5.2.	Islanding Detection Using Lissajous Figure	86
5.2.1.	Representation of Lissajous Figure	86
5.2.2.	Islanding Detection	87

5.2.3.	Implementation of the Proposed Algorithm	88
5.3.	Simulation Results	90
5.3.1.	Threshold Selection	90
5.3.2.	Evaluation of Islanding Detection Algorithm	91
5.3.3.	Evaluation Under NDZ Region	94
5.3.4.	UL1741 Test Conditions	94
5.3.5.	Effect of Load Quality Factor	95
5.3.6.	Effect of Load Switching	96
5.3.7.	Effect of Faults	97
5.3.8.	Effect of Sensing Errors	98
5.3.9.	Hardware-in the-Loop Testing	99
5.4.	Comparative Assessment	101
5.5.	Conclusion	102

Chapter 6: Pareto Optimal Based Unbalance Voltage Compensation in the Microgrid **103-118**

6.1.	Introduction	103
6.2.	Proposed Control Scheme	106
6.2.1.	Control Scheme for DGs	106
6.2.2.	Mathematical Modelling	109
6.3.	Problem Formulation and Optimization Algorithm	111
6.3.1.	Objective Functions	111
6.3.1.1.	Minimization of VUF	111
6.3.1.2.	Minimization of DG Output Current	112
6.3.2.	Multi-Objective Function and Pareto Optimal Solution	112
6.3.2.1.	Multi-Objective Artificial Cooperative Search Algorithm	113
6.3.2.2.	Implementation of the Optimization Strategy	115
6.4.	Simulation Results	115
6.4.1.	Case (i)	117
6.4.2.	Case (ii)	121

6.4.3.	Case (iii)	123
6.4.4.	Case (iv)	124
6.4.5.	Case (v)	125
6.4.6.	Case (vi)	126
6.4.7.	Case (vii)	126
6.5.	Comparative Assessment	127
6.6.	Customized Negative Sequence Voltage Compensation at Load Buses	130
6.7.	Conclusion	132

Chapter 7: A Two Level DG Control Strategy for Flexible Operation of Microgrid System **134-157**

7.1.	Introduction	134
7.2.	Problem Formulation and Control Objectives	136
7.2.1.	Active Power Control	136
7.2.2.	Positive Sequence Voltage Support	137
7.2.3.	Unbalance Voltage Compensation	138
7.2.4.	DG Current Limitation	139
7.3.	Proposed Multi-Objective Control Strategy	141
7.3.1.	Local Control	142
7.3.2.	Central Control	142
7.3.3.	Application of the Proposed Multi-Objective Control Strategy	144
7.4.	Simulation Results	145
7.4.1.	Case 1 : During Small Voltage Sag	145
7.4.2.	Case 2 : During Moderate Voltage Sag	148
7.4.3.	Case 3 : Under Grid Imbalance	151
7.4.4.	Case 4 : DG Unavailability	154
7.4.5.	Case 5 : Communication Failure	155
7.5.	Comparative Assessment	156
7.6.	Conclusion	157

Chapter 8: Conclusions	158-160
8.1. Conclusions	158
8.2. Future scope	159
List of Figures	161-164
List of Tables	165-166
List of Publications	167
Nomenclature	168-170
References	171-181
Appendix	182-185

CHAPTER 1

Introduction

1.1. Microgrid and the Challenges

The production of the electrical power has increased in the recent years significantly because of the rapid enhancement in the load demand. More than 80% of the generation is obtained by using the conventional energy sources which are not only fast depleting and finite but also emit vast amount of greenhouse gases into the environment and also the cost is volatile. On the other hand, the world statistics indicates that load demand will increase rapidly in the coming years. Therefore, there is an urgent need for ecofriendly, cost effective and reliable alternative energy sources. In recent years, renewable energy (RE) sources such as solar, wind and biomass gained more attention as a substitute for the fossil fuels as they are available in large amount and generates green energy. At present the RE sources are contributing about 10-20% of the total load demand. Moreover, in the second half of the 21st century this figure might go beyond 50%. The main problem with these RE sources is reliability since these are dependent on the weather conditions and nature. For example, sunlight and desired wind speed may not be available all the time. Therefore, individually these RE sources are not able to deliver the power continuously to the load. To overcome this problem two or more RE sources can be integrated together as hybrid system to meet the load demand effectively.

The integration of renewable sources into the modern power systems brings several benefits such as high efficiency, reliability and improved power quality which have escalated the concept of hybrid renewable energy systems (HRES) leading to the formation of microgrid. Microgrids are active distribution networks having distributed generation (DG) units, energy storage systems and loads that can be operated in grid connected mode as well as in islanded mode. Unlike traditional microgrids, in the modern microgrids the usage of power electronic interfaces makes the control of DGs more flexible and adds the self-healing ability. Therefore, in recent years the microgrids gained more attention. However, there are many challenges in microgrids due to the intermittent and variable nature of the renewables. The key concerns for designing a microgrid are power management, system's reliability and economic feasibility which complicate the microgrid modelling and operation. Hence, it is difficult to obtain the optimal sizing of the renewables and the high integration of the DGs into the distribution network causes several security and protection

issues.

Majority of the renewable based DGs are connected to the microgrid through the power electronic inverters. The fault characteristics of these inverter interfaced distribution generation (IIDG) units are dependent on the design and inverter control strategy used and also on the grid connection type. The maximum output fault currents of the IIDGs are limited to 150% of the rated current of the DG which is very small compared to the conventional synchronous generation based DG which can be 10 times the rated current. These aspects make the protection of the IIDG based microgrid more complex compared to the traditional microgrid. Another issue is islanding detection of the DGs. Failure to trip the islanded DG can cause severe problems and in the case of unintentional islanding, the DG must be disconnected within 2s as per IEEE 1547 standard. On the other hand, the presence of non-linear and single phase loads in the microgrid creates different power quality issues for the consumers, among which voltage unbalance is the major concern which can lead to additional power loss, voltage quality reduction and creates adverse effect on the operation of the electrical equipment connected to the system.

1.2. Research Objectives

The aim of this thesis is to understand the main difficulties and challenges for effective operation and protection of the microgrid networks and increase the microgrid resilience. In this work the optimal size of the DGs has been identified for the microgrid systems under economic and reliable operation, different methods such as islanding and fault detection are developed to ensure the safety of the microgrid and the voltage quality issues are handled by controlling the DG operation. Firstly, optimal photovoltaic, wind, biomass, and battery-based grid integrated microgrid system is developed using multi-objective artificial cooperative search algorithm (MOACS) to minimize annual life cycle costing (ALCC) and loss of power supply probability (LPSP). The battery based energy storage system (ESS) is chosen to provide backup power supply for at least 30 minutes during peak load condition and the probability density functions (PDFs) are utilized to characterize the variable nature of the RE sources. Later on a fault detection technique has been developed based on the phase change in the positive sequence current for the grid tied IIDG dominated microgrid system under different fault and operating conditions. Different types of DGs are considered and also various load power factors are assumed to make the system more practical. Further, islanding detection in the microgrid has been addressed by developing the novel approach by using the Lissajous patterns of the local voltage and current signals. The islanding detection method is validated under all IEEE standards with different

operating conditions including real time hardware in loop testing. Later on optimization based multi objective control strategy is developed for the IIDGs in the microgrid to compensate the voltage unbalance at the load buses by supplying the negative sequence quantities by the IIDGs. Further, the control strategy is improved and a flexible multi objective control strategy has been developed to address the multiple objectives simultaneously.

1.3. Literature Survey

The load demand is rising each day and the fossil fuels are depleting. There is a need to achieve the objective of reducing emissions in the environment while ensuring cost reduction with increase in the installed generation capacity [1]. This has resulted in renewed interest and attention towards usage of renewable based microgrid systems and the percentage growth of the RE sources is about 24% according to Ministry of Power, India. The enhancement in the dependency on the microgrid systems has raised focus on the challenges in the microgrid systems. The main challenges in the microgrid can be arranged in to three groups such as microgrid design, protection and the issues inherent in the microgrid (stability, voltage unbalance, frequency control, power sharing, etc.).

Due to the variable nature of the renewable sources, the key concerns for designing of microgrid are power management, system's reliability and economic feasibility. To handle these sensible concerns there is a need to achieve multiple objectives and design renewable energy based hybrid system using a proper methodology. In recent years several investigations have been carried out on optimal sizing of the HRES. Majority of these studies are focused on the modelling of islanded systems [2-6]. The authors in ref. [2] proposed a standalone hybrid energy system based on the wind and solar photovoltaic for an un-electrified village. This study considered the hourly meteorological data and load demand for one year and the ant colony optimization algorithm is used for the sizing of the hybrid energy system. A methodology to optimize the sizing of a standalone wind, solar photovoltaic and diesel generator based hybrid system has been presented in ref. [3]. The proposed method follows the deterministic approach to model the hybrid system by using the available six months data to realise a cost effective system while ensuring the energy availability. Ref. [4] presents a novel approach to design an autonomous hybrid system based on PV, wind and battery energy system with the objectives of reducing the loss of power supply probability (LPSP) and lowest embodied energy. The proposed approach utilises metrological data of the particular area to model the system by using single and multi-objective algorithms with the considerations of the ecological aspects. The authors in ref. [5] proposed a

new optimal design of a hybrid system with different energy generation units along with the storage system. The multi objective problem has been solved by particle swarm optimization algorithm with e- constraint to minimise the total unmet load, total cost and fuel emissions. Later on the sensitivity analysis has been carried out for each sensitive parameters of the hybrid system. An optimization model is developed based on the wind, PV and biomass to deliver the load demand with maximum output from each resource [6]. The priority based control strategy is implemented to deliver the load demand with available resources at that particular moment like no irradiation periods, less wind available periods.

The main drawback of the standalone system is its less reliability because of its varying nature. Therefore, by integrating these systems to the utility grid, the system becomes more reliable since the grid acts as backup to the hybrid systems. However, integration of these hybrid systems to the grid still remains a challenging job due to the intermittent, variable, and stochastic nature of the RE sources, which cause frequency deviation, load mismatch, and voltage instability [7,8]. The drastic variable nature of the wind makes power system more vulnerable. To tackle the uncertainty of the wind power and minimising the risk of wind power commitment the energy storage systems (ESS) can be utilised while integrating these hybrid systems to the utility grid [9-10]. Therefore, the ESS gained more importance in the integration of hybrid systems to the grid in recent time [11]. Later the researchers proposed different methods for optimal design of grid integrated hybrid systems. In [12] the authors proposed a methodology to minimize the power fluctuations of hybrid systems by introducing pumped energy storage. The fluctuations in the power generation by renewable energy sources are analysed in the inverter substation and later the optimal scheduling strategy for the wind, pumped energy storage and PV in VSC-HVDC grid is developed based on the t-location scale. Basaran et al. [13] presented a novel power management strategy for the PV, wind, and battery based grid integrated system to power the small loads. The inverter used in this study is able to change the mode of operation from standalone to grid connected mode depending on the requirement. The designed energy management strategy unit measures the energy flow from each resource and according to the need it will transfer the energy to the energy storage system and to the grid. But the authors did not consider cost optimization or reliability, but only focused on energy transfer aspects. Fuzzy logic and grey wolf optimization algorithm based novel expert system has been developed in ref. [14] with an objective to minimize the operating cost of HRES system. The proposed intelligent Meta heuristic approach is aimed for the proper energy management and battery sizing in the grid connected microgrid system but proper mathematical modelling of the RE sources is not considered in the system design. Usman and Yang in ref. [15] proposed an energy management

system for the grid integrated PV and battery based energy storage system. The proposed energy management system works in two stages which are forecasting and optimization, the duty of the forecasting is to forecast the solar irradiance, temperature and load demand and the optimization block schedule the optimal power generation and load demand a day ahead. In [16] the authors proposed an effective control strategy for the energy management to integrate the microgrid system consisting of wind, PV, fuel cell and energy storage system. The multi objective particle swarm optimization algorithm has been utilised to obtain the optimal sizes of the RE sources with cost minimization and maximization of utilization of the sources. However, detailed cost analysis and the time varying nature of the renewable sources and load are not considered. To serve the load demand of a typical village, artificial bee colony algorithm based PV and biomass based hybrid grid connected system is developed by Singh and Kaushik in [17]. The authors have developed the model to obtain the optimal hybrid system configuration which delivers the energy at low cost and the analysis revealed that the grid integrated hybrid system is more reliable compared to the standalone system. In [18] authors proposed a PV, wind and battery hybrid grid integrated micro-grid system which reduces the annual cost and maximizes the reliability. The study proposes a two constraints based iterative search algorithm which works in two stages, in the first the optimal sizing algorithm gives the optimal sizes of the RE sources and the battery optimizing algorithm determines the optimal capacity of the battery energy storage system. The drawback of this study is that the varying nature of the load is not considered.

Most of these existing methods are lacking the proper mathematical modelling of the RE sources and the analysis carried out by the authors in [19-20] reveals that to design a proper reliable grid integrated microgrid system it is essential to model the RE sources. Moreover the stochastic and variable nature of the RE resources (such as solar PV and wind) should be characterized to make the system more reliable. To achieve this the researchers has put more efforts on characterizing the stochastic nature of the RE sources by using the probability density functions (PDFs) such as Weibull, Beta, Gama, Normal, Generalized extreme value (GEV), and lognormal PDFs [21]. By using the available previous year's data of solar irradiance, wind and load demand, these PDFs predict the present solar irradiance, wind speed and load demand. The study presented in [22] suggests that the best suited PDF for the data of that particular chosen site has to be considered to model the stochastic behaviour of the RE sources. Goodness-of-fit tests such as Kolmogorov-Smirnov test (K-S test) and R^2 test are used to measure deviation between measured the statistical distribution and the modeled distribution. A larger value of R^2 and lesser value of K-S for a PDF indicate that the particular PDF models the data accurately [22]. The authors in [23] establishes a procedure to calculate the probability density function to a load flow

for an electrical power network in the presence of the wind power generation.

The convolution based probabilistic approach to assess the long term performance of the multi-mode hybrid system has been proposed in [24]. The reliability analysis of grid connected hybrid system has been performed by using the energy index of reliability to estimate the energy performance and to validate the proposed probabilistic model numerical example application has been included. In [25] a hybrid intelligent algorithm has been developed to model the behaviour of the hybrid system based on artificial neural network. To represent the behaviour of the hybrid system the proposed approach considered the uncertainty related to the wind speed and solar irradiance. To generate the input output samples of the data base, probabilistic approach has been used which has been used later to train the artificial neural network. In [26] the authors proposed a novel probabilistic approach for a hybrid system which includes either one axis or two axis solar tracking system along with the wind energy system. The effect of the solar tracking system on the annual energy gain is discussed in this study. Moreover, the reliability analysis and the impact of the tracking system on the hybrid system energy performance is validated. But they did not consider in the design of HRES. The studies presented in [27, 28] reveal that the solar and wind based power generation in HRES is intermittent in nature. Hence, one of the major challenges of HRES design involving solar and wind generations is satisfying the load demand at all times irrespective of generation uncertainty. The loss of power supply probability (LPSP), which is a measure of reliability in serving the load demand has to be reduced as much as possible to give the continuous power supply to the load. The literature indicates that to design a reliable grid integrated renewable based hybrid system, the variable nature of the RE sources and load has to characterised and also the energy storage system plays an important role in maintaining the stability. Hence it is difficult to obtain the optimal sizing of the renewables. Therefore, to handle the complexity in designing hybrid system and to determine the optimal sizes of the renewables a powerful multi objective optimization algorithms is needed [29, 30].

In the other hand the majority of these renewable based DGs are connected to the microgrid through the power electronic inverters. The fault characteristics of these inverter interfaced distribution generation (IIDG) units are dependent on the design and inverter control strategy used and also on the grid connection type. The maximum output fault currents of the IIDGs are limited to 150% [31,32] of the rated current of the DG which is very small compared to the conventional synchronous generation based DG which can be 10 times the rated current [32]. The microgrid can operate in grid connected mode or islanded mode but the power distribution operators and utilities usually do not prefer the islanded mode of operation due to the intermittent nature of the DGs [33,34]. All these aspects make the protection of the IIDG based microgrid more complex

compared to the traditional microgrid. Therefore, there is an urgent need to develop proper fault detection technique for the microgrids. In recent years the fault detection in the renewable based microgrid gained more interest among the researchers.

During the initial phase the conventional fault detection schemes are developed for the protection of the microgrids which are over current principle based schemes, distance based relaying schemes and current harmonic distortion based methods [35]–[37]. In [35] the authors proposed an adaptive over current protection scheme for the distribution system which is dominated by the distributed generation units. The method utilizes the local information of the system and the relay trip characteristics are updated by detecting the mode of operation of the system (islanded or grid connected). The distance relay based protection scheme is designed for the distribution system in [36]. This scheme is specially designed for the network circuits in UK where the communication networks and the voltage transformers are installed on the 11kV circuits. The primary and back up protection is provided by the developed scheme by measuring the restraint signal (voltage) at the secondary winding of the distribution transformer. By measuring the local currents ref. [37] proposed a protection scheme for distribution system based on the sequence components such as positive, negative and zero sequence. Only using the positive sequence current is not feasible therefore, the proposed method utilized the zero and negative sequence currents to detect the upstream and downstream faults. The main drawback of these schemes is that these are applicable in only unidirectional power flow systems. But the integration of the renewable based DGs into the microgrid makes the power flow in the microgrid bidirectional [38]. Hence, the conventional protection schemes are incapable to protect the renewable based microgrid.

To overcome these drawbacks later on differential protection schemes [39-41] are proposed. In [39], the primary protection of the microgrid based on the classical differential relay principle has been presented. The authors discussed the details of relay settings, communication requirements needed for the current transformer selection and presented different protection strategies for different sections like feeder protection, DG protection and bus protection. But the authors did not address the significant issues like data synchronization and charging current effects on differential protection. Comparing the sending end and receiving end spectral energy content of the current with the use of Stockwell transform (S-transform), differential schemes have been presented in [40,41]. Initially the currents measured at the local buses are transferred through the S-transform to create the time frequency counters. Later by using the spectral energy content of these counters the faults signals has been analyzed. But the complexity of the S-transform is very high which is not desirable in the practical applications where fast response is demanded.

Wavelet transformation (WT) and Park's vector approach (PVA) based fault detection technique is given in [42]. The fault patterns are recognized by transforming the three phase voltages and currents to dq0 components which are filtered through the wavelet transformation. The faults are identified by using the finite difference between the filtered signals but the algorithm has the limitation with high impedance fault resistances. Discrete wavelet transformation (DWT) and deep neural network based intelligent fault detection scheme is presented in [43]. The statistical features of the measured branch currents are extracted by preprocessing through the wavelet transformations. The proposed method assures fast detection of the fault location, type and phase; however, DWT has the limitation in the low frequency band. To overcome the real time limitations of the Wavelet transformation, Un-decimated wavelet transformation (UWT) based algorithm has been proposed in [44] for PV based microgrid. The UWT is used to detect the power quality disturbances in the microgrid by utilizing the measured voltage signals. The benefit of the UWT is that it reduces the noise and oscillation in the voltage signal but this method is only applicable for the PV based microgrid. The authors in [45] proposed a method using mathematical morphology and recursive least square method by measuring the voltage and currents data at every distribution line. This method uses the dilation and erosion median filter on the measured signals to identify and classify the faults. However, due to high complexity, data overflowing may occur. In [46] the authors proposed a central monitoring system based method by sensing the sending and receiving end current directions. The local bus voltages and current signals are continuously monitored and transmitted in the form of movable window patterns which requires powerful monitoring system which is not economical.

In recent years the researchers have put forward the fault detection techniques in microgrid based on the sequence components. The studies presented in [47,48] focused on the fact that unlike the negative sequence and zero sequence phasors, the positive sequence phasors exist for all types of faults. Therefore, it opens the window for the new researchers to develop the protection schemes on the basis of the positive sequence components of the system. In ref. [49] the authors proposed a fault detection technique in radial distribution system using the phase change in the positive sequence current considering the pre fault current phasors and post fault currents phasors. By utilizing the phase difference a rule base is developed to detect the faults in the system. By using the phase change in negative sequence current a directional relaying algorithm for single pole tripping is presented in [50]. The algorithm is attractive since it does not use the fault voltage and only utilizes the negative sequence current phase change. But the fault detection in the branch feeders was not considered.

The fault characteristics of the IIDGs will vary according to the control strategy implemented

in the DGs [51]. The fault characteristics of the v/f controlled IIDG exhibits different characteristics compared to the PQ controlled IIDG. Therefore, consideration of specific control strategy of the IIDGs is needed [52]. The equivalent fault models and control strategies for IIDGs under different control modes are presented in [52, 53]. The IIDGs are able to supply the positive and negative active power and reactive power into the network and it is required that the IIDGs have to supply the reactive power in order to support the grid codes. Under islanded mode the droop control is responsible to supply the required amount of the reactive power while in grid connected mode the IIDGs have the low voltage ride through (LVRT) facility to supply the specific amount of the reactive current for specific amount of voltage drop at the PCC [54]. In [55] the authors proposed a novel fault detection technique based on the phase difference between the positive sequence fault component of the bus voltage and fault component of the bus current. This study has considered different types of DGs in the microgrid and the fault characteristics of each DG is analyzed under the specific individual control strategy. The drawback of this study is that it requires the large amount of information of measured signals and the effect of different load power factors may alter the performance of the method.

Another issue in the microgrid is islanding detection which is the predominant one and widely debated over years. Failure in the detection of islanding event may create several power quality issues and stability problems and in the case of unintentional islanding, the DG must be disconnected within 2s as per the standards mentioned in IEEE 1547 standards [56]. Therefore, this issue gained rapid interest and the researchers presented various methods for islanding detection in the microgrid. The islanding detection techniques presented in the literature can be broadly categorized into two categories which are remote and local control techniques. In remote control approach the communication channel plays an important role to access the information from the remote terminals. The studies presented in [57,58] monitored and analyzed the remote data constantly with the help of the supervisory control and data acquisition (SCADA). The rate of change of power at the generator terminals is considered to detect the islanding in the prior method and the voltage change at the point of common coupling is considered in the later method. The authors in [59] developed an innovative anti- islanding method based on the power line signaling. In this study a signal has been sent from the substation to the DG site through the distribution feeders, if the signal reaches the DG site it is considered that the DG is not islanded and in case if the signal is not received at the DG site it is considered that the DG is islanded. These remote communication-based methods are not economical for the small network systems and these studies are not suitable where regional monitoring is required.

Therefore, to overcome these issues the local control approaches are introduced. In the local

control approaches the system parameters such as current, voltage and frequency are regionally monitored. These approaches are basically grouped into three categories, which are passive, active and hybrid methods. The passive approach basically depends on the variations of the system parameters such as rate of change of voltage phase angle, rate of change of kinetic energy over reactive power (ROCOKORP), sequence impedance, phase angle difference of impedance and adaptive rate of change of frequency [60-65]. Since all the inverter interfaced DGs are equipped with the Phase locked loop (PLL), the authors in [60] proposed an islanding detection technique based on the rate of change of phase angle of the voltage at the PCC. This method is simple, economical and also offers less non detection zone. Ref. [61] presents another islanding detection technique based on the rate of change of kinetic energy over reactive power for each DG at the PCC. The study revealed that the proposed method shows good performance even during the full match between the generation and load demand. The superimposed angle of the negative sequence voltage is utilized for islanding detection in [62], the proposed methods considered different types of RE sources and it is able to detect the islanding during 0% power mismatch. The presence of the nonlinear loads in the system causes the power system signals to contain a considerable amount of inter harmonics. Therefore, full cycle least error square method has been used to identify the frequency of the voltage and current signals. Later the rate of change of superimposed negative sequence impedance is used to detect islanding in [63]. Using the phase angle difference of the superimposed impedance at the DG as well as PCC, an anti-islanding method is developed in [64]. Initially directional relay algorithm is used to detect and discriminate the grid side events and the PCC side end signal is transmitted to the DG site to detect the islanding event. A passive islanding detection technique is proposed based on the rate of change of frequency for both the generator based microgrid as well as generator and hybrid RE sources based microgrid in [65].

The drawbacks of the passive methods are inability to detect islanding when power mismatch is low and at perfect power balance conditions. Moreover, these methods have large NDZ. Active islanding detection approaches gained more interest because of the shortcomings of passive islanding detection methods [66-70]. In the active islanding techniques, the concept of intentional frequency perturbation allows the researchers to define the thresholding for the frequency relays in islanding detection. The researchers in [66] analyzed the effect of the rate of change of frequency during these perturbations. Ref. [67] introduces a novel method for islanding detection in the microgrid by using two additional compensators along with the active and reactive power control feedback loops. The proposed scheme improves the stability during the system disturbances. A classical periodic q-axis current controller is designed for the inverter with a continuous periodic current of a small value and with the help of absolute average frequency value

it detects the islanded frequency which deviates from the reference value [68]. In [69] the grid synchronization based phase distribution analysis is carried out. With the help of phase distribution, a third harmonic is injected into the system and by accurately extracting the third harmonic at the PCC the authors developed an islanding method for the grid connected microgrid system. The active islanding techniques which are based on the injection of the harmonics or disturbances into the system have lot of limitations. Therefore, to address those limitations the authors in [70] presented a study on the investigations on those limitations such as disturbances caused during the parallel operation of the multiple inverters and output current distortion. The study revealed that if the injection is done without the knowledge of the inverters, the inter harmonics are not suitable to utilize during inverters parallel operation. The main problem of these active islanding methods is that due to the insertion of additional disturbance signal, the power quality of the system deteriorates. To avail the benefits of both active and passive methods, hybrid islanding detection methods are developed. One of such methods is presented in the literature which is based on the parallel inductance switching [71].

Later on the researchers developed S-transform and wavelet transform based islanding detection techniques [72-74]. In [72] a novel islanding detection technique based on wavelet singular entropy, in which the voltage at the DG site has been monitored and measured. Then the voltage signals are processed through the wavelet transform to obtain the coefficient values at different levels of decompositions. The machine learning and wavelet based islanding detection method is developed in [74]. In this study to determine the filter coefficients for a newly designed wavelet, procrustes analysis is used. The computational time for S-transform based methods is very high which is not suitable for practical applications and also it is not possible for S-transform to incorporate all signals inside the predetermined Gaussian window. Wavelet transform based methods have drawbacks such as hardware limitations and high sampling rate. Subsequently, Hilbert Huang transform based approaches have been proposed for islanding detection applying empirical mode decomposition [75,76]. The method presented in [75] is based on the positive sequence voltage signal variations and the signal energy is extracted from the positive sequence voltage signal variations intrinsic modes. The proposed method is applicable in direct fed type or inverter based DG type systems. The voltage and current signals of the DGs which are measured at the PCC are transformed by the Hilbert Huang transform to detect the islanding in [76]. Initially the empirical mode decomposition is used to obtain the intrinsic modes, then the Hilbert Huang transform is used to obtain the analytical signal. An adaptive neuro fuzzy interface system based islanding method is developed in [77] for the low voltage microgrid systems. The proposed method monitored the input signals such as voltage, current, harmonics, active and reactive power

and then trains the neuro fuzzy interface to detect the event. Later the authors in [78] proposed a probabilistic neuro fuzzy system to detect the islanding event by monitoring the system parameters for any system topology. However, large number of neurons, complex training process and large training sets are the disadvantages of these approaches.

The authors in [79] developed an event index value based on the super imposed components of the sequence impedance by acquiring the local data. The authors in this work have not considered synchronous generator based DG. In [80] an islanding detection technique has been developed by injecting disturbance in the maximum power point control when the voltage exceeds the desired threshold. But it is only limited to the photovoltaic based systems. A new islanding detection index is proposed in [81] based on the rate of change of potential energy function. In [82] the authors proposed a PMU based technique which has been developed considering the change in the phasors of the pre disturbance and post disturbance voltage and current signals. In recent years the utilization of waveform measurement units (WMU) as a smart sensor has been introduced. The WMU can provide precise information of the time synchronized current and voltage waveform measurements and has high reporting rate. Lissajous figure can be developed from the voltage and current waveforms which can be utilized to detect the power system disturbances like islanding [83].

The presence of non-linear and single phase loads in the microgrid creates different power quality issues for the consumers, among which voltage unbalance is the major concern which can lead to additional power loss, voltage quality reduction and creates adverse effect on the operation of the electrical equipment connected to the system [84, 85]. It also leads to the voltage sags and due to voltage sags IIDG control systems may experience disturbance which hampers the continuous and safe operation of power distribution. Moreover, the operation of the sensitive loads may be disrupted. Therefore, the IIDGs should have the voltage support abilities and low voltage ride through (LVRT) capability for operation in the non-ideal conditions [86, 87]. Alongside, during these non-ideal conditions the DG may produce high amount of currents which will cause damage to the semiconductor devices present in the IIDGs and also it may experience sudden loss in the active power injection. These issues such as unbalance compensation, voltage support, active power control and current limitations have to be properly addressed to maintain the safe and continuous operation. Therefore, in the first stage the unbalance voltage compensation gained more interest. The active power filters have been largely used for voltage unbalance compensation [88]. The compensation can also be carried out using hybrid compensators which are formed by combining series and shunt active power filters. Unified power quality conditioners (UPQC) are widely used as hybrid compensators [89] to improve the power quality in distribution systems.

Static synchronous compensators (STATCOMs) are also being used to reduce the detrimental effects of unbalance in the grid [90]. But these devices introduce additional cost and also enhance the complexity in the overall system.

Microgrid is considered as a controllable entity and the power electronic interfaces connecting the DGs to the microgrids add significant flexibility to utilize DGs as compensating devices under non ideal conditions. By properly controlling the DG converters, several objectives can be accomplished, such as maintaining the system frequency, voltage and also power quality requirements within the acceptable limits injecting both active power and reactive power to the grid and load [91]. Therefore, the need of additional devices such as active power filters, STATCOM, UPQC, etc. can be eliminated which results in reduced cost as well as reduction in the complexity of the network. In [92], a control strategy has been developed for single phase photovoltaic to mitigate the unbalance voltage by curtailing the active power and controlling the reactive power supplied by the single phase PVs connected to the system where the compensation is carried out. But considering large applications of three phase inverters in the networks, this scheme is not suitable for wide applications. A control technique has been proposed for voltage unbalance compensation at the DG terminals by controlling the DG converter where negative sequence reactive power has been utilized to generate the reference for unbalance voltage compensation [93]. The authors in [94] proposed a control technique consisting of primary and secondary control to compensate the unbalance voltage. The secondary control is responsible for unbalance voltage control but the proposed method is only focused on sensitive load bus. In [95] the authors proposed a new distributed control scheme for unbalance voltage compensation in an islanded AC microgrid, in which the primary control layer and cyber layer based two-layer control framework with event triggered communication is used for effective unbalance compensation. A secondary control scheme for power quality improvement with effective load sharing for multiple microgrids has been proposed in [96]. The proposed scheme helps the DGs to share the individual phase currents accurately so that over current stresses can be avoided in the system. In [97] authors proposed a novel voltage and current unbalance mitigation in the microgrid using the aggregated PV inverters. These studies are only focused on the compensation at specific point such as PCC or sensitive load bus which may show a negative impact on other load buses. Ref. [98] introduces a control scheme to mitigate the voltage unbalance and equal distribution of negative sequence current to each DG in the microgrid by using the communication link and complex form of proportional resonant controller. In [99] the authors proposed an optimal voltage regulation method based on the multiple agent system for multi-microgrids, where the agents collect the data from multiple microgrids. The control schemes in these studies are highly complex and

communication links play a major role in the data transfer increasing the risk of malfunction.

A state space modelling for multiple inverter based unbalanced microgrid using dynamic phasor method is presented in [100]. The authors focused on the stability analysis of the microgrid in order to achieve the unbalance compensation but the authors did not consider customized voltage quality requirements. In [101] an optimal multi objective scheme is presented to regulate the active and reactive power flow and unbalance compensation. The presence of single phase DGs injects the active power unevenly into the three phase system therefore, this work focused to balance the active power injection and the unbalance compensation is not addressed properly. The authors in [102] developed multiple current control damping schemes to control the DGs autonomously to compensate the voltage unbalance while sharing the compensation effort with the help of primary, secondary and auxiliary loops. In [103] optimization based customized voltage unbalance compensation technique has been proposed. The authors have reduced the negative sequence voltage at different buses but they did not focus on the improvement of VUF by improving the positive sequence voltage. In [104] the authors proposed a control strategy for voltage imbalance mitigation in inverter-based distribution system considering local current and voltage variables. The implementation of the proposed algorithm has not been established in a microgrid. Moreover, they considered VUF only up to 4%. An optimized control strategy for grid connected inverter has been developed in [105], but the authors did not consider the coordinated optimized operation of the DGs in the microgrid for mitigation of voltage unbalance at different buses. A hierarchical control system comprising of primary, secondary and tertiary control has been used in [106] which results in execution delay due to the implementation of secondary and tertiary control mechanism. Also, the tertiary control is dependent on the secondary control which results in more complexity. In [107] the authors proposed a proportional resonant controller in complex form using communication link to mitigate the voltage unbalance. The proposed technique shares the compensation burden to each DG. Ref. [108] proposed a multiple agent system in multi microgrids for voltage regulation in which the agents collect data from each microgrid and communicate within the microgrids. To implement these methods, large amount of data is required to be collected and they are prone to malfunction due to any communication failure.

On other hand during these unbalanced conditions it has become difficult to maintain the nominal grid voltage and therefore the researchers proposed different methods to support the grid voltage by supplying the reactive power. In [109] the authors proposed an analytical study on different approaches to supply both the active and reactive powers during unbalanced conditions. The method first analytically calculates the maximum allowable active power and reactive power

and it also makes sure that the phase currents are operating within the safety limit. During the unbalance grid fault ride through the converter may experience the over current problem, therefore the inherent phenomenon of the over current cases has been analyzed quantitatively by using the three phase over current control strategy in [110]. The proposed control techniques will deliver constant amount of reactive power from the DG to support the PCC voltage. The main drawback of this control technique is that the voltage is not supported effectively and also it is difficult to select a proper power reference which may result in overcurrent scenario. To overcome this drawback, the LVRT strategy has been incorporated in which the DGs inject the required amount of reactive current to mitigate the voltage drop. The symmetric sequence based voltage support schemes have been proposed in [111,112] where the unbalanced voltage has been decomposed into the positive sequence and negative sequence voltages and the control technique determines the references for the current from the symmetric voltage components. Based on the positive sequence and negative sequence susceptance and conductances the authors in [113] proposed a control scheme with the help of instantaneous active power theory, but it only focuses to compensate the short term voltage sags. During the unbalanced grid conditions a control strategy has been developed in [114] for each phase individually for the voltage control converter in the PV based microgrid. To maintain the grid codes the DG will supply the reactive power and during that phase the over voltage condition has been analyzed in the proposed approach. Under the unbalanced grid voltages, the PWM rectifier reduces the active power injection because of the over current limitation. To address this issue the authors in [115] developed a control strategy to reduce the instantaneous active power oscillations of the PWM rectifier during the voltage dips. The proposed control method offers balanced positive sequence control and instantaneous active power control. In these studies the authors have considered the long term voltage sags in the low voltage microgrids. However, these methods depend highly on the system parameters and X/R ratio. From the existing literature survey it has been observed that there is a need to consider multiple objectives such as voltage support, unbalance compensation, current limitation and active power control. The control objectives have to be considered simultaneously for better operation of the IIDGs in the microgrid. Also, when multi-objectives are present in the control strategy, especially when they are conflicting to each other, it is hard to get a proper solution which can satisfy all the objectives. Therefore, it is suitable to consider optimization algorithms to obtain proper optimal solution to get the desired performance [116].

1.4. Outcome of the Reported Research

The following outcomes are enlisted as the consequences of this research which are aimed to develop novel approaches for the optimal design, fault detection, islanding detection and the voltage quality improvement in the microgrid system.

- ❖ Variable nature of the RE sources complicates their modeling, operation, and integration to the grid. Therefore, it is difficult to choose optimal RE sources with proper energy storage system for economic and reliable operation of the grid integrated hybrid renewable energy system. There is a need to solve this optimal HRES problem using efficient algorithms due to high cost and model complexity involved. In this study, optimal photovoltaic, wind, biomass, and battery-based grid integrated HRES is proposed using multi-objective artificial cooperative search algorithm (MOACS) to minimize annual life cycle costing (ALCC) and loss of power supply probability (LPSP). ESS is chosen to provide backup power supply for at least 30 minutes during peak load condition. A Probabilistic approach is used to consider time varying nature of the RES and load while solving optimal HRES design problem by employing MOACS. Comparative analysis is provided at the end which shows that MOACS can provide better optimal design of HRES.
- ❖ A new algorithm is developed for fault detection in grid-tied microgrids with inverter interfaced distributed generators. To support the Grid codes, the DGs require a low voltage ride through capability. The control strategy used in the DGs result in large changes in the fault characteristics of the microgrid. Hence, it is required to study the fault characteristics of the DGs in a microgrid under various operating conditions. The study presents fault detection for microgrid with PQ controlled DGs having LVRT capability under different DG voltages as well as different fault conditions (high impedance and low impedance). The fault location has been identified using the phase change in the positive sequence current under specific DG voltages. The reliability of the proposed scheme has been validated under diverse fault conditions through extensive simulations in Matlab/ Simulink environment and the comparison with other fault detection techniques proves the efficacy of the proposed scheme for fault detection in microgrids.
- ❖ A novel technique is developed for islanding detection in microgrid based on Lissajous figure of voltage and current signals. The Lissajous figure reveals distinct pattern during islanding which can segregate the islanding event from other non-islanding disturbance events such as switching transients and faults. Lissajous figures have been considered as

images to capture the characterizing patterns in their shapes. The area of the Lissajous figure has been considered for successive intervals to develop an index mathematically and an appropriate adaptive threshold value of index has been formulated to detect the islanding phenomenon. The proposed technique does not require the information about the network configuration. The efficacy of the proposed technique has been established through fast islanding detection with load inside the non-detection zone (NDZ) and under the condition of complete match between the distributed sources and the load. To establish the efficacy of the proposed technique, comparative analysis has been carried out with other recent islanding detection techniques

- ❖ Voltage unbalance control plays an important role in maintaining the power quality standard in microgrid. This study presents a multi-objective control strategy to realize optimal voltage unbalance compensation in a multibus microgrid, satisfying customized power quality requirement of the consumers at different buses. The distributed generators in the microgrid share the compensation effort cooperatively to satisfy the power quality standard at different buses. Multi-objective Artificial Cooperative Search Algorithm has been proposed to solve the multi-objective pareto optimization problem. The algorithm assigns compensation reference to all the DGs so that the DGs can accordingly compensate the negative sequence voltage at different buses and thereby mitigate voltage unbalance. The effectiveness of the proposed scheme has been established through the results obtained from simulation and real time digital simulator..

- ❖ A novel two stage multi-objective control strategy has been presented for low voltage microgrid systems consisting of inverter interfaced distributed generators. To ensure continuous and safe operation of the IIDGs during unbalanced voltage sags, the proposed control strategy supplies the optimal positive sequence voltage support, voltage unbalance compensation considering the current limitation of the inverters. The positive and negative sequence quantities of the IIDGs are controlled in such a way so that these objectives can be achieved simultaneously. The voltage profile can be maintained as desired by the grid operator by operating the DGs in coordination with each other. To solve the optimization problem and to generate the optimal references for the DG control unit, artificial cooperative search algorithm has been utilized. The multi-objective control strategy has been tested under different operating conditions and tested in hardware-in-the-loop environment to ensure the robustness and effectiveness of the proposed approach.

1.5. Outline of the Thesis

This thesis has been organized into 8 chapters. The first chapter explains the evolution of the microgrids and its challenges in the current scenario. Then, a brief literature survey is presented to examine the recent research on the issues in the microgrid. Later the outcomes of this research work has been reported and the chapter wise details of the thesis have been given at the end of the chapter 1.

In Chapter 2, a probabilistic approach for the optimal design of the grid integrated microgrid system is presented. The stochastic nature of the RE sources and load is characterized by using the probability density functions and a probabilistic power dispatch strategy is implemented. The performance of the proposed MOACS algorithm is compared with the standard multi objective optimization algorithms. The simulation results show that the proposed probabilistic approach delivers better optimal results.

Chapter 3 describes the modelling of the RE sources in the hybrid system with the help of mathematical expressions. The meteorological data such as solar irradiance, temperature and wind speed at the chosen site is used to determine the output power of the RE sources by deterministic approach. The mathematical expressions are derived for the charging and discharging of the ESS according to the proposed control strategy. The MOACS algorithm is developed and utilized to solve the conflicting objectives in the renewable based hybrid system.

A novel fault detection technique for the IIDG based microgrid system is described in Chapter 4. The phase change in the positive sequence current at each feeder is utilized to detect the faults in the microgrid. The fault characteristics of different types of DGs are analyzed at different DG voltages in the microgrid. The fault detection technique is not sensitive to the fault resistance and it can detect both the HIF and LIF faults. The proposed method is tested for different fault types under different load power factors.

Chapter 5 presents a Lissajous pattern based islanding detection technique for the microgrid system. The Lissajous figure patterns are observed during pre and post disturbances. Based on the change in the patterns of the Lissajous figure, a new islanding technique is developed. The adaptive thresholding is considered and the proposed method has been validated under diverse conditions and the results show that the proposed islanding detection technique gives satisfactory results.

Chapter 6 describes the pareto optimal unbalance voltage compensation in the microgrid. The

proposed control strategy is aimed to supply the negative sequence quantities from the DGs in the microgrid to compensate the negative sequence quantities consumed by the unbalanced loads. Moreover, the proposed method has a flexibility to adjust the negative sequence voltage limit at each load bus according to the requirement.

Chapter 7 presents a two stage multi objective control strategy for the IIDG based microgrid. The control strategy works locally as well centrally to satisfy the multiple objectives. The positive sequence voltage support, unbalance voltage compensation and the active power maximization is prioritized based on the requirement by controlling the positive and negative sequence quantities of the DGs. The control strategy is designed in such a way that the DG current will not exceed the safety limit during the compensation process.

Chapter 8 contains the concluding remarks and the discussion on the future scope of this research work.

CHAPTER 2

A Probabilistic Optimal Design of a Grid Connected Microgrid System

2.1. Introduction

In 2023, the total installed power generation in India reached 417 GW. The majority of the generation comes from the combustion of the fossil fuels. The installed capacity of the renewables is only 10-20%. As of now the power generation from the installed wind and solar sources are 42.86 GW and 67.07 GW, respectively. To improve the reliability of power supply, biomass generation can be added to wind and PV hybrid system. India is a land of agriculture; the issue with agricultural residue is its inefficient usage and these are burnt in the open fields in majority of the areas causing pollution, health issues and soil infertility. It is estimated that 1800-2500MW of power can be generated from these residues. The demand is rising each day and the fossil fuels are depleting. There is a need to achieve the objective of reducing emissions in the environment while ensuring cost reduction with increase in the installed generation capacity [1]. This has resulted in renewed interest and attention towards usage of renewable based hybrid energy systems (HES). The percentage growth of the RES is about 24% according to Ministry of Power, India. Due to the variable nature of the renewable sources, the key concerns for designing of HRES are power management, system's reliability and economic feasibility. To handle these sensible concerns there is a need to achieve multiple objectives and design renewable energy based hybrid system using a proper methodology [1].

In recent years several investigations have been carried out on optimal sizing of the HRES. Majority of these studies are focused on the modelling of off-grid HRES [2-6]. By integrating these systems to the utility grid, the system becomes more reliable since the grid acts as backup to the hybrid system. However, integration of HRES to the grid still remains a challenging job due to the intermittent, variable, and stochastic nature of the RES, which cause frequency deviation, load mismatch, and voltage instability [7,8]. Therefore, energy storage systems (ESS) gained more importance in the integration of microgrid to the grid [9,10,11]. Different methods are employed for optimal design of grid integrated microgrid. In [12] the authors proposed a methodology to minimize the power fluctuations of hybrid system by introducing pumped energy storage. Basaran et al. [13] presented a PV, wind, and battery based grid integrated system designed to power small loads. The authors did not consider cost

optimization or reliability. Bidairi et al. [14] presented a fuzzy logic- grey wolf optimization technique with an objective to minimize the operating cost of hybrid system. In [15,16] PV-battery-grid integrated system is designed based on cost minimization and maximization of utilization of the sources. However, detailed cost analysis and the time varying nature of the renewable sources and load are not considered. Singh and Kaushik [17] proposed a methodology based on the ABC algorithm considering the annualized cost of the system as the objective for optimal hybrid system design. In [18] authors proposed a PV, wind and battery hybrid grid integrated micro-grid system which reduces the annual cost and maximizes the reliability without considering the varying nature of the load. To design reliable grid integrated hybrid system, proper mathematical modelling is required [19,20] and the stochastic nature of the resources should be characterized. Probability density functions (PDF) are needed to model the stochastic nature of the resources [21-23]. In [24,25] the authors used PDFs for the analysis of the HRES. Giuseppe et al. [26] used probability density function (PDF) to compute power produced by a PV system equipped with tracking system and a wind energy conversion system. But they did not consider in the design of HRES. Inclusion of biomass generation in hybrid system which improves the reliability [20], is not considered in many of the above mentioned optimal HRES designs.

To overcome the drawbacks in the existing literature, in this study, a PV-wind-biomass based grid integrated system with ESS presented in Fig. 2.1 is proposed using a multi-objective artificial cooperative search algorithm (MOACS). Optimal HRES is designed based on the key essentials of annual cost minimization and reliability maximization (reliability measured in terms of loss of power supply probability (LPSP)) [2,4,5]. Solar and wind based power generation in HRES is intermittent in nature. Hence, one of the major challenges of HRES design involving solar and wind generations is satisfying the load demand at all times irrespective of generation uncertainty. Therefore, minimization of LPSP [27,28], which is a measure of reliability in serving the load demand, is considered as an objective in this study. Detailed mathematical modelling of RES is considered for optimal HRES design. The battery energy storage system (BESS) is chosen to supply the peak load demand for at least 30 minutes during the non-availability of power from the renewable energy sources. Further, the results obtained with the MOACS are compared with the standard multi-objective algorithm NSGA-II [29] as well as improved multi-objective harmony search (IMOHS) [30] algorithm.

The main contributions of this work are summarized as:

- Consideration of the probabilistic nature of the generation and load in optimal microgrid design which provides better and reliable operation of microgrid system.

- Probabilistic models are blended with a multi-objective meta-heuristic algorithm to develop a probabilistic approach for optimal design of grid integrated hybrid renewable energy system using locally available resources to fulfil the load demand.
- The proposed probabilistic approach is able to serve the load demand with less unit cost. MOACS, which is capable to solve multi-objective optimization problems, is employed to find the optimal sizing of the grid-integrated hybrid renewable energy system by minimizing the annual life cycle costing (ALCC) and LPSP.
- The comparison metrics analysis of the proposed approach using MOACS with NSGA-II and IMOHS indicates the reliability of the hybrid system.

This chapter is organized in 6 sections. Modelling of renewable energy sources using probabilistic power generation models for solar, wind and load is explained in section 2.2, problem formulation is discussed in section 2.3 and proposed approach using the MOACS algorithm is presented in section 2.4. Results obtained by the MOACS, NSGA-II, and IMOHS algorithms are discussed in section 2.5 and finally the conclusion of this work is presented in section 2.6.

2.2. Modelling of Grid Integrated Hybrid System

The proposed system consists of biomass, wind, PV, batteries and utility grid. For efficient design of HRES system, accurate modelling of sources and load is required. Mathematical modelling of renewable sources is complex as the power generation from these sources is highly dependent on the meteorological conditions. Hence, in this work probabilistic models are used in HRES design to account for their time varying and stochastic nature. In this section modelling of HRES is presented.

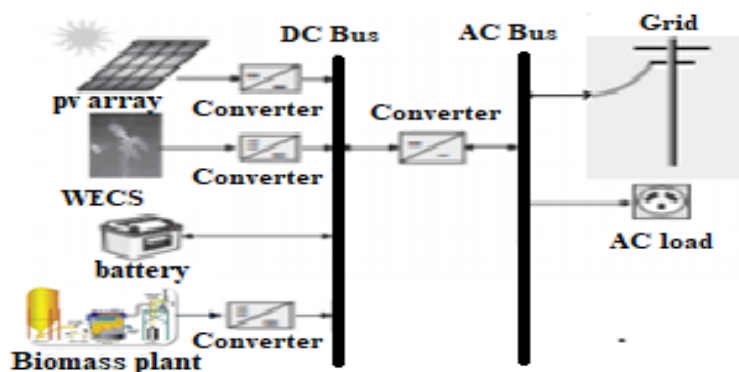


Fig. 2.1. Grid integrated Hybrid system.

2.2.1. Modelling of Solar PV system

Different PDFs such as Weibull, Beta, Gama, Generalized extreme value (GEV) and lognormal PDFs have been used to model the solar irradiance in this work. Goodness-of-fit tests such as Kolmogorov-Smirnov test (K-S test) and R^2 test [24] are used to measure deviation between measured statistical distribution and modelled distribution. A larger value of R^2 and lesser value of K-S for a PDF indicate that the particular PDF models the data accurately.

For example, for the month of April at typical hour 9, solar irradiance histogram (measured statistical distribution) along with modeled distributions is shown Fig. 2.2. It can be seen that Weibull distribution closely fits the histogram compared to other distributions. K-S test and R^2 test errors are tabulated in Table 2.1 from which it can be seen that Weibull PDF models the solar irradiance distribution more accurately than other PDFs. Similarly, for every hour in every month this analysis was carried out and finally Weibull PDF is chosen considering a typical day (24 hourly PDFs) in every month. For 12 months, 288 PDFs are used (12 months \times 24 PDFs). The obtained shape parameters (k) and scale parameters (c) for each month are tabulated in Table 2.2 and Table 2.3.

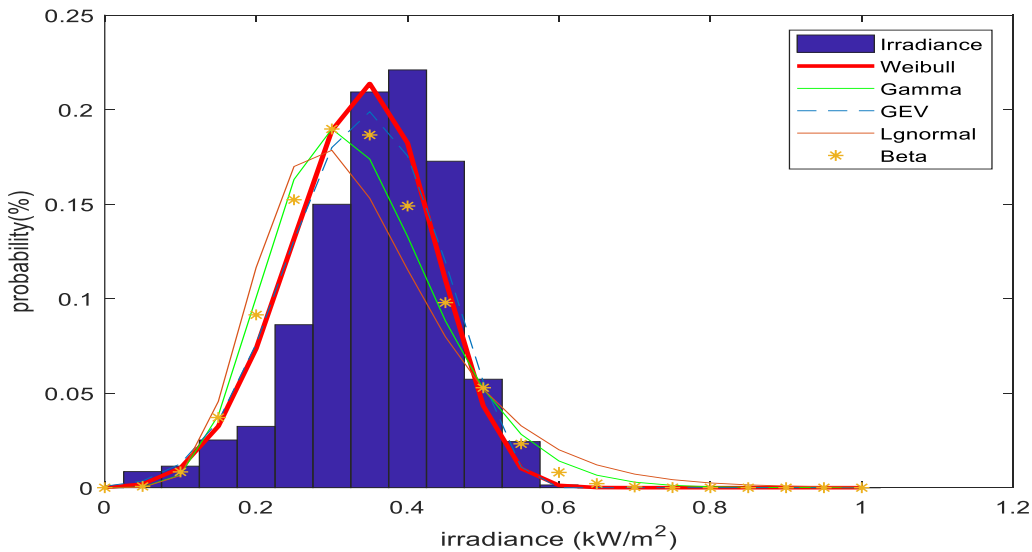


Fig. 2.2. Predicted and observed solar irradiance distribution.

Table 2.1. Statistical errors for different distribution functions for solar irradiance

PDF	K-S error	R^2
Weibull	0.0338	0.9957
Beta	0.0768	0.9768
Gama	0.0972	0.9515
Lognormal	0.1205	0.9131
GEV	0.0423	0.9831

Table 2.2. Solar data parameters from January to June

	January		February		March		April		May		June	
Hrs	<i>k</i>	<i>c</i>	<i>k</i>	<i>c</i>	<i>k</i>	<i>c</i>	<i>k</i>	<i>c</i>	<i>k</i>	<i>c</i>	<i>k</i>	<i>c</i>
1	NAN	NAN	NAN	NAN	NAN	NAN	NAN	NAN	NAN	NAN	NAN	NAN
2	NAN	NAN	NAN	NAN	NAN	NAN	NAN	NAN	NAN	NAN	NAN	NAN
3	NAN	NAN	NAN	NAN	NAN	NAN	NAN	NAN	NAN	NAN	NAN	NAN
4	NAN	NAN	NAN	NAN	NAN	NAN	NAN	NAN	NAN	NAN	NAN	NAN
5	NAN	NAN	NAN	NAN	NAN	NAN	NAN	NAN	NAN	NAN	NAN	NAN
6	NAN	NAN	NAN	NAN	NAN	NAN	1.8172	1.785	1.7157	2.507	1.4883	2.252
7	1.2145	7.865	1.1512	9.8432	0.9918	12.954	0.9602	29.27	1.2282	48.16	1.1163	39.35
8	1.9887	102.4	2.1717	129.0	2.1312	134.2	2.5336	184.4	2.5132	206.5	1.9278	168.5
9	3.777	294.7	4.4584	354.1	3.9977	351.8	4.5257	395.0	3.3191	398.2	2.3264	342.3
10	5.7623	501.0	7.1702	577.9	6.266	574.7	6.2698	605.6	4.2441	595.2	2.7779	517.2
11	6.1728	660.4	11.113	756.8	8.1745	759.2	8.8096	781.6	5.5683	763.4	3.1276	664.9
12	6.7334	764.7	13.468	866.0	9.5172	876.7	11.621	895.9	5.7617	867.9	2.9604	723.4
13	8.3656	804.2	14.064	899.0	11.563	938.0	11.981	925.5	5.9894	902.8	2.8301	742.7
14	6.9069	760.8	14.588	859.3	11.557	923.1	12.516	911.9	5.9454	879.1	2.7551	718.2
15	6.3285	646.0	11.676	750.2	8.5537	833.2	9.5878	825.7	5.1649	790.9	2.6218	634.8
16	4.9469	474.5	7.9213	568.0	6.4446	679.5	7.2307	669.3	3.8643	622.6	2.6871	523.3
17	3.2166	264.8	4.449	343.9	5.0955	475.3	5.604	462.7	2.955	427.2	2.508	390.1
18	1.4292	72.91	2.1833	122.9	3.1452	246.4	3.2783	251.2	2.4164	232.7	2.1165	214.7
19	1.3066	4.23	1.2361	8.7219	1.2613	54.7	1.3464	62.31	1.4961	68.08	1.595	72.55
20	NAN	NAN	NAN	NAN	1.7097	2.4076	1.4029	3.189	1.232	5.62	1.1966	7.020
21	NAN	NAN	NAN	NAN	NAN	NAN	NAN	NAN	NAN	NAN	NAN	NAN
22	NAN	NAN	NAN	NAN	NAN	NAN	NAN	NAN	NAN	NAN	NAN	NAN
23	NAN	NAN	NAN	NAN	NAN	NAN	NAN	NAN	NAN	NAN	NAN	NAN
24	NAN	NAN	NAN	NAN	NAN	NAN	NAN	NAN	NAN	NAN	NAN	NAN

Weibull PDF is used to characterize the stochastic behaviour of the solar irradiance as it provided good fit (less K-S error, and high R^2 value [25]) for the irradiance data of the chosen site compared to Beta, Gama, lognormal and GEV PDFs. At any timeframe ' t ', the Weibull distribution for the solar irradiance s (W/m²) is given by Equation (2.1), the shape parameter (k^t) and the scale factor (c^t) are calculated at time frame ' t ' using the maximum likelihood estimation (MLE) method.

$$f(s_t) = \frac{k^t}{c^t} \cdot \left(\frac{s^t}{c^t}\right)^{k^t-1} \cdot \exp\left(-\left(\frac{s^t}{c^t}\right)^{k^t}\right) \text{ for } c^t > 1; k^t > 0 \quad (2.1)$$

To analyse the solar PV output power, the continuous PDF is divided into different states for a particular time frame. Solar irradiance will be within limits in each state, the probabilities of all possible states for that particular hour are obtained and these probabilities are used to obtain power generation in the t^{th} time segment. The average power output of the solar PV array for a particular time frame ' t ' or hour is given by

$$P_{pv}(t) = \sum_{st=1}^{N_S} P_{pv_{st}} \times P_S(s_{st}^t) \quad (2.2)$$

As shown in equation 2.3, each hour is divided into N_s number of states, i.e. from state 1 to state N_s , where N_s is the highest state number. Each state will have the probability of the average solar irradiance and the overall probability can be obtained from the probabilities of the all states in that particular hour ‘ t ’. Hence, during any particular time frame or any particular hour ‘ t ’, for a given state, the solar irradiance probability can be expressed as (2.3).

$$P_s(s_{st}^t) = \begin{cases} \int_0^{(s_{st}^t + s_{st+1}^t)/2} f(s_t) ds & \text{for } st = 1 \\ \int_{(s_{st-1}^t + s_{st}^t)/2}^{(s_{st}^t + s_{st+1}^t)/2} f(s_t) ds & \text{for } st = 2, \dots, (N_s - 1) \\ \int_{(s_{st-1}^t + s_{st}^t)/2}^{\infty} f(s_t) ds & \text{for } st = N_s \end{cases} \quad (2.3)$$

Power generated by PV array with the average solar irradiance (i.e. if a state represents solar irradiance (W/m^2) lying between 0 to 100, then the average (S_{st}^t) will be $50 \text{ W}/\text{m}^2$) for st^{th} state is calculated as

$$P_{pv_{st}} = N_{pv} \cdot f_{pv} \cdot \eta_{mppt} \cdot ff \cdot I_{sc}(st) \cdot V_{oc}(st) \quad (2.4)$$

Table 2.3. Solar data parameters from July to December

Hrs	July		August		September		October		November		December	
	k	c	k	c	k	c	k	c	k	c	k	c
1	NAN	NAN	NAN	NAN	NAN	NAN	NAN	NAN	NAN	NAN	NAN	NAN
2	NAN	NAN	NAN	NAN	NAN	NAN	NAN	NAN	NAN	NAN	NAN	NAN
3	NAN	NAN	NAN	NAN	NAN	NAN	NAN	NAN	NAN	NAN	NAN	NAN
4	NAN	NAN	NAN	NAN	NAN	NAN	NAN	NAN	NAN	NAN	NAN	NAN
5	NAN	NAN	NAN	NAN	NAN	NAN	NAN	NAN	NAN	NAN	NAN	NAN
6	2.5563	1.4	2.1835	1.706	1.5996	2.13	NAN	NAN	NAN	NAN	NAN	NAN
7	0.9839	26.37	0.9461	20.9	0.8767	21.0	0.9336	23.49	0.9292	13.4164	1.0241	11.0419
8	1.9298	143.6	1.8121	132.4	1.7565	146.9	2.2593	167.7	1.7138	118.3102	1.8197	113.5052
9	2.3731	313.6	2.2654	324.7	2.1484	322.1	3.317	374.7	2.437	289.6865	2.8455	298.3613
10	2.8169	473.4	2.7644	507.7	2.55	511.1	4.3889	582.0	2.6337	467.1448	3.5132	483.9472
11	2.9293	593.8	2.8742	653.3	2.4372	644.2	5.2565	741.8	2.5558	600.3559	4.438	635.6401
12	2.5937	639.8	2.5445	700.6	2.3867	718.3	4.8985	829.1	3.0276	703.6943	4.7168	726.3297
13	2.491	656.6	2.3431	701.0	2.3537	733.6	4.7803	861.7	2.9316	715.6866	5.3731	758.2688
14	2.3785	656.8	2.1765	655.6	2.2783	700.5	4.4566	808.7	2.5711	664.6639	5.0076	693.9959
15	2.3978	593.0	2.0425	565.5	2.1491	602.1	4.1401	699.1	2.5284	559.8439	4.3861	574.3767
16	2.3516	478.1	2.264	491.8	2.0151	470.1	3.6379	533.7	2.429	411.9572	3.6588	396.3934
17	2.1717	344.4	2.101	355.5	1.9215	312.4	2.8798	330.4	1.9867	237.267	2.4994	192.9432
18	2.0824	203.2	1.937	202.6	1.6699	151.04	1.9546	132.4	1.521	79.9604	0.9341	31.321
19	1.5753	76.6	1.3695	59.0	0.9481	29.35	0.9454	13.98	1.1957	7.2371	2.2214	1.657
20	1.1995	7.73	1.1449	5.2	1.5741	2.520	NAN	NAN	NAN	NAN	NAN	NAN
21	NAN	NAN	NAN	NAN	NAN	NAN	NAN	NAN	NAN	NAN	NAN	NAN
22	NAN	NAN	NAN	NAN	NAN	NAN	NAN	NAN	NAN	NAN	NAN	NAN
23	NAN	NAN	NAN	NAN	NAN	NAN	NAN	NAN	NAN	NAN	NAN	NAN
24	NAN	NAN	NAN	NAN	NAN	NAN	NAN	NAN	NAN	NAN	NAN	NAN

$$ff = (V_{oc} \cdot I_{sc}) / (V_{stc} \cdot I_{stc}) \quad (2.5)$$

The variation of I_{sc} and V_{oc} with temperature and irradiance is given by (2.6) - (2.8).

$$I_{sc}(st) = I_{stc} + k_i \cdot (T_{cell}(st) - T_{stc}) \cdot (s_{st}^t / s_{stc}) \quad (2.6)$$

$$V_{oc}(st) = V_{stc} + k_v \cdot (T_{cell}(st) - T_{stc}) \quad (2.7)$$

$$T_{cell}(st) = T_a + (s / s_{stc}) \cdot (T_{Noct} - T_{aNoct}) \quad (2.8)$$

2.2.2. Modelling of Wind Energy System

Different PDFs have been used such as Weibull, Gama, Generalized extreme value (GEV) and lognormal PDFs to model the statistical wind speed. For example, for the month of April at typical hour 17, the wind speed histogram (measured statistical distribution) along with modelled distributions is shown in Fig. 2.3. It can be seen that Weibull distribution closely fits the histogram compared to other distributions. K-S test and R^2 test errors are tabulated in Table 2.4 from which it can be observed that Weibull PDF models the wind speed distribution more accurately than other PDFs. Similarly, for every hour in every month this analysis was carried out and finally Weibull PDF is chosen and the obtained shape parameters (k) and scale parameters (c) are tabulated in Table 2.5 and Table 2.6.

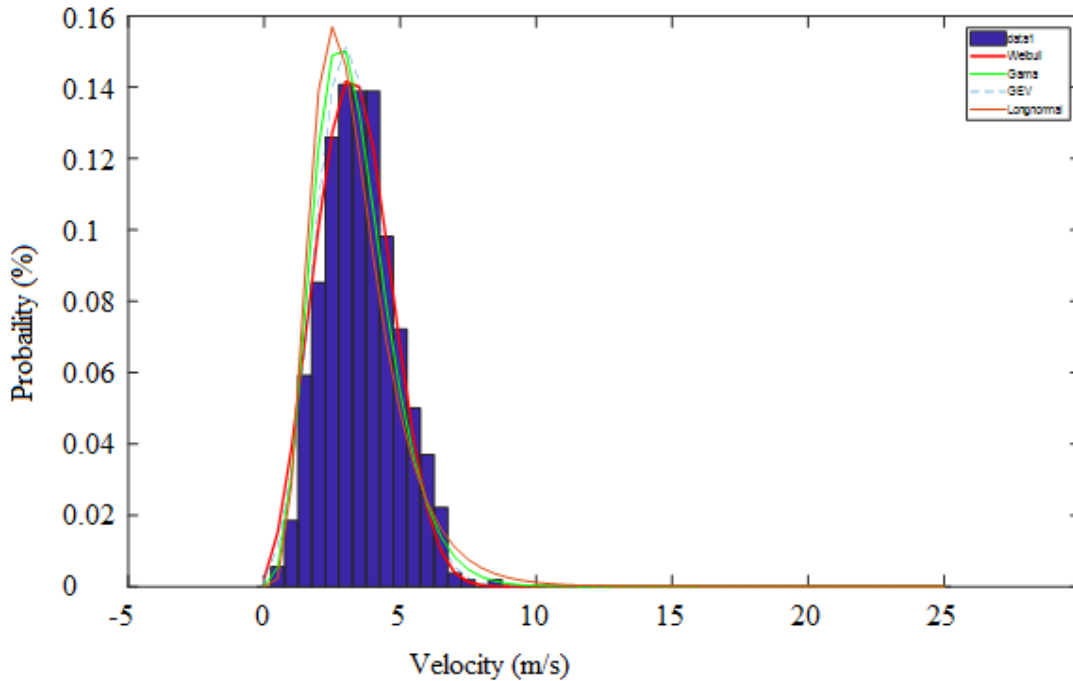


Fig. 2.3. Predicted and observed wind speed distribution.

Table 2.4. Statistical errors for different distribution functions for wind speeds

PDF	K-S error	R ²
Weibull	0.0245	0.9991
Gama	0.0571	0.9899
Lognormal	0.0686	0.9768
GEV	0.0313	0.9986

Table 2.5. Wind data parameter from January to June

Hrs	January		February		March		April		May		June		
	<i>k</i>	<i>c</i>	<i>k</i>	<i>c</i>	<i>k</i>	<i>c</i>	<i>k</i>	<i>c</i>	<i>k</i>	<i>c</i>	<i>k</i>	<i>c</i>	
1	5.553	7.183	5.673	7.416	4.925	6.751	3.8622	5.8804	2.8569	7.5443	5.2152	10.8863	
2	4.803	6.871	5.264	7.078	4.951	6.395	3.30	3	5.7956	2.7639	7.7828	5.7846	10.8789
3	4.316	6.427	4.470	6.661	4.650	6.021	3.2595	5.519	2.9509	8.1187	6.3323	10.8134	
4	3.985	6.011	3.830	6.273	4.449	5.699	3.1309	5.3925	2.9985	8.1494	6.4597	10.8257	
5	4.018	5.681	3.501	5.863	3.854	5.404	2.9857	5.0607	2.8889	8.0211	6.3733	10.4246	
6	3.68	5.330	3.211	5.408	3.893	5.040	2.7106	4.819	2.9356	7.8658	6.1928	10.1223	
7	3.489	4.978	3.238	4.915	3.405	4.721	2.8765	4.6725	2.9456	7.697	6.1296	9.9546	
8	3.251	4.675	3.033	4.569	2.794	4.363	2.533	4.5345	2.5754	7.4325	5.1555	9.4	
9	2.703	4.058	2.830	4.070	2.544	3.757	2.3264	4.1255	2.534	7.4801	5.105	9.8261	
10	2.863	3.489	2.488	3.757	2.246	3.557	2.3177	3.8535	2.8238	7.4342	4.8805	10.3883	
11	3.153	3.990	2.693	4.092	2.649	3.850	2.484	3.7017	2.9706	7.0722	4.6158	10.4243	
12	3.411	4.619	3.201	4.448	2.799	4.112	2.739	3.5213	2.8634	6.6893	4.3779	10.3842	
13	3.641	4.929	3.677	4.746	2.771	4.484	2.9619	3.4352	2.8525	6.1798	4.1923	10.4164	
14	3.832	5.114	3.359	4.974	3.006	4.882	2.8563	3.6803	2.9212	5.8283	3.8212	10.3116	
15	3.787	5.207	3.312	5.187	3.124	5.192	2.9125	3.9886	2.788	5.5142	3.4351	10.2154	
16	3.945	5.362	3.577	5.357	3.422	5.511	3.0369	4.2839	2.6838	5.4287	3.2461	10.1578	
17	4.182	5.569	3.694	5.568	3.357	5.784	3.1887	4.64	2.3118	5.3191	3.5526	10.1185	
18	4.458	6.077	4.173	6.023	3.351	6.225	2.9956	5.1651	2.284	5.3893	3.2286	10.3162	
19	5.529	6.793	4.513	6.834	3.707	6.966	2.9229	6.1609	2.0854	5.4379	3.053	10.6054	
20	6.925	7.544	5.484	7.590	4.633	7.791	3.1956	6.6219	2.3752	5.8299	3.4675	11.1039	
21	9.844	8.095	7.304	8.235	5.602	8.337	3.738	7.147	2.2974	6.7026	4.321	11.2834	
22	9.248	8.265	7.253	8.422	6.162	8.436	4.1787	7.4638	2.6164	7.1702	5.1172	11.1963	
23	7.652	8.016	7.148	8.129	5.262	7.948	4.6082	7.0307	2.6124	7.1967	5.4408	11.0461	
24	6.590	7.523	5.950	7.741	5.145	7.364	4.1011	6.557	2.6854	7.3891	5.3962	11.0791	

Weibull PDF is suited to express the wind speed stochastic behavior [24], as it provides good fit for the wind speed distribution at the chosen site. Weibull PDF for the wind speed v (m/s) for any time frame ‘ t ’ can be expressed as

$$f(v_t) = \frac{k^t}{c^t} \cdot \left(\frac{v^t}{c^t}\right)^{k^t-1} \cdot \exp\left[-\left(\frac{v^t}{c^t}\right)^{k^t}\right] \text{ for } c^t > 1; k^t > 0 \quad (2.9)$$

Average output power of the wind turbine for a particular time frame ‘ t ’ or a particular hour is given by

$$P_{wt}(t) = \sum_{st=1}^{N_y} P_{wt_{st}} \times P_v(v_{st}^t) \quad (2.10)$$

Table 2.6. Wind data parameter from July to December

Hrs	July		August		September		October		November		December	
	<i>k</i>	<i>c</i>	<i>k</i>	<i>c</i>	<i>k</i>	<i>c</i>	<i>k</i>	<i>c</i>	<i>k</i>	<i>c</i>	<i>k</i>	<i>c</i>
1	0.807	4.17	4.428	10.236	2.971	7.626	2.486	5.158	0.950	3.6647	4.1263	6.3649
2	0.793	4.168	3.972	9.816	3.455	7.950	2.373	5.063	0.958	3.4002	3.8894	6.0747
3	0.788	4.06	4.059	9.574	3.738	8.132	2.248	5.036	0.974	3.1843	3.6411	5.6403
4	0.786	3.987	4.943	9.428	4.565	8.193	2.103	4.979	0.971	3.0322	3.5499	5.3175
5	0.757	3.801	4.454	9.174	5.281	8.015	2.161	4.942	0.964	2.8053	3.1504	4.9974
6	0.731	3.653	4.539	8.962	5.011	7.941	2.143	4.956	1.014	2.6158	2.8286	4.5962
7	0.726	3.576	4.643	8.712	4.532	7.784	2.067	4.795	0.990	2.4698	2.812	4.3368
8	0.777	3.695	4.812	8.24	4.690	7.345	1.801	4.553	0.985	2.3106	2.6184	4.104
9	0.851	4.012	4.002	8.901	3.924	7.242	1.823	4.220	1.172	2.1174	2.2022	3.5839
10	0.860	4.245	4.173	9.785	3.883	7.689	1.886	4.138	1.267	2.1221	2.0868	3.2032
11	0.904	4.562	4.010	10.047	3.430	7.803	2.095	4.584	1.261	2.6021	2.2928	3.6596
12	0.925	4.644	3.651	9.767	2.986	7.710	2.198	4.818	1.351	2.9774	2.8631	4.353
13	0.934	4.781	3.56	9.957	2.820	7.768	2.389	4.952	1.472	3.1949	3.3515	4.8062
14	0.942	4.770	3.356	9.891	2.791	7.563	2.541	5.055	1.508	3.2512	3.6638	4.9238
15	0.936	4.663	3.22	9.875	2.730	7.401	2.696	4.992	1.556	3.318	4.0398	5.0169
16	0.915	4.657	3.246	9.787	2.982	7.223	2.519	5.050	1.442	3.2578	4.1652	5.1368
17	0.904	4.660	3.223	9.939	2.746	7.239	2.243	5.194	1.404	3.2967	4.584	5.2297
18	0.854	4.472	2.811	9.725	2.452	6.863	2.429	5.309	1.285	3.4318	4.6406	5.381
19	0.804	4.196	2.894	9.639	2.466	6.677	2.588	5.347	1.122	3.6568	4.5748	5.8213
20	0.774	4.177	3.315	9.383	2.250	6.499	2.365	5.392	1.119	3.8831	4.5472	6.4047
21	0.778	4.211	3.332	9.751	2.346	6.648	2.452	5.398	1.054	4.0382	4.4632	6.7873
22	0.801	4.140	3.617	9.947	2.544	6.991	2.344	5.300	1.024	4.0265	4.8338	6.8892
23	0.822	3.937	3.678	10.076	2.301	6.990	2.408	5.458	1.019	4.0256	4.953	6.8995
24	0.8259	3.983	3.901	10.333	2.576	7.325	2.346	5.479	0.999	3.8283	4.6113	6.6052

The power generation of the wind turbine (WT) depends on the velocity of the wind at that particular time. Therefore, the power generated by WT at the average wind speed v_{st}^t for any state st is determined as

$$P_{wt_{st}} = \begin{cases} p_{rw} \cdot N_w \cdot \left(\frac{v_{st}^t - v_{ci}}{v_r - v_{ci}} \right)^3 & \text{for } v_{ci} < v_{st}^t < v_r \\ p_{rw} \cdot N_w & \text{for } v_r < v_{st}^t < v_{co} \\ 0 & \text{else} \end{cases} \quad (2.11)$$

The probability of the wind speed for a given state during any particular time frame or any particular hour is given as [21]

$$P_v(v_{st}^t) = \begin{cases} \int_0^{(v_{st}^t + v_{st+1}^t)/2} f(v_t) ds & \text{for } st=1 \\ \int_{(v_{st}^t + v_{st+1}^t)/2}^{(v_{st}^t + v_{st+1}^t)/2} f(v_t) ds & \text{for } st=2 \dots (N_v - 1) \\ \int_{(v_{st-1}^t + v_{st}^t)/2}^{\infty} f(v_t) ds & \text{for } st=N_v \\ \int_{(v_{st-1}^t + v_{st}^t)/2}^{(v_{st-1}^t + v_{st}^t)/2} f(v_t) ds & \text{for } st=N_v \end{cases} \quad (2.12)$$

2.2.3. Modelling of Biomass Gasifier

A thermochemical conversion technology is used to convert biomass into clean and cool gas by partial combustion under restricted air supply. This produced gas is used as an input for the fuel engine to generate electricity. In this study, 10 kW rated biomass gasifier is considered which is operated 12 hours per day during the peak load. The total annual biomass energy generated [20] is given by (2.13).

$$E_{bio} = N_{bio} \times P_{bio} \times t_w \quad (2.13)$$

The maximum rating of the gasifier depends on the total available biomass in a year, the calorific value of biomass and on the efficiency of biomass gasifier which is given by (2.14).

$$P_{bio}^{max} = \frac{total_agriwaste * 1000 * CV_{bm} * \eta_{bio}}{860 * t_w} \quad (2.14)$$

2.2.4. Load Modelling

To model the load data different PDFs has been used and it is observed that Normal PDF [23] is giving good fit for the load demand hence Normal PDF is chosen for modeling the load data. The obtained mean (μ) and the standard deviation (σ) are given in Tables Table 2.7 and Table 2.8. Normal probability distribution function is used to describe the probabilistic character of the load [23] since it follows a normal PDF. Normal PDF for load demand (kW) over any time frame 't' is described as

$$f(x | \mu, \sigma^2) = \frac{1}{\sqrt{2\pi\sigma^2}} \left(-\frac{(x-\mu)^2}{2\sigma^2} \right) \quad (2.15)$$

$P_t(l_{st}^t)$ (probability of load demand of a given state during any time frame 't') is given by

$$P_t(l_{st}^t) = \begin{cases} \int_0^{(l_{st}^t + l_{st+1}^t)/2} f(x | \mu, \sigma^2) ds & \text{for } st = 1 \\ \int_{(l_{st}^t + l_{st+1}^t)/2}^{(l_{st}^t + l_{st+1}^t)/2} f(x | \mu, \sigma^2) ds & \text{for } st = 2 \dots (N_t - 1) \\ \int_{(l_{st-1}^t + l_{st}^t)/2}^{\infty} f(x | \mu, \sigma^2) ds & \text{for } st = N_t \\ \int_{(l_{st-1}^t + l_{st}^t)/2}^{(l_{st-1}^t + l_{st}^t)/2} f(x | \mu, \sigma^2) ds & \text{for } st = N_t \end{cases} \quad (2.16)$$

Table 2.7. Load data parameters from January to June

Hrs	January		February		March		April		May		June	
	μ	σ	μ	σ	μ	σ	μ	σ	μ	σ	μ	σ
1	0.57	0.0555	0.6064	0.0414	0.634	0.094	0.6453	0.0481	0.6812	0.5558	0.5558	0.0897
2	0.5541	0.0527	0.5954	0.0349	0.6107	0.0872	0.6106	0.0462	0.654	0.5495	0.5495	0.0757
3	0.5386	0.0459	0.5764	0.0347	0.5894	0.0824	0.5808	0.0363	0.6408	0.5459	0.5459	0.0701
4	0.5239	0.0463	0.5742	0.0382	0.5767	0.0757	0.5517	0.049	0.628	0.5429	0.5429	0.0678
5	0.5148	0.0458	0.5714	0.0423	0.5669	0.0719	0.5453	0.0362	0.613	0.5436	0.5436	0.0569
6	0.5111	0.0437	0.5682	0.0441	0.5525	0.0656	0.5305	0.038	0.5724	0.5411	0.5411	0.0691
7	0.4981	0.0427	0.5454	0.0478	0.5133	0.0481	0.5086	0.0435	0.5413	0.5269	0.5269	0.0645
8	0.4708	0.0451	0.5129	0.0469	0.4824	0.0526	0.4967	0.0616	0.5143	0.5602	0.5602	0.1009
9	0.425	0.0458	0.4782	0.0488	0.4553	0.0552	0.4681	0.0552	0.4947	0.5849	0.5849	0.1062
10	0.4116	0.0388	0.4591	0.0474	0.4514	0.0442	0.4619	0.0692	0.4851	0.5948	0.5948	0.0879
11	0.4095	0.0443	0.458	0.061	0.4573	0.055	0.4726	0.0571	0.4801	0.6204	0.6204	0.1112
12	0.4085	0.0385	0.4654	0.0645	0.468	0.0635	0.4947	0.0577	0.4911	0.6586	0.6586	0.112
13	0.4136	0.0386	0.4666	0.0483	0.4743	0.0736	0.5072	0.0701	0.5148	0.7195	0.7195	0.1205
14	0.4168	0.0383	0.4583	0.0564	0.4864	0.0927	0.5237	0.0769	0.5277	0.7526	0.7526	0.1106
15	0.422	0.0545	0.4745	0.0514	0.496	0.0901	0.566	0.0856	0.5267	0.7543	0.7543	0.1104
16	0.4303	0.0913	0.4963	0.0713	0.5101	0.0936	0.5574	0.0757	0.5532	0.7274	0.7274	0.1272
17	0.4758	0.1185	0.5751	0.1013	0.5469	0.1189	0.5504	0.0917	0.5682	0.77	0.77	0.1083
18	0.7287	0.1281	0.7073	0.1273	0.6685	0.1257	0.5927	0.1078	0.5474	0.7617	0.7617	0.1062
19	0.8023	0.1061	0.8217	0.1131	0.819	0.0968	0.6937	0.1381	0.5658	0.7422	0.7422	0.1355
20	0.8197	0.0728	0.8505	0.0718	0.8514	0.0705	0.7677	0.1179	0.5912	0.7147	0.7147	0.1409
21	0.7734	0.0777	0.8292	0.0578	0.8159	0.0908	0.817	0.0976	0.6538	0.6671	0.6671	0.1333
22	0.7356	0.074	0.7833	0.0535	0.8033	0.1038	0.8126	0.08	0.6816	0.6231	0.6231	0.1291
23	0.6663	0.1014	0.7268	0.0473	0.7595	0.0999	0.758	0.0758	0.6888	0.6002	0.6002	0.1172
24	0.6266	0.0847	0.6851	0.0611	0.7188	0.0898	0.7229	0.0779	0.6882	0.5716	0.5716	0.1054

Table 2.8. Load data parameters from July to December

Hrs	January		February		March		April		May		June	
	μ	σ	μ	σ	μ	σ	μ	σ	μ	σ	μ	σ
1	0.5763	0.077	0.6551	0.1153	0.5288	0.0689	0.688	0.1821	0.6194	0.0424	0.5475	0.0897
2	0.5582	0.0644	0.6258	0.1065	0.5152	0.0618	0.6495	0.1677	0.6051	0.043	0.53	0.0895
3	0.5243	0.0595	0.5831	0.0978	0.4895	0.0649	0.6071	0.1416	0.5915	0.0378	0.5057	0.0978
4	0.5068	0.064	0.5569	0.0881	0.4799	0.0605	0.5843	0.134	0.5737	0.037	0.4827	0.0921
5	0.4983	0.0679	0.5339	0.079	0.4607	0.0575	0.555	0.1335	0.5616	0.04	0.459	0.0807
6	0.4739	0.0728	0.5107	0.0735	0.4375	0.045	0.5348	0.1314	0.5321	0.0499	0.4483	0.0724
7	0.4545	0.0758	0.4709	0.0652	0.424	0.0588	0.5279	0.1354	0.4861	0.0544	0.5269	0.0645
8	0.4375	0.0836	0.4459	0.0676	0.3871	0.0483	0.4997	0.1318	0.4519	0.043	0.4355	0.0853
9	0.431	0.085	0.4269	0.0749	0.3726	0.0403	0.4862	0.1223	0.4226	0.035	0.3913	0.0428
10	0.4375	0.1053	0.3976	0.0531	0.3647	0.0419	0.4706	0.0925	0.4212	0.0416	0.3786	0.0458
11	0.4359	0.1042	0.4031	0.0543	0.3571	0.0382	0.4517	0.0817	0.4117	0.0535	0.3676	0.045
12	0.4383	0.1198	0.407	0.0717	0.3893	0.048	0.4598	0.0709	0.4352	0.0646	0.3605	0.0518
13	0.4511	0.1286	0.4234	0.0574	0.408	0.0418	0.4627	0.0828	0.4398	0.0571	0.3712	0.0667
14	0.4689	0.1238	0.443	0.0614	0.4009	0.0383	0.4888	0.0922	0.4547	0.0678	0.3796	0.0709
15	0.46	0.1152	0.4567	0.0665	0.394	0.0402	0.4937	0.0836	0.4414	0.052	0.376	0.0639
16	0.4587	0.1009	0.4598	0.0688	0.3946	0.039	0.4852	0.083	0.4567	0.0562	0.3706	0.0629
17	0.492	0.101	0.4793	0.0916	0.4261	0.0516	0.5147	0.0849	0.5115	0.113	0.4535	0.1256
18	0.5696	0.1098	0.5265	0.0959	0.5612	0.0908	0.6157	0.1714	0.7545	0.1428	0.7584	0.0669
19	0.6576	0.0893	0.5985	0.1362	0.6711	0.0544	0.6608	0.1914	0.8291	0.1409	0.8073	0.063
20	0.7053	0.0969	0.6439	0.1229	0.6944	0.0471	0.6891	0.2093	0.865	0.0578	0.7841	0.0688
21	0.7313	0.083	0.7004	0.1296	0.6913	0.0762	0.7078	0.1848	0.8545	0.0698	0.7367	0.1101
22	0.7175	0.0984	0.727	0.103	0.6651	0.094	0.7448	0.1471	0.8106	0.0824	0.6849	0.1224
23	0.5582	0.0644	0.709	0.1021	0.6177	0.0949	0.7378	0.1569	0.7261	0.0801	0.63	0.1008
24	0.6662	0.1308	0.6935	0.1187	0.5762	0.0922	0.7207	0.1644	0.6748	0.0771	0.6001	0.1004

The hourly average load demand for a time segment ‘ t ’ is formulated as

$$P_l(t) = \sum_{st=0}^{N_l} P_{l_{st}} * P_l(l_{st}^t) \quad (2.17)$$

2.2.5. Battery Energy System Modelling

Lead–acid batteries are used in this study due to their short response time, low self-discharge rate (3-20%), high cycle efficiency (70-85%), and low capital cost. BESS is chosen to supply the peak load demand for at least 30 minutes [10]. To operate BESS in a reliable and efficient way, complete study of battery requirements while charging and discharging, energy loss, and efficiency is required. If the total energy generated from the PV, biomass, and wind is more than the energy demand then the battery bank will charge and whenever there is an energy deficit to meet the load, the energy stored in battery will supply the deficit energy to the load. The state of charge (SOC) (which represents the amount of energy stored in battery) controls the performance of the hybrid system.

2.2.5.1. State of Charge

The original state of charge of battery in charging mode is given by

$$SOC_{org}(t+1) = SOC(t) + \frac{I_{bat}(t) \cdot \Delta t}{C_{bat}} \quad (2.18)$$

But due to battery self-discharging rate (sdr) (which depends on health state of the battery and accumulated charge) and battery charge efficiency factor (η_c) the actual state of charge of battery is less than SOC_{org} and is described as

$$SOC(t+1) = SOC(t) \cdot (1 - sdr) + \frac{I_{bat}(t) \cdot \Delta t \cdot \eta_c(t)}{C_{bat}} \quad (2.19)$$

The charge efficiency factor is described as

$$\eta_c(t) = 1 - \exp \left[\frac{a \cdot (SOC(t) - 1)}{(I_{bat}(t) / I_{10} + b)} \right] \quad (2.20)$$

where working condition parameters of the battery (a , b , I_{10}) are considered as 20.73, 0.55, and

10 respectively. The charging current ($I_{bat}(t)$) at any time t can be derived for hybrid system (which gives the amount of excess power generated by RES after supplying the load) and is given by

$$I_{bat}(t) = \frac{P_{pv}(t) + P_{wt}(t) \cdot \eta_{re} + N_{bio} \cdot P_{bio}(t) \cdot \eta_{re} - (P_l(t) \cdot \eta_{in})}{Nb_{st} \cdot Nb_{se} \cdot V_{bat}} \quad (2.21)$$

To convert AC power generated by biomass and wind into constant voltage DC power, rectifier is used.

In the discharging process (when power obtained from RES is not adequate to supply the load) state of charge is given as

$$SOC_{org}(t+1) = SOC(t) - \frac{I_{bat}(t) \cdot \Delta t}{C_{bat}} \quad (2.22)$$

The actual state of charge is less than the original state of charge due to the self-discharge rate. The actual SOC is given as

$$SOC(t+1) = SOC(t) \cdot (1 - sdr) - \frac{I_{bat}(t) \cdot \Delta t}{C_{bat}} \quad (2.23)$$

where

$$I_{bat}(t) = \frac{(P_l(t) \cdot \eta_{in}) - (P_{pv}(t) + P_{wt}(t) \cdot \eta_{re} + N_{bio} \cdot P_{bio}(t) \cdot \eta_{re})}{Nb_{st} \cdot Nb_{se} \cdot V_{bat}}$$

$$Nb_{st} = \frac{\max(P_l) * 0.5}{Nb_{se} \cdot V_{bat} \cdot I_{bat,max}} \quad (2.24)$$

and

$$SOC_{min} \leq SOC(t) \leq SOC_{max} \quad (2.25)$$

$$I_{bat,max}(t) = \max\{0, \min[I_{max} \cdot C_{bat} \cdot (c \cdot (SOC_{max} - SOC(t)) + (SOC(t) - SOC_{min}) \cdot (1 - c)) / \Delta t]\} \quad (2.26)$$

where SOC_{max} is the SOC maximum value which is 1, SOC_{min} is the SOC minimum value which is chosen as 30%. The maximum achievable current rate of battery $I_{bat,max}$ at any given

point of time depends on the state of the battery. Here, I_{max} is considered as 20% of its nominal capacity for long life of battery, c is considered to be zero while discharging and it is chosen as 1 while charging.

2.3. Problem Formulation

Due to the high load demand, many of the conventional grids are unable to give continuous supply to a load, which results in power cuts in many areas. In addition, the depletion of fossil fuels is a major issue in recent years, which leads to an increase in focus on renewable technologies for power generation. In this work, a grid-integrated HRES is designed with an objective to reduce the cost and increase the reliability by reducing LPSP. The objectives are formulated as given in the following subsections.

2.3.1. Annual Life Cycle Costing

Minimization of the total annual life cycle cost (ALCC) of the microgrid integrated to grid is one of the objectives in this study which includes the total costs of PV, wind, biomass, battery, inverter (all costs are annualized) and also the grid sale and purchase cost (annual). The objective function is formulated as

$$f1 = ALCC = (\sum_{pv,wt,bio,b,inv} C_x) - C_{gs} + C_{gp} \quad (2.27)$$

The total cost (annualized) of each component (PV/wind/battery/biomass/inverter) includes capital cost, replacement cost, maintenance cost, and salvage cost (all costs are annualized) of that component. The detailed cost analysis for any component is given as

$$C_x = C_x^{acap} + C_x^{am} + C_x^{asg} + C_x^{arp} \quad (2.28)$$

where x could be PV/wind/ biomass/battery/ inverter.

2.3.1.1. Annualized Capital Cost

The annualized capital cost of any component (wind, PV, biomass, inverter, and battery bank) is computed by using the present worth factor (PWF) and capital cost as shown in (29).

$$C_x^{acap} = C_x^{cap} / PWF \quad (2.29)$$

PWF is present worth factor which is defined as

$$PWF = \frac{1+f}{i-f} * \left(1 - \left(\frac{1+f}{1+i} \right)^n \right) \quad (2.30)$$

2.3.1.2. Maintenance Cost

The repair cost, running cost and any other costs that are included in the maintenance cost of each component, is expressed as

$$C_x^{am} = C_x^m * N_x \quad (2.31)$$

2.3.1.3. Annualized Salvage Cost

The salvage value of a component at the end of the lifetime of the project is treated as salvage cost of that component. In this work, the salvage cost of every component is taken as 10% of its capital cost. The annualized salvage cost is formulated as

$$C_x^{asg} = C_x^{sg} / PWF \quad (2.32)$$

2.3.1.4. Annualized Replacement Cost

When the lifetime of the project is more than the lifetime of a component, then replacement of that component is required. PV panels, wind turbines, and biomass do not require replacement. In the designed microgrid, battery bank needs to be replaced every 5 years. For each replacement the annualized replacement cost is

$$C_x^{arp} = C_x^{rp} \left(\frac{1+f}{1+i} \right)^n / PWF \quad (2.33)$$

2.3.1.5. Energy Purchased from the Grid and Energy Sold to the Grid

Apart from these cost functions, in grid integrated microgrid, the bidirectional power flowing from the grid plays an effective role in the operation of the microgrid. The total cost of energy purchased from the utility grid is given as

$$C_{gp} = C_g^p * \sum_{t=1}^{8760} (P_{gp}(t)) \quad (2.34)$$

For grid integrated system, the total cost of the energy sold to the grid is

$$C_{gs} = C_g^s * \sum_{t=1}^{8760} (P_{gs}(t)) \quad (2.35)$$

Further unit cost of the electricity produced by the hybrid system is expressed as

$$Unit\ cost = \frac{ALCC(Rs / yr)}{Load\ served(kWh / yr)} \quad (2.36)$$

2.3.2. Loss of Power Supply Probability

Minimization of LPSP [2, 28] (which can be described as the probability of hybrid system not being able to serve the load demand) is considered as another objective in this study.

$$f_2 = LPSP = \frac{\sum_{t=1}^{8760} (P_t^{need} - P_t^{supplied})}{Total_load} \quad (2.37)$$

The following constraints are considered in this study.

$$\begin{aligned} N_{pv}^{\min} &\leq N_{pv} \leq N_{pv}^{\max}, & N_w^{\min} &\leq N_w \leq N_w^{\max} \\ N_{bio}^{\min} &\leq N_{bio} \leq N_{bio}^{\max}, & P_{gp}(t) &\leq P_{gp}^{\max} \\ P_{gs}(t) &\leq P_{gs}^{\max}, & P_{dump} &\leq P_{dump}^{limit} \end{aligned} \quad (2.38)$$

2.3.3. Operational Strategy

Weibull PDF and Normal PDF are chosen to model the stochastic nature of wind power, solar power and load considering a typical day (24 hourly PDFs) for every month. The hourly average power obtained from PV, wind and average load demand are computed as explained in section 2.2. Using 288 PDFs (12 months×24 PDFs) each for irradiance, wind speed and load, data for 8760 hours is synthesized. The power balance equation is shown in (2.39).

$$\Delta P_1(t) = (P_{wt}(t) \cdot \eta_{re} + P_{pv}(t) + N_{bio} P_{bio}(t) \cdot \eta_{re}) - P_l(t) / \eta_{inv} \quad (2.39)$$

The following strategy is used in this work for the HRES operation, which is depicted in the flowchart shown in Fig. 2.4.

- If power from RES is more than the load that is needed to be served (i.e. $\Delta P1(t) > 0$), the battery bank will be charged with the remaining power available after serving the load. If still there is any excess power, then it will be pumped into the grid. The amount of power sold to the grid is described as

$$P_{gs}(t) = (\Delta P1(t) - P_{bat_c_max}(t)) \eta_{inv} \quad (2.40)$$

The time frame chosen in this work is one hour. The maximum power sold to the grid should not be greater than the maximum allowable limit of the grid (P_{gs}^{max}). If it exceeds P_{gs}^{max} , the remaining power is wasted in the dump load.

- If power generated by the RES is not enough to meet the load (i.e. $\Delta P1(t) < 0$), then the energy stored in the battery will be used to serve the load up to its maximum limit, and $\Delta P2(t)$ is given as follows:

$$\Delta P2(t) = (P_{pv}(t) + P_{wt}(t) \cdot \eta_{re} + N_{bio} P_{bio}(t) \cdot \eta_{re}) + I_{bat,max} \cdot V_{bat} \cdot N_b - P_L(t) / \eta_{inv} \quad (2.41)$$

- If $\Delta P1(t) < 0$, & $\Delta P2(t) > 0$, the energy delivered from the battery bank is able to meet the deficit power ($\Delta P1(t)$).
- If $\Delta P1(t) < 0$, & $\Delta P2(t) < 0$, the energy delivered from the battery bank is also not sufficient to serve the load. Then the remaining power will be purchased from the grid. Power purchased from the grid is expressed as

$$P_{gp}(t) = P_L(t) - (P_{pv}(t) + P_{wt}(t) \cdot \eta_{re} + N_{bio} P_{bio}(t) \cdot \eta_{re} + P_{bat_d_max}(t)) \times \eta_{inv} \quad (2.42)$$

Nevertheless, the maximum amount of power purchased from the grid should not exceed the maximum grid purchased power P_{gp}^{max} . If it exceeds, then remaining deficit power will be treated as loss of power that is accounted for in LPSP.

2.3.4. Multi Objective Formation

If $f_1, f_2, f_3, \dots, f_n$ are the objective functions which are conflicting in nature, then the multi-objective optimization problem will be given as

$$\text{minimize } \{ f_1(x), f_2(x), \dots, f_n(x) \} \quad (2.43)$$

where $x \in R$ and n and x are the total number of objectives and decision vectors respectively, confined to the feasible search space R . As these objective functions $f_1, f_2, f_3, \dots, f_n$ are conflicting to each other, it is hard to get the single optimal solution which consists of all optimized objectives. Therefore, multiple non-dominated solutions (set of non-dominated solutions in objective space is referred as pareto front) can be obtained by using suitable algorithms. In this microgrid system, the objective functions f_1 (ALCC) and f_2 (LPSP) are conflicting in nature. Hence, a powerful algorithm is required to find optimal sizing of the grid-integrated microgrid system by minimizing the two objective functions.

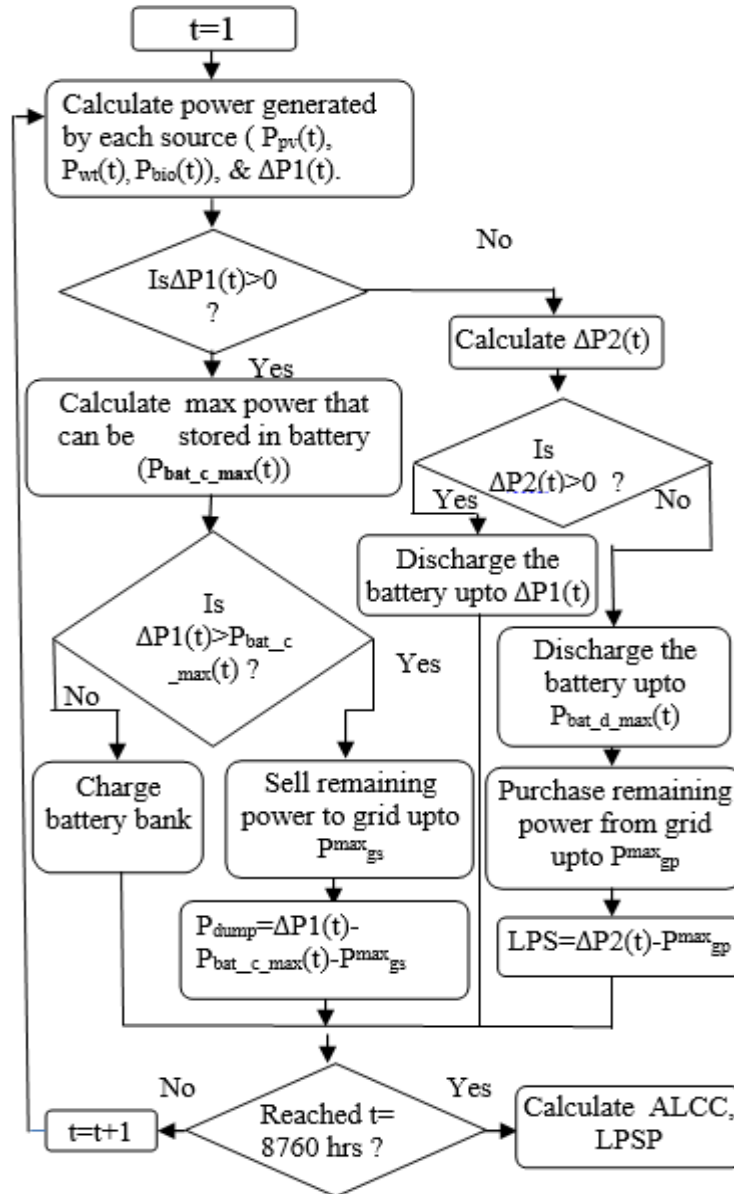


Fig. 2.4. Flowchart for operational strategy.

2.4. ACS Algorithm

In this work, Artificial cooperative search algorithm [19], which is able to solve single objective optimization problems, is modified as multi-objective artificial cooperative search algorithm (MOACS) to solve optimal hybrid system problem. In this section, detailed explanation about the basic ACS algorithm and the modifications done to it to solve multi-objective problem is given. In addition, application of MOACS for optimal HRES system design is explained.

2.4.1. Artificial Cooperative Search (ACS) Algorithm

ACS algorithm is inspired by the natural species or superorganisms (e.g. bird species, honey bees, butterflies). Many of the super organisms will go for seasonal migration in different areas to reach the food because the food available in that area is very vulnerable to climatic changes and is highly varied in nature. The steps of the algorithm are explained below.

Step 1: Initially define the objective function and initialize the population and its decision variables, boundary limits.

The objective function can be defined as

$$\text{Minimise } f(x)$$

$$\text{Subjected to } X_{i \text{ LOW}} \leq X_i \leq X_{i \text{ UP}} \quad (i=1,2,\dots,D)$$

Initialize the two superorganisms randomly subjected to its boundary limits by using the following equation.

$$\begin{aligned} A_{(i,j)} &= \text{low}_j + \text{rnd} \cdot (\text{up}_j - \text{low}_j) \\ B_{(i,j)} &= \text{low}_j + \text{rnd} \cdot (\text{up}_j - \text{low}_j) \end{aligned} \quad (2.44)$$

where $i=1,\dots,N$, where N is population size and $j=1,\dots,D$, dimension of the problem is D . Fitness value($f(x)\dots$) will be evaluated for each sub-superorganism (A,B).

Step 2: Two superorganisms A , B which consists of random solutions (sub-superorganisms) of related problem migrate to productive feeding areas. These superorganisms are used to detect the predator and prey randomly by using two random variables. If $\text{rnd1} < \text{rnd2}$ then the predator will be initialized with superorganism A and a key value of '1' is assigned for predator, otherwise the predator will be initialized with superorganism B and a key value of '2' is assigned for the predator. Similarly, prey is also

initialized.

Step 3: The superorganisms cooperate with each other and also, they interact biologically. When they are trying for global minimum of the problem, they undergo cooperation and biological interaction with each other. The organisms, which are involved in the biological interaction are known as active individuals. Their interaction depends on the scale factor R . The predator superorganism is updated by the biological interaction as follows:

$$X_{(i,j)} = predator_{(i,j)} + R.(prey_{(i,j)} - predator_{(i,j)}) \quad (2.45)$$

where scale factor R can be computed as follows:

$$\begin{aligned} & \text{if } rnd < rnd \\ & \quad R = 4.rnd.(rnd - rnd) \\ & \text{else} \\ & \quad R = \Gamma(4.rnd, 1) \\ & \text{end} \end{aligned} \quad (2.46)$$

where shape parameter is 4 and scale parameter is 1 with gamma distribution (Γ)

Step 4: The newly obtained superorganism (X) is updated with the predator for active individuals by using the mapping rule subjected to the boundary limits. Then fitness is calculated for each sub-superorganism of new superorganism and it is compared with the predator superorganism. The sub-superorganisms of predator will be updated if new superorganisms have better fitness according to the objective function. The updated predator will be transferred into A if key value is 1 or transferred into B if key value is 2.

Step 5: Repeat the steps 2 - 4 up to the maximum number of iterations.

2.4.2. Multi-Objective Artificial Cooperative Search Algorithm

ACS algorithm is modified as MOACS to solve multi-objective problems by using the non-dominated sorting and crowding distance principle. Steps of MOACS are discussed in this section.

Step 1: Initialize population and decision variables within the boundary limits as discussed in the above section which is given by (2.44). Calculate individual fitness ($f_1(x), f_2(x), \dots, f_n(x)$) for both superorganisms (A, B). Rank sub-superorganisms of A and B using non-dominated sorting principle [29]. For similar ranked solutions, assign crowding distance as described in [29]. Fitness, rankings, and crowding distances of superorganisms (A, B) are stored in other memory location.

Step 2: Determine the predator and prey and initialize key values as discussed in step 2 of previous section (2.4.1).

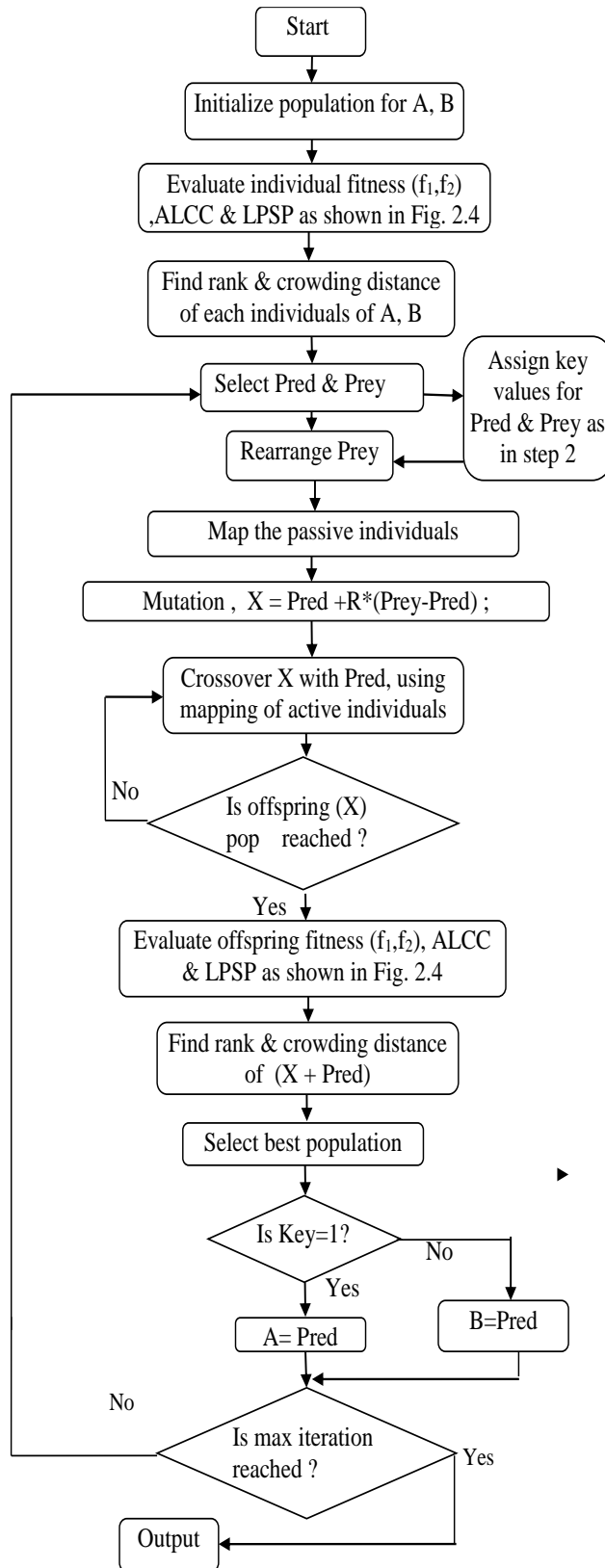


Fig. 2.5. Flowchart for application of MOACS for optimal HRES system design.

Step 3: The new superorganism (X) will be formed with the biological interactions between the two superorganisms depending on passive individuals (based on mapping) controlled by the scale factor R as shown in (2.45) and (2.46). Detailed explanation for this is given in steps 2 and 3 of the above section.

Step 4: Calculate the individual fitness for each sub-superorganism in X .

Step 5: To get the best population between the predator and X , combine them and rank them based on their fitness values using non-dominated sorting principle and crowding distance [29,30]. Sort the combined population (size $2N$) based on ranking and crowding distance and choose the best ranked N solutions (if the ranks are same for the two solutions, then the solution which has more crowding distance will be sorted out to be best solution) from them as predator superorganism.

Step 6: The updated predator will be transferred into A if key value is 1 or transferred into B if key value is 2.

Step 7: Repeat steps 2-6 until maximum number of iterations is reached. The best-compromised solution from the Pareto front (related to predator) which comprises of rank one solutions is obtained using a max-min approach [30].

2.4.3. Proposed Probabilistic Approach

The proposed probabilistic approach, which uses MOACS for optimal microgrid design, is explained here. The main steps involved to implement the MOACS algorithm for the above stated optimization problem for the grid integrated microgrid is given as follows:

- (i) Initialize control parameters of the MOACS algorithm which are population size (chosen as $N=50$), maximum iteration number ($iter_{max}=300$), number of variables to be optimized, input data of annual horizontal irradiance data, wind speed data, and annual load demand.
- (ii) Superorganisms A and B are generated randomly subjected to the boundaries described. Typical solution vectors of A and B is given by (2.47).

$$\begin{bmatrix} N_{sol}^1 & N_{wt}^1 & N_{bio}^1 \\ \vdots & \vdots & \vdots \\ N_{sol}^N & N_{wt}^N & N_{bio}^N \end{bmatrix} \quad (2.47)$$

- (iii) For each guess solution vector (Sub-superorganism) of A and B perform the following steps.

- Measure the power generated by the solar PV modules, WT, and biomass using (2.2),

(2.10) and (2.13).

- Compute $\Delta P1(t)$ and $\Delta P2(t)$ using (2.39) and (2.41).
- Obtain ALCC and LPSP of the sizing components as stated in the flowchart shown in Fig. 2.4.

Follow the same procedure for the rest of the solutions (sub-superorganism) of *A* and *B*.

(iv) Follow the steps 2 and 3 in section 2.4.2 to select prey, predator and obtain new population. Compute ALCC and LPS for each sub-superorganism of new population (*X*).

(v) Follow the steps 5 and 6 in section 2.4.2 to update predator.

(vi) Repeat the procedure explained in (ii)-(v) until maximum iteration number is reached. Best compromised solution from predator which provides good trade-off between ALCC and LPSP has been chosen as the optimal sizing configuration of the microgrid. Flowchart for application of MOACS for HRES design is shown in Fig. 2.5.

2.5. Simulation Results

A hamlet (a group of houses) near Gangadevipalli around 120 kilometres from Kadapa (latitude - $4^{\circ}34'24.1$ and longitude - $78^{\circ}19'44.9$) Andhra Pradesh, India is chosen as a site for optimal HRES design, which is having a peak load of 100kW and average load of 50kW. The inputs for the designing of the grid integrated HRES are solar irradiance, temperature, and wind speed at a given site collected from National Institute of wind energy (NIWE) [117]. Hourly load demand data is collected from the local substation. The efficiencies of rectifier and inverter are taken as 95% and 97%. To produce one unit of energy from biomass gasifier, 1.5 kg of residue is required and the cost of the residue is taken as Rs. 0.30/kg [20]. To serve the peak load for at least 30 minutes, the required capacity of energy storage system is 249.5kVAh (4 batteries in series ($N_{b_{se}}$) and 26 parallel paths ($N_{b_{st}}$)). The SDR of the battery is considered as 0.02%, V_{bat} is 12V, V_{ci} , V_{co} , V_r are 2.7, 25, 11(m/s). V_{oc} , I_{sc} , k_i , k_v , and T_{stc} of PV panel are available in [118]. 17 number of 300 Wp solar panels have been used to build 5kW array. The cost of energy sold to grid and energy purchased from the grid is taken as Rs.6/kWh. Grid purchase capacity is taken as 10 kWh and grid sale capacity is chosen as 20 kWh. A low value of grid purchase capacity is considered to limit the dependency on the grid power. The capital cost, annual maintenance cost, and replacement cost of the equipment used in this study is given in Table 2.9.

Table 2.9. Component Specifications

Solar	Wind	Biomass	Battery
Rated power: 5kW/300W	Rated Power: 5kW	Rated power: 10kW	Rated capacity: 200Ah
Mppt factor: 0.97	Cut out speed: 25 m/s m/s	Operating hours: 12 h	Rated voltage: 12 V
Derating factor: 0.95	Rated power wind speed: 11	Capital cost (Rs): 6.23 lack	Lead acid batteries
Capital cost (Rs): 3.5 lacks	Cut in Speed: 2.7 m/s	O& M cost (Rs): 10000	SOC minimum: 30%
O&M cost (Rs): 10000	O&M cost (Rs): 25000	Residue cost (Rs): 0.30 /kg	Capital cost (Rs): 15000
Open circuit voltage: 37 V	Capital cost (Rs): 5 lacks	Calorific value: 4015 kcal/kg	O&M cost (Rs): 1000
Short circuit current: 8.11 A			Replacement cost (Rs): 15000

2.5.1. Grid Integrated Hybrid Renewable Energy System

In the absence of grid integration, if power obtained by the RES is not enough to meet the load, the energy stored in the battery will be used to serve the load. If battery bank is unable to meet the deficit power, then the remaining power will be treated as loss of power supply (LPS). By integrating microgrid into the grid, the remaining power will be purchased from the grid. If the remaining power is more than the maximum grid purchased power, then the balance deficit power which is equal to difference of remaining power and maximum grid purchased power will be treated as LPS. This is quite small implying enhancement in reliability due to grid integration. Even though the hybrid system is linked with the grid, the priority of the renewable sources is to cater the load demand. The proposed probabilistic approach and the operational strategy employed are not dependent on the sizes of the renewable sources and load. Modelling of wind speed and irradiance is dependent on the site but not on wind and PV generator sizes. Hence, the approach is scalable and flexible enough to accommodate generation sources of different types and sizes for designing large scale microgrid. In this study, two scenarios are considered while designing microgrid system, which demonstrate the flexibility of the approach in accommodating different types of sources using MOACS, IMOHS [30] and NSGA-II [29] algorithms.

Scenario I (S-I): HRES integrated to grid, which includes wind, PV, and battery.

Scenario II (S-II): HRES integrated to grid, which includes battery, PV, wind, and biomass generation.

2.5.1.1. Scenario - I (Without Biomass Gasifier)

In this scenario, the hybrid system consists of PV and wind generators integrated into the grid with ESS. Table 2.10 presents the optimal solution, which has reasonably less objective function values f_1 (ALCC) as well as f_2 (LPSP). In Table 2.10, RE sources are represented in units, which means each unit of solar panel is equal to 300 W (i.e. 242 units means 242*300 W=72.6 kW); similarl., each unit of wind model is equal to 5kW and each unit of biomass model is equal to 10kW. As seen from Table 2.10, by using optimal hybrid system obtained with MOACS, the LPSP is 10%. On the contrary, LPSP with optimal hybrid system design using IMOHS and NSGA-II is 11% and per unit cost obtained from all algorithms is almost same indicating that MOACS gave better-compromised solution. LPSP in this scenario is high, which is expected as grid purchase capacity is limited to 10 kWh. The optimal front obtained in this scenario is shown in Fig. 2.6. As seen from Table 2.12, the majority of the generation comes from the wind generator to meet the load demand since the PV generation is not available in the night times.

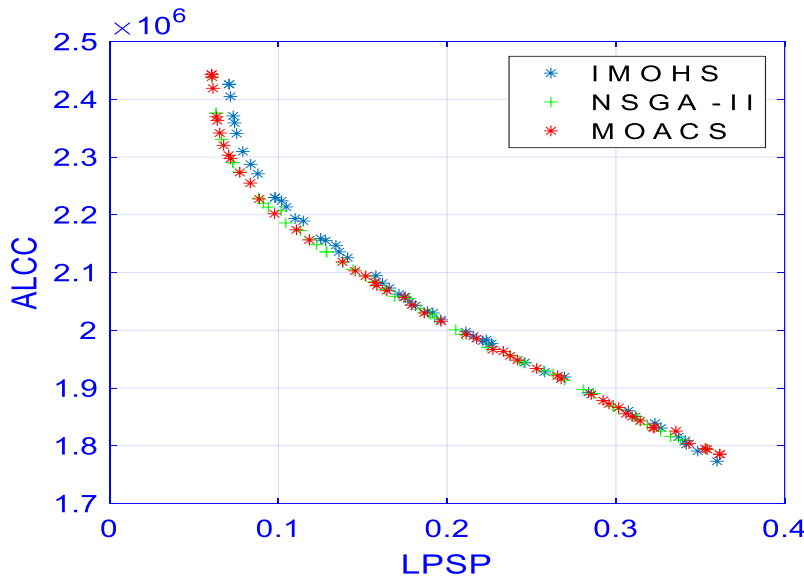


Fig. 2. 6. Optimal pareto front for scenario I.

2.5.1.2. Scenario - II (With Biomass Gasifier)

In case of scenario I, the biggest challenge is the moderate reliability of the system (indicated by high LPSP). LPSP is high as the peak load of the system occurs in the evening and due to the unavailability of solar energy, the system is unable to meet the load effectively resulting in more loss of power supply. To overcome this, in scenario II biomass is included in the system which is operated from 5PM to 5AM daily. By including biomass in the system, the LPSP and cost of the system can be reduced, because biomass feed is available at lower price.

The optimal front obtained in this scenario is shown in Fig. 2.7. MOACS algorithm is used to obtain optimal sizes of the grid integrated hybrid system, and then the results are compared with the results obtained by IMOHS and NSGA-II.

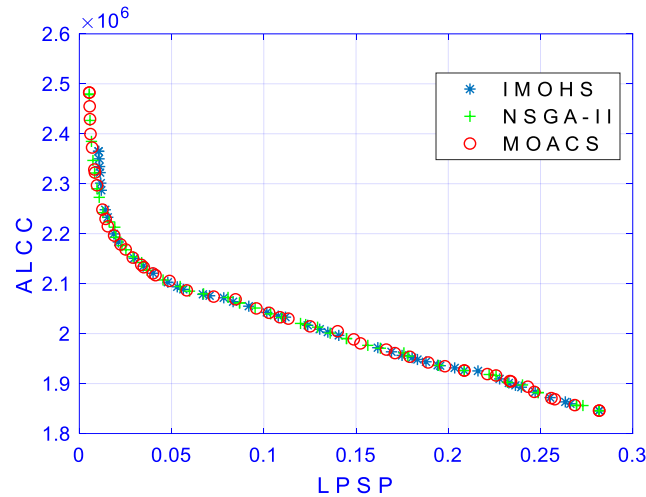


Fig. 2.7. Optimal pareto front obtained for Scenario II.

As shown in Table 2.10, the introduction of biomass into the hybrid system (scenario II) improves the reliability compared to scenario I by reducing the LPSP to 4% from 10%. Also, the unit price is reduced because of low cost of biomass. MOACS algorithm gave better optimal results compared to other algorithms (which can be seen from the additional 1% decrease in LPSP with almost same per unit cost). Table 2.11 shows the detailed ALCC calculations and costs and Table 2.12 shows the energy production and power balance for the hybrid system designed using MOACS. To figure out the effectiveness of the optimal grid connected microgrid design, energy balance (energy generation from different sources, energy exported to grid, the energy imported from the grid, and energy not served to the load) is carried out which is mentioned in Table 2.12. Energy balance should be equal to zero which means that the generated power (power from RES and purchased from grid) after losses should be equal to the load served, energy sold to the grid, and annual dump. Table 2.12 shows that there is proper energy balance of the microgrid for both the scenarios.

2.5.1.3. Comparison of MOACS with IMOHS and NSGA-II

The performance of MOACS is compared with multi-objective algorithms IMOHS and NSGA-II. The population size, number of decision variables and their limits are considered same for all the algorithms. The algorithms are executed for 50 runs and the final non-dominated solutions (pareto front solutions) obtained with each algorithm are stored as outcome for each

run. It is more complex to find out the quality of multi-objective optimization solutions compared to single objective optimization.

Table 2.10. Optimal sizes of hybrid system

Algorithm	Pv Units (N _{pv})	Wind Units (N _w)	Biomass gasifier units (N _{bio})	Grid purchase capacity kW(h)	Grid sale capacity kW(h)	LPSP	ALCC (Rs)	Unit cost (Rs)
<i>S - I (without biomass)</i>	242	24	-	10	20	0.10	2185265.1	4.95983
<i>NSGA-II</i>	256	23	-	10	20	0.11	2174637.7	4.95455
<i>IMOHS</i>	258	23	-	10	20	0.11	2178439.7	4.95723
<i>MOACS</i>	280	17	3	10	20	0.04	2115934.8	4.47895
<i>NSGA-II</i>	287	16	3	10	20	0.05	2104026.5	4.47235
<i>IMOHS</i>	264	17	3	10	20	0.05	2107228.7	4.47450

Table 2.11. ALCC of hybrid system designed using MOACS pertaining to S - II

Costs (Rs/year)	PV	WT	Battery	Biomass	Inverter	Total
Capital cost	348913.35	502364	92198.58	110460.49	59101.65	+1113142.69
Replacement cost	-	-	235377.59	-	-	+235399.59
O and M cost	168674.7	425000	104000	207390.00	10000	+915064.69
Salvage cost	25154.79	36217.77	-	-	-	-61378.29
Purchased energy cost	+108863.20					
Sold energy cost	-195157					
ALCC	2115934.8					

Table 2.12. Energy balance for hybrid system

Component	S - II			S - I		
	Production (kWh/year)	After inverter (kWh/year)	Balance	Production (kWh/year)	After inverter (kWh/year)	Balance
WT	268520.22	255094.209		379087.37	360133.0032	
PV	143021.51	135870.43		123611.45	117430.87744	
Biomass	127458	121085.1		0.00	0.00	
(-)Battery waste	3741.64	3554.558		4092.15	3887.54135	
Total	535258.09	508495.1	508495.1	498606.67	473676.27	473676.2
Purchased from Grid	18143.87		526638.97	30626.79		504302.9
(-)Load	493471.78			493471.78		10831.12
LPS Power	20112.92			51685.44		62516.56
(-)Sold to Grid	32526.17		20753.94	30498.17		32018.39
(-)Dump	20753.939		0.00	32018.389		0.00
Overall balance	0.00			0.00		

An efficient multi-objective optimization algorithm should obtain rank one solutions closer to the optimal true pareto front and the non-dominated solutions of the pareto front should be uniformly distributed with less spacing between them. The non-dominated solutions should cover large range of values for every objective. By considering all these aspects, some comparison metrics such as convergence metric (*C-metric*) and spaced metric(*SP-metric*) are used to find out the quality of the multi-objective optimization algorithm. Since the true optimal pareto front is not known, in this study comparison is done by plotting pareto fronts obtained with each algorithm and considering the *C-metric* and *SP-metric*[29-30]. *SP-metric* is used to quantify how uniformly the solutions in pareto front are distributed. In addition, *box plot* is used to assess the quality of the obtained results.

C-metric: After obtaining the non-dominated solutions for each algorithm, the solution sets or pareto set solutions were compared by C-metric for the quality check. For the given two pareto set solutions, the function (I_C) figures out the domination of pair (A, B) in the interval [0, 1] as shown below.

$$I_C(A, B) = \frac{\text{size}(\{b \in B, \exists a \in A : a \leq b\})}{|B|} \quad (2.25)$$

Here, size (**y**) gives the number of elements present in set ‘y’ and $|B|$ refers to the size of set *B*.

$I_C(A, B)=1$, indicates that all the decision vectors in *B* are weakly dominated by the decision vectors in *A*. $I_C(A, B)=0$ indicates that no decision vector in *B* are weakly dominated by the decision vectors in *A*. Similarly, in other direction, $I_C(B, A)$ also will be computed.

Sp- metric: Spacing metric measures the range of (distance) variation of neighbouring decision vectors present in pareto front and is given as follows:

$$SP = \sqrt{\frac{1}{n-1} \sum_{i=1}^n (\bar{d} - d_i)^2} \quad (2.26)$$

where $d_i = \min(\sum_{k=1}^m |f_k^i - f_k^j|), i, j = 1, \dots, n$.

and *n* is the number of decision vectors in the pareto front.

Sp-metric ‘0’, means that all the non-dominated solutions present in that specified set are spaced at equal distance. The visualization of the distribution of obtained samples can be done by means of box plot. By executing the algorithms for 50 runs, a 50 C-metric average values for

a pair of I_c (*MOACS,NSGA-II*), I_c (*NSGA-II,MOACS*), I_c (*MOACS, IMOHS*) and I_c (*IMOHS,MOACS*) are obtained. The two edges of the box plot are the boundary limits (upper, lower) of the average C-metric values and central mark is the median.

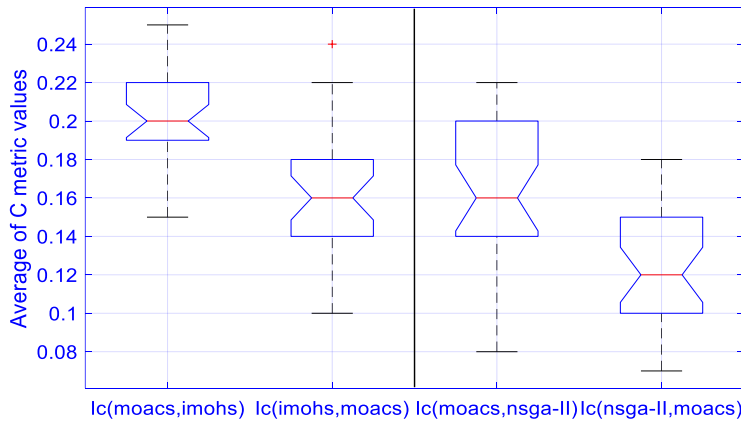


Fig. 2.8. Distribution of obtained C-metrics for scenario I by box-plot.

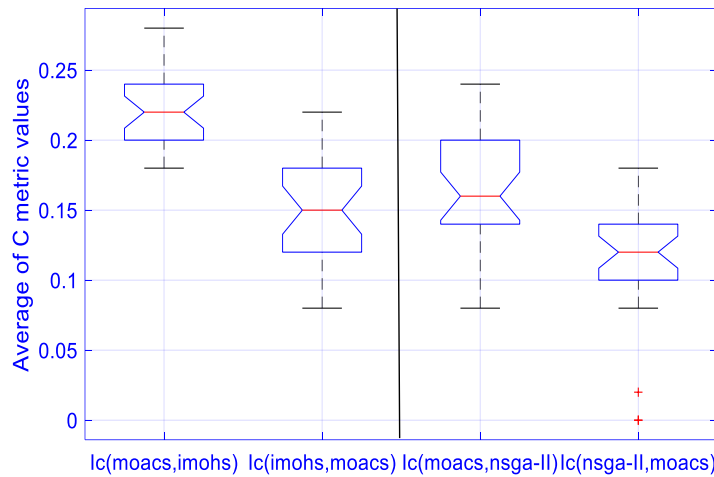


Fig. 2.9. Distribution of obtained C-metrics for scenario II by box-plot.

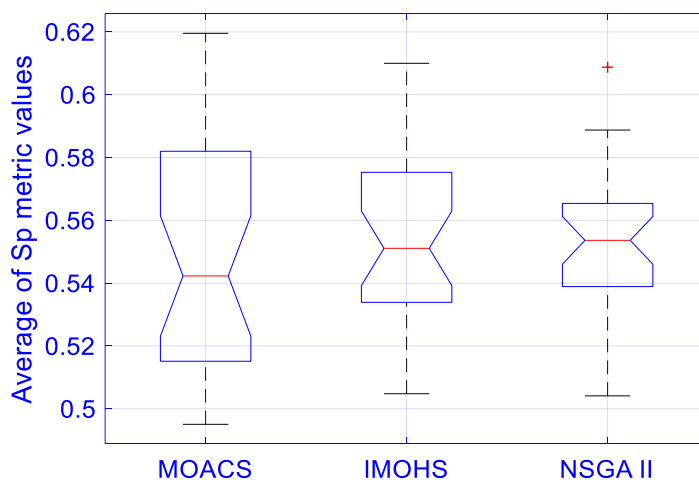


Fig. 2.10. Box-plot of average Sp-metric for scenario I.

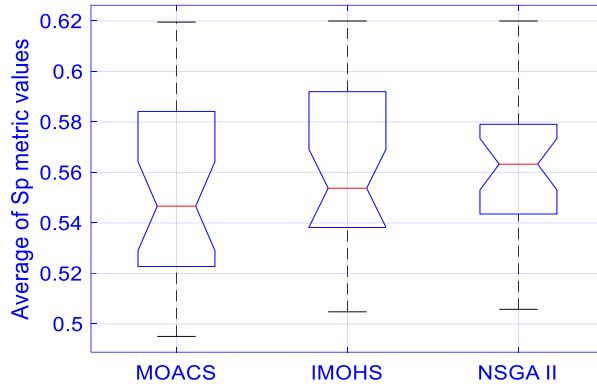


Fig. 2.11. Box-plot of average Sp-metric for scenario II.

Table 2.13. C-metric results

Avg C metric	Ic (MOACS,NS GA-II)	Ic (NSGA-II, MOACS)	Ic (MOACS, IMOHS)	Ic (IMOHS, MOACS)
<i>S- I</i>	0.1623	0.1301	0.205	0.16047
<i>S-II</i>	0.166667	0.115333	0.22066	0.15247

Table 2.14. Sp-metric results

Avg SP metric	MOACS	NSGA-II	IMOHS
<i>S- I</i>	0.547666	0.553171	0.55935
<i>S- II</i>	0.552253	0.561504	0.5603

Fig. 2.8 and Fig. 2.9 illustrate the box plot (distribution) of the 50 average C-metric results of both the scenarios and Table 2.13 shows the C-metric results. From Table 2.13 it is evident that MOACS is significantly better than the other two algorithms. From Fig. 2.8 and Fig. 2.9 it is evident that, $I_C(MOACS, NSGA-II)$ median is higher compared to $I_C(NSGA-II, MOACS)$ and $I_C(MOACS, IMOHS)$ median is higher compared to $I_C(IMOHS, MOACS)$. As per the C-metric analysis, $I_C(MOACS, NSGA-II)$ is the ratio of number of solutions of NSGA-II(which are weakly dominated by solutions of MOACS) to the total number of MOACS solutions. In case of Scenario-II, $I_C(MOACS, NSGA-II)$ equal to 0.166667 indicates that 16.67% pareto front solutions of NSGA-II are dominated by pareto front solutions of MOACS whereas $I_C(NSGA-II, MOACS)$ equal to 0.115333 indicates that 11.53% solutions of MOACS are dominated by solutions of IMOHS. For the same scenario, $I_C(MOACS, IMOHS)$ and $I_C(IMOHS, MOACS)$ equal to 0.22066 and 0.15247 respectively, indicate that on average 22.06% solutions of IMOHS are dominated by solutions of MOACS whereas 15.24% solutions of MOACS are dominated by

solutions of IMOHS. It implies that MOACS has better search capability in finding superior pareto front solutions. From Fig. 2.6 and Fig. 2.7, it is evident that the pareto set obtained by the MOACS have wider range of functional values compared to that obtained with NSGA-II and IMOHS. Table 2.14 shows the results of the Sp-metric values obtained with the three algorithms. Sp-metric with MOACS is less compared to that obtained with NSGA-II and IMOHS indicating that MOACS is capable of finding better evenly distributed solutions. From Fig. 2.10 and Fig. 2.11, it can be seen that the median values are less with MOACS indicating that pareto front solutions obtained have better diversity compared to NSGA-II and IMOHS. Based on C-metric, Sp-metric results and the pareto fronts it can be concluded that MOACS has better search capability in finding evenly distributed superior pareto front solutions.

2.6. Conclusion

This chapter presents a probabilistic approach for the design of a photovoltaic, wind, and biomass-based grid integrated microgrid with ESS for a group of houses (colony) in a small village in Andhra Pradesh (India). The time varying nature of wind power, solar power, and load are mathematically modelled using probabilistic models and considered for analysis while designing a microgrid system. MOACS, IMOHS and NSGA-II algorithms are employed for the sizing, costing, and performance analysis of the grid integrated hybrid system. From the analysis, it is evident that by including biomass gasifier in hybrid system, the system becomes more reliable and the unit cost of energy with the optimized sizing configuration is much lesser than the unit cost of energy purchased from the grid. The designed battery size can provide 30 minutes backup power during peak load in the absence of grid power and hybrid system power. It is evident from the C-metric and Spacing metric analysis that MOACS performs better than IMOHS and NSGA-II in finding evenly distributed superior pareto front solutions. With almost same ALCC, MOACS algorithm results in lesser LPSP compared to other two algorithms. The sizing configuration obtained in this study is able to serve the total load of a colony in a small village with low cost and low loss of power supply.

CHAPTER 3

A Deterministic Approach for Optimal Design of Grid Connected Microgrid System

3.1. Introduction

The production of the electrical power has been increased in the recent years significantly because of the rapid enhancement in the load demand. More than 80% of the generation is obtained by using the conventional energy sources which are not only fast depleting and finite but also emits vast amount of greenhouse gases into the environment and also the cost is volatile. On the other hand, the world statistics indicates that load demand will increase rapidly in the coming years. Therefore, there is an urgent need for ecofriendly, cost effective and reliable alternative energy sources. In recent years, renewable energy (RE) sources such as solar, wind and biomass gained more attention as a substitute for the fossil fuels as they are available in large amount and generates green energy. At present the RE sources are contributing about 10-20% of the total load demand. Moreover, in the second half of the 21st century this figure might go beyond 50%. The main problem with these RE sources is reliability since these are dependent on the weather conditions and nature. For example, sunlight and desired wind speed may not be available all the time. Therefore, individually these RE sources are not able to deliver power continuously to the load. To overcome this problem two or more RE sources can be integrated together as hybrid system to meet the load demand effectively.

The integration of renewable sources in the power system evolved the concept of microgrids which are active distribution networks having distributed generation units, energy storage systems and loads that can be operated in grid connected mode as well as islanded mode. The intermittent and variable nature of the renewables complicates the hybrid system modelling and operation. Hence, it is difficult to obtain the optimal sizing of the renewables. Therefore, to handle the complexity in designing hybrid system, an efficient modelling is needed.

In the literature many studies are proposed to design the optimal hybrid systems and many researchers have focused on the islanded system [2]–[4]. However, these hybrid systems can be integrated to the grid, which can act as backup power supply so that the system becomes more reliable. On other hand, the stochastic, intermittent and variable nature of these sources cause several issues like voltage instability, load mismatch and frequency deviation which make the integration of hybrid system to the grid a challenging job [7]. To overcome this issue, energy

storage systems (ESS) can be used to stabilize the system fluctuations [11]. The authors in [13] proposed a power transfer strategy to serve the small loads by using hybrid system connected to the grid. In [14] a fuzzy based optimization technique to optimize the operational cost has been presented. To increase the reliability of solar and wind based hybrid system, biomass generation can be included which is available at lower cost.

In this study a microgrid consisting of solar, biomass, wind and battery energy system is designed with multi objective artificial cooperative search algorithm (MOACS) to minimize the loss of power supply probability (LPSP) and annual life cycle costing (ALCC). The battery energy storage system is considered in such way that it is able to meet the load demand at least for 30 minutes in the absence of the power generation from the renewables [11].

3.2. Modelling of the Microgrid System

The proposed grid connected hybrid system consists of wind, solar, biomass and battery energy storage system as shown in Fig. 2.1. To design an efficient hybrid system, the real time behavior of each source is needed, which can be expressed in time varying equations. In this section the detailed modeling of the renewable sources and battery energy storage system is presented.

3.2.1. Wind Energy System Modeling

The power generated by the wind energy system is dependent on the wind velocity at that particular time which will vary according to the weather conditions. Therefore, wind turbine output power at any time frame ‘ t ’ (hour) can be obtained by using (3.1).

$$P_{wt}(t) = \begin{cases} P_{rw} \cdot N_w \cdot \left(\frac{v(t) - v_{ci}}{v_r - v_{ci}} \right)^3 & \text{for } v_{ci} < v(t) < v_r \\ P_{rw} \cdot N_w & \text{for } v_r < v(t) < v_{co} \\ 0 & \text{else} \end{cases} \quad (3.1)$$

where N_w is the number of wind turbines, P_{rw} is rated power of the wind turbine (kW), $v(t)$ is the wind velocity (m/s) at time ‘ t ’, v_{ci} is the cut-in velocity(m/s), v_{co} is the cut out velocity (m/s) and v_r is the rated velocity (m/s).

3.2.2. Solar Energy System Modelling

The output power of the solar PV array depends on various factors which are placement and efficiency of the PV array, solar irradiation (W/m^2) and air temperature. While considering maximum power point factor (η_{mpp}) and derating factor (f_{pv}), the output power of PV array at any given time 't' can be expressed as (3.2).

$$P_{pv}(t) = f_{pv} \cdot N_{pv} \cdot \eta_{mpp} \cdot I_{sc}(t) \cdot V_{oc}(t) \cdot ff \quad (3.2)$$

where N_{pv} is number of PV modules and ff is fill factor. The fill factor, short circuit current (I_{sc}) and open circuit voltage (V_{oc}) are given in (3.3)-(3.6).

$$ff = (V_{oc} \cdot I_{sc}) / (V_{stc} \cdot I_{stc}) \quad (3.3)$$

where I_{stc} and V_{stc} are the short circuit current and open circuit voltage at standard test condition (STC).

$$I_{sc}(t) = I_{stc} + k_i \cdot (T_{cell}(t) - T_{stc}) \cdot (s(t) / s_{stc}) \quad (3.4)$$

$$V_{oc}(t) = V_{stc} + (T_{cell}(t) - T_{stc}) \cdot k_v \quad (3.5)$$

$$T_{cell}(t) = T_a + (s(t) / 0.8) \cdot (T_{Noct} - 20) \quad (3.6)$$

where T_{stc} is PV module temperature under STC. k_v , k_i are temperature coefficients of voltage and current, s is solar irradiance (W/m^2) at time frame 't', s_{stc} is module irradiance under STC (1000W/m^2) and T_a is air temperature ($^{\circ}\text{C}$).

3.2.3. Biomass Energy System Modelling

Partial combustion process can be used to produce cool and clean gas from the biomass under restricted air supply. The produced clean gas is utilized to generate the power with the help of fuel engine. The biomass plant is operated for 12 hours in a day to serve the peak load hours. The energy generated from biomass plant in a year is given in (3.7).

$$E_{bio} = N_{bio} \times P_{bio} \times t_w \quad (3.7)$$

where t_w is the working hours of biomass gasifier per annum, N_{bio} represents the number of

biomass gasifiers and P_{bio} is the output power of biomass gasifier.

The maximum rating of the biomass is dependent on the calorific value of the biomass (CV_{bm}), efficiency of the biomass gasifier (η_{bio}) and availability of biomass throughout the year. The maximum rating can be expressed as shown in (3.8).

$$P_{bio}^{\max} = \frac{\text{total_agriwaste} * 1000 * CV_{bm} * \eta_{bio}}{860 * t_w} \quad (3.8)$$

3.2.4. Battery Energy System Modelling

The battery energy system plays a major role in the hybrid system design. It can be charged when there is an excess power generated by renewables after serving the load and on the other hand it can discharge the energy when RE sources are not able to meet the load. Lead acid batteries are considered as BESS in this study due to its low investment cost, high efficiency and low discharging rates. To use the BESS effectively, detailed modelling of state of charge (SOC) is necessary. In this study the BESS is designed such way that to serve the load at least for 30 minutes when output of RE sources is zero.

In charging mode the state of charge of battery is given as

$$SOC(t+1) = (1 - sdr) \cdot SOC(t) + \frac{\eta_c(t) \cdot I_{bat}(t) \cdot \Delta t}{C_{bat}} \quad (3.9)$$

where charge efficiency factor is represented as η_c , C_{bat} is the nominal battery capacity, sdr is the self-discharging rate and Δt is the time step which is considered as 1.

Similarly, in discharging process the SOC of the battery is given in (3.10).

$$SOC(t+1) = (1 - sdr) \cdot SOC(t) - \frac{\Delta t \cdot I_{bat}(t)}{C_{bat}} \quad (3.10)$$

The charging current or discharging current of the battery (I_{bat}) at any time frame 't' is given by (3.11). In charging condition I_{bat} represents the available excess power after serving the load and during discharging mode I_{bat} indicates the amount of energy needed to be discharged from the battery to meet the load.

$$I_{bat}(t) = \frac{\left| \eta_{re} \cdot P_{wt}(t) + P_{pv}(t) + \eta_{re} \cdot N_{bio} \cdot P_{bio}(t) - (P_L(t) \cdot \eta_{inv}) \right|}{Nb_{st} \cdot Nb_{se} \cdot V_{bat}} \quad (3.11)$$

where V_{bat} is the terminal voltage of battery (12V), Nb_{st} is the number of batteries connected in shunt, Nb_{se} is the number of batteries connected in series and η_{re} and η_{inv} are efficiencies of rectifier (AC power output of wind and biomass are converted into DC power by rectifier) and inverter respectively. To ensure long life of the battery, the maximum allowable current at any given point of time is considered as 20% of rated capacity.

3.3. Data Collection

The chosen site for the design of hybrid system is Gangadevipalli, which is located 120 km from Kadapa, Andhra Pradesh, India having latitude as 4⁰34'24.1 and longitude as 78⁰19'44.9. The village consists of a group of houses having an average load of 50kW and peak load of 100kW. The load data is taken from the local substation and the meteorological data such as solar irradiance, wind speed and temperature at selected site is obtained from the National Institute of wind energy (NIWE) [117].

3.4. Power Dispatch Strategy

The power generation from renewables and also the battery charging and discharging will vary with time. Therefore, the information of power generation from each source at every point of time is essential while designing the system. The power balancing equations as given in (3.12) and (3.13) are used to define the operational strategy. In the operational strategy, the power generated from the renewables is given higher priority to serve the load.

$$\Delta P1(t) = (P_{wt}(t) \cdot \eta_{re} + P_{pv}(t) + N_{bio} \cdot P_{bio}(t) \cdot \eta_{re}) - P_L(t) / \eta_{inv} \quad (3.12)$$

$$\Delta P2(t) = (P_{wt}(t) \cdot \eta_{re} + P_{pv}(t) + \eta_{re} \cdot N_{bio} \cdot P_{bio}(t)) + N_b \cdot I_{bat,max} \cdot V_{bat} - P_L(t) / \eta_{inv} \quad (3.13)$$

where $\Delta P1(t)$ is difference between the load demand and power generation from RE sources and $\Delta P2(t)$ is the difference between the load demand and power generation from RE sources, battery storage. The following operational strategy is employed in this study:

- $\Delta P1(t) > 0$, indicates that the power generation from the RE sources is more than the load demand. In this case the remaining excess power will be used to charge the battery storage. After charging the battery if excess power is available, that power will be sold to the grid. Here, there are limits on the power that can be sold and purchased from the grid. Therefore, if still power is left after pumping the maximum allowable power into the grid, that power will be wasted in the dump load.
- $\Delta P1(t) < 0$ & $\Delta P2(t) > 0$, indicates that the deficit power $\Delta P1(t)$ can be met from the BESS.
- $\Delta P1(t) < 0$ & $\Delta P2(t) < 0$, indicates that the deficit power $\Delta P1(t)$ cannot be accommodated from the BESS. In this case, the remaining deficit power after the battery is discharged to its minimum level will be supplied by the grid. The grid has purchase power limit and if the deficit power is more than the allowable limit then remaining deficit power appears in loss of power supply and LPSP is updated.

3.5. Problem Formulation

In this study, the objective is to supply power to the chosen site with low unit cost and high reliability. Therefore, two objectives are considered in this study which are minimization of loss of power supply probability (LPSP) and minimization of the annualized life cycle costing (ALCC). Here, the reliability of the system is measured in terms of loss of power supply and lesser LPSP indicates lesser power cuts which means the system is more reliable.

3.5.1. Annual Life Cycle Costing

The annual life cycle costing is the annualized overall cost of the system consisting of total cost of biomass, wind, battery, solar, inverter, grid sold energy cost (C_{gs}) and grid purchased energy cost (C_{gp}). Here, all the costs are annualized and ALCC of the proposed system can be expressed as below:

$$ALCC = f1 = \left(\sum_{pv, wt, bio, b, inv} C_x \right) + C_{gp} - C_{gs} \quad (3.14)$$

The total cost of inverter, solar, biomass and wind includes annualized capital cost ($acap$), replacement cost (arp), maintenance cost (am) and salvage cost (asg) as given in (3.15).

$$C_x = C_x^{acap} + C_x^{am} + C_x^{asg} + C_x^{arp} \quad (3.15)$$

where, x may be solar or wind or battery or biomass generator or inverter. In this study, interest and inflation rates are considered in the cost calculations with the help of present worth factor (PWF). The annualized value of each cost (capital, maintenance, etc.) can be calculated from (3.16).

$$C_x^{a(y)} = C_x^y (g + w * \left(\frac{1+f}{1+i} \right)^n) / PWF \quad (3.16)$$

where, y could be replacement cost or capital cost or salvage cost or maintenance cost. g is 0 and w is 1 while calculating replacement cost and vice versa while calculating other costs. The PWF can be expressed by (3.17).

$$PWF = \left(1 - \left(\frac{1+f}{1+i} \right)^n \right) * \frac{1+f}{i-f} \quad (3.17)$$

where, i is the interest rate and f is the inflation rate. Further, the unit cost of the produced electricity by proposed system can be given as follows.

$$Unit\ cost = \frac{ALCC(Rs / yr)}{Load\ served(kWh / yr)} \quad (3.18)$$

3.5.2. Loss of Power Supply Probability

LPSP can be described as the probability of the hybrid energy system not being able to cater the load. LPSP can be expressed as

$$LPSP = f2 = \frac{\sum_{t=1}^{8760} (P_t^{need} - P_t^{supplied})}{Total_load} \quad (3.19)$$

3.6. Optimization Algorithm

Optimization is a process to select the best compromised solution for a particular problem while satisfying all the constraints of the system. When multiple objectives are present it is hard to get the best compromised solution with single objective optimization algorithms especially when the objectives are conflicting to each other. To overcome this difficulty, pareto optimization based multi objective algorithms can be used. In this study, (MOACS) algorithm is presented to solve the optimization problem. The detailed procedure

to implement the algorithm is given below:

Step 1: Initialise the control parameters for the MOACS (number of iterations=300, population size $N=50$), design variables, parameters and input data of annual wind speed, load and solar irradiance. Generate the population for super organisms A, B subjected to the boundary conditions.

Step 2: For each solution of superorganisms A and B, calculate the solar, wind and biomass power generation as mentioned in (3.1), (3.2) and (3.7). Then calculate $\Delta P1(t)$ and $\Delta P2(t)$ as given in (3.12) and (3.13) to get the objective function values ALCC and LPSP.

Step 3: Calculate fitness (Objective functions f_1, f_2) of each solution for both the super organisms as mentioned in step 2. Rank each solution of A, B with the help of non-dominated sorting principle and assign crowding distance (CD) for similar ranked solutions. Randomly assign predator and prey superorganisms from A, B and assign key values. Generate new population (X) from predator and prey with biological interactions using mapping. Then calculate the fitness, ranking and CD for X.

Step 4: To get the best population combine super organisms X and predator (size becomes $2N$), rank them and assign CD for combined population. Then sort the population by rankings and CD, and choose the top solutions (size N) as predator solutions.

Step 5: Transfer the updated predator solutions to A or B based on key values. Repeat steps 2 to 5 up to the maximum number of iterations. Pick the best optimal solution which gives low ALCC and LPSP from the best solutions (predator) by min max approach.

3.7. Simulation Results

MATLAB 2021a platform with 2.80GHz i5-8400 processor has been used to validate the proposed method. The power generation from solar energy is very limited during the night time (peak load time). Therefore, to serve the load effectively, the biomass gasifier is operated 12h per day from 5PM to 5AM. Biomass gasifier requires 1.5 kg of residue to produce one unit of electricity. The required battery energy storage to serve the load for at least 30 minutes is 249.5 kVAh. Therefore, 26 batteries are connected in parallel (Nb_{st}) and four batteries are connected in series (Nb_{se}). The SDR of the battery is 0.02%. 300W solar panels are used to build 5 kW array which requires 17 (300W) panels. The solar panel details are available in reference [118]. Even though the system is connected to the utility grid, maximum priority is given to the renewables to serve the load and hence the maximum grid purchasing capacity and maximum grid sold capacity is considered as 10kW and 20kW respectively. The unit cost of the bidirectional energy from the utility grid is considered as Rs. 6/kWh. The cost and

component specifications are presented in Table 2.9. In this study, two scenarios are considered, which are off-grid mode and grid-connected mode. Further, the results are compared with the weighted sum optimization approach (WSA).

3.7.1. Scenario - I (Off-Grid Mode)

In scenario I, the microgrid consists of wind, solar, biomass generators and the battery is operated in off grid mode. In this mode the power generated from the renewables is used to serve the load and generated excess power is used to charge the battery. On the other hand in case of power deficit, the battery is used to serve the deficit power. The optimal sizes obtained with MOACS for this scenario and respective ALCC (f_1) and LPSP (f_2) are tabulated in Table 3.1. Obtained pareto front for this scenario is shown in Fig. 3.1. From Table 3.1 it can be seen that the LPSP is 8% with unit cost of the electricity produced Rs. 4.90. It is expected that LPSP is more because the system is not connected to the utility grid which could act as backup for the hybrid system. Also, it is observed that the hybrid system tries to generate more power in the absence of grid to reduce the LPSP, but due to the dump constraint the obtained optimal size produces more LPSP.

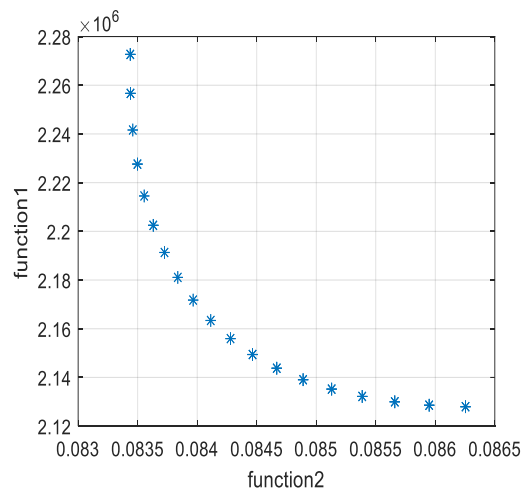


Fig. 3.1. Optimal pareto front with MOACS for Scenario I.

3.7.2. Scenario - II (Grid Connected Mode)

In scenario I the reliability of the system is vulnerable since there is no back up for the system which results in high LPSP as well as high unit cost. To overcome the drawbacks in scenario I, in scenario II the microgrid is connected to the utility grid. The optimal sizes obtained with MOACS are given in Table 3.1 and the obtained pareto front is given in Fig.

3.2. By connecting the microgrid to the utility grid, the LPSP is reduced to 5% from 8% (scenario I) because the grid is acting as backup and also the unit price of the electricity is reduced to Rs. 4.47 from Rs. 4.90 (scenario I) since the excess power generated by the renewables after serving the load and after charging the battery is sold to the utility grid. Therefore, the system becomes more reliable and cost effective by integrating to the utility grid.

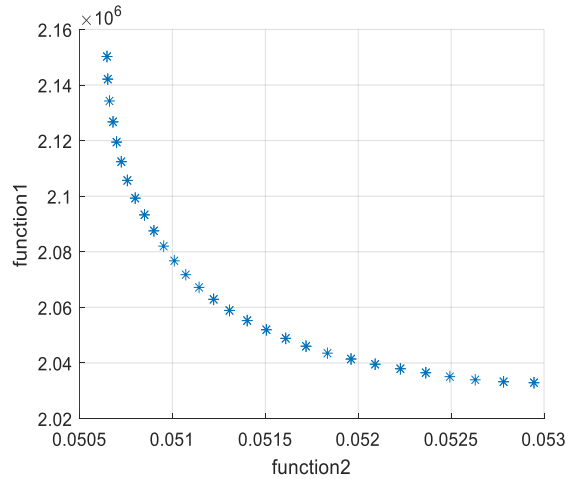


Fig. 3.2. Optimal pareto front with MOACS for Scenario II.

Table 3.1. Obtained Optimal Sizes of the Proposed System

	Approach	Wind Units (N_w)	PV units (N_{pv})	Biomass gasifier units (N_{bio})	LPSP	Unit cost (Rs)	ALCC (Rs)
<i>Scenario I (off-grid mode)</i>	<i>MOACS</i>	<i>14</i>	<i>379</i>	<i>3</i>	<i>0.08</i>	<i>4.90</i>	<i>2219080.93</i>
	<i>WSA</i>	<i>14</i>	<i>377</i>	<i>3</i>	<i>0.09</i>	<i>4.90</i>	<i>2215563.33</i>
<i>scenario II (grid tied mode)</i>	<i>MOACS</i>	<i>14</i>	<i>382</i>	<i>3</i>	<i>0.05</i>	<i>4.47</i>	<i>2096138.89</i>
	<i>WSA</i>	<i>13</i>	<i>387</i>	<i>3</i>	<i>0.06</i>	<i>4.48</i>	<i>2087488.34</i>

3.7.3. Comparison of the Proposed Approach with WSA

The performance of the proposed MOACS algorithm is compared with the weighted sum optimization by ACS algorithm (WSA). WSA is one of the conventional approaches which is used to solve the multi objective optimization problem with the help of single

objective optimization problem by applying the weight coefficients to each objective function. Therefore, the objective function consisting of multiple objectives can be solved using single objective optimization algorithms. The weight coefficients may vary for each objective based on the priority of that objective in the overall objective function. The objective function of this proposed approach for WSA can be expressed by (3.20).

$$\text{minimise } f(x) = \sum_{k=1}^m W_k * f'_k(x) \quad (3.20)$$

where, W_k is the weight coefficient which is considered as 0.5 (sum of weight coefficients should be 1) and m is the number of objective functions which is 2.

$$f'_1 = \frac{ALCC(Rs / yr)}{Load \ served(kWh / yr) * C_g^p} \quad (3.21)$$

$$f'_2 = \frac{\sum_{t=1}^{8760} (P_t^{need} - P_t^{supplied})}{Total_load} * C_{lpsp} \quad (3.22)$$

where, $C_g^p = Rs. 6/kWh$ and C_{lpsp} is 10.

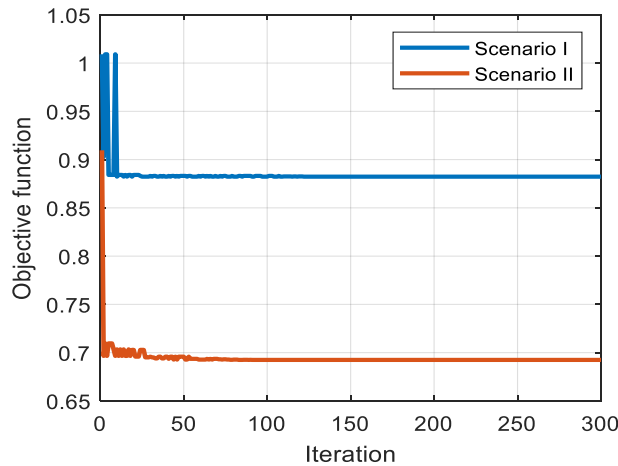


Fig. 3.3. Convergence characteristics with WSA in both scenarios.

The results obtained with WSA and with the proposed MOACS algorithm are tabulated in Table 3.1. The convergence characteristics of the proposed system with WSA are shown in Fig. 3.3. From the obtained results in both the scenarios, the proposed MOACS algorithm is giving the best optimal solutions for the objective functions ALCC and LPSP compared to the weighted sum optimization approach. It can be seen that the optimal sizes obtained with

MOACS in scenario II results in 5% LPSP with less unit cost compared to the results obtained with WSA in which LPSP is 6%.

3.8. Conclusion

In this study, grid integrated microgrid consisting of wind, solar, biomass and battery energy system is designed to serve the load in a village or hamlet consisting of a group of houses in Andhra Pradesh (India). MOACS algorithm is employed to obtain the optimal sizes of the proposed system. Result analysis shows that integration of the proposed hybrid system with the utility grid increases reliability (less LPSP) and reduces unit cost. Further, the obtained results are compared with WSA and it is observed that the MOACS gives best optimal solutions for the proposed system.

CHAPTER 4

Microgrid Fault Detection Technique Using Phase Change of Positive Sequence Current

4.1. Introduction

Technological advance in recent years has enhanced the penetration of renewable-based distributed generation units such as solar and wind in microgrids. A majority of these renewable-based DGs are connected to the microgrid through power electronic inverters. The fault characteristics of these inverter interfaced distribution generation (IIDG) units are dependent on the design and inverter control strategy used and also on the grid connection type. The maximum output fault currents of the IIDGs are limited to 150% [31,32] of the rated current of the DG, which is very small compared to the conventional synchronous generation-based DGs, which can be 10 times the rated current [32]. The microgrid can operate in grid connected mode or in islanded mode, but the power distribution operators and utilities usually do not prefer the islanded mode of operation due to the intermittent nature of the DGs [33,34]. All these aspects make the protection of IIDG-based microgrids more complex compared to the traditional microgrid. Therefore, there is an urgent need to develop a proper fault detection technique for the microgrids.

The conventional fault detection schemes for the protection of the microgrid are over current principle-based schemes, distance-based relaying schemes and current harmonic distortion-based methods [35–37]. Most of these schemes are used for unidirectional power flow systems, but the integration of the renewable-based DGs into the microgrid makes the power flow bidirectional [38]. The conventional protection schemes are incapable of protecting the renewable-based microgrid. Therefore, differential protection schemes [39-41] are proposed. In ref. [39], the primary protection of the microgrid based on the classical differential relay principle has been presented. The authors discussed the details of relay settings and communication requirements needed for the current transformer selection and presented different protection strategies for different sections like feeder protection, DG protection and bus protection. But the authors did not address the significant issues like data synchronization and charging current effects on the differential protection. Comparing the sending end and receiving end spectral energy content of the current with the use of Stockwell transform (S-transform), differential schemes have been presented in ref. [40,41]. But the complexity of the S-transform

is very high, which is not desirable in practical applications where fast response is demanded.

Wavelet transformation (WT) and Park's vector approach (PVA) - based fault detection techniques are presented in ref. [42]. The fault patterns are recognized by transforming the three phase voltages and currents to dq0 components, which are filtered through the wavelet transformation. But the algorithm has the limitation with high impedance fault resistances. Discrete wavelet transformation (DWT) and deep neural network-based fault detection scheme are presented in ref. [43]. However, DWT has the limitation in the low frequency band. To overcome the real-time limitations of the Wavelet transformation, the undecimated wavelet transformation (UWT)-based algorithm has been proposed in ref. [44] for only PV-based microgrids. The authors in ref. [45] proposed a method using mathematical morphology and recursive least squares method by measuring the voltage and currents data at every distribution line. However, due to high complexity, data overflowing may occur. In ref. [46], the authors proposed central monitoring system-based methods by sensing the sending and receiving end current directions, which require powerful monitoring system that is not economical.

In recent years, the researchers have put forward the fault detection techniques in microgrids based on the sequence components. Unlike the negative sequence and zero sequence phasors, the positive sequence phasors exist for all types of faults [47,48]. In ref. [49], the authors proposed a fault detection technique in radial distribution systems using the phase change in the positive sequence current considering the prefault current phasors. By using the phase change in negative sequence current, a directional relaying algorithm is presented in ref. [50] although the fault detection in the branch feeders was not performed. The fault characteristics of the IIDGs will vary according to the control strategy implemented in DGs [51,52]. Therefore, consideration of the specific control strategy of the IIDGs is needed. The equivalent fault models and control strategies for IIDGs are presented in refs. [52,53]. A fault detection method has been proposed in ref. [55] based on the phase change in the positive sequence bus voltage and positive sequence feeder currents.

This chapter presents a fault detection method for the grid connected renewable-based microgrid using the phase change in the positive sequence feeder currents for different DG voltages. The PQ control strategy has been used in the IIDGs. The DGs are designed to support the LVRT requirement of the grid connected microgrid [54]. The fault characteristics of the microgrid have been analyzed for different faults, viz. LIFs and HIFs. To present the supremacy of the proposed fault detection method, different load power factors (pfs) are considered in the study. This chapter has been organized in six sections. In section 4.2, the control strategy of IIDGs is presented. In section 4.3, the proposed fault detection scheme is explained. Simulation

results are presented in section 4.4, and comparative assessment in section 4.5. Finally, the conclusion has been summarized in section 4.6.

4.2. Control Strategy of Inverter-Interfaced Distributed Generators

The inverter-interfaced distributed generators (IIDGs) connected to the microgrid have different types of control strategies, which use current control mode or voltage control mode based on the grid connection, i.e. grid –tied and islanded mode. The IIDGs are controlled using voltage control mode like V/f control and droop control in off –grid or islanded mode. V/f control is widely applied in IIDGs to sustain frequency and voltage stability in a microgrid, whereas droop control is used in IIDGs because of its advantages of virtual inertia, load sharing and plug and play characteristic[51,52]. On the other hand, the IIDGs are controlled in current control mode such as active and reactive power (PQ) control and constant current control to provide preset power to the utility grid in grid connected mode. In this study, the PQ control strategy is applied to the IIDGs to get the desired active and reactive power from the DG by controlling the change in active current and reactive current references.

The DGs (photovoltaic power generators (PPGs) or turbine generators (TGs)) in a microgrid should have the low voltage ride through capability to support the grid codes. This capability enhances the voltage level by supplying the reactive power when fault occurs in a microgrid. The DGs in a microgrid produce only active power under normal operating conditions as PPGs and TGs operate at unity power factor to avoid the losses. Therefore, the reactive current output of DGs is zero under normal operating conditions. There is no reactive current output supply if the grid voltage coefficient is between 90% and 100%. The DGs in a microgrid should start to supply the reactive current output when the voltage sag exceeds 10%. When the grid voltage coefficient ranges between 50% and 90%, the DGs supply 2% reactive current output for every 1% voltage drop. If the grid voltage coefficient falls below 50%, the DGs supply 100% reactive current output, which reaches its maximum value I_{max} and remains constant. In this case, the DG supplies only reactive power to support the voltage level and provides no active current output. Equation (4.1) represents the reactive current output I_q when the grid voltage coefficient ranges between 50% and 90%.

$$I_q = 2I_{max} \left(1 - \frac{V_{d,f}}{V_n} \right) \quad (4.1)$$

The maximum permissible value of the reference current is I_{max} which is usually less than twice

the DG rated current.

The active current output is given as

$$I_d = \begin{cases} P_{ref} / V_{d.f}, & 0.9 V_n < V_{d.f} \leq V_n \\ \min\left(\frac{P_{ref}}{V_{d.f}}, \sqrt{I_{max}^2 - I_q^2}\right), & 0.5 V_n < V_{d.f} \leq 0.9 V_n \\ 0, & 0 < V_{d.f} \leq 0.5 V_n \end{cases} \quad (4.2)$$

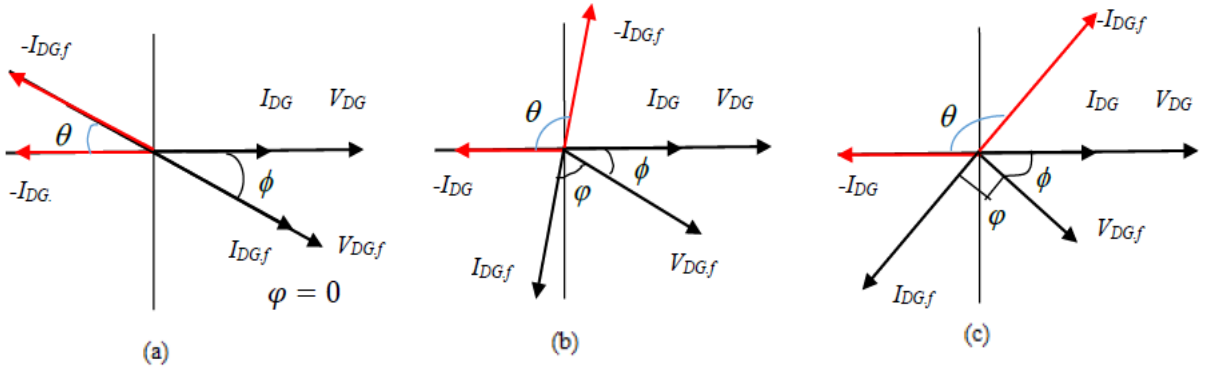


Fig. 4.1. DG voltages and current phasors. (a) Voltage coefficient above 90%. (b) Voltage coefficient between 50%-90%. (c) Voltage coefficient below 50%.

Under normal conditions, the DGs are operated at unity power factor. Therefore, DG current (I_{DG}) is in phase with DG voltage (V_{DG}) as shown in Fig. 4.1 (a). When the voltage sag is very small (the grid voltage coefficient between 90% and 100%), then the DG supplies only active current output and there is no reactive current output. Therefore, $I_{DG,f}$ is in phase with $V_{DG,f}$ and the angle ϕ between them is zero. In this case, the post-fault positive sequence DG current $I_{DG,f}$ makes an angle θ with the pre fault-positive sequence current I_{DG} , which is less than 90° . As the voltage drop is small, the angle ϕ between $V_{DG,f}$ and V_{DG} is small.

When the grid voltage coefficient is between 50% and 90%, the DG starts to supply the reactive current in addition to the active current, and hence, the post-fault DG current starts to lag the post-fault DG voltage by an angle ϕ , which can increase maximum up to 90° , and therefore, the angle θ can be greater than 90° , as shown in Fig. 4.1(b). When the grid voltage coefficient is below 50%, the DGs supply only reactive current output. Since the DG produces only reactive current, $I_{DG,f}$ lags with respect to $V_{DG,f}$ by 90° , and therefore, θ is more than 90° as shown in Fig. 4.1 (c).

4.3. Proposed Fault Detection Scheme

4.3.1. Test System

The simplified model of microgrid connected to the grid at the point of common coupling (PCC) is shown in Fig. 4.2. The feeders connected to the buses at both the ends are known as main feeders (L3, L4), and the feeders connected to the bus at only one end are called branch feeders (L1, L2, L5-L8). The circuit breakers are placed at both the ends of main feeders, and for branch feeders, the circuit breakers are placed only at the upstream end. The inverter interfaced wind generator PQ-DG is connected as DG1, and inverter-interfaced photovoltaic solar PQ-DG is connected as DG2.

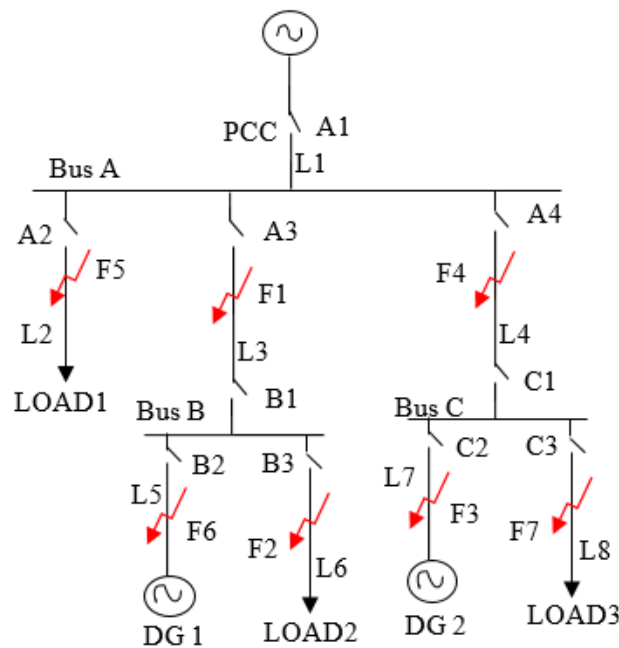


Fig. 4.2. Grid-connected microgrid simplified model.

From the analysis in section 4.2, it can be seen that the PQ controlled DG is equivalent to the controlled positive sequence current source. Hence, when fault occurs at F_1 in the microgrid, the positive sequence fault component of the network can be represented as shown in Fig. 4.3.

4.3.2. Fault Detection Scheme for both DG Voltages Greater than 0.9

The fault analysis is carried out for the grid connected microgrid shown in Fig. 4.2. As described in section 4.2, the DG characteristics will change when the grid voltage level changes

since the DGs are having the LVRT control mechanism. As the microgrid consists of DGs, the fault characteristics of the microgrid vary according to the DG voltage variations with respect to the voltage at the grid connection point.

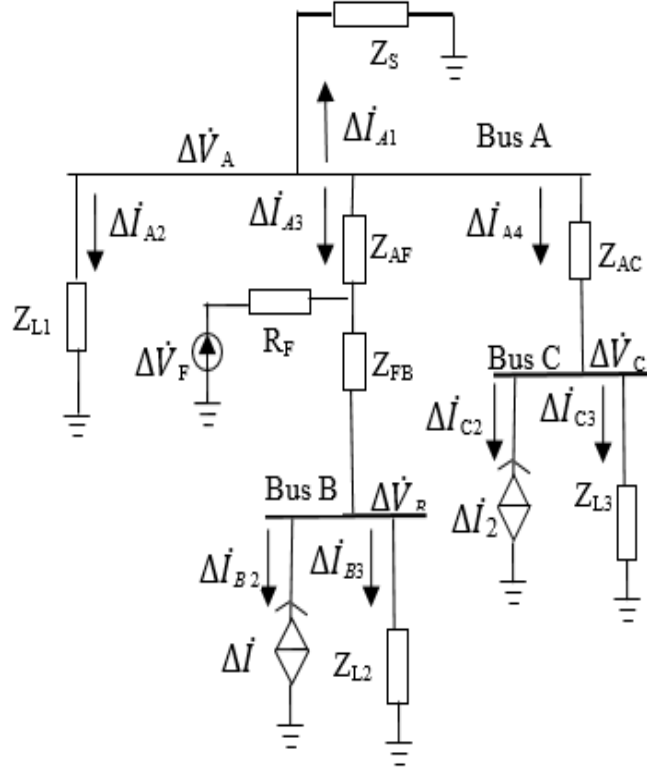


Fig. 4.3. Positive sequence network when F1 fault occur in the microgrid.

When HIF occurs at F1, the bus voltage coefficients at bus A, bus B and bus C all range between 90%-100%. Then, both the DGs will supply only active power. From Fig. 4.3, the following expressions can be obtained for bus B:

$$\Delta \dot{I}_{B2} = -\Delta \dot{I}_1 \quad (4.3a)$$

$$\Delta \dot{I}_{B3} = \Delta \dot{V}_B / Z_{L2}. \quad (4.3b)$$

Similarly, the following expressions can be obtained for bus C and bus A:

$$\Delta \dot{I}_{C2} = -\Delta \dot{I}_2 \quad (4.4a)$$

$$\Delta \dot{I}_{C3} = \Delta \dot{V}_C / Z_{L3} \quad (4.4b)$$

$$\Delta \dot{I}_{A1} = \Delta \dot{V}_A / Z_S \quad (4.5a)$$

$$\Delta \dot{I}_{A2} = \Delta \dot{V}_A / Z_{L1} \quad (4.5b)$$

$$\Delta \dot{I}_{A3} = -(\Delta \dot{I}_{A1} + \Delta \dot{I}_{A2} + \Delta \dot{I}_{A4}) \quad (4.5c)$$

$$\Delta \dot{I}_{A4} = (\Delta \dot{I}_{C2} + \Delta \dot{I}_{C3}) \quad (4.5d)$$

The positive sequence impedance of the load feeders in medium voltage distribution systems is usually inductive. When HIF occurs at F1, the phase difference of load feeder current after and before fault will be very small (post-fault positive sequence load feeder current almost in phase with pre-fault positive sequence load feeder current, which makes $\theta \cong 0^0$). Hence, the following conclusions can be obtained:

$$\arg(I_{C3,f}) - \arg(I_{C3}) < t_2 \quad (4.6a)$$

$$\arg(I_{B3,f}) - \arg(I_{B3}) < t_2 \quad (4.6b)$$

where t_2 is a threshold, which is very small.

According to (4.3), (4.4) and (4.5), the positive sequence current phasors in bus A, bus B and bus C are shown in Fig. 4.4.

It can be observed from Fig. 4.1 that θ lies between 0^0 and 90^0 , but as fault occurred at F1, the phase difference of the positive sequence post-fault and pre-fault feeder current is small and remains within the threshold limit. Therefore,

$$\arg(I_{B2,f}) - \arg(I_{B2}) < t_1 \quad (4.7a)$$

$$\arg(I_{C2,f}) - \arg(I_{C2}) < t_1 \quad (4.7b)$$

where t_1 is another threshold.

Now, the phase difference variations of positive sequence post-fault and pre-fault feeder currents at bus A are as follows:

$$\arg(I_{A2,f}) - \arg(I_{A2}) < t_2 \quad (4.8a)$$

$$\arg(I_{A4,f}) - \arg(I_{A4}) < t_1 \quad (4.8b)$$

$$\arg(I_{A3,f}) - \arg(I_{A3}) \geq t_1 \quad (4.8c)$$

From (4.6), (4.7) and (4.8), it can be observed that there is a significant difference in the phase angle deviation between the faulty feeder and healthy feeder. For faulty feeders, the phase difference variation is greater than the threshold value, which is not applicable for healthy feeders.

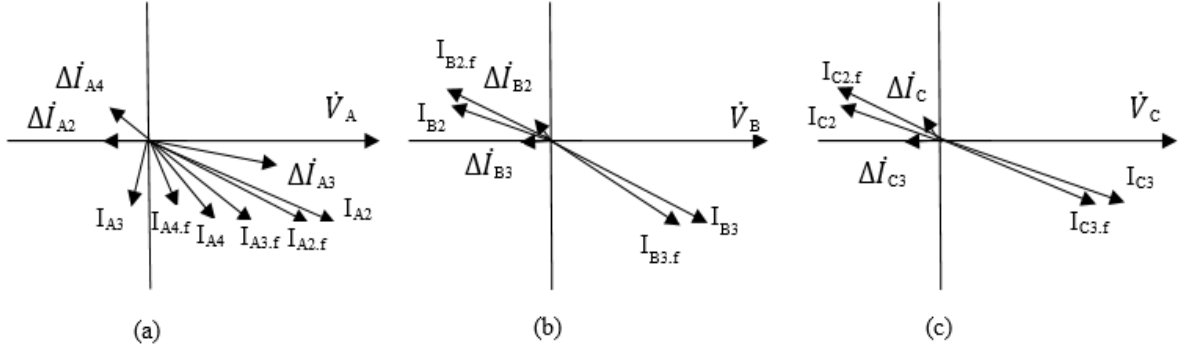


Fig. 4.4. Positive sequence current phasors for both DG voltages > 0.9. (a) Bus A. (b) Bus B. (c) Bus C.

As seen in Fig. 4.2, the branch feeders (L5-L6 and L7-L8) are connected to the main feeders (L3 and L4). Therefore, for any change in the branch feeders, the characteristics of the main feeders will be affected (i.e. if fault occurs in L5 and L6 feeders, the characteristics of the L3 feeder will vary). Hence, based on the main feeder current phase variations, the fault detection is carried further for branch feeders. The same analysis can be carried out for the faults F2-F7, and the flowchart shown in Fig. 4.5 can be proposed to detect the faulty feeder when HIF occurs in the microgrid.

The steps to detect the fault in the microgrid when both the DG voltages are greater than 0.9 are given below:

Step 1: Measure the phase angles of the positive sequence feeder currents. Find the phase change in the main feeder current I_{A3} .

- If $I_{A3.f}$ is leading with respect to I_{A3} by an angle greater than or equal t_1 , then the fault is at either at F1 or F2 or F6. Then, find the phase change of I_{B2} . If $I_{B2.f}$ is leading with respect to I_{B2} by an angle greater than or equal to t_1 , then fault is at F6.
- If the phase change in I_{B2} is less than t_1 , then find the phase change in I_{B3} . If it is greater than t_2 , then fault is at F2, otherwise fault is at F1.

Step 2: If the phase change in I_{A3} is less than t_1 , find out the phase change of I_{A4} . If $I_{A4.f}$ is not leading with respect to I_{A4} by an angle greater than or equal to t_1 , then fault is at F5 and faulty feeder is detected.

Step 3: If $I_{A4,f}$ is leading with respect to I_{A4} by an angle greater than or equal to t_1 , then fault is at F3 or F4 or F7. Then, find whether $I_{C2,f}$ is leading with respect to I_{C2} by an angle greater than or equal to t_1 . If yes, then fault is at F3.

Step 4: If the phase change in I_{C2} is less than t_1 , then find the phase change in I_{C3} . If it is greater than t_2 , fault is at F7, otherwise fault is at F4.

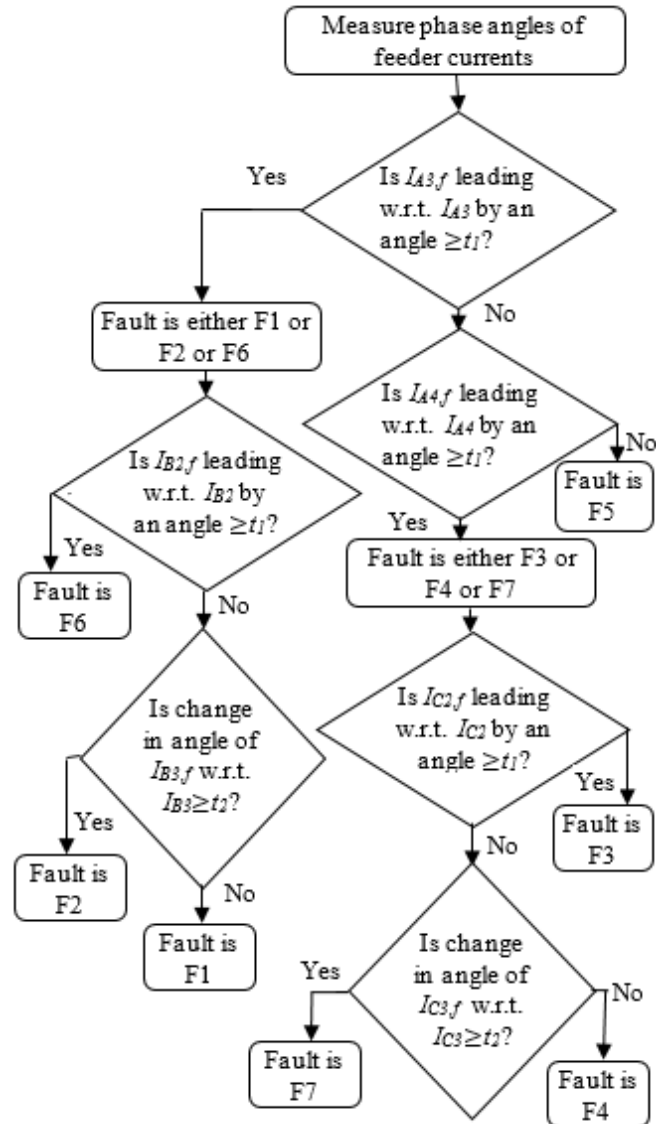


Fig. 4.5. Flowchart for fault detection in microgrids for both DG voltages > 0.9.

4.3.3. Fault Detection Scheme for both DG Voltages Less than 0.9

When LIF occurs at F1, the bus voltage coefficient of bus A, bus B and bus C will range between 50% and 90% or may fall below 50%. In this case, the DGs will supply both active power and reactive power simultaneously or may supply only reactive power. Therefore, from

Fig. 4.1, the following conclusions can be obtained:

$$0^\circ \leq \arg(I_{B2,f}) - \arg(I_{B2}) < 180^\circ \quad (4.9a)$$

$$0^\circ \leq \arg(I_{C2,f}) - \arg(I_{C2}) < 180^\circ \quad (4.9b)$$

The characteristics of the load connected feeders will not change. Hence, similar conclusions can be obtained as shown in (4.6a, 4.6b).

$$\arg(I_{C3,f}) - \arg(I_{C3}) < t_2 \quad (4.10a)$$

$$\arg(I_{B3,f}) - \arg(I_{B3}) < t_2 \quad (4.10b)$$

Now, as the bus voltages are below 90%, the DGs are supplying reactive power in addition to the active power and the phase of post-fault positive sequence main feeder current will change with respect to the phase of pre-fault positive sequence main feeder current. The phase variations of feeder currents at bus A can be summarized as follows:

$$90^\circ \leq \arg(I_{A4,f}) - \arg(I_{A4}) \leq 180^\circ \quad (4.11a)$$

or

$$-180^\circ \leq \arg(I_{A4,f}) - \arg(I_{A4}) \leq -90^\circ \quad (4.11b)$$

$$-90^\circ \leq \arg(I_{A3,f}) - \arg(I_{A3}) \leq 90^\circ, \quad (4.12a)$$

$$\arg(I_{A2,f}) - \arg(I_{A2}) < t_2 \quad (4.12b)$$

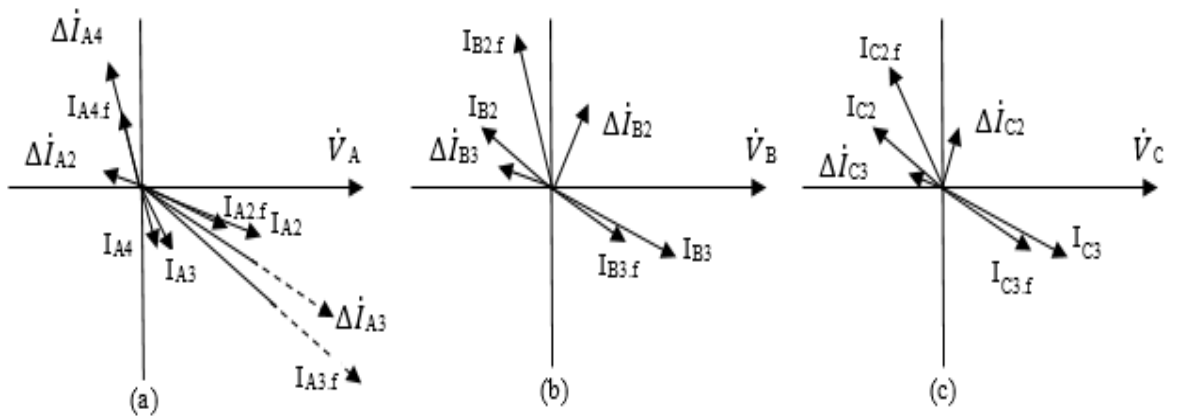


Fig. 4.6. Positive sequence current phasors for both DG voltages < 0.9. (a) Bus A. (b) Bus B. (c) Bus C.

The positive sequence current phasors in bus A, bus B and bus C when both DG voltages are less than 0.9 are shown in Fig. 4.6. It can be seen from (4.11) that when fault occurs in the main feeder, the phase change of that main feeder current will be less than 90° , which is not applicable for the healthy main feeder. The faulty feeder in the microgrid can be detected by using the flowchart depicted in Fig.4.7 when both DG voltages are less than 0.9.

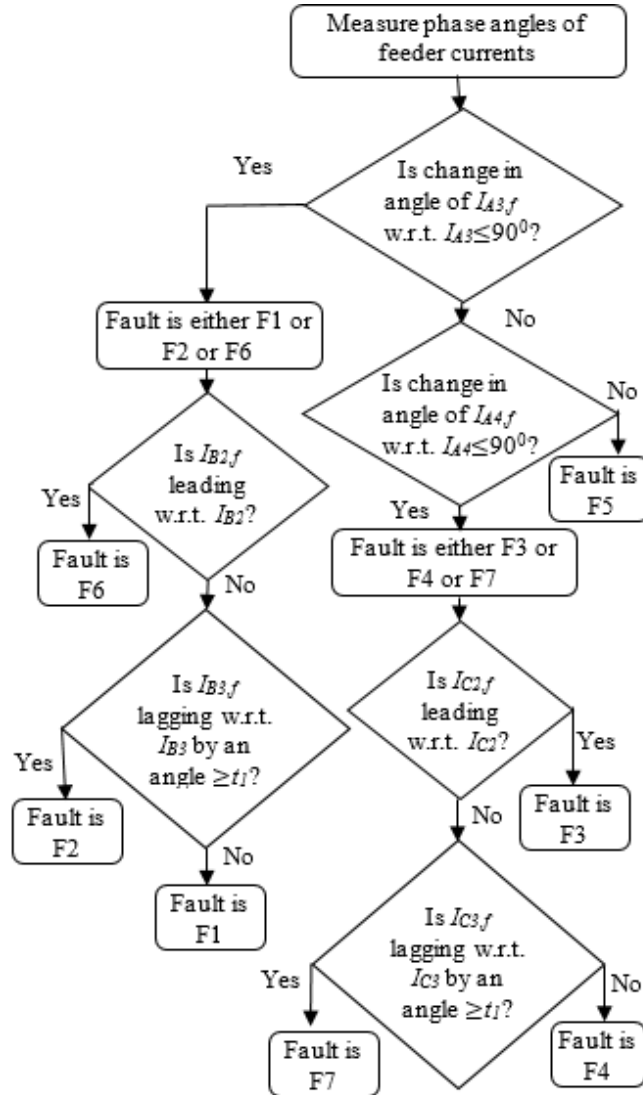


Fig. 4.7. Flowchart for fault detection in the microgrid for both DG voltages < 0.9.

4.3.4. Fault Detection Scheme for one DG Voltage Greater than 0.9 and another DG Voltage Less than 0.9

When fault occurs at F1, there is a possibility that the voltage coefficient at bus B is less than 90% since it is located downstream and the bus C voltage coefficient remains greater than 90%. Therefore, DG1 will supply both active power and reactive power simultaneously, whereas

DG2 will supply only active power in this case. Similar conclusions can be obtained in this case as that of the previous two cases; therefore, the analysis is not repeated here.

It can be seen from Fig. 4.2 that the feeders L3, L5 and L6 are connected to bus B to which DG1 is connected. When fault occurs in these feeders, it is possible that DG1 voltage may fall below 90% with DG2 voltage remaining above 90%. Similarly, DG2 voltage may fall below 90% when fault occurs in L4, L7 and L8 with DG1 voltage remaining above 90%. Therefore, the fault can be identified using DG voltage variation, and the flowchart for faulty feeder detection is shown in the flowchart in Fig. 4.8.

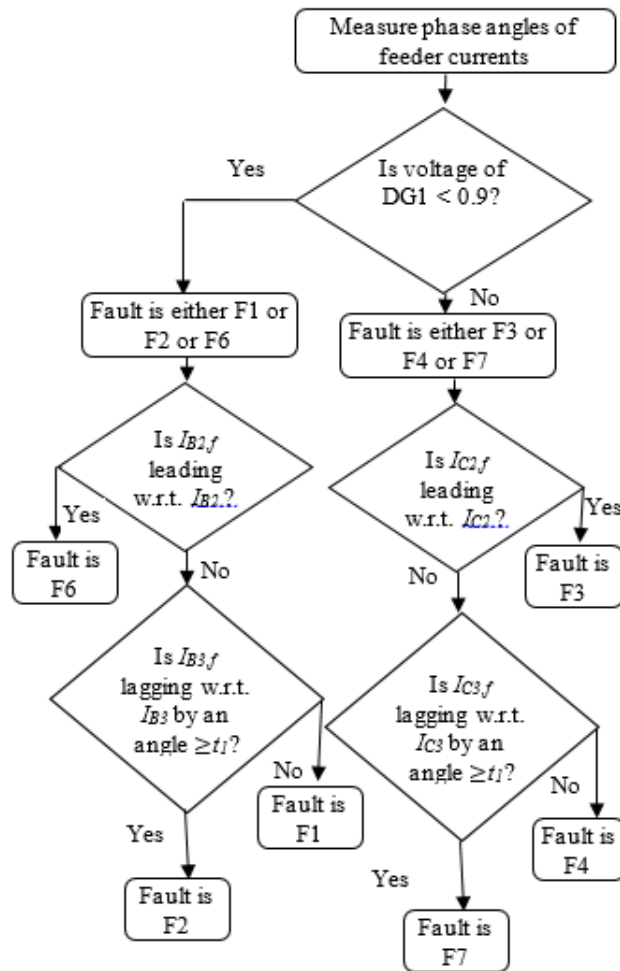


Fig. 4.8. Flowchart for fault detection in the microgrid for one DG voltage > 0.9 and another DG voltage < 0.9.

4.4. Simulation Results

To evaluate the performance of the proposed fault detection method, the grid connected microgrid as shown in Fig. 4.2 has been simulated in the MATLAB platform. The frequency of

the system is considered as 50 Hz, and the two main 10 kV transmission lines in the microgrid are connected to the 110 kV distribution system through a step-up transformer. DG1 is connected to feeder L5 with the capacity of 500 kW, and DG2 is connected to feeder L7 with the capacity of 600 kW. DG1 and DG2 are modelled according to the LVRT requirement of the system, and the rated voltage of the DGs is 10 kV. The positive sequence feeder resistance and reactance are considered as $0.38+j0.45\Omega/\text{km}$, and the zero sequence feeder resistance and reactance are considered as $0.76+j 1.32\Omega/\text{km}$. The threshold values t_1 and t_2 have been considered to be 5 and 1.5, respectively, for both DG voltages greater than 0.9, for both DG voltages less than 0.9, they are 10 and 3, respectively, and for one DG voltage greater than 0.9 and other DG voltage less than 0.9, t_1 and t_2 have been considered as 8 and 3, respectively. Different load power factors are considered under different case studies. In case (i), all load (LD1, LD2 and LD3) power factors are considered as unity, in case (ii), the load power factor for LD1 is considered as unity, for LD2, it is 0.95 and for LD3, it is 0.90. In case (iii), the load power factor for LD1 is considered to be 0.85, for LD2, it is 0.95 and for LD3, it is 0.9. Different faults F1-F7 are considered in all the feeders in the microgrid with different fault resistances. The simulation results are presented in this section under different DG voltage conditions with different faults F1-F7.

4.4.1. Simulation Results for both DG Voltages Greater than 0.9

When HIF occurs in the microgrid, the DG voltage coefficients remain above 0.9. The fault types considered here are single-phase ground fault (SPGF) in F1, F5 and F6, phase-phase ground fault (PPGF) in F2, F3 and F4 and phase-phase fault (PPF) in F7. The fault resistances of the fault points considered are 50Ω at F6, 100Ω at F1, F4 and F5 and 200Ω at F2, F3 and F7. Before fault occurs, both the DG voltages are at 1 p.u. When fault occurs at F1, the DG1 voltage drops to 0.985 and DG2 voltage drops to 0.994. When fault occurs at F2, the DG1 and DG2 voltages are dropped to 0.986 and 0.995, respectively. For fault at F3, the DG1 and DG2 voltages are changed to 0.99 and 0.985, respectively. Similarly, for the remaining faults (i.e. F4-F7), both the DG voltages remain above 0.9. Therefore, both DGs will supply only active power output and the reactive power output is zero.

Table 4.1 shows the phase angles of the feeder currents before and after fault when the load pfs are the same as discussed in case (i). For faults at F1, F2 and F6, it can be seen that $I_{A3,f}$ is leading with respect to I_{A3} by an angle greater than the threshold value t_1 which is not true for any other faults. For fault at F6 only, $I_{B2,f}$ is also leading with respect to I_{B2} by an angle greater than t_1 . For fault at F2 only, the change in the angle of I_{B3} after fault is greater than threshold t_2 .

Similarly, from Table 4.1, it is clear that for faults F3, F4 and F7 only, $I_{A4,f}$ is leading with respect to I_{A4} by an angle greater than the threshold value t_1 . For fault at F3 only, I_{C2f} is leading with respect to I_{C2} by an angle greater than t_1 . For fault at F7 only, the change in the angle of I_{C3} after fault is greater than threshold t_2 . If neither $I_{A3,f}$ nor $I_{A4,f}$ is leading with respect to the pre-fault currents by an angle greater than t_1 , then fault is F5.

Further simulation results are presented in Table 4.2 and Table 4.3 for different load power factors as described in case (ii) and case (iii) for both DG voltages greater than 0.9. The pre-fault phase angles are different in each case due to the change in load power factors. From Table 4.2 and Table 4.3, it is evident that the change in the phase angles of all the feeder currents follows the same logic as depicted in the flowchart in Fig. 4.5. Hence, the proposed fault detection method is capable of detecting the faulty feeder with different load power factors.

Table 4.1. Phase change of positive sequence feeder currents when both DG voltages >0.9 (load pf - unity)

Feeder currents	Pre-fault	F1 fault	F2 fault	F3 fault	F4 fault	F5 fault	F6 fault	F7 fault
I_{A3}	-64	-44	-46	-65	-65	-65	-45	-64
I_{A4}	-64	-66.5	-66	-40	-40	-66	-66.5	-50
I_{B2}	152	151.2	151	151	151.2	151.2	160	151.5
I_{C2}	149.3	149	149	-73	147.5	148.6	149	148.5
I_{B3}	-35	-35.5	-36.6	-35.5	-35.5	-35.5	-35.5	-35.1
I_{C3}	-36.1	-36.4	-36.4	-37	-37.4	-36.7	-36.4	-38.8
I_{A2}	-35.5	-35.8	-35.8	-36.2	-36	-37.2	-35.8	-35.7

Table 4.2. Phase change of positive sequence feeder currents when both DG voltages >0.9 (LD1-1 pf, LD2- 0.95 pf, LD3-0.9 pf)

Feeder currents	Pre-fault	F1 fault	F2 fault	F3 fault	F4 fault	F5 fault	F6 fault	F7 fault
I_{A3}	-102	-65	-67	-102	-102	-103	-65	-103
I_{A4}	-111	-113	-112	-75	-76	-114	-113	-67
I_{B2}	152.7	152	152	152.3	152.2	152	162	152
I_{C2}	150.5	150	150.1	-152	149.3	149.8	150.1	149
I_{B3}	-49.4	-50.1	-46	-49.8	-49.8	-50.1	-50.1	-49.9
I_{C3}	-56.4	-56.8	-56.7	-57.4	-57.4	-57.1	-56.8	-50
I_{A2}	-35	-35.5	-35.3	-35.3	-35.3	-36.9	-35.3	-35.5

Table 4.3. Phase change of positive sequence feeder currents when both DG voltages >0.9 (LD1-0.85 pf, LD2-0.95 pf, LD3-0.9 pf)

Feeder currents	Pre-fault	F1 fault	F2 fault	F3 fault	F4 fault	F5 fault	F6 fault	F7 fault
I_{A3}	-102	-64.6	-60	-104	-103	-104	-52	-105
I_{A4}	-112	-113.5	-115	-60	-76	-115	-115	-58
I_{B2}	153.2	152.4	152	152.2	152.6	152.6	-67	152.4
I_{C2}	151	150.4	150.4	-152	150	150.2	150.3	148.9
I_{B3}	-49	-49.6	-45	-49.5	-49.3	-49.6	-50.4	-49.8
I_{C3}	-56	-56.4	-56.6	-58	-57	-56.7	-56.7	-47
I_{A2}	-61.2	-61.6	-61.8	-62	-61.6	-50	-62	-62.1

4.4.2. Simulation Results for both DG Voltages less than 0.9

When LIF occurs in the microgrid, both the DG voltage coefficients fall below 0.9 and can drop below 0.5 also. The fault resistances of the fault points considered in this case are 0.01 Ω at F1, F3 and F6, 0.5 Ω at F4 and F7 and 1 Ω at F2 and F5. Single-phase ground fault (SPGF) is considered in F1 and F5, phase-phase ground fault (PPGF) in F2, F7 and F4 and three phase ground fault (TPGF) in F3 and F6.

Table 4.4 represents the phase angles of the feeder currents before and after fault when the load power factors are the same as discussed in case (i). It is seen that when fault occurs at F1, the DG1 voltage drops to 0.59 and the DG2 voltage drops to 0.78. When fault occurs at F2, the DG1 and DG2 voltages are dropped to 0.79 and 0.89, respectively, for fault at F4, the DG1 and DG2 voltages are changed to 0.81 and 0.57 respectively, for F5, the DG1 voltage is 0.82 and the DG2 voltage is 0.83 and for fault F7, the voltages are 0.85 and 0.6 at DG1 and DG2, respectively. Hence, for all these faults, the DG voltages have dropped below 0.9 and remain above 0.5. Therefore, the DGs supply both active and reactive power simultaneously. For fault at F3, the DG1 voltage drops to 0.88, and DG2 voltage at 0.37, and hence, DG1 supplies both active and reactive power, whereas DG2 supplies only reactive power. For fault at F6, the DG1 voltage becomes 0.2 and the DG2 voltage becomes 0.8, so DG2 supplies both active and reactive power, whereas DG1 supplies only reactive power.

From Table 4.4, it can be seen that for faults F1, F2 and F6, the change in the angle of $I_{A3,f}$ with respect to I_{A3} is less than 90^0 , whereas the change in the angle of $I_{A4,f}$ with respect to I_{A4} is more than 90^0 . Again for faults F3, F4 and F7, the change in the angle of $I_{A4,f}$ with respect to, I_{A4} is less than 90^0 , whereas the change in the angle of $I_{A3,f}$ with respect to, I_{A3} is more than 90^0 . When the change in the phase angle of $I_{A3,f}$ and $I_{A4,f}$ is more than 90^0 , then fault is at F5. It is also observed that I_{B2f} is leading with respect to I_{B2} only when fault occurs at F6. The change in

Table 4.4. Phase change of positive sequence feeder currents when both DG voltages <0.9 (load pf- unity)

Feeder currents	Pre-fault	F1 fault	F2 fault	F3 fault	F4 fault	F5 fault	F6 fault	F7 fault
I_{A3}	-75	-80	-82.5	50	115	118	-79	75
I_{A4}	-79	100	111	-84	-82	106	110	-83
I_{B2}	152	120	137	140	115	140	-83	135
I_{C2}	149	126	138.3	-88	110	131	136	112
I_{B3}	-37.9	-39	-78	-37.4	-37.7	-37.6	-38.6	-37.6
I_{C3}	-39	-39.5	-39	-37.5	-38.5	-38.9	-39.4	-80
I_{A2}	-35.4	-37.9	-35.3	-35.1	-35.5	-80	-35.9	-35.3

Table 4.5. Phase change of positive sequence feeder currents when both DG voltages <0.9 (LD1-1 pf, LD2-0.95 pf, LD3-0.9 pf)

Feeder currents	Pre-fault	F1 fault	F2 fault	F3 fault	F4 fault	F5 fault	F6 fault	F7 fault
I_{A3}	-102	-81.5	-83	150	135	145	-80	120
I_{A4}	-110	130	150	-80	-82	150	150	-82
I_{B2}	152.7	122	124	132	130	132	-82	130
I_{C2}	150.5	126	131	-80	110	131	129	110
I_{B3}	-49.4	-50	-80	-50	-50	-49.5	-50.5	-49.8
I_{C3}	-56.5	-56.7	-56.4	-58	-56.2	-56.5	-57	-80
I_{A2}	-35	-35.3	-35	-35.5	-35.3	-80	-35.5	-35.2

Table 4.6. Phase change of positive sequence feeder currents when both DG voltages <0.9 (LD1-0.85 pf, LD2-0.95 pf, LD3-0.9 pf)

Feeder currents	Pre-fault	F1 fault	F2 fault	F3 fault	F4 fault	F5 fault	F6 fault	F7 fault
I_{A3}	-102	-80	-80	100	100	100	-80	115
I_{A4}	-110	130	150	-81	-83	150	145	-82
I_{B2}	152	70	124	127	125	127	-81	129
I_{C2}	151	125	130	-82	110	131	128	113
I_{B3}	-49	-51.5	-81	-50	-49.5	-49.4	-50.5	-49.5
I_{C3}	-56	-57	-56.2	-57.7	-56.7	-56.3	-56.7	-80
I_{A2}	-61.2	-62.2	-61.4	-62.1	-61.7	-80	-62	-61.6

the phase angle of I_{B3} is more than threshold t_1 only when fault occurs at F2. Similarly, it is seen that I_{C2f} is leading with respect to I_{C2} only when fault is at F3. The change in the phase angle of I_{C3} is more than threshold t_1 only when fault occurs at F7. Therefore, all the fault criteria as described in the flowchart in Fig. 4.7 are satisfied. In Table 4.5 and Table 4.6, the phase angle variation information of all the feeder currents is given for case (ii) and case (iii), respectively. The simulation results as depicted in these tables show that the proposed fault detection method presented in Fig. 4.7 is capable of detecting the faulty feeder in the presence of different load power factors.

4.4.3. Simulation Results for one DG Voltage Less than 0.9 and another DG Voltage Greater than 0.9

As two DGs are present in the microgrid, it may happen that DG1 voltage is less than 0.9 and DG2 voltage is greater than 0.9. On the other hand, it is also possible that the DG1 voltage is greater than 0.9 and the DG2 voltage is less than 0.9. Different faults are considered in this section, which satisfy these two conditions. The fault resistances of the fault points considered in this case are 2Ω , 5Ω and 8Ω at (F1, F6), (F3, F4) and (F2, F7), respectively. Single-phase ground fault (SPGF) is considered in F1, F3, F4 and F6 and phase-phase ground fault (PPGF) in F2 and F7. Phase variation information for case (i), case(ii) and case(iii) is shown in Tables 4.7-4.9, respectively. It can be seen that from the simulation results that when F1, F2, and F6 faults occur, the DG1 voltage becomes less than 0.9 whereas the DG2 voltage remains above 0.9. Similarly, when F3, F4, F7 faults occurs, the DG1 voltage remains above 0.9 and the DG2 voltage drops below 0.9. For fault at F5, this condition does not arise as when fault occurs at F5, either both DG voltages are less than 0.9 or both are more than 0.9. From Tables 4.7- 4.9, it is seen that the faulty feeders can be identified following the same logic as depicted in the flowchart shown in Fig. 4.8 and described in the previous section.

Table 4.7. Phase change of positive sequence feeder currents when one DG voltage <0.9 and other DG voltage >0.9 (load pf - unity)

Feeder currents	Pre-fault	DG1 voltage<0.9 DG2 voltage >0.9			DG2 voltage<0.9 DG1 voltage >0.9		
		F1 fault	F2 fault	F6 fault	F3 fault	F4 fault	F7 fault
I_{A3}	-69	-60	-64	-76	-81	-85	-86
I_{A4}	-64	-108	-126	-87	-68	-62	-64
I_{B2}	152	135	130	-93	151	150	150
I_{C2}	149.3	145	148.2	149.2	-79	123	120
I_{B3}	-36	-38.4	-66	-36.5	-36.8	-37.5	-37.4
I_{C3}	-36.1	-37.5	-37.5	-36.2	-38.4	-37.9	-64
I_{A2}	-34.3	-35.5	-35.8	-34.7	-35.1	-35.7	-35.6

Table 4.8. Phase change of positive sequence feeder currents when one DG voltage <0.9 and other DG voltage >0.9 (LD1-1 pf, LD2- 0.95 pf, LD3-0.9 pf)

Feeder currents	Pre-fault	DG1 voltage<0.9 DG2 voltage >0.9			DG2 voltage<0.9 DG1 voltage >0.9		
		F1 fault	F2 fault	F6 fault	F3 fault	F4 fault	F7 fault
I_{A3}	-102	-78	-69	-80	-110	-112	-113
I_{A4}	-110	-134	-132	-120	-72	-66	-67
I_{B2}	153	128	125	-94	152	151	151
I_{C2}	150.5	148.5	149	150.4	-80	122	120
I_{B3}	-49.3	-50.5	-68	-49.9	-50	-50.9	-50.9
I_{C3}	-56.5	-56.9	-57.5	-56.6	-58.7	-57.9	-66
I_{A2}	-35	-35.5	-36.4	-35.2	-35.8	-36.4	-36.5

Table 4.9. Phase change of positive sequence feeder currents when one DG voltage <0.9 and other DG voltage >0.9 (LD1-0.85 pf, LD2- 0.95 pf, LD3-0.9 pf)

Feeder currents	Pre-fault	DG1 voltage<0.9 DG2 voltage >0.9			DG2 voltage<0.9 DG1 voltage >0.9		
		F1 fault	F2 fault	F6 fault	F3 fault	F4 fault	F7 fault
I_{A3}	-102	-63	-65	-80	-111	-113	-114
I_{A4}	-112	-127	-131	-121	-76	-66	-68
I_{B2}	153	133	128	-99	152	151	152
I_{C2}	151	150.5	150	150.9	-78	120	127
I_{B3}	-49	-51.2	-65	-49.5	-50	-50.5	-50.4
I_{C3}	-56	-57.5	-57.5	-56.1	-58.4	-57.9	-65
I_{A2}	-61.2	-62.7	-62.8	-61.5	-62	-62.7	-62.7

4.5. Comparative Assessment

The comparative assessment has been carried out with other recent fault detection schemes for the microgrids to highlight the robustness of the proposed fault detection scheme. In this study, the low voltage ride through capability is included in the DGs to support the grid codes, which has not been included in other works [34, 38, 42, 44, 46]. Also, the specific control strategy (PQ control) has been used and a new fault detection algorithm has been derived based on the fault characteristics of the DGs in the microgrid. Unlike ref. [34, 38, 44, 46], different load power factors are considered in this study and the proposed scheme is able to detect the fault at different load power factors. The scheme is not dependent on the fault resistances, and it can detect the faulty feeder even when high impedance faults occur, whereas the schemes proposed in ref. [34, 42] can detect only low impedance faults. Different faults are considered in different feeders so that the proposed scheme can detect the fault in any feeder (main feeder or branch feeder), whereas in ref. [46], the proposed technique can detect fault in main feeders only. Therefore, the proposed scheme is not dependent on the type of fault and fault impedance. It can detect fault in all types of feeders and also insensitive to load changes. The proposed scheme did not utilize any transform-based or artificial intelligence-based technique ensuring low computational burden unlike ref. [42-44], and the technique is also independent of synchronization of signals. The technique proposed in ref. [55] uses the phase angles of both voltage and current to detect fault, whereas the proposed technique uses only the phase change in current to detect the fault, and hence, the computational burden in the proposed technique is less. Moreover, in the proposed technique, tests have been performed at different sampling frequencies, viz. 6.5 kHz, 10 kHz and 20 kHz, and results have been validated.

4.6. Conclusion

This chapter presents a new fault detection scheme based on the phase change in positive sequence feeder current for microgrids with inverter-interfaced distributed generators. The low voltage ride through capacity requirement of grid-connected IIDGs has been considered in this study. The characteristics of the DGs are explained under different voltage conditions. The phase variations of the positive sequence feeder currents are examined under different fault conditions in the microgrid. The proposed scheme can detect faults in any feeder such as main feeders and branch feeders, and also, it is not dependent on the fault resistances as it can detect both high and low impedance faults. This scheme has a low computational burden and does not need synchronization of signals. The simulation results show that the proposed scheme is not affected by different power factors of the loads. From the comparative assessment, it is evident that the proposed scheme is robust, efficient and reliable and suitable for practical applications.

CHAPTER 5

A New Lissajous-Based Technique for Islanding Detection in Microgrid

5.1. Introduction

The remarkable escalation of the renewable energy-based distributed generation has created several challenges, among which islanding detection is the predominant one and widely debated over the years. Failure in the detection of islanding event may create several power quality issues and stability problem. Over the years, different techniques have been proposed to detect the islanding phenomenon. The existing commercial schemes such as remote control (RC), local control (LC), transform based, artificial intelligence (AI) and signal processing (SP) based techniques have certain drawbacks. The RC based techniques are expensive when it comes to the small networks whereas in LC based techniques, it is difficult to define the threshold. Also, it suffers from large NDZ region, degraded power quality and high detection time. The computational time for transform based methods is very high. The AI algorithms are difficult to implement in practice and SP methods require high sampling frequency and gives poor response under noisy conditions. Therefore, the authors in this work seek to outline a comprehensive data-driven framework which is based on Lissajous figure obtained by plotting voltage waveforms versus current waveforms. The shape of the Lissajous figures can provide distinct insight about the type of disturbance in the power distribution network. The proposed technique exploits the characterizing patterns of the Lissajous figure to detect islanding phenomenon.

The depletion of the fossil fuels and growing concerns on environmental issues lead to the rapid enhancement in the penetration of renewable based distributed generation (DG) units into the distribution network. The integration of the DGs into the modern power systems brings several benefits such as high efficiency, reliability and improved power quality which have escalated the concept of smart microgrid. But the high integration of the DGs into the distribution network causes several security and protection issues, one of the important issues is islanding detection of the DGs. Failure to trip the islanded DG can cause severe problems and in the case of unintentional islanding, the DG must be disconnected within 2s as per the standards mentioned in IEEE 1547 standards [56]. Therefore, this issue gained rapid interest and the researchers presented various methods for islanding detection in the microgrid. The islanding detection

techniques presented in the literature can be broadly categorized into two categories which are remote and local control techniques. In remote control approach the communication channel plays an important role to access the information from the remote terminals. The studies presented in [57,58] monitored and analyzed the remote data constantly with the help of the supervisory control and data acquisition (SCADA). In [59] the authors presented a remote control method for islanding detection. These remote communication-based methods are not economical for the small network systems and these studies are not suitable where regional monitoring is required. Therefore, to overcome these issues the local control approaches are introduced. In the local control approaches the system parameters such as current, voltage and frequency are regionally monitored. These approaches are basically grouped into three categories, which are passive, active and hybrid methods. The passive approach basically depends on the variations of the system parameters such as rate of change of voltage phase angle [60], rate of change of kinetic energy over reactive power (ROKORP) [61], sequence impedance [62,63], phase angle difference of impedance [64] and adaptive rate of change of frequency [65]. The drawbacks of these passive methods are inability to detect islanding when power mismatch is low and at perfect power balance conditions. Moreover, these methods have large NDZ. Active islanding detection approaches gained more interest because of the shortcomings of passive islanding detection methods. Some of the active islanding detection studies presented in the literature are active ROCOF [66], reactive and active power control based method for synchronous machine type DGs [67], frequency deviation [68], phase disturbance [69] and sliding mode frequency shift [70]. The main problem of these active islanding methods is that due to the insertion of additional disturbance signal, the power quality of the system deteriorates. To avail the benefits of both active and passive methods, hybrid islanding detection methods are developed. One of such methods is presented in the literature which is based on the parallel inductance switching [71].

Later on the researchers developed S-transform and wavelet transform based islanding detection techniques [72]–[74]. The computational time for S-transform based methods is very high which is not suitable for practical applications and also it is not possible for S-transform to incorporate all signals inside the predetermined Gaussian window. Wavelet transform based methods have drawbacks such as hardware limitations and high sampling rate. Subsequently, Hilbert Huang transform based approaches have been proposed for islanding detection applying empirical mode decomposition [75, 76]. The authors in [77, 78] proposed islanding detection methods based on the pattern recognition and neuro fuzzy interface system. However, large number of neurons, complex training process and large training sets are the disadvantages of these approaches.

The authors in [79] developed an event index value based on the super imposed components of the sequence impedance by acquiring the local data. The authors in this work have not considered synchronous generator based DG. In [80] an islanding detection technique has been developed by injecting disturbance in the maximum power point control when the voltage exceeds the desired threshold. But it is only limited to the photovoltaic based systems whereas, in this work different types of DGs have been considered. A new islanding detection index is proposed in [81] based on the rate of change of potential energy function. In [82] the authors proposed a PMU based technique which has been developed considering the change in the phasors of the pre disturbance and post disturbance voltage and current signals.

In recent years the utilization of waveform measurement units (WMU) as a smart sensor has been introduced. The WMU can provide precise information of the time synchronized current and voltage waveform measurements and has high reporting rate. Lissajous figure can be developed utilizing the voltage and current waveforms [83]. The Lissajous figure reveals different behavior under different conditions which can be utilized to identify the cause of events in the system. Therefore, the authors in this work seek to propose a new islanding detection method for microgrid by utilizing the characteristics of the Lissajous figure.

This work presents a novel approach for islanding detection in the microgrid which consists of various types of DGs based on the Lissajous figure characteristics at each DG. The main contributions of this work can be summarized as follows:

- A new approach for islanding detection in microgrid based on the change of shape of Lissajous curve has been proposed. The shape of the Lissajous curve which is an ellipse under normal condition changes when disturbance occurs. The distinct pattern in the change of shape during islanding condition has been captured to segregate the islanding event from other disturbances.
- Adaptive thresholding based on Otsu algorithm has been considered for threshold selection to differentiate the non-islanding and islanding events.
- The proposed method has been tested under diverse islanding conditions such as NDZ, UL1741, variation in load quality factor, etc. Also, various case studies which may confuse islanding event with other events such as load changes, short circuit faults, induction motor starting and capacitor bank switching have been performed to test the efficacy of the proposed method.
- The proposed scheme does not require synchronized measurement of voltage and current signals and hence, it does not require expensive communication devices and free from

synchronization error. It also involves low computational complexity compared to other transform based and AI based schemes.

- The sampling frequency used in this study is 10 kHz which is much less than the sampling frequency required in conventional travelling wave-based methods.

5.2. Islanding Detection Using Lissajous Figure

The voltage and current signals collected from the PCC in the microgrid can be graphically represented in the form of a Lissajous curve.

5.2.1. Representation of Lissajous Figure

The instantaneous voltage and current signals can be represented as

$$v = V_m \sin (wt) \quad (5.1)$$

$$i = I_m \sin (wt + \theta) \quad (5.2)$$

where θ is the power factor angle and V_m and I_m are the amplitudes of the voltage and current signal respectively. The Lissajous figure is constructed with the current signal in the x-axis and the voltage signal in the y-axis. Eliminating the time variable wt from (5.1) and (5.2), formula correlating v and i can be obtained as follows

$$wt = \sin^{-1} \left(\frac{i}{I_m} \right) - \theta = \sin^{-1} \left(\frac{v}{V_m} \right) \quad (5.3)$$

Solving (5.3) using the trigonometric identities, (5.4) can be obtained.

$$\frac{i^2}{I_m^2} + \frac{v^2}{V_m^2} \cos^2 \theta - 2 \frac{vi}{I_m V_m} \cos \theta = \sin^2 \theta \quad (5.4)$$

The quadratic equation (5.4) can be written as shown in (5.5).

$$Ax^2 + Bxy + Cy^2 + D = 0 \quad (5.5)$$

where

$$A = \frac{1}{I_m^2}, B = -2 \frac{\cos \theta}{I_m V_m}, C = \frac{1}{V_m^2}, D = -\sin^2 \theta$$

$$\text{and } B^2 - 4AC = -\frac{4\sin^2\theta}{I_m^2 V_m^2} \quad (5.6)$$

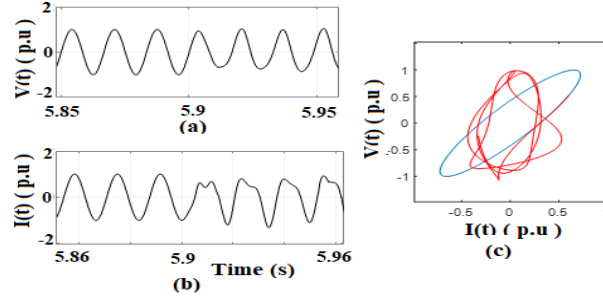


Fig. 5.1. Example of Lissajous figure: (a) Voltage signal, (b) Current signal, (c) Lissajous figure corresponding to voltage and current signal.

From (5.6) it can be observed that $B^2 - 4AC$ is a negative term regardless of the amplitude of I_m and V_m , and quadratic equation (5.4) represents an ellipse. Hence, mathematically it is evident that under normal conditions the Lissajous figure represents an ellipse. When islanding occurs, it creates disturbance in the voltage and current signals at the islanded circuit breaker which results the Lissajous figure to deviate from its original shape of an ellipse. Therefore, the shape of the Lissajous figure is different under islanding event. Fig. 5.1 depicts how Lissajous figure can be obtained from the voltage and current signals. Fig. 5.1(a) and Fig. 5.1(b) show the voltage and current signals and Fig. 5.1(c) shows the Lissajous figure obtained from the voltage and current signals. Under normal condition, the Lissajous curve is shown in blue color in Fig. 5.1(c) which represents an ellipse but when islanding occurs at 5.9s, the Lissajous curve deviates from the shape of an ellipse which is shown in red color. In this work, the distinct change in the pattern of Lissajous curve has been utilized to develop the islanding detection technique.

5.2.2. Islanding Detection

As mentioned in the above section, the Lissajous pattern varies under different conditions and accordingly the area of the Lissajous figure will also vary. Therefore, by determining the area of the Lissajous figure for successive intervals, a similarity index can be formulated to detect the disturbance event. The area of the Lissajous figure at time ' t ' can be calculated using (5.7).

$$A_{v-i}(t) = \left| \int_{i(\tau=t-T)}^{i(\tau=t)} v(\tau) di(\tau) \right| \quad (5.7)$$

Under normal condition the successive areas are almost same. For example, if $A_{v-i}(t)$ is the area

at time ‘ t ’ and $A_{v-i}(t-\Delta t)$ is the area at time ‘ $t-\Delta t$ ’, both will be almost same under normal operating condition where ‘ Δt ’ is the time interval. If any event occurs at time ‘ t ’, there will be significant difference between the $A_{v-i}(t)$ and $A_{v-i}(t-\Delta t)$. Therefore, a similarity index has been formulated based on the area of the Lissajous figure as shown in (5.8) to detect the islanding condition.

$$SI(t) = 1 - \left| \frac{A_{v-i}(t) - A_{v-i}(t - \Delta t)}{\max\{A_{v-i}(t), A_{v-i}(t - \Delta t)\}} \right| \quad (5.8)$$

The value of SI will vary from 0 to 1. Under normal condition or before islanding the successive areas are almost equal and hence, the value of SI is near to 1 whereas, after islanding there is a significant difference between the successive areas which results in the value of SI to deviate from 1. Even after the islanding event it is observed that there is a significant change in the successive areas and the value of SI remains less than 1. Therefore, by choosing a proper threshold for SI , islanding condition has been detected in this study.

5.2.3. Implementation of the Proposed Algorithm

Based on the above analysis, an algorithm has been developed to detect islanding in the test system shown in Fig.5.2. The test system consists of three different DGs which are connected to the system through the circuit breakers [61]. As different types of DGs are connected in the microgrid, it is possible that the behavior of each DG may vary due to change of events. Hence, to accurately detect the islanding in the proposed system, a threshold (SI_{th}) has been determined for the SI . The SI value at CB3 is considered initially followed by SI at other breakers to identify islanding condition. It is noteworthy to mention that the change in the area of Lissajous figure may occur not only due to islanding event but also due to the short circuit faults, load switching and other transient events. If SI at CB3 is less than SI_{th} , then islanding condition occurs at CB3. It is also possible that in this case there is multiple islanding involving DG at CB3. Next, the SI values will be checked at CB1 and CB2. SI values will remain less than SI_{th} for more than 5 cycles if the DGs at CB1 and CB2 are islanded. The detailed flowchart of the proposed algorithm is shown in Fig. 5.3.

Though the algorithm shown in the flowchart considers SI values at CB3 first, the algorithm can start considering CB1 or CB2 also. It is to be noted that during islanding, the duration for which SI values remain below the threshold value in case of synchronous based DG, is less than other two DGs which has been discussed in the next section. The flowchart shown in Fig.5.3 can be modified considering SI values at CB1 or CB2 at starting instead of CB3. Moreover, the

developed algorithm is not network specific. It can be applied to other networks also.

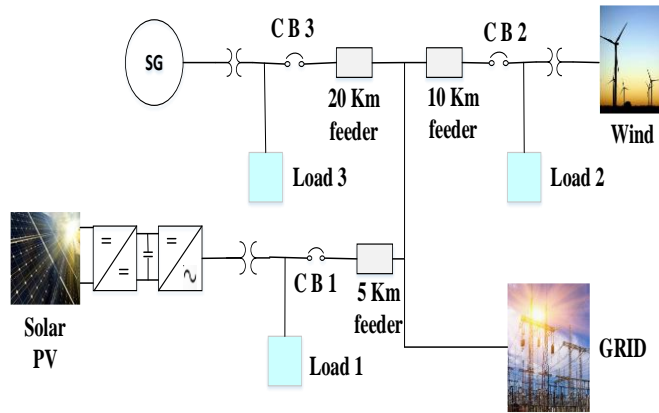


Fig. 5.2. Microgrid test system.

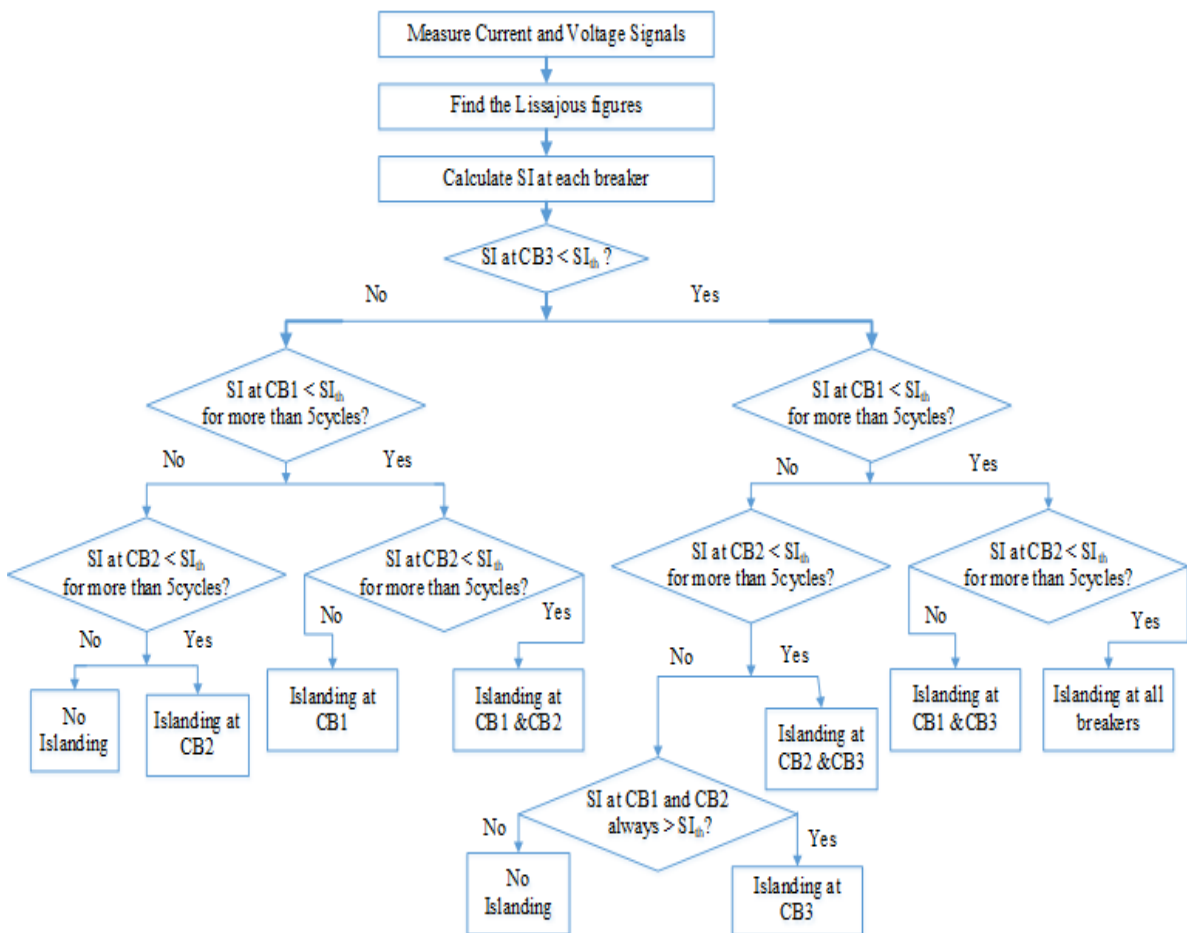


Fig. 5.3. Proposed islanding detection algorithm.

5.3. Simulation Results

The test system considered in this study as shown in Fig. 5.2 consists of three types of DGs which are photovoltaic, wind and synchronous generator based DGs with the rating of 250kW, 500kW and 200kW, respectively. Three different parallel RLC loads are connected to each DG. Load 1 consists of $R_1=2.5 \text{ k}\Omega$, $L_1=4.421 \text{ H}$ and $C_1=1.59 \text{ }\mu\text{F}$, load 2 consists of $R_2=1.25 \text{ k}\Omega$, $L_2=2.21 \text{ H}$ and $C_2=3.183 \text{ }\mu\text{F}$, load 3 consists of $R_3=3.125 \text{ k}\Omega$, $L_3=5.53 \text{ H}$ and $C_3=1.237\mu\text{F}$, respectively. The DG input voltage, reference temperature and voltage of photovoltaic DG are 500V, 45°C and 260V (ph-ph), respectively. Inertia constant, friction factor and output voltage for synchronous generator based DG are 3.2, 0 and 13.8kV, respectively and for wind based DG those are 0.685, 0.01 and 575V, respectively. The grid frequency is considered as 60Hz, operating voltage is 25 kV and the feeder lengths are shown in Fig. 5.2. The proposed islanding detection technique has been evaluated under different conditions as discussed in the following subsections. Under normal condition the SI remains above the threshold but under islanding condition it will be lower than the threshold value. It is possible that the shape of the Lissajous figure at non islanded breakers may alter due to other transient conditions resulting the SI values at the non-islanded CBs to come down below the SI_{th} . Therefore, to accurately detect the islanding condition another additional criterion is considered in the decision making. If SI remains less than SI_{th} for more than 5 consecutive samples at CB1 and CB2, then islanding event is detected. To detect islanding the proposed algorithm requires at least 5 consecutive cycles data and the maximum computational time to execute the algorithm is 0.1179s.

5.3.1. Threshold Selection

It is important for an islanding detection method to distinguish islanding from other disturbance events such as short circuit faults, load switching, capacitor bank switching, etc. Therefore, the threshold selection plays an important role to properly distinguish the islanding from other disturbance events. To achieve this, in this study, Otsu algorithm based thresholding method has been used to select a robust threshold, which is reliable and has been widely used in threshold based techniques [75]. Initially the SI values for islanding scenarios and the non-islanding scenarios have been separated as class 1 and class 2 respectively. The probability density function (PDF) is assigned for both the classes in which the probability of different ranges of SI value is predicted based on the measured data. Then histogram has been plotted to obtain the probability of predicted SI for both the classes. A comparative assessment has been carried out considering Weibull, Gama, and lognormal PDFs as shown in Table 5.1. Weibull

PDF is used to characterize the behaviour of the class 1 and class 2 events as it provided good fit (less K-S error, and high R^2 value) for the obtained histogram of the different scenarios in this study compared to Gamma and lognormal PDFs. The fitted PDF curves are intersecting at some point which is considered as the threshold to differentiate the class 1 and class 2 events. Fig. 5.4. represents the PDF based Otsu thresholding analysis at CB1. It can be seen from Fig. 5.4 that the islanding and non-islanding PDF curves are intersecting at 0.9. Hence, the threshold for PV (CB1) is considered as 0.9. The same analysis is carried out for other DGs and the same value of threshold has been obtained for other DGs as well.

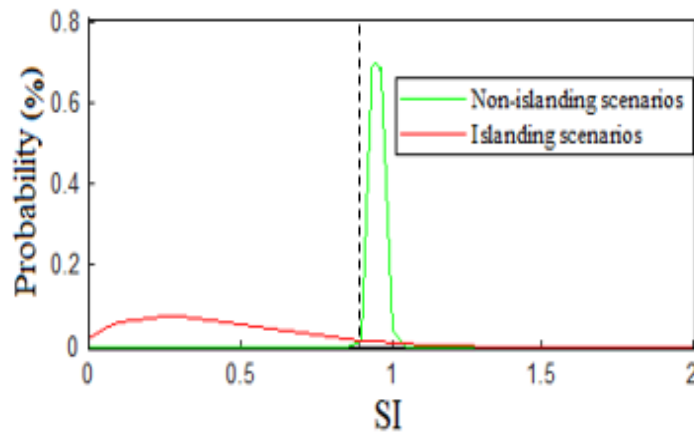


Fig. 5.4. Otsu thresholding analysis for PV.

Table 5.1. Statistical errors for different distribution functions

PDF	K-S error	R^2
Weibull	0.2704	0.8297
Gama	0.2728	0.7925
Lognormal	0.2781	0.7314

5.3.2. Evaluation of Islanding Detection Algorithm

In this case study the results are presented for different islanding conditions, such as CB of only one DG is opened and other CBs are closed (single islanding) or the CBs of multiple DGs are opened simultaneously (multiple islandings). The islanding condition is considered to occur at 5.9s and the voltage and current signals at each breaker have been used to get the Lissajous figure as shown in Fig. 5.5. The blue color line indicates Lissajous curve before islanding and the red color line indicates after islanding. It can be seen from Fig. 5.5 that when islanding occurs at CB1, only the shape of the Lissajous figure at CB1 is altered (red color) whereas the shape of the Lissajous figures at other breakers remain same as before. The area of the Lissajous figure is calculated for each cycle and SI is calculated using (5.8) and presented in Fig. 5.6.

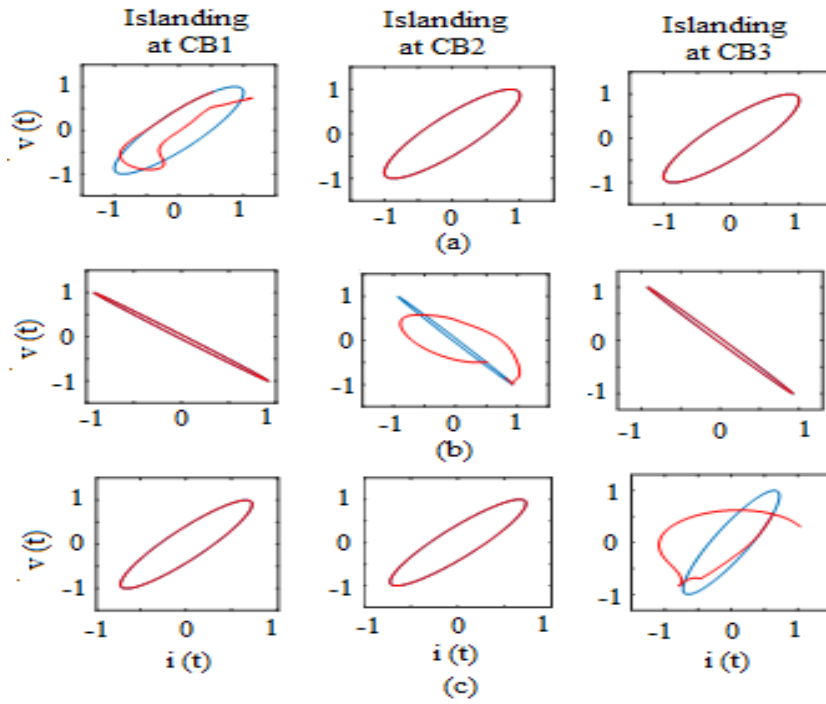


Fig. 5.5. Lissajous figures when islanding occurs at different DGs: (a) Lissajous figure at CB1, (b) Lissajous figure at CB2, (c) Lissajous figure at CB3.

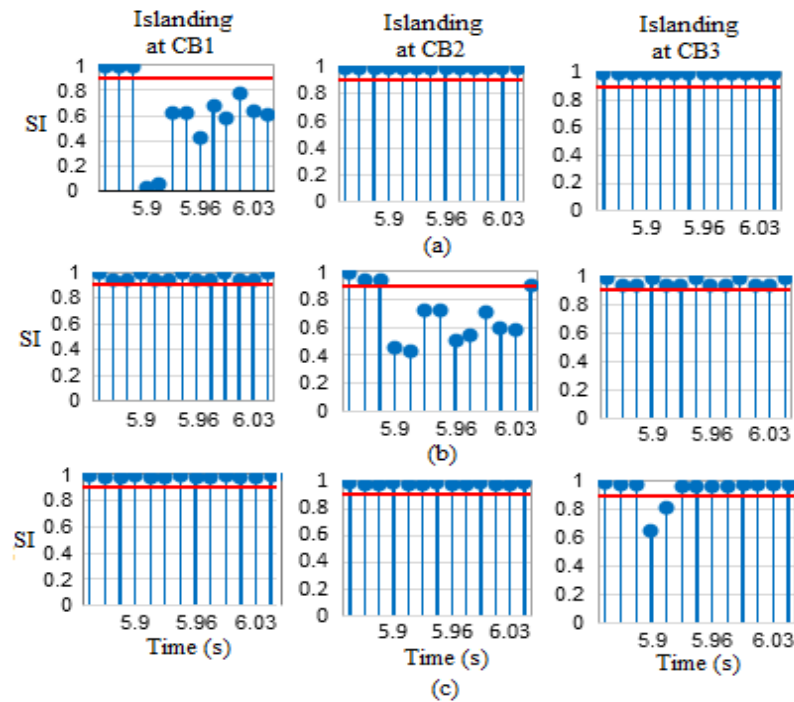


Fig. 5.6. *SI* values when islanding occurs at different DGs: (a) *SI* at CB1, (b) *SI* at CB2, (c) *SI* at CB3.

From Fig. 5.6(a) it is observed that under normal condition (till 5.9s) the *SI* values at each breaker are above the threshold value but when islanding occurs at CB1 only, the value of *SI* at CB1 is less than the threshold for more than 5 consecutive samples after 5.9s and the value of *SI*

at other breakers are above the threshold value. Similarly, when wind based DG is islanded, the value of SI at CB2 only is less than the threshold for more than 5 continuous samples after 5.9s as shown in Fig. 5.6(b). When islanding at CB3 occurs, the value of SI at CB3 is below the threshold and at other breakers it is above the threshold as shown in Fig. 5.6 (c). Therefore, the SI value detects islanding at 5.9s in all the three cases.

The proposed algorithm is evaluated when multiple breakers are opened simultaneously. Lissajous figures are obtained at different combinations of multiple islandings and it is observed that the shape of the Lissajous figures after islanding are deviating significantly only at the islanded CBs. In Fig. 5.7, the SI values at each breaker are shown when the DGs connected to CB1 and CB2 are islanded simultaneously at 5.9s. It is visible that the value of SI at CB1 and CB2 is below the threshold value for more than 5 consecutive samples and it is above the threshold value at CB3. Similarly, when all the CBs opened simultaneously, the values of SI at CB1 and CB2 are below the threshold value for more than 5 consecutive samples and also it is less than the threshold value at CB3 after 5.9s. Therefore, islanding at all the breakers is detected. It is to be noted that to detect islanding event at CB1 and CB2, the voltage and current signals collected only from the respective terminals are required. Islanding at the particular CB can be identified if the SI value is less than 5 consecutive cycles. But, to distinguish islanding event from other transient events at CB3, it requires the information of SI from other two breakers also. Hence, any communication delay in the data transfer may lead to the delay in the islanding event detection at CB3.

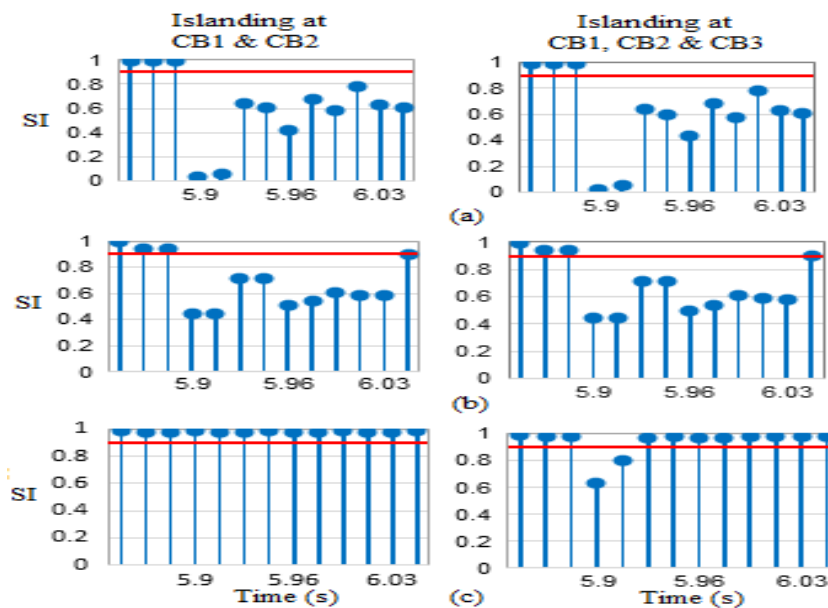


Fig. 5.7. SI values under multiple islanding condition: (a) SI at CB1, (b) SI at CB2, (c) SI at CB3.

5.3.3. Evaluation Under NDZ Region

The proposed algorithm has been tested under the NDZ region of the frequency and voltage relays. Various loads have been considered inside of the NDZ region of voltage (0.88 to 1.1 p.u) and frequency (59.3 to 60Hz) with different active power imbalance (ΔP). The selection of the loads is done to assure that the reactive power imbalance is zero which makes the islanding detection difficult for the conventional relays. The performance of the algorithm has been analyzed under two cases as shown in Fig. 5.8. The active power imbalance is considered with zero reactive power imbalance. In the first case, the active power imbalance is considered as -5kW and Fig. 5.8 shows the performance of the proposed algorithm when islanding occurs at CB2 at 5.9s. It can be seen that the value of the *SI* is less than the threshold for more than 5 consecutive samples at CB2. In the second case, the active power imbalance is considered as 10 kW, the *SI* values are shown when islanding occurs at CB3 at 5.9s. In both the cases the proposed algorithm is able to identify the islanding event.

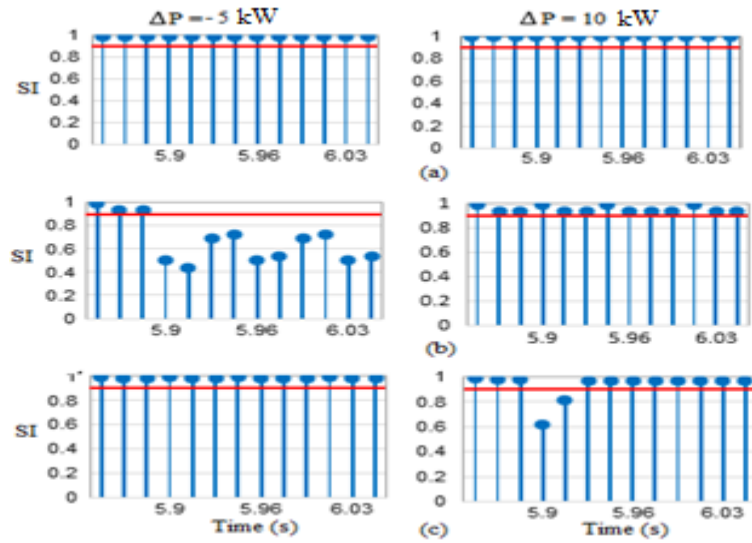


Fig. 5.8. Analysis of *SI* under NDZ region: (a) *SI* at CB1, (b) *SI* at CB2, (c) *SI* at CB3.

5.3.4. UL1741 Test Conditions

The reliability of the proposed method is verified under the test conditions of UL1741 for islanding protection of the DGs. As per the UL1741 test conditions, the load active power of the DG is adjusted to 100%, 50% and 25% and also the reactive power is adjusted between -5% to 5%. Based on these conditions five scenarios of simulation studies are conducted on the test system shown in Fig. 5.2 to evaluate the proposed method.

Case 1: The active power and reactive power consumption of the load is 100% and 0%, respectively (unity pf).

Case 2: The active power and reactive power consumption of the load is 50% and 0%, respectively (unity pf).

Case 3: The active power and reactive power consumption of the load is 25% and 0%, respectively (unity pf).

Case 4: The active power and reactive power consumption of the load is 100% and -1%, respectively (leading pf).

Case 5: The active power and reactive power consumption of the load is 50% and 1%, respectively (lagging pf).

To establish the above mentioned scenarios, different sets of RLC loads are considered at each DG. For each scenario, the simulation studies are conducted for all the three DG islandings and the performance of the proposed method is tested. In Fig. 5.9 the obtained results of *SI* when CB2 is opened in scenario 4 and when CB1 is opened in scenario 2 are presented. The obtained results show that the performance of the proposed method is satisfactory under UL1741 test conditions.

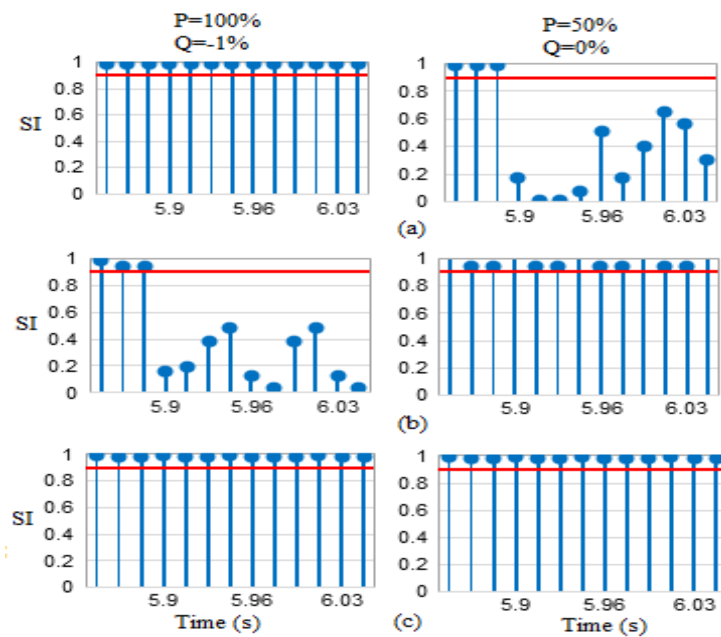


Fig. 5.9. Performance of the proposed algorithm under UL1741 test conditions: (a) *SI* at CB1, (b) *SI* at CB2, (c) *SI* at CB3.

5.3.5. Effect of Load Quality Factor

The behavior of the proposed algorithm under different Quality factors (Q_f) has been

verified in this case study. The standards emphasize that the most critical value of Q_f is 2.5 and it varies from 1 to 2.5. The higher Q_f creates problems in islanding detection. Assuming parallel RLC load, the values of R, L and C are computed as shown in (5.9) to (5.11).

$$R = \frac{V_r^2}{P_r} \quad (5.9)$$

$$L = \frac{V_r^2}{2\pi f_r P_r Q_f} \quad (5.10)$$

$$C = \frac{P_r Q_f}{2\pi f_r V_r^2} \quad (5.11)$$

where, V_r is the rated grid voltage, f_r is the resonant frequency, P_r is the rated power and Q_f is the quality factor. The performance of the proposed method is shown in Fig. 5.10 when the CBs are opened at 5.9s. When CB1 is opened, $Q_f=1$ and when CB3 is opened, $Q_f=2.5$. It can be seen from Fig. 5.10 that the islanding is detected at 5.9s.

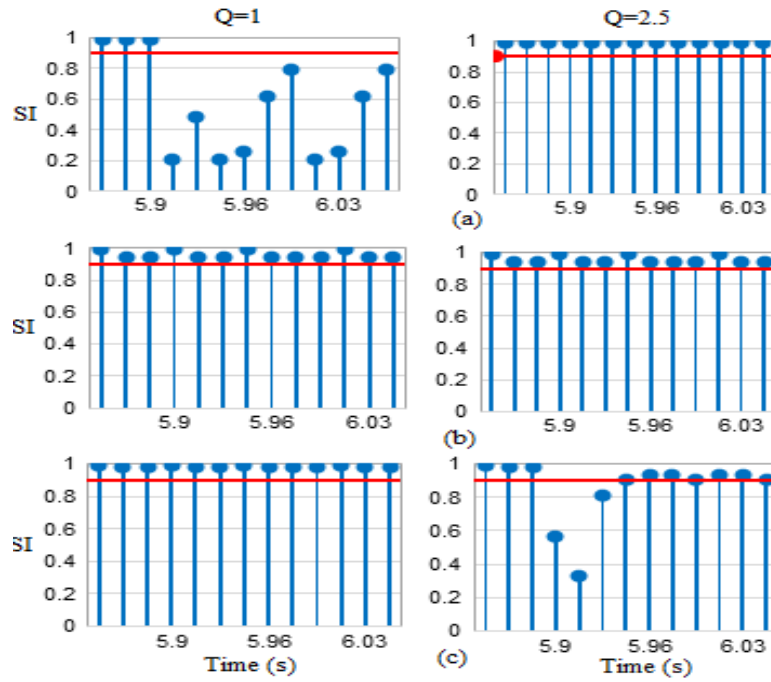


Fig. 5.10. Performance of SI under different Q_r : (a) SI at CB1, (b) SI at CB2, (c) SI at CB3.

5.3.6. Effect of Load Switching

The test model under this study is monitored while switching different linear and non-linear loads. In this section starting of 160 kVA induction motor and switching of 0.4 MVar capacitor bank are considered as tabulated in Table 5.2. The change of SI values when induction motor is

started at PV based DG bus and capacitor bank switching at CB2 at 5.9s is presented in Fig. 5.11. From Fig. 5.11 it can be seen that the values of SI are not below the threshold for more than 5 consecutive samples and hence the proposed method does not detect switching events as islanding.

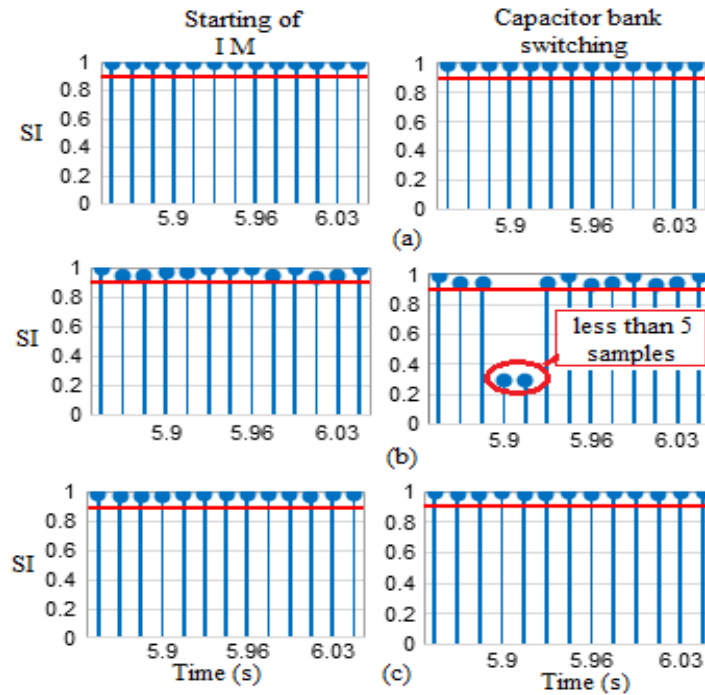


Fig. 5.11. Behavior of SI during load switching: (a) SI at CB1, (b) SI at CB2, (c) SI at CB3.

Table 5.2. Switching and Faults

Type	Value
Starting of induction motor	0-160 kVA
Capacitor bank switching	0-0.4 MVar
Faults (LG, LL, LLG, LLL, LLLG)	0-10 Ω

5.3.7. Effect of Faults

In this section the effect of different types of faults on the performance of the proposed method is discussed. In this case different fault types with different fault resistances are considered and the fault has been applied at each feeder at 5.9s. The Lissajous figures for some selected cases are presented in Fig. 5.12. When fault occurs at any location, it is observed that all the DG terminals experience disturbance in voltage and current signals which results in the abrupt change in the shape of the Lissajous figure at every breaker. But the shape of the Lissajous figure at each breaker regain its original shape within 5 cycles.

The SI values have been calculated and presented in Fig. 5.13. From Fig. 5.13 it can be observed that when fault occurs there is a change in the value of SI at all breakers but the value of SI is not below the threshold for more than 5 consecutive samples. Therefore, it is not satisfying the criteria of islanding according to the proposed method and hence it is not detected as islanding event.

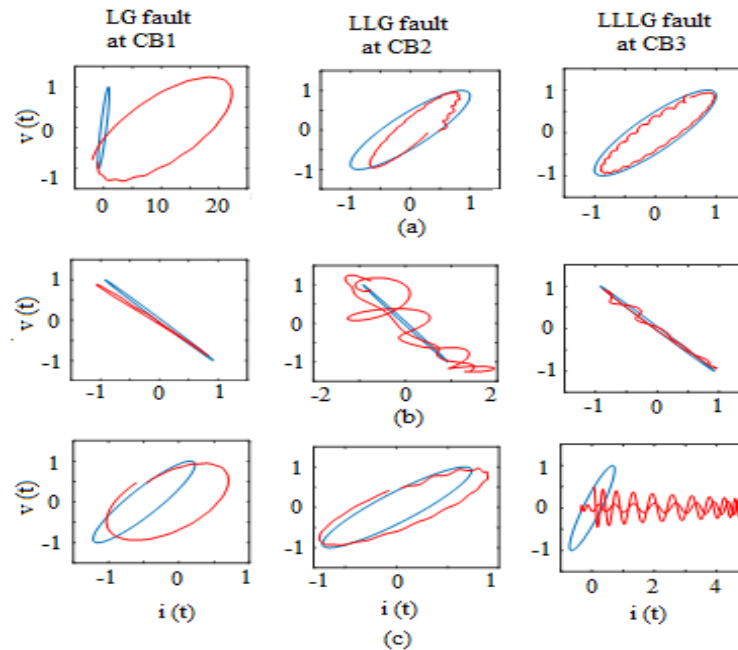


Fig. 5.12. Lissajous figure under faults: (a) Lissajous figure at CB1, (b) Lissajous figure at CB2, (c) Lissajous figure at CB3.

5.3.8. Effect of Sensing Errors

The proposed approach has been tested in the presence of sensing errors in the measured voltage and current signals within the range of $\pm 3\%$ following IEEE/ANSI standards. Two cases are considered to evaluate the proposed approach. In case 1 it is considered that the signals measured from CB3 are having sensing errors from 5.9s under normal condition. From Fig. 5.14(a) it can be seen that there is a slight change in the shape of the Lissajous curve at CB3 due to presence of sensing errors (in red color). Then SI has been computed at CB3 as shown in Fig. 5.14(b). Fig. 5.14 (b) reveals that there is not much change in the behavior of the SI at CB3. In case 2 it is considered that the sensing errors are present in the measured signals from the beginning and islanding event occurs at CB1. The Lissajous curve corresponding to the signals at CB1 is shown in Fig. 5.14(c) and the behavior of SI at CB1 is depicted in Fig. 5.14(d). The results indicate that the performance of the proposed approach has not deteriorated due to the sensing errors.

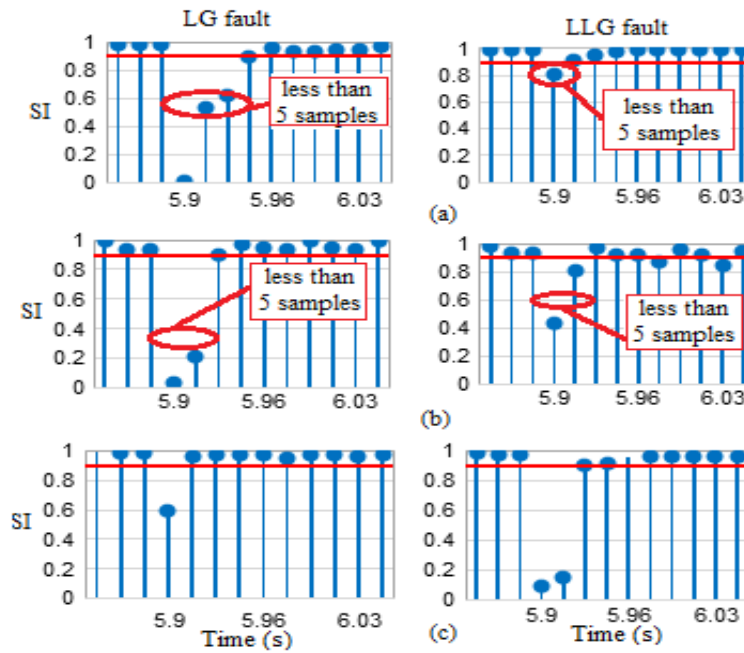


Fig. 5.13. Behaviour of SI under different types of faults: (a) SI at CB1, (b) SI at CB2, (c) SI at CB3.

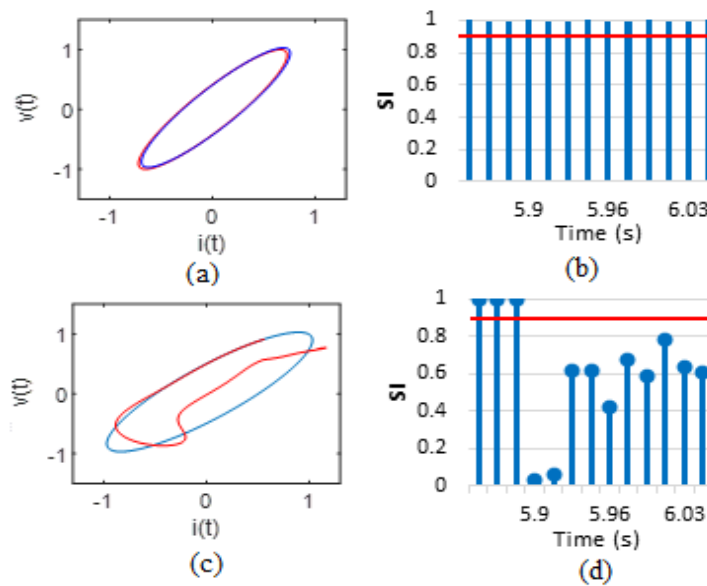


Fig. 5.14. Performance of the proposed approach under sensing errors: (a) Lissajous curve at CB3 in Case 1, (b) Behavior of SI at CB3 in Case 1, (c) Lissajous curve at CB1 in Case 2, (d) Behavior of SI at CB3 in Case 2.

5.3.9. Hardware-in-the-Loop Testing

In recent times the hardware in loop testing (HIL) has become the alternative to traditional simulation testing for validating proposed technique before deployment which is being widely as used industry standard around the world. The HIL simulation creates the similar dynamics of the real hardware with the real time simulator; indirectly it produces the virtual plant which

duplicates the real hardware. Therefore, using the HIL testing the proposed method has been validated for the real time applications in this study. The HIL testing setup considered in this study consists of four parts which are i) RT Lab software which is used to run the simulation in real time digital simulator, ii) Real time digital simulator (RTDS) which is the industrial standard HIL testing equipment; RTDS simulates the proposed system in real time. iii) Multi-channel digital oscilloscope which acts as the external waveform measurement unit (WMU) hardware to store and save the waveform data, iv) Computer unit which runs the RT lab, stores the measurement data and executes the algorithm.

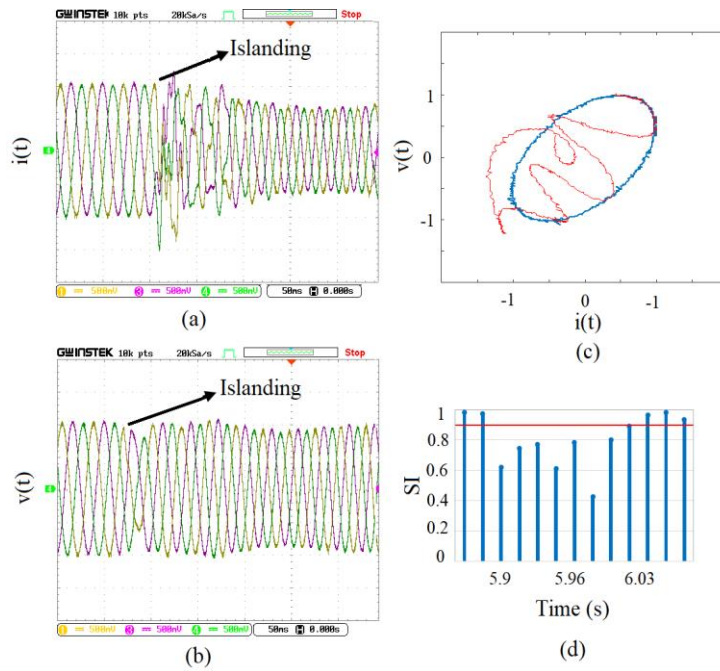


Fig. 5.15. HIL testing results of islanding at CB1 under UL1741: (a) Measured current signal, (b) Measured voltage signal, (c) Lissajous figure, (d) Similarity index.

The test model considered in Fig. 5.2 has been simulated in RTDS through the RT lab software for case (iv) of UL1741 when islanding occurs at CB1 to check the suitability of the proposed technique in real time applications. The voltage and current signals are collected from the digital oscilloscope at every circuit breaker to develop the Lissajous figures and the similarity index has been computed. The measured voltage and current signals at CB1 are shown in Fig. 5.15 (a) and 5.15 (b). The Lissajous figure and SI at CB1 are shown in Fig. 5.15 (c) and 5.15 (d), respectively. It can be seen from Fig. 5.15, that the islanding occurs at 5.9s and SI value is less than the threshold for more than 5 consecutive cycles which is not true for other CBs. Therefore, the proposed algorithm detects the islanding at CB1 only.

Table 5.3. Comparative assessment

Method	Type of DG	Faults	Q_f	Capacitor Switching	IMS	NDZ	UL1741	AI (%)	RTV
Ref [64]	PV	√	√	√	×	×	×	-	√
Ref [76]	SG	×	×	√	×	√	×	68.6	×
Ref [61]	PV, SG & WT	√	√	√	√	√	√	99	√
Ref [60]	Inverter based DG	√	√	×	×	√	√	-	×
Ref [77]	PV	√	√	×	×	√	√	78	√
Ref [69]	Inverter based DG	×	×	×	×	×	×	-	×
Proposed Method	PV, SG & WT	√	√	√	√	√	√	99	√

IMS- Induction motor starting, AI- Accuracy of islanding, RTV- Real time validation

5.4. Comparative Assessment

The performance of the proposed method has been compared with the recent islanding detection methods based on the specifications as summarized in Table 5.3. The methods reported in [69, 76, 77] can be operated only in the presence of the specified DG type. The ability of handling different types of DGs at different locations has not been considered. The proposed analysis considered various types of DGs widely used and is able to detect multi-islanding situations also. The islanding detection under NDZ region of voltage and frequency is sensible under small and zero power imbalances. Unlike the studies presented in [64,69], different active power and reactive power unbalance have been considered in the proposed method which makes it robust against the NDZ. Different case studies under the test conditions of UL1741 for the protection of islanding DGs have been conducted in this work and accuracy of the islanding detection of the proposed method under UL1741 conditions is 100% unlike methods proposed in [64,69,76]. The robustness of the proposed method has been validated for several non-islanding conditions which are having similar dynamics as that of islanding such as short circuit faults, capacitor switching and induction motor starting, etc. Unlike [61, 64, 76, 77], the proposed method can distinguish other similar conditions which produce similar transients as that of islanding. The proposed method uses voltage and current signals at PCC only to detect islanding and synchronization of signals at different location is not necessary unlike [64]. The proposed method does not depend on the model architecture and complexity. Therefore, the proposed method is accurate and has less computational burden. Moreover, unlike the methods proposed in [60, 69, 76] the proposed method has been validated using HIL testing for real time applications.

5.5. Conclusion

This work presents a novel technique to detect islanding in microgrid by utilizing the Lissajous figure patterns. A similarity index has been developed based on the characteristics of the Lissajous figure at each circuit breaker of the DG to identify the islanding condition and distinguish it from other similar conditions. Otsu algorithm based adaptive thresholding is considered in this study to select the threshold and the proposed algorithm utilizes only the voltage and current signals at the particular DG. The simulation results show that the proposed method is able to detect the islanding even in the presence of different DG types. The proposed algorithm is tested under diverse conditions and the performance of the proposed algorithm is satisfactory. Moreover, the proposed method is validated on HIL testing for real time applications and the comparative study shows that the proposed method has 99% accuracy.

CHAPTER 6

Pareto Optimal Based Unbalance Voltage Compensation in the Microgrid

6.1. Introduction

In the present scenario of smart grids, the utilization of microgrids has enhanced due to increased installation of the DGs. The presence of non-linear and single phase loads in the microgrid creates different power quality issues for the consumers, among which voltage unbalance is the major concern which can lead to additional power loss, voltage quality reduction and creates adverse effect on the operation of the electrical equipment connected to the system. Therefore, unbalance voltage compensation gained more interest recently. The active power filters have been largely used for voltage unbalance compensation [88]. The compensation can also be carried out using hybrid compensators which are formed by combining series and shunt active power filters. Unified power quality conditioners (UPQC) are widely used as hybrid compensators [89] to improve the power quality in distribution systems. Static synchronous compensators (STATCOMs) are also being used to reduce the detrimental effects of unbalance in the grid [90]. But these devices introduce additional cost and also enhance the complexity in the overall system.

Microgrid is considered as a controllable entity and the power electronic interfaces connecting the DGs to the microgrids add significant flexibility to utilize DGs as compensating devices under non ideal conditions. By properly controlling the DG converters, several objectives can be accomplished, such as maintaining the system frequency, voltage and also power quality requirements within the acceptable limits injecting both active power and reactive power to the grid and load [91]. Therefore, the need of additional devices such as active power filters, STATCOM, UPQC, etc. can be eliminated which results reduction in the cost as well as complexity of the network. In [92], a control strategy has been developed for single phase photovoltaic to mitigate the unbalance voltage by curtailing the active power and controlling the reactive power supplied by the single phase PVs connected to the system where the compensation is carried out. But considering large applications of three phase inverters in the networks, this scheme is not suitable for wide applications. A control technique has been proposed for voltage unbalance compensation at the DG terminals by controlling the DG converter where negative sequence reactive power has been utilized to generate the reference for

unbalance voltage compensation [93]. The authors in [94] proposed a control technique consisting of primary and secondary control to compensate the unbalance voltage. The secondary control is responsible for unbalance voltage control which only focused on sensitive load bus. A control scheme has been presented in [86] for the PV system to mitigate the voltage unbalance at its terminal bus by analyzing its terminal voltage. In [95] the authors proposed a new distributed control scheme for unbalance voltage compensation in an islanded AC microgrid, in which the primary control layer and cyber layer based two-layer control framework with event triggered communication is used for effective unbalance compensation. A secondary control scheme for power quality improvement with effective load sharing for multiple microgrids has been proposed in [96]. The proposed scheme helps the DGs to share the individual phase currents accurately so that over current stresses can be overcome. In [97] authors proposed a novel voltage and current unbalance mitigation scheme in the microgrid using the aggregated PV inverters. These studies are only focused on the compensation at specific point such as PCC or sensitive load bus which may show a negative impact on other load buses. Ref. [98] introduces a control scheme to mitigate the voltage unbalance and equal distribution of negative sequence current to each DG in the microgrid by using the communication link and complex form of proportional resonant controller. In [99] the authors proposed an optimal voltage regulation method based on the multiple agent system for multi-microgrids, where the agents collect the data from multiple microgrids. The control schemes in these studies are highly complex and communication links play a major role in the data transfer increasing the risk of malfunction.

A state space modelling for multiple inverter based unbalanced microgrid using dynamic phasor method is presented in [100]. The authors focused on the stability analysis of the microgrid in order to achieve the unbalance compensation, but the authors did not consider customised voltage quality requirements. In [101] an optimal multi-objective scheme is presented to regulate the active and reactive power flow and unbalance compensation. Due to the presence of single phase DGs, this work focused to balance the active power curtailment and the unbalance compensation is not addressed properly. The authors in [102] developed multiple current control damping schemes to control the DGs autonomously to compensate the voltage unbalance while sharing the compensation effort with the help of primary, secondary and auxiliary loops. In [103] optimization based customised voltage unbalance compensation technique has been proposed. The authors have reduced the negative sequence voltage at different buses but they did not focus on the improvement of VUF by improving the positive sequence voltage. The authors in [85] proposed a power quality control strategy for unbalance

voltage compensation at different buses. In [104] the authors proposed a control strategy for voltage imbalance mitigation in inverter-based distribution system considering local current and voltage variables. The implementation of the proposed algorithm has not been established in a microgrid. Moreover, they considered VUF only up to 4%. An optimized control strategy for grid connected inverter has been developed in [105], but the authors did not consider the coordinated optimized operation of the DGs in the microgrid for mitigation of voltage unbalance at different buses. Later the researchers focussed on the effectiveness of unbalanced voltage compensation by controlling DG's negative sequence current to remain in phase with the grid negative sequence current. A hierarchical control system comprising of primary, secondary and tertiary control has been used in [106] which results in execution delay due to the implementation of secondary and tertiary control mechanism. Also, the tertiary control is dependent on the secondary control which results in more complexity. The DGs present in the microgrid should have low voltage ride through (LVRT) capability to support positive sequence voltage [55] during voltage sags. When multi-objectives are present in the control strategy, especially when they are conflicting to each other, it is hard to get a single optimal solution using single objective optimization algorithm which has all optimized objectives. Therefore, it is suitable to consider non dominated sorting principle based multi-objective pareto optimization algorithm [116] to obtain desired performance.

This chapter presents a multi-objective pareto optimal unbalance voltage compensation in the microgrid. The authors have considered voltage unbalance due to the presence of unbalanced single phase loads [86, 103]. Multi-objective artificial cooperative search algorithm has been utilized to generate the optimal unbalance voltage compensation references for each DG and max-min method has been used to select the best compromised solution. The main contributions of this research can be summarized as:

- An efficient multi-objective algorithm has been proposed for optimized operation of DGs to reduce the voltage unbalance at different buses.
- The voltage unbalance limits for different buses can be customized according to the distinctive requirement of the consumers.
- The negative sequence voltage has been reduced as much as possible and the positive sequence voltage has been increased by incorporating LVRT capability in the DG control.
- The DG output current is also optimised since the power interfacing converter consists of semiconductor devices which cannot withstand excessive currents.

6.2. Proposed Control Scheme

The unbalanced load present in the distribution network causes voltage unbalance which has many adverse effects. Voltage unbalance factor defined by the International Electrotechnical Commission (IEC), can be used to analyze the voltage quality. Due to the adverse effects of voltage unbalance, VUF has a limitation of acceptable compatibility level which varies from country to country and the range is 1-5%. As far as power quality is concerned, it is better to consider VUF to be less than 2% to maintain the IEC standards. Majority of the DGs are connected through power electronic interfaces to the microgrid, which are known as inverter interfaced distribution generators (IIDGs). These IIDGs have different control strategies based on the connection type to the microgrid. When unbalanced load is applied to the load bus, the load bus experiences consumption of negative sequence current (I^-), which causes voltage unbalance in the microgrid. The DGs in the microgrid can be utilized as compensation units for voltage unbalance compensation.

PQ control strategy is used in grid connected mode of operation, in which the control loop produces d and q reference signals which are responsible for the active and reactive power control of the DG. The voltage and frequency references are obtained from the utility grid and PLL synchronizes the converter operation with the grid. In addition, in grid connected mode, low voltage ride through (LVRT) capability is included in the PQ control strategy to support the voltage by supplying reactive power under voltage sag. It is noteworthy to mention that under unbalanced condition negative sequence control loop is used in addition, to control the negative sequence quantities as explained in section 6.2.1. When the microgrid operates under islanded mode, the reference signals are obtained by controlling the voltage source inverters as the reference signals cannot be obtained from the grid. In islanded mode of operation, V/f control and droop control strategies are used. A voltage control loop is added whose reference is generated by the voltage formation loop. The voltage formation loop is different for V/f control and droop control. The required voltage reference and frequency reference are directly given to the voltage formation loop in V/f control whereas in droop control the voltage and frequency references are obtained from droop characteristics of measured active and reactive powers.

6.2.1. Control Scheme for DGs

The DGs are capable to control the negative sequence voltage at the load buses as per requirement. The DG control scheme is presented in Fig. 6.1(a). The voltage reference signal is

given to the power converter of the DG through PWM which can be calculated from the sum of positive sequence and negative sequence components as given in (6.1).

$$\begin{bmatrix} V_a \\ V_b \\ V_c \end{bmatrix} = \begin{bmatrix} V_a^+ \\ V_b^+ \\ V_c^+ \end{bmatrix} + \begin{bmatrix} V_a^- \\ V_b^- \\ V_c^- \end{bmatrix} \quad (6.1)$$

The voltages and currents in the synchronous reference frame are required for the control scheme. Applying Park transformation, positive and negative voltages in synchronous frame can be expressed as

$$\begin{bmatrix} V_0^+ \\ V_d^+ \\ V_q^+ \end{bmatrix} = \frac{2}{3} \begin{bmatrix} 1/2 & 1/2 & 1/2 \\ \cos(\theta) & \cos(\theta - \frac{2\pi}{3}) & \cos(\theta + \frac{2\pi}{3}) \\ \sin(\theta) & \sin(\theta - \frac{2\pi}{3}) & \sin(\theta + \frac{2\pi}{3}) \end{bmatrix} \begin{bmatrix} V_a \\ V_b \\ V_c \end{bmatrix} \quad (6.2)$$

$$\begin{bmatrix} V_0^- \\ V_d^- \\ V_q^- \end{bmatrix} = \frac{2}{3} \begin{bmatrix} 1/2 & 1/2 & 1/2 \\ \cos(-\theta) & \cos(-\theta - \frac{2\pi}{3}) & \cos(-\theta + \frac{2\pi}{3}) \\ \sin(-\theta) & \sin(-\theta - \frac{2\pi}{3}) & \sin(-\theta + \frac{2\pi}{3}) \end{bmatrix} \begin{bmatrix} V_a \\ V_b \\ V_c \end{bmatrix} \quad (6.3)$$

Similarly, the current quantities can be obtained in dq frame for the positive sequence control as represented in Fig. 6.1(b). The d component is responsible for the active power control and q component is responsible for the reactive power control. The positive and negative sequence components in three phase frame can be obtained using the reverse Park transformation as given in (6.4) and (6.5).

$$\begin{bmatrix} V_a^+ \\ V_b^+ \\ V_c^+ \end{bmatrix} = \begin{bmatrix} \cos(\theta) & -\sin(\theta) & 1 \\ \cos(\theta - \frac{2\pi}{3}) & \sin(\theta - \frac{2\pi}{3}) & 1 \\ \sin(\theta - \frac{2\pi}{3}) & \sin(\theta + \frac{2\pi}{3}) & 1 \end{bmatrix} \begin{bmatrix} V_d^+ \\ V_q^+ \\ V_0^+ \end{bmatrix} \quad (6.4)$$

$$\begin{bmatrix} V_a^- \\ V_b^- \\ V_c^- \end{bmatrix} = \begin{bmatrix} \cos(-\theta) & -\sin(-\theta) & 1 \\ \cos(-\theta - \frac{2\pi}{3}) & \sin(-\theta - \frac{2\pi}{3}) & 1 \\ \sin(-\theta - \frac{2\pi}{3}) & \sin(-\theta + \frac{2\pi}{3}) & 1 \end{bmatrix} \begin{bmatrix} V_d^- \\ V_q^- \\ V_0^- \end{bmatrix} \quad (6.5)$$

The voltage reference signal shown in (6.1) is given to the power converter. Fig. 6.1(c) represents the microgrid central control system (MCCS) which is explained in section 6.3.2.

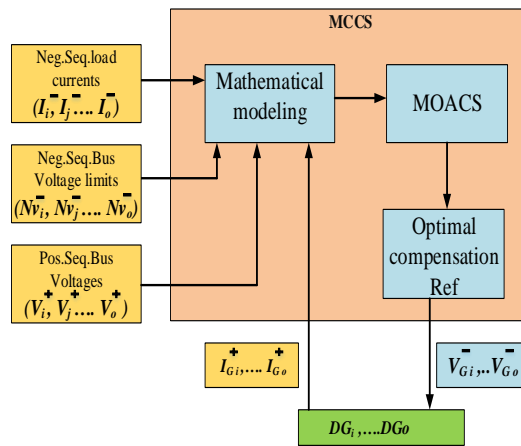
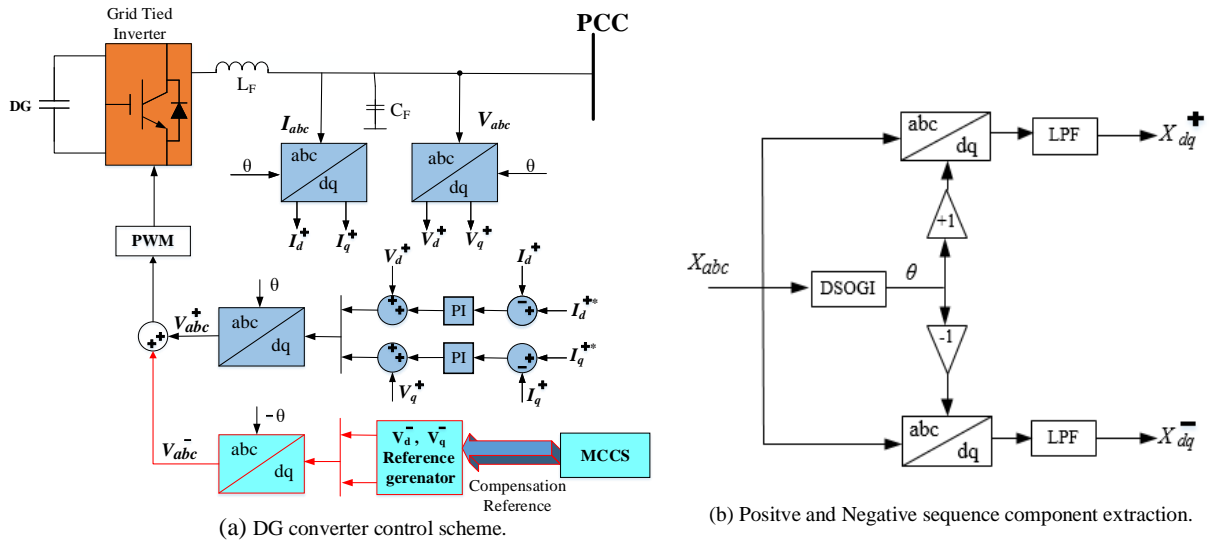


Fig. 6.1. Proposed control scheme.

High penetration of the DGs into the grid causes voltage fluctuations at the PCC. To maintain the nominal voltage, the DG inverters operate according to Volt–Var curve which is a decentralized and autonomous form of voltage control. The Volt-Var curve is usually centred around the nominal voltage. If the voltage is above the set point, the inverter absorbs the reactive power and when the voltage is below the set point the inverter delivers the reactive power. The grid connected DGs have the LVRT capability which delivers the reactive power to support the grid voltage during the voltage sags. The LVRT function starts when the voltage sag exceeds 10% and supplies both active and reactive power until voltage exceeds 50% when it starts supplying reactive power only. LVRT capability of the DGs has been considered here to improve the positive sequence voltage during voltage unbalancing. The DG will supply 2 % reactive current for every 1% voltage drop when the voltage at PCC drops below 0.9 p.u of the rated voltage. When the voltage at the PCC is above 0.9 p.u of rated voltage, the DG will supply only active power and reactive power output is zero. Under severe voltage drop i.e. if the voltage is

below 0.5 p.u of rated voltage, the DG will provide maximum amount of reactive power and under this condition the active power output of the DG will be zero. Hence, with the decrease in the negative sequence voltage there has been an increase in the positive sequence voltage when the voltage drops below 0.9 due to unbalancing, resulting in improved VUF. The reactive power requirement curve is represented in Fig. 6.2.

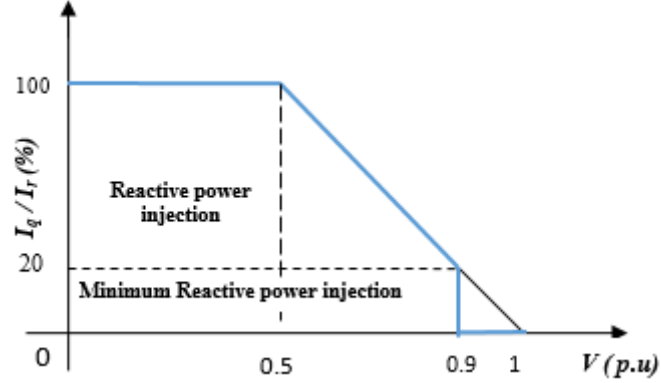


Fig. 6.2. Reactive power requirement.

6.2.2. Mathematical Modelling

To evaluate the voltage quality in the microgrid, power flow and bus voltages are required to be calculated. For this, the negative sequence equivalent network of the microgrid is used. The negative sequence load current at any bus k can be expressed as follows:

$$I_k^- = (V_{Gk}^- - V_k^-)Y_{Gk}^- + \sum_{j=1}^n (V_j^- - V_k^-)Y_{jk}^- \quad (6.6)$$

where V_{Gk}^- is the negative sequence DG voltages which are taking part in the voltage unbalance compensation. Here, Y_{Gk}^- and V_{Gk}^- will be zero if no DG is connected to the node k and Y_{jk}^- will be zero if nodes j and k are not connected. It is to be noted that I_k^- includes both d and q components. Equation (6.6) can be written as

$$V_{Gk}^- Y_{Gk}^- - I_k^- = V_k^- (Y_{Gk}^- + \sum_{k=1}^n Y_{jk}^-) - \sum_{\substack{j=1 \\ j \neq k}}^n V_j^- Y_{jk}^- \quad (6.7)$$

From (6.7), n number of linear equations can be formed with n number of unknowns, V_1^- , V_2^- , \dots , V_n^- . The feeder tie line and DG tie line negative sequence admittances are known and the load currents I_1^- , I_2^- , \dots , I_n^- can be measured. V_{Gk}^- is the design variable and the negative

sequence bus voltages V_1^- , V_2^- , ..., V_n^- can be calculated by solving the linear equations. In order to maintain the negative sequence voltage at different buses under the limit, the DG currents should not rise beyond the safe value. The semiconductor devices used in the converter have hard limitations. Under unbalanced condition when DG compensation is considered, the DG phase currents should be under the acceptable limits, which is considered as 1.2 p.u of the rated DG current [105]. The DG phase currents can be calculated at any node k from (6.8).

$$[I_{Gk}^a, I_{Gk}^b, I_{Gk}^c]^T = A \cdot [I_{Gk}^0, I_{Gk}^+, I_{Gk}^-]^T \quad (6.8)$$

Zero sequence quantities are negligible for three phase three wire system and positive sequence currents can be calculated. From the information of DG side and bus voltage, the negative sequence current of the DG connected to any node k can be calculated from (6.9).

$$I_{Gk}^- = (V_{Gk}^- - V_k^-) \cdot Y_{Gk}^- \quad (6.9)$$

For the positive sequence quantities also same load flow equations can be formulated similar to (6.6) and (6.7) representing all the parameters in positive sequence. By controlling the positive sequence quantities of the DG, the positive sequence voltages can be varied at each load bus. Here, the reference for positive sequence voltage (d and q components) of DG is provided by the current control loop as shown in Fig. 6.1(a) where d and q components of currents can be varied to obtain the desired performance. Hence, the positive sequence load flow equations are not repeated here. The power output of the DG is purely dependent on the control of the positive sequence quantities (d and q). From (6.8) it can be seen that the DG phase currents will be changed by the change in positive sequence DG current. Therefore, the control strategy responds to the change in the DG current which gives optimal references to the DGs. Hence, the positive sequence quantities are included in the control scheme.

The extraction principle of both negative and positive sequence quantities is shown in Fig. 6.1(b). First the three phase quantities are fed to the second order generalized integrator-phase locked loop (DSOGI-PLL) and from DSOGI ' θ ' is extracted. θ is multiplied by +1 and -1 respectively and then given to the dq transformation block followed by low pass filter with cut off frequency of 2 Hz.

6.3. Problem Formulation and Optimization Algorithm

6.3.1. Objective Functions

Due to the presence of unbalanced loads at the load buses, VUF may increase at respective buses and also at adjacent buses. Therefore, in order to maintain the voltage quality in the microgrid, VUF needs to be minimized. Secondly, in order to minimize VUF, the DGs will start to compensate the negative sequence voltage at respective buses which will result in rise in DG output currents. The power converters have semiconductor devices which should be able to withstand the DG output currents. Hence, the safety of the converter is important and the output DG currents have to be under the acceptable limits. Therefore, in this study two objectives are considered which are VUF minimization and minimization of the DG current. The objective functions can be formulated as follows:

6.3.1.1. Minimization of VUF

The VUF at any bus can be calculated from the knowledge of positive and negative sequence voltages at that particular bus. The objective function F_1 can be expressed as follows:

$$F_1 = VUF = \sum_{k=1}^n \frac{V_k^-}{V_k^+} \times 100 \quad (6.10)$$

$$V_k^- < V_{lk}^- \quad (6.11)$$

Here, V_k^- is the negative sequence voltage at bus k which can be calculated as described in section 6.2 and V_k^+ is positive sequence voltage at bus k which can be measured and n is the number of buses. It is possible that different buses may have different voltage quality limits (V_{lk}^-) in a microgrid. The voltage unbalance limit at different buses has been customized and the limits have been set accordingly. The negative sequence voltage is considered as a constraint in this study, a penalty factor has been introduced (f_{p1}) and it is desired that the negative sequence voltage at all buses will be less than the acceptable limits. The value of f_{p1} is 0 when $V_k^- < V_{lk}^-$ and if V_k^- is not under the limit, the adaptive penalty can be calculated from (6.12), which will be added to the objective function F_1 .

$$f_{p1} = c_1 \sum_{k=1}^n (V_k^- - V_{lk}^-)^2 \quad (6.12)$$

6.3.1.2. Minimization of DG Output Current

When a DG is participating in the voltage unbalance compensation process, it is possible that any phase of the DG current may increase beyond its safety limit. Hence the minimization of the output DG phase current is essential which is considered as the second objective in this study.

$$F_2 = \sum_{k=1}^{ndg} \text{Max}(I_{Gk}^a, I_{Gk}^b, I_{Gk}^c) \quad (6.13)$$

$$I_{Gk}^{a,b,c} < I_{Gk}^{limit} \quad (6.14)$$

The DG phase currents should be within the limit which is set as 1.2 p.u of the rated current of the DG. The penalty factor is considered which will add adaptive penalty (f_{p2}) to the objective function F_2 as given in (6.15) when DG phase current violates the limit and its value is 0 when DG phase currents are under the limit.

$$f_{p2} = c_2 \sum_{k=1}^{ndg} (\max(I_{Gk}^a, I_{Gk}^b, I_{Gk}^c) - I_{Gk}^{limit})^2 \quad (6.15)$$

6.3.2. Multi-Objective Function and Pareto Optimal Solution

The objective functions and constraints described above can be summarized as multi-objective function as given in (6.16).

$$F = \begin{cases} \min (F_1) \\ \min (F_2) \\ V_k^- < V_{lk}^- \\ I_{Gk}^{a,b,c} < I_{Gk}^{limit} \end{cases} \quad (6.16)$$

Here the objective functions F_1 and F_2 are conflicting to each other, it is hard to get the single optimal solution which has all optimized objectives. Therefore, it is suitable to consider non dominated sorting principle to get the optimal pareto front solution. The pareto optimization technique does not need weights for converting multi-objective function to single objective optimization, and all the solutions in the pareto front will be considered as optimized solutions. Moreover, in the pareto optimization the aim is to leave the dominated solutions and reserve the non-dominated solutions aiming to realize the pareto predominance equilibrium between the conflicting objective functions. Hence, an efficient algorithm is needed which should have essential qualities like generating reasonable initial population in the given space, effective

application of the iterative computation in less time and capability of leaving the dominated solutions and reserving the non-dominated solutions scientifically [116]. Multi-objective Artificial Cooperative Search Algorithm (MOACS) has been used in this study to solve the proposed multi-objective pareto optimization problem.

6.3.2.1. Multi-Objective Artificial Cooperative Search Algorithm

MOACS algorithm is developed based on the Artificial cooperative search algorithm which is capable of solving single objective optimization inspired by the super organisms or natural species like bird species, honey bees etc. Non-dominated sorting principle has been used in MOACS to make the algorithm suitable for solving multi-objective pareto optimization problems. The MOACS algorithm has been explained briefly in the following steps.

Step 1: Population initialization and fitness evaluation: Create the initial population for both the superorganisms A and B as given in (6.17). Then calculate the fitness ($f_1(x), f_2(x) \dots f_n(x)$) for each individual of the superorganisms A, B. Give the rankings to each individual of A,B using non-dominated sorting principle and calculate the crowding distance (CD) of each individuals . Then store the fitness, rankings and CD of each individual in A, B superorganisms.

$$\begin{aligned} A_{(i,j)} &= low_j + rnd.(up_j - low_j) \\ B_{(i,j)} &= low_j + rnd.(up_j - low_j) \end{aligned} \quad (6.17)$$

where $i=1 \dots N$ (population size) and $j=1 \dots D$ (problem dimension)

Step2: Offspring generation: Transfer the superorganisms A, B into predator and prey randomly and assign key values. Then generate new population (X) (offspring) using biological interactions between predator and prey. Calculate the fitness, rankings, CD for offspring (X) and store them in separate location.

Step 3: Finding the best population: To find out the best population, combine the predator (*size N*) and offspring (X) (*size N*). Sort the combined population (*size 2N*) based on the fitness and rankings. If both solutions have same ranking, then the priority is given to the solution which has more CD. The top individual (*size N*) is considered as the best population which will be transferred to predator superorganism. Based on the key values, superorganism A or B will be updated with predator.

Step 4: Finding optimal solution: Step 2 to step 4 will be repeated up to the maximum number

of iterations. Once the optimal pareto frontier is obtained, the best compromised solution within the pareto front will be selected by using Max-Min method. This metric is used to evaluate how the non-dominated solutions satisfy the optimization problem based on the value of the objective functions. The best compromised solution has been selected by Max-Min method as shown in (6.18).

$$\max_y \left\{ \min \left\{ \dots, \frac{f_z^{max} - f_{yz}}{f_z^{max} - f_z^{min}}, \dots \right\} \right\} \quad (6.18)$$

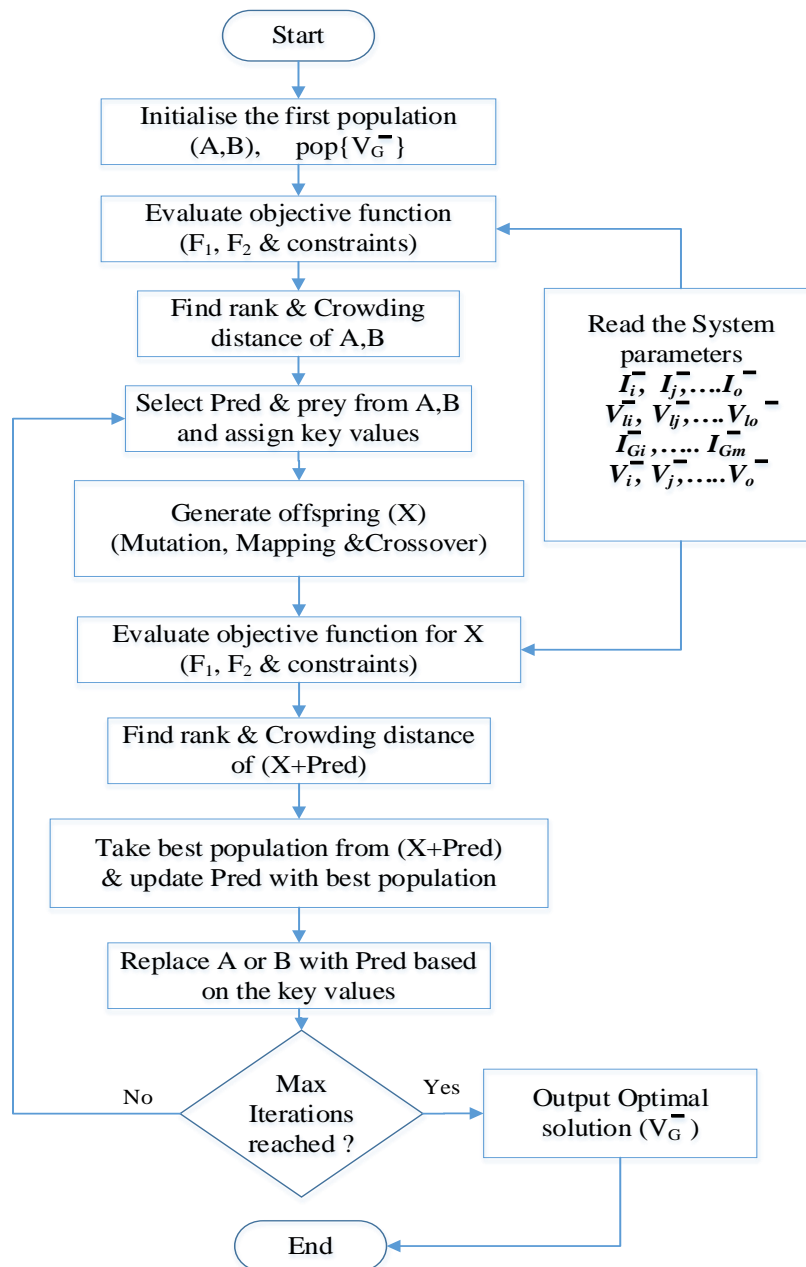


Fig. 6.3. Overall optimization procedure.

6.3.2.2. Implementation of the Optimization Strategy

The operational strategy is given in Fig. 6.1(c), where the microgrid central control system (MCCS) plays the key role. The MCCS consists of three blocks viz. mathematical model, optimization algorithm and reference generator for the DG reference negative sequence voltage. MCCS will read the input parameters of the system which are negative sequence load currents at each bus (I_k^-), positive sequence voltages at each bus V_k^+ and the consumer requirements of voltage quality at different buses (V_k^-) which can vary according to the requirement. Positive sequence DG current (I_{Gk}^+) can be extracted as shown in Fig. 6.1(b) and fed to the MCCS. Based on the mathematical modelling, the optimization algorithm will send the compensation reference V_{Gk}^- (dq components) to the DG. Then the MCCS will communicate with the DG to exchange the information. The optimization algorithm is shown in Fig. 6.3.

6.4. Simulation Results

Simulation has been carried out for the low voltage microgrid test system shown in Fig. 6.4 [103] in Matlab/ Simulink platform and the proposed scheme has also been evaluated in real time simulator OPAL-RT with RTS OP5600 chassis and RT lab version 19.3.0.228. The test system consists of four DGs which are DG_j , DG_m , DG_l and DG_n connected to bus j , m , l and n respectively through three phase three leg inverter with rated power of 10kW, 10 kW, 3kW and 5 kW respectively. The frequency of the system is considered as 50 Hz and line to line voltage is 400V. The negative sequence conductance and susceptance of the feeders connected between the buses j and k , l and m , l and n , n and o are 0.3032 S and 1.7148 S respectively and for the feeders connected between buses i and j are 0.1269 S and 0.6379 S respectively, k and l are 0.4683 S and 3.923 S respectively. The conductance and susceptance are considered as 0.3032 S and 1.7148 S for all DG connected feeders. The three phase balanced delta connected loads connected in bus i is 588.2Ω , in bus j is 1425.6Ω and in the buses $k \dots o$ are 588.2Ω per phase. To create unbalancing, single phase loads are added to different buses. Different voltage quality limits are considered at different buses since the consumer requirement may vary at different load buses. The negative sequence voltage limits at the buses $i, j \dots o$ are considered as {5,10,5,10,10,10,5}V respectively. All four DGs in the microgrid have LVRT capability and are utilized to compensate the unbalance voltage at the load buses by negative sequence control with minimization of VUF and DG phase currents.

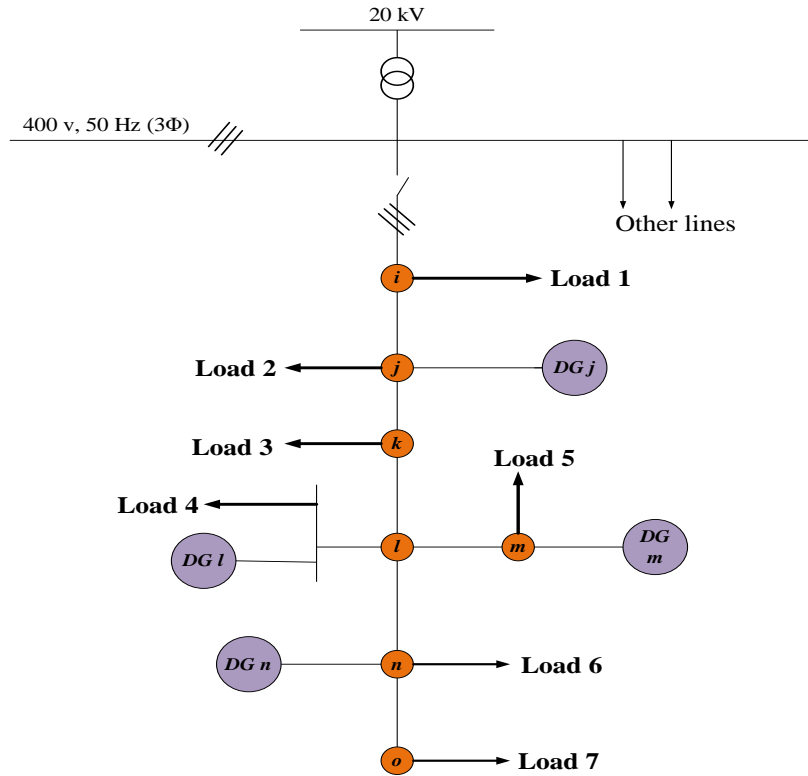


Fig. 6.4. Low voltage microgrid test system.

The negative sequence equivalent model of the microgrid test system considered in this study is shown in Fig. 6.5. The test system has seven number of nodes viz. i, j, k, l, m, n and o . From (6.7) and Fig. 6.5, seven number of linear equations can be formed with *seven* number of unknowns $V_i^-, V_j^-, \dots, V_o^-$. Here feeder tie line and DG tie line negative sequence admittances are known. $I_i^-, I_j^-, \dots, I_o^-$ can be measured and $V_{Gi}^-, V_{Gj}^-, \dots, V_{Go}^-$ are the design variables. Hence the negative sequence bus voltages $V_i^-, V_j^-, \dots, V_o^-$ can be calculated.

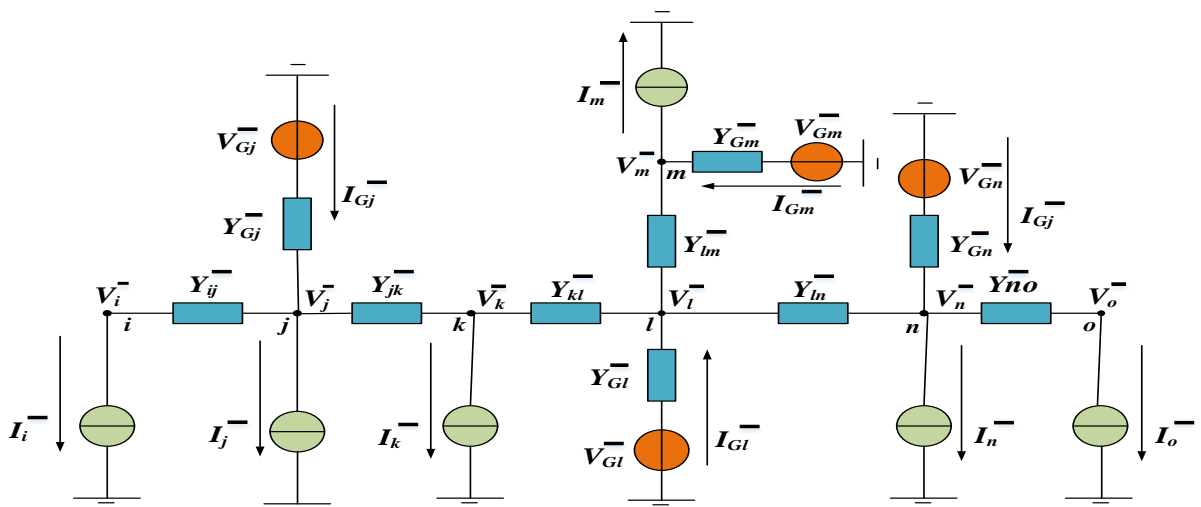


Fig. 6.5. Simplified negative sequence network of the test system.

6.4.1. Case (i)

In this case single phase loads are connected between phase a and b at the load buses in addition to three phase loads as mentioned earlier. A 40Ω single phase load is connected to load bus j at 2 s, then at 3s single phase loads of 100Ω , 143Ω and 45Ω are connected to load buses k , l and m respectively and at 4s, 100Ω load is connected to bus i , followed by 58Ω load to bus n at 5s. The VUF values before and after compensation at different buses are shown in Fig. 6.6(a) and the negative sequence voltages at the corresponding buses are shown in Fig. 6.6(b). It can be seen from Fig. 6.6 that after connecting single phase loads, the VUF and negative sequence voltages at each bus have increased. After 5s the positive sequence voltages at DG terminals of DG_j , DG_m , DG_l and DG_n have dropped to 0.892p.u., 0.87p.u., 0.875p.u. and 0.871p.u. respectively. The MCCS collects the information from each node and the compensation control is started at 6s. After 6s it can be seen from Fig. 6.6(a) that the VUF at every bus is reduced to the minimum value which is tabulated in Table 6.1 and the maximum VUF at the buses is observed as 0.91% which is well under the VUF limit. Further from Fig. 6.6(b) it is evident that the negative sequence voltage at all the buses are under the desired limit, the limit values are shown by blue colored line. As the DG voltages are dropped below 0.9 p.u., the DGs supply reactive current to support the voltage level as shown from Fig. 6.7(a). It can be seen that the positive sequence voltages at the DG terminals have increased up to their maximum level and the values are tabulated in Table 6.2. The active power sharing of the DGs are shown in Fig. 6.7(b) which indicates that during the compensation the active power sharing by the DGs is maintained.

Table 6.1. VUF and negative sequence voltages at load buses

Bus	Case (ii)		Case (iii)		Case (iv)		Case (v)		Case (vi)		Case (vii)		Case (viii)	
	V^- (V)	VUF %	V^- (V)	VUF %	V^- (V)	VUF %	V^- (V)	VU F	V^- (V)	VUF %	V^- (V)	VUF %	V^- (V)	VUF %
i	3.5	0.91	1.6	0.4	2.9	0.8	3.7	1	2.9	0.8	1.8	0.45	2.2	0.56
j	1.8	0.42	1.5	0.41	1.8	0.4	3.5	0.9	1.7	0.45	2	0.5	2.1	0.55
k	2	0.52	1.8	0.49	0.6	0.155	4	1.08	2	0.53	2.2	0.57	2.4	0.6
l	1.9	0.48	1.95	0.5	0.45	0.1	4.3	1.2	2.2	0.6	2.25	0.6	2.5	0.61
m	2.4	0.6	2	0.5	1.2	0.35	4.4	1.2	2	0.58	2.3	0.61	2.6	0.68
n	2.1	0.54	1.4	0.38	1.7	0.42	5	1.3	2.7	0.7	1.75	0.46	2.4	0.6
o	2	0.5	1.4	0.38	1.6	0.41	4.9	1.35	2.7	0.72	1.74	0.47	2.4	0.6

As the DGs are participating in the compensation process, the DG phase currents increase. The DG phase currents are shown in Fig. 6.8(a) from where it is visible that the DG phase currents during compensation are under 1.2 p.u. of the rated current of the DG and the values are tabulated in Table 6.2 which confirms that the security of the power converter is fulfilled. The three phase voltage before and after compensation at load bus j is shown in Fig. 6.8(b). As observed from Fig. 6.8(b), the maximum phase voltage difference is 8V after the compensation process whereas the maximum phase voltage difference is 120V for uncompensated system or before compensation. The optimal pareto front obtained by MOACS for case (i) is shown in Fig. 6.9(a).

The DGs are not operating at their rated capacity and when the active power production by a DG is not at its rated capacity, the surplus capacity of the DG can be used to serve other requirements without active power curtailment [103]. In this work, before compensation the injecting active powers of DG_j , DG_m , DG_l and DG_n are 7.3 kW, 7.3 kW, 2.2 kW and 3.7 kW respectively and it can be observed from Fig. 6.8(a), initially the DG current is not at its maximum capacity. As the DGs operating with an active power lower than the rated capacity of 10kW, 10kW, 3kW and 5kW there is a surplus capacity which allows the microgrid to use that surplus capacity to inject the compensating current. Therefore, in this work the surplus capacity of the DG is utilised to mitigate the unbalance voltage at the load bus without active power curtailment as shown in Fig. 6.7(b) the DG continued to supply the same amount of active power after 6s. It is noteworthy to mention that when severe voltage unbalance occurs and the DGs are not able to serve the voltage quality requirements within its capacity with proper active power supply, the DGs can be prioritised to serve voltage quality requirements through active power curtailment by adjusting the control mechanism shown in Fig. 6.1.

Table 6.2. DG positive sequence voltage and DG current in p.u

DG	Case (i)			Case (ii)			Case (iii)		
	V^+ Before	V^+ After	Max (I_a, I_b, I_c)	V^+ Before	V^+ After	Max (I_a, I_b, I_c)	V^+ Before	V^+ After	Max (I_a, I_b, I_c)
DG j	0.892	0.978	1.137	0.95	0.955	0.88	0.96	0.964	0.82
DG m	0.87	0.985	1.165	0.94	0.947	0.878	0.954	0.958	0.825
DG l	0.875	0.976	1.182	0.942	0.949	0.9	0.954	0.958	0.845
DG n	0.871	0.975	1.179	0.936	0.943	0.89	0.955	0.959	0.9

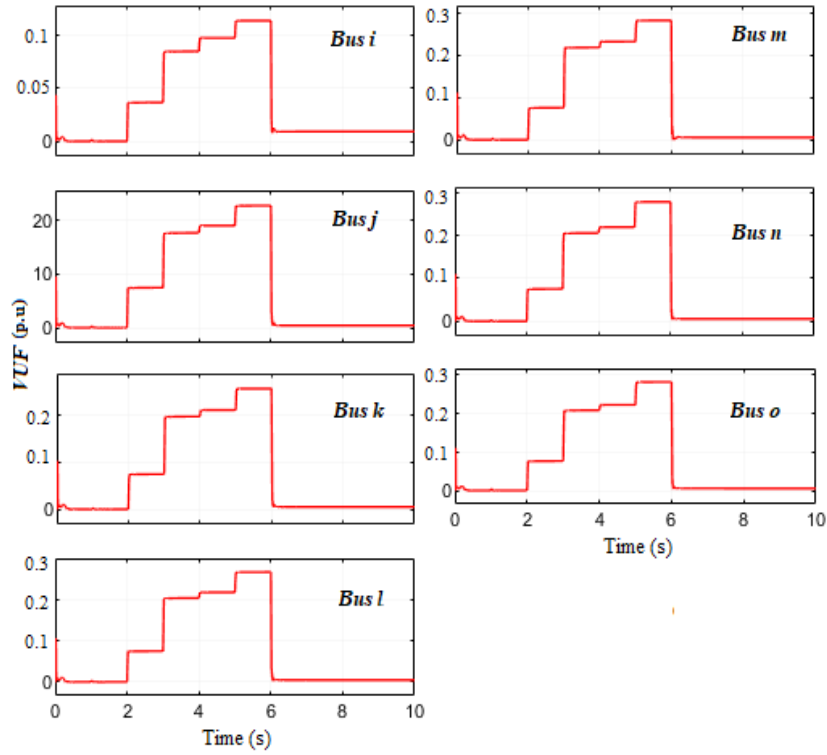


Fig. 6. 6(a). VUF at different buses for case (i).

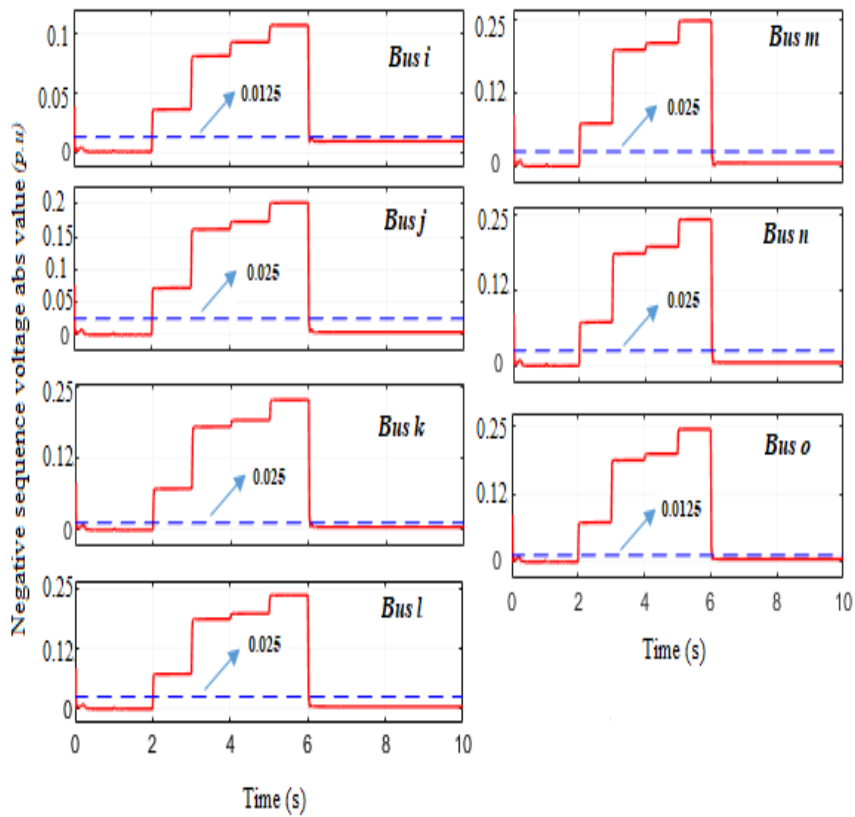


Fig. 6. 6(b). Negative sequence bus voltages at different buses for case (i).

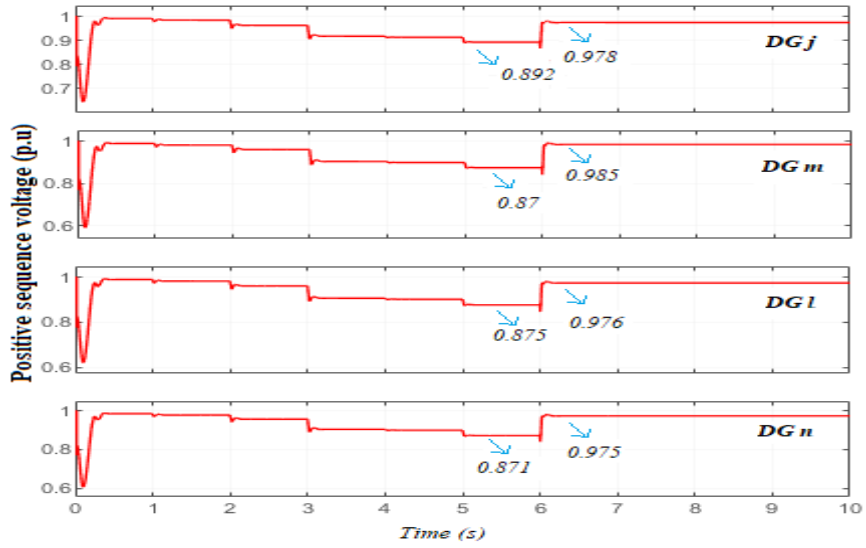


Fig. 6.7 (a). Positive sequence voltage at DG terminals for case (i).

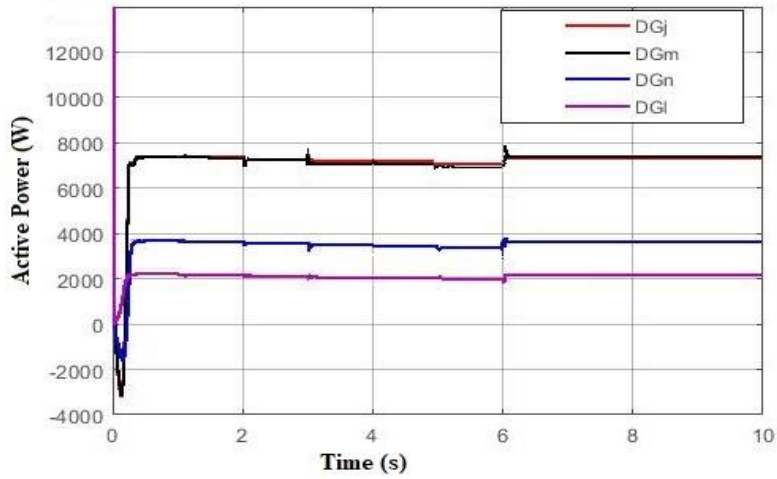


Fig. 6.7(b). Active power output at DG terminals for case (i).

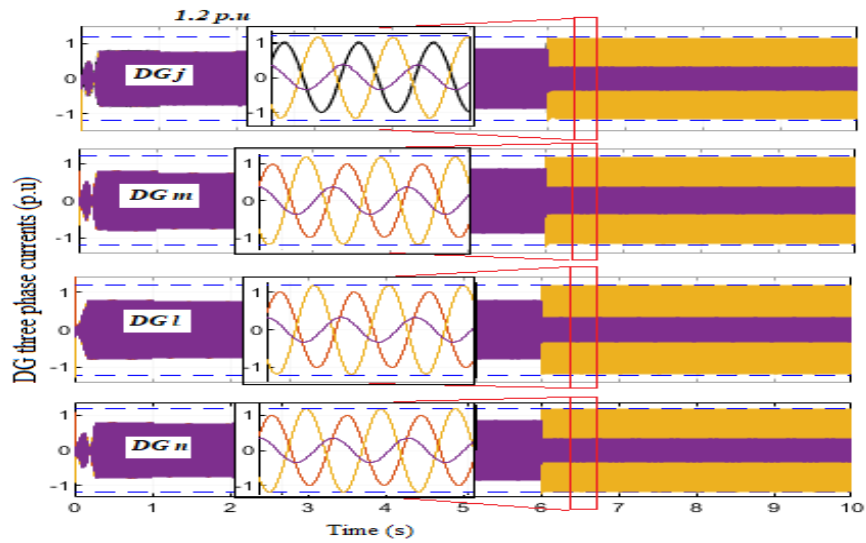


Fig. 6.8(a). Three phase DG output currents for case (i).

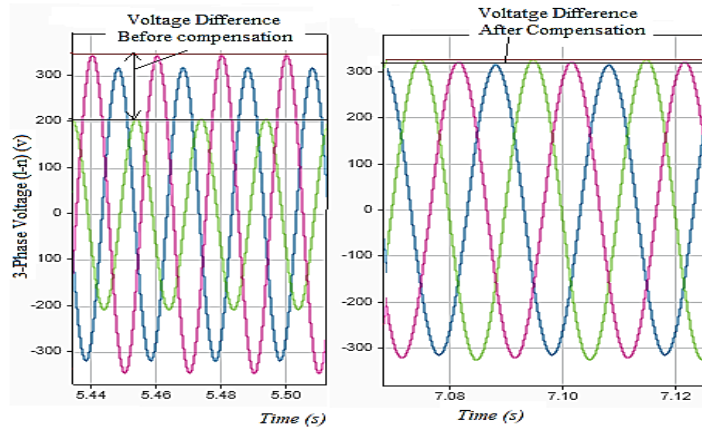


Fig. 6.8(b). Bus voltages before and after compensation for case (i).

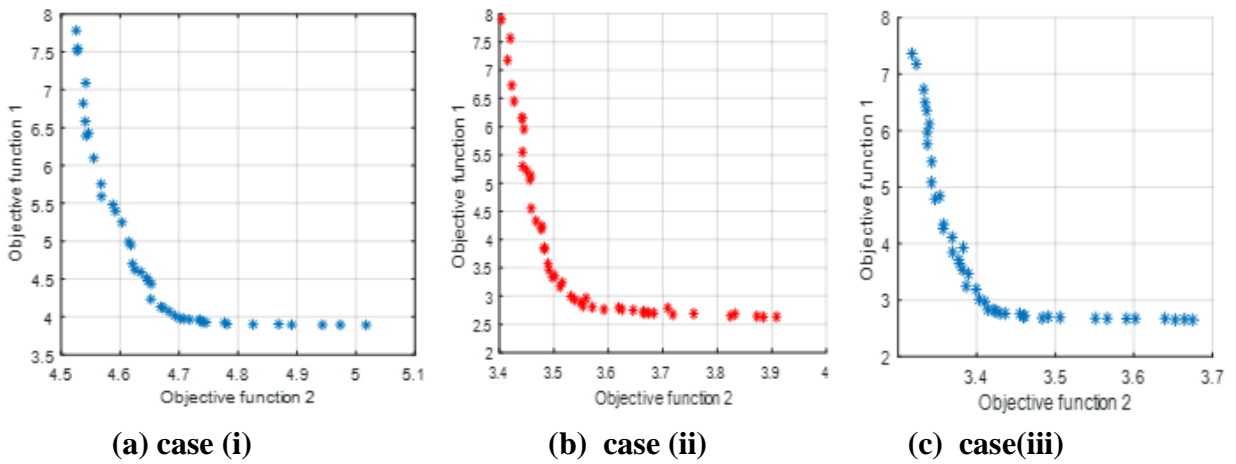


Fig. 6.9. Optimal Pareto front.

6.4.2. Case (ii)

With the evolution of power system network caused by increased diffusion of distributed energy sources, it is necessary to validate any proposed technique before deployment. Hardware-in-the-Loop (HIL) simulation is an alternative to traditional testing method and it has become the standard for testing complex systems around the globe. In other words, HIL simulator can accurately reproduce the plant and its dynamics, The OPAL-RT consists of a real-time simulator including HIL testing which creates the real time environment. The simulation is executed in the real time simulator which works with physical clock and allows the simulator to duplicate the real hardware. OPAL-RT considers real time issues such as noise and randomness of events which do not exist in simulation-only system. Moreover, in conventional simulation-only system, the objective is to obtain the results as fast as possible and the time required to compute all the functional blocks and equations representing a system during that particular time step may be longer or shorter depending upon the computational power of the system and model

complexity. In real time simulation, the accuracy of the computation depends on the length of the time used to produce the results in addition to the system dynamics. The time required to accurately produce the internal variables and outputs is same as that of its physical counterpart. Thus it permits the RTDS to perform all the necessary operations relevant to real time applications.

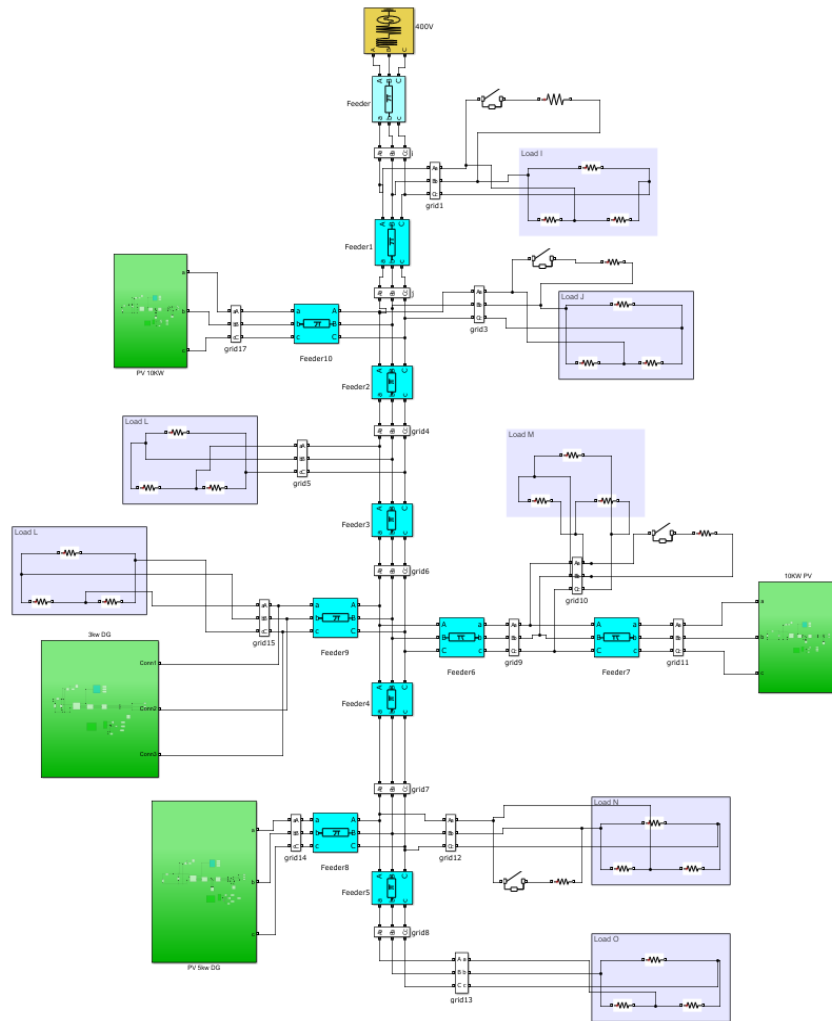


Fig. 6.10(a). Figure simulation of real time digital simulator.

To validate the reliability of the proposed method, the model shown in Fig. 6.4 is simulated in real time digital simulator OPAL-RT with RTS OP5600 chassis and RT lab version 19.3.0.228. The model fixed step size has been considered as $100\mu\text{s}$ in the RT lab of the target flat form (hardware synchronised real time simulator), the number of steps without overruns have been considered as 10 and PF511127S01 hardware system has been used with 12 cores. The figure simulation of the main subsystem is shown in Fig. 6.10(a) and the overall OPAL RT setup is shown in Fig. 6.10(b). The single phase loads of $143\ \Omega$, $100\ \Omega$, $75\ \Omega$ and $100\ \Omega$ are connected

at load buses i , j , m and n respectively and the maximum value of VUF at the load buses is 13.5%. Further, the DG voltages have dropped to 0.95, 0.94, 0.942 and 0.936 for DG_j , DG_m , DG_l and DG_n respectively as shown in Table 6.2. The three phase bus voltages before and after compensation are shown in Fig. 6.11 and VUF at different buses are shown in Fig. 6.12 as obtained from the oscilloscope. The compensation procedure is started at 6s when the M CCS sends the optimized references to the DGs. The maximum VUF reduces to 0.5% as tabulated in Table 6.1. Also, the negative sequence bus voltages and DG output currents are well under the limits as shown in Table 6.2. The optimal pareto front for case (ii) is shown in Fig. 6.9 (b).

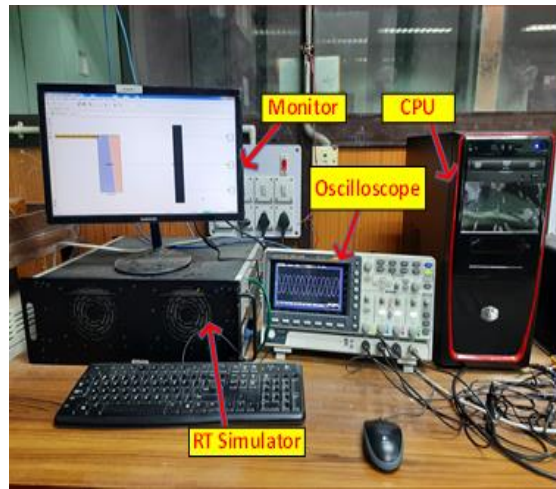


Fig. 6.10(b). OPAL RT overall set up.

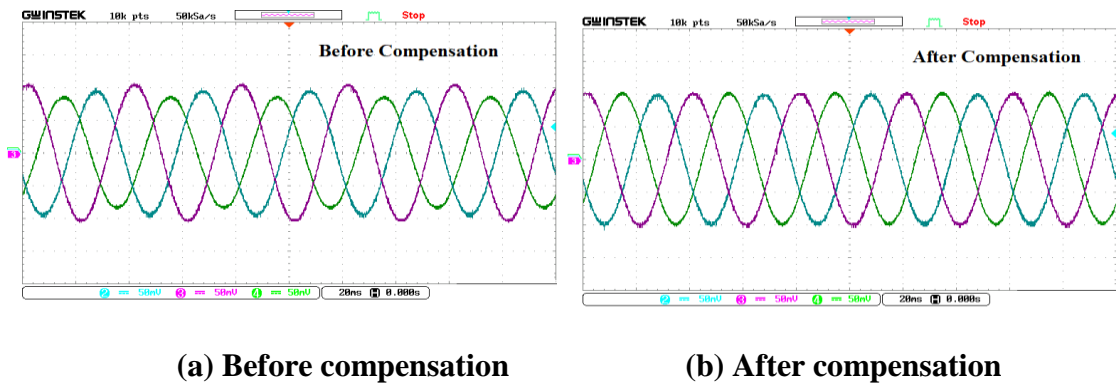


Fig. 6. 11. Three phase load bus voltage at bus i from RTDS for case (ii).

6.4.3. Case (iii)

This case study is carried out to examine whether the proposed scheme is able to serve the critical or sensitive load bus demand. Bus k has been considered as critical bus and it is assumed that the VUF at this bus should be less than 0.25 % [106] and negative sequence voltage limit

has been considered as 1V. The single phase loads that are connected at buses i , j and m are 143Ω , 100Ω and 75Ω respectively. The compensation control is started at 6s. It can be observed from Table 6.1 that VUF at the critical bus is 0.155% after compensation and the negative sequence voltage at the critical bus is 0.6V. The VUF and negative sequence voltage at each bus are tabulated in Table 6.1. The voltage at the DG terminals and the DG output currents are tabulated in Table 6.2. Hence, from this analysis it is evident that the proposed scheme is able to serve the critical load demand. The optimal pareto front obtained by MOACS for case (iii) is shown in Fig. 6.9(c).



Fig. 6.12. VUF at different load buses from RTDS for case (ii).

6.4.4. Case (iv)

The compensation control is dependent on the optimal reference sent by the microgrid central control system. It may be possible that due to some communication failure one of the DGs is unable to receive the reference signal and that particular DG is unable to participate in

the compensation process. To illustrate the performance of the system under this scenario, it is assumed that DG_l is unable to get the reference signal from the MCCS. The loads are considered to be same as in case (ii). After 6s the compensation control is started, but only three DGs are participating in the compensation control process. The performance is observed and the VUF at each bus is tabulated in Table 6.1. Although DG_l is not participating, the system is able to perform as per the requirement as the negative sequence voltages at all buses are under the limit. Hence, the proposed scheme is able to compensate voltage unbalance as per requirement under communication failure.

6.4.5. Case (v)

The proposed control strategy is tested when only three DGs are available to participate in the compensation process initially and the fourth DG participates later. The compensation is started at 6s and the negative sequence voltages and VUF at load buses are tabulated in Table 6.1. At 8s, DG_l is available for compensation, therefore the MCCS will send the updated references to all the four DGs. The unbalanced condition at different buses is improved and the new values of VUF at the buses are 0.6, 0.32, 0.39, 0.41, 0.42, 0.54 and 0.55% after 8s. From the DG currents presented in Fig. 6.13(a), it can be seen that DG_l is producing the unbalanced current after 8s and the active power output of the DGs given in Fig. 6.13(b) shows that the system performance is not disturbed due to the sudden availability of DG_l .

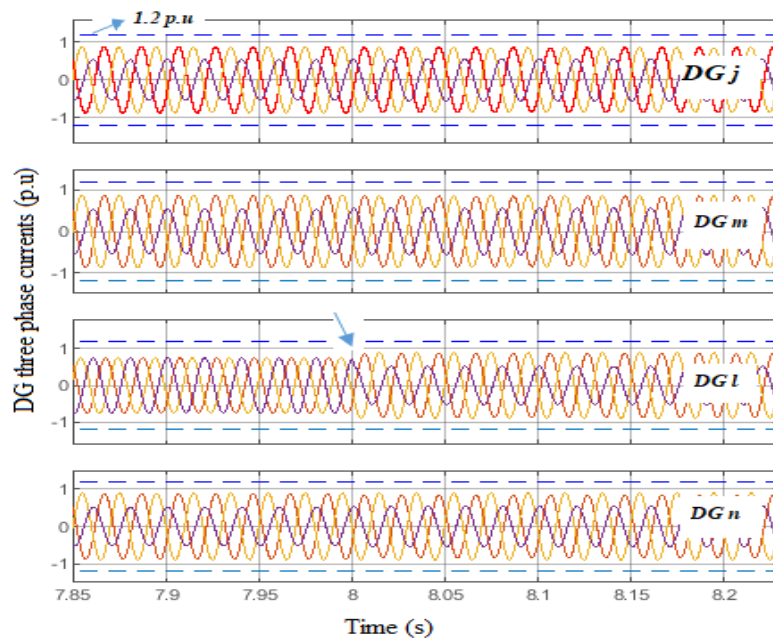


Fig. 6.13(a). Three phase DG currents of DGs for case (v).

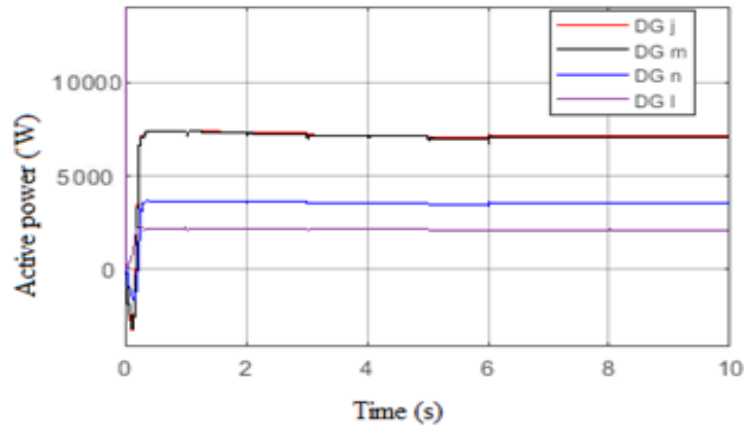


Fig. 6.13(b). Active power output of DGs for case (v).

6.4.6. Case (vi)

In this case study the robustness of the proposed methodology is evaluated for the inaccuracy in the input line parameters. To illustrate the scenario, the same test system has been considered as in case (ii). The input line parameters has been changed by $\pm 10\%$ and the performance of the system is observed. The obtained results are presented in Table 6.1. It can be seen that the negative sequence voltage at every bus is under the desired limit and the VUF values obtained are satisfactory. Therefore, the proposed methodology is robust against inaccuracy of the input line parameters.

6.4.7. Case (vii)

In this case study the performance of the proposed methodology is evaluated when the power quality issues occur while all the DGs are operating at their rated capacity. All the DGs are considered to deliver the rated output power and the single phase loads are connected to create unbalance similar to case (ii). The compensation is started at 6s and the obtained results are tabulated in Table 6.1. It can be seen from Table 6.1, the negative sequence voltage at each bus is reduced to below the desired limit after compensation. From Fig. 6.14 it is visible that the DG output current is well under the safety limit after compensation while delivering the rated output power. It is noteworthy to mention here that in case of severe unbalancing, the DGs have to sacrifice the output power to serve the unbalance compensation in order to maintain the DG safety.

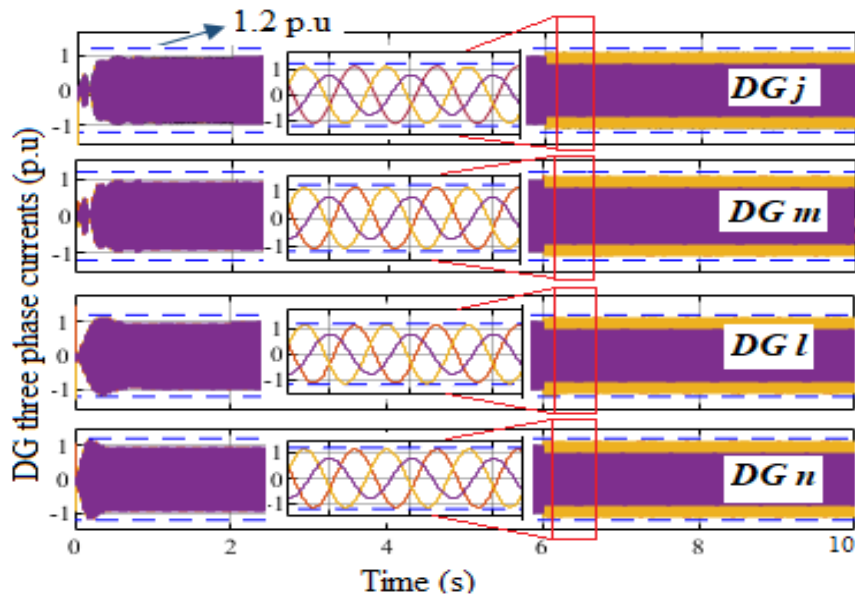


Fig. 6.14(a). Three phase currents of the DGs for Case (vii).

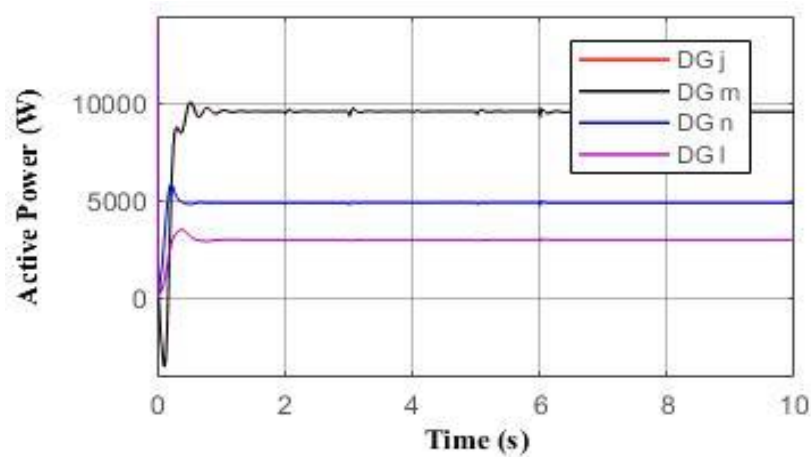


Fig. 6.14(b). Active power output of the DGs for Case (vii).

6.5. Comparative Assessment

Comparative study has been carried out with recent literature to highlight the robustness of the proposed method. The proposed method is able to serve severe unbalance upto 28% VUF whereas in ref. [91, 104] the authors considered VUF upto 4%. In this study the phase to phase voltage difference before compensation has been considered as 120V whereas in ref. [103] it is only 22V for the same system voltage. Unlike ref. [86, 91] the proposed method utilises all the available DGs for the compensation and compensation burden is distributed optimally among the DGs. Therefore, the DGs have the flexibility to serve as per requirement. The proposed method uses multi-objective pareto optimal approach (which is more suitable when the

objectives are conflicting in nature) to find the optimal compensation reference which makes the proposed approach more robust and suitable to serve the critical load bus unlike single objective function used in ref. [103]. The proposed approach is able to compensate unbalance at all the load buses whereas the authors in ref. [85,86] only focused a particular load bus and sacrificed the unbalance at DG connected bus in order to serve the load bus. This study proposes proper methodology for unbalance compensation, whereas ref. [101] concentrated mainly on the power flow regulation and active power curtailment. The authors in ref. [98] used multiple agent systems where, the agents require data from multiple microgrids which can lead to data mismatches. The proposed approach utilises the local voltage and current measurements for compensation reference. Therefore, the computational burden is less. Unlike ref. [85,86,91,98,101,103], in this study different case studies have been carried out and even during the communication failure the performance of the proposed approach is satisfactory. Moreover, the proposed method has been implemented in real time digital simulator (OPAL RT-RTDS) which shows that the proposed approach is suitable for practical applications.

The results obtained from the proposed optimization algorithm have been compared with the results obtained from Artificial cooperative search (ACS) algorithm using single objective function. The negative sequence voltage limit at each load bus is considered as one constraint and the DG maximum phase current is considered as another constraint. The objective function is considered as shown in (6.19).

$$\text{Objective function} = \sum_{k=1}^n (1 - V_k^d) \quad (6.19)$$

where $V_k^d = V_k^+ - V_k^-$

To visualize the performance of the optimization technique with ACS algorithm, the same loads have been considered as in case (i). The convergence characteristic of the optimization problem with ACS algorithm is given in Fig. 6.15. The results obtained from the optimization technique with ACS algorithm are tabulated in Table 6.3 and Table 6.4. From Table 6.3 it can be observed that the negative sequence voltage and VUF at each load bus obtained from the proposed MOACS algorithm is less compared to the results obtained with ACS approach. Table 6.4 reveals that the maximum phase currents of the DGs obtained from ACS approach are higher than that obtained from the proposed optimization technique. Therefore, from the comparative results it can be seen that the proposed approach with MOACS is more effective and reliable.

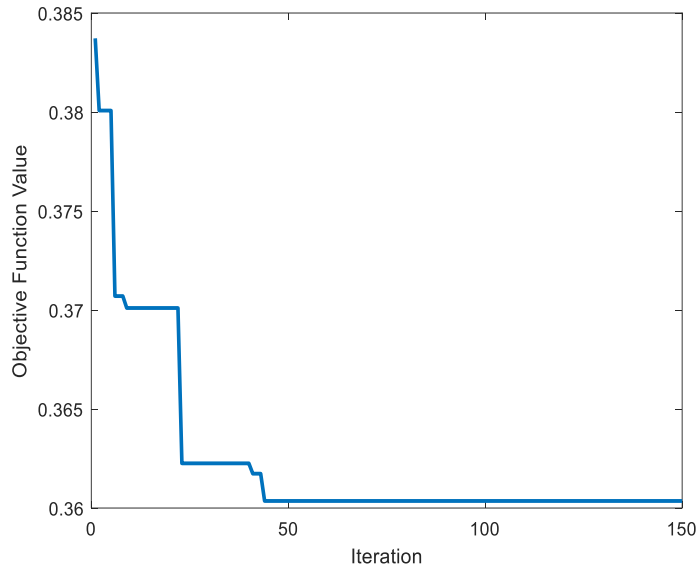


Fig. 6.15. Convergence characteristic of objective function with ACS.

Table 6.3. Comparative results of VUF and negative sequence voltages at load buses

Bus	Proposed approach with MOACS		Optimization approach with ACS	
	V^- (V)	VUF (%)	V^- (V)	VUF (%)
<i>i</i>	3.5	0.91	4.3	1.1
<i>j</i>	1.8	0.42	3.5	0.9
<i>k</i>	2	0.52	4.2	1.1
<i>l</i>	1.9	0.48	4	1
<i>m</i>	2.4	0.6	3.45	0.9
<i>n</i>	2.1	0.54	4.4	1.15
<i>o</i>	2	0.5	4.4	1.15

Table 6.4. Comparative results of DG positive sequence voltage and DG current

DG	Proposed approach with MOACS		Optimization approach with ACS	
	V^+ (p.u)	Max (I_a, I_b, I_c)	V^+ (p.u)	Max (I_a, I_b, I_c)
DG j	0.978	1.137	0.974	1.14
DG m	0.985	1.165	0.981	1.15
DG l	0.976	1.182	0.974	1.2
DG n	0.975	1.179	0.9725	1.15

6.6. Customized Negative Sequence Voltage Compensation at Load Buses

Due to the presence of unbalanced loads, the negative sequence voltage at load buses will increase and at some buses it may exceed the allowable limit. At each load bus the consumer voltage quality requirement may vary and therefore, different negative sequence voltage limits will be applicable for different buses. In this case the objective is to keep the negative sequence voltage at each load bus within the desired limit by using DGs so that the consumer voltage quality requirements will be achieved. All the DGs connected to the microgrid, participate in the compensation process and while trying to reduce the negative sequence voltage at each bus, the DGs will supply the negative sequence quantities in addition to the positive sequence quantities which cause rise in DG output currents. It is also possible that the phase currents of DG may exceed the safety limit of the converter which is not desirable since the converter cannot withstand high currents. Therefore, to achieve these objectives, the overall optimization problem can be formulated as given in (6.22), and ACS algorithm has been utilised to solve the mentioned optimization problem.

$$f_1 = \sum_{k=1}^n \max(0, |V_k^-| - V_{lk}^-) \quad (6.20)$$

$$f_2 = \sum_{n=1}^{ndg} \max(0, \max(I_{Gk}^a, I_{Gk}^b, I_{Gk}^c) - I_{Gk}^{limit}) \quad (6.21)$$

$$f_{obj} = w_1 * f_1 + w_2 * f_2 \quad (6.22)$$

Initially, three phase balanced loads are connected to each load bus and then single phase loads are connected between phase *a* and phase *b* of three phase loads at different time intervals. The negative sequence voltage limits at the buses *i, j...o* are considered as {5,10,5,10,10,10,5}V respectively. MCCA collects the required data from the microgrid and calculates the optimal reference of negative sequence voltage for each DG with the help of optimization algorithm. The obtained results are given in Fig. 6.16 and 6.17 which can be classified into three stages.

Stage (i): From 0-4 s, different single phase loads viz. 500Ω, 250Ω and 200Ω for the buses *j, i* and *m* are connected at 2s, 3s and 4s respectively. After the addition of single phase loads into the system the negative sequence voltage (represented in green color) at each load bus has

increased as shown in Fig. 6.16. Except at bus j , at all other buses the negative sequence voltage exceeded the allowable limit (represented in blue color) and during this period no DG is providing the compensation.

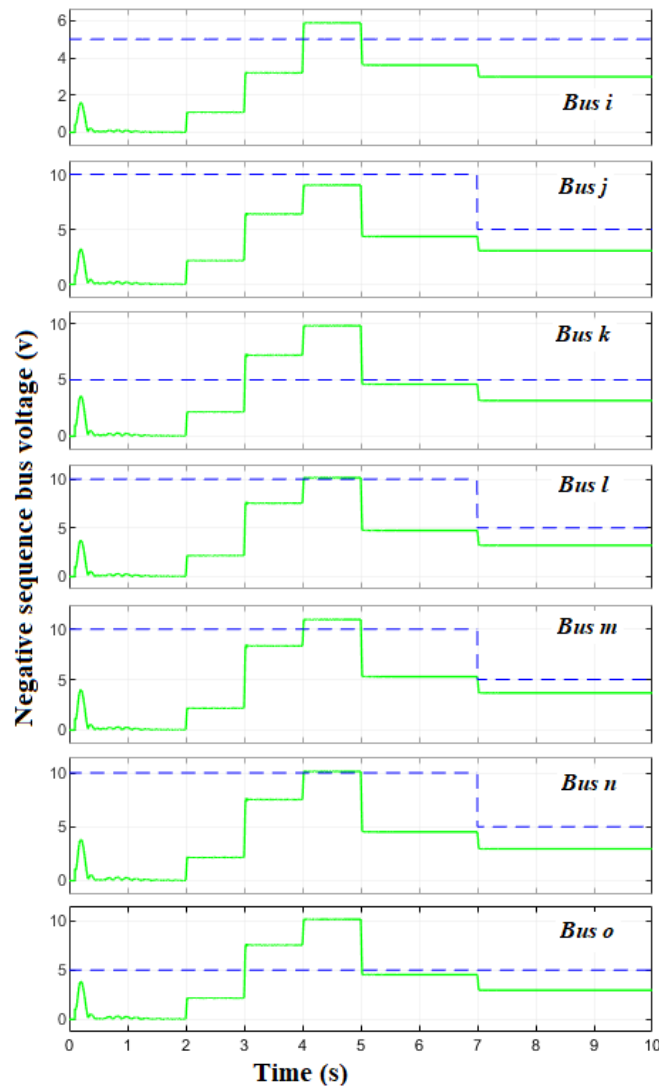


Fig. 6.16. Negative sequence bus voltages.

Stage (ii): The compensation is started at 5s. Initially the MCCS obtains the positive sequence DG currents and consumer voltage quality limits i.e. negative sequence voltage limits at each bus and also the negative sequence load currents. After the objective function converges from optimization algorithm, MCCS collects the optimal references for each DG. From Fig. 6.18 it can be seen that the objective function convergence within 50 iterations. At 5 s the DGs receive reference signals from MCCS. Therefore, the DGs start to provide the compensation current in order to reduce the negative sequence voltage at load buses. It can be seen that from Fig. 6.16 that after 5s the negative sequence voltage at all the load buses becomes lower than the allowable limits as the DGs are supplying the compensating negative sequence voltage.

Stage (iii): In this stage it is assumed that the consumer voltage quality requirement has been changed. At 7s, the negative sequence voltage limits at all load buses are changed to 5V. Then the MCCS sends the updated references to each DG so that the system performs as per the requirement. It can be seen from the Fig. 6.16 that after 7 s the negative sequence voltage at all the load buses are well under the desired limits and the DG phase currents of all the DGs are well under the safety limits. The DG phase current of DG_j is shown in Fig. 6.17.

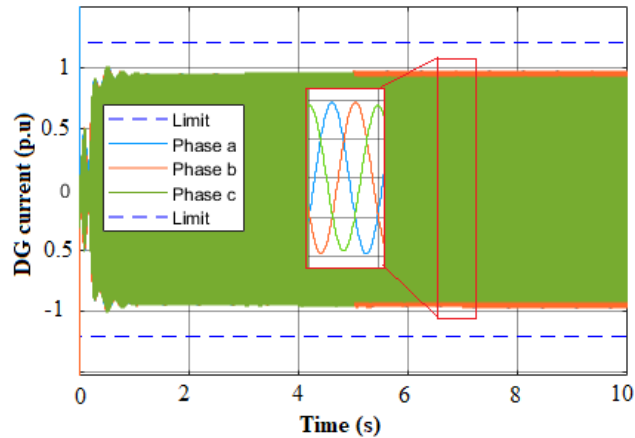


Fig. 6.17. DG_j phase currents.

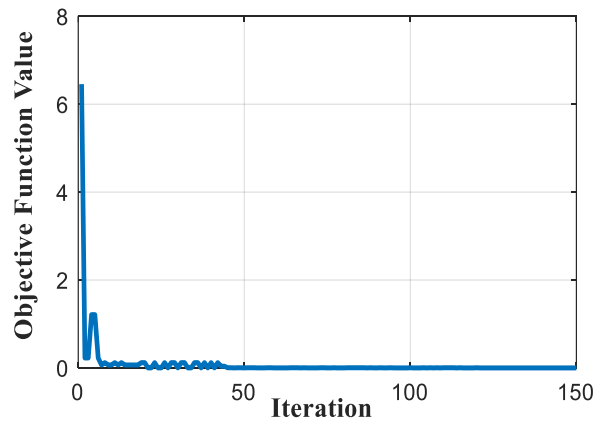


Fig. 6.18. Convergence characteristics with ACS algorithm.

6.7. Conclusion

This study presents an optimization based control strategy for the customised unbalance voltage compensation in the microgrid using the multi-objective artificial cooperative search algorithm. The proposed control scheme is capable to reduce VUF at each load bus with the DG output current under the safety limit. Simulation results show that the proposed scheme can serve the customised voltage quality service based on the consumer requirements in addition to

enhancement of the positive sequence voltage. The control algorithm not only compensates the unbalance voltage at a particular point, but provides a general reduced voltage unbalance profile in the grid. The voltage unbalance compensation process works satisfactorily in case of communication failure and is applicable to microgrid with higher voltage level. Simulation results have been provided and have been compared with the results of another optimization algorithm to establish the superiority of the proposed algorithm. The results indicate that the proposed scheme can perform satisfactorily under diverse conditions and therefore, the proposed control strategy is suitable for practical applications. From the simulation study it is evident that the proposed approach is capable to reduce the negative sequence voltage at the load buses to maintain the voltage quality required by the consumers. Moreover, the negative sequence voltage limits at the load buses can be customized based on the requirement and the method will not be affected by the change in load.

CHAPTER 7

A Two Level DG Control Strategy for Flexible Operation of Microgrid System

7.1. Introduction

The rapid enhancement in the growth of the renewable energy sources (RES) as a solution for the global climate changes and energy crisis brings more attention towards the integration of renewable sources into the power network. The microgrids are controllable entities consisting of multiple renewable energy sources, energy storage devices and loads which can be controlled and operated locally. The power electronic interfaces are used to connect the RES to the microgrid, which makes the IIDG control more flexible during the non-ideal conditions. The power quality issues often become very critical in the microgrids and the voltage unbalance is one of the most severe issues. There are different reasons for voltage unbalance in the microgrid viz. faults, unmatched transformer impedance and most common one is the presence of single phase loads and unbalanced loads. Moreover, the IIDG control systems are often exposed to the voltage sags.

Due to voltage sags IIDG control systems may experience disturbance which hampers the continuous and safe operation of power distribution. Moreover, the operation of the sensitive loads may be disrupted. Therefore, the IIDGs should have the voltage support abilities and low voltage ride through (LVRT) capability for operation in the non-ideal conditions [54, 87]. Alongside, during these non-ideal conditions, the DG may produce high amount of currents which will cause damage to the semiconductor devices present in the IIDGs and also it may experience sudden loss in the active power injection. To handle these issues such as voltage support, unbalance compensation, active power control and current limitations, the IIDG control systems should be flexible and should be able to respond quickly as per requirement. In recent times the researchers proposed different techniques for the DG control during the unbalanced conditions. The authors in [109,110] proposed control techniques which can deliver constant amount of reactive power from the DG to support the PCC voltage. The main drawback of this control technique is that voltage is not supported effectively and also it is difficult to select a proper power reference which may result in overcurrent scenario. To overcome this drawback, the LVRT strategy has been incorporated in which the DGs inject the required amount of reactive current to mitigate the voltage drop. The symmetric sequence based voltage support schemes

have been proposed [111,112] where the unbalanced voltage has been decomposed into the positive sequence and negative sequence voltages and the control technique determines the references for the current from the symmetric voltage components. Based on the positive sequence and negative sequence susceptance and conductance, the authors in [113] proposed a control scheme utilizing instantaneous active power theory, but it only focused to compensate the short term voltage sags. In [114,115] the authors have considered the long term voltage sags in the low voltage microgrids. However, these methods depend highly on the system parameters and X/R ratio.

In recent times some researchers put efforts on the unbalance voltage compensation [100,107,108]. In [107] the authors proposed a proportional resonant controller in complex form using communication link to mitigate the voltage unbalance. The proposed technique shares the compensation burden to each DG. Ref. [108] proposed a multiple agent system in multi-microgrids for voltage regulation in which the agents collect data from each microgrid and communicate within the microgrids. To implement this method, large amount of data is required to be collected and it is prone to malfunction due to any communication failure. A dynamic phasor method is proposed based on the state space analysis for the microgrid consisting of multiple IIDGs [100]. The authors in ref. [103] proposed an optimisation based voltage unbalance compensation for multi-bus microgrid, but there is no provision for giving priority to voltage support. Later on Lagrange multiplier based techniques has been utilized to reduce the load bus negative sequence voltages so as to maximise the voltage support. Ref. [105] introduced a new control strategy for grid tied IIDG but it is mainly focused to support the voltage by supplying the maximum amount of reactive power. An imbalance voltage mitigation technique based on the minimum current control for the IIDGs is introduced in [104], in which the authors have considered multi-objective control.

From the existing literature survey it has been observed that there is a need to consider multiple objectives such as voltage support, unbalance compensation, current limitation and active power control. The control objectives have to be considered simultaneously for better operation of the IIDGs in the microgrid. Hence, this study presents a new optimization based two stage multi-objective control strategy for the microgrid which consists of two stage IIDG control. The main aim of the proposed approach is to supply the positive sequence quantities in order to support the positive sequence voltage near to the nominal voltage and to inject the negative sequence quantities to reduce the voltage unbalance abiding the current limitation. The contributions of the proposed approach can be summarised as follows:

- A two stage flexible multi-objective control strategy has been developed for the microgrid consisting of different IIDGs. The control strategy operates locally and also centrally. The local control works individually for each DG and coordinates with the central control to deliver the optimised references for each IIDG.
- The positive sequence voltage at the terminals of the DGs has been supported as much as possible by supplying the required amount of reactive power.
- The voltage unbalance factor (VUF) at the load buses has been reduced as much as possible by supplying the negative sequence quantities from the DGs.
- The DG control is able to inject the maximum amount of active power during the compensation process and the DG currents are maintained within the safety limits.
- Moreover, the proposed approach is tested for diverse conditions including grid imbalance.

7.2. Problem Formulation and Control Objectives

The presence of single phase loads as well as unbalanced loads creates several detrimental issues in the microgrids. Voltage unbalance is one of the major issues that occur due to these unbalance loads. Moreover, the voltage quality becomes vulnerable at the load buses because of the reduction in the positive sequence voltage. The DGs are connected to the microgrid via power electronic interfaces which make the microgrid operation flexible to overcome these issues by properly controlling the DGs. The studies revealed that while compensating these issues, the DGs present in the microgrid start to inject more current and it may be possible that the overall DG output current may exceed the safety limit. Moreover, it creates uncertainty in the active power management. To overcome all these issues, this study aims to supply the positive sequence quantities in order to support the positive sequence voltage, minimising the unbalance voltage compensation through supply of negative sequence quantities and also ensuring the DG overall current under the safety limit with proper active power control. The control objectives of this study are explained in the following subsections.

7.2.1. Active Power Control

During the voltage sags there is always a risk of sudden active power drop. To mitigate it and to use the full DG capacity, in the proposed method the control strategy is designed in such way that the DG will deliver the maximum allowable active power to the grid. Therefore, the

average active power output of the DG can be expressed in dq domain as given in equation (7.1).

$$P = I_d^+ V^+ + I_d^- V^- \quad (7.1)$$

where, V^+ and V^- are the positive and negative sequence voltages. In this work, for simplicity the active power of the DG is injected through positive sequence current I_d^+ and I_d^- is zero. Therefore, from (7.1) the reference value for I_d^+ can be obtained as follows with the known value of active power output (P).

$$I_{d_ref}^+ = \frac{P}{V^+} \quad (7.2)$$

The current reference obtained from (7.2) is the initial reference which injects the maximum amount of active power in the microgrid. The current reference ($I_{d_ref}^+$) can be updated depending on the DG current limitation.

7.2.2. Positive Sequence Voltage Support

To maintain the voltage stability during non-ideal conditions, the positive sequence voltage has to be maintained near to the nominal voltage. The conventional methods may not be able to fully support the positive sequence voltage. Therefore, in this work the reactive power has been supplied by the DGs as much as possible to support the positive sequence voltage. The reactive power supplied from the DG according to the voltage drop is given in Fig.7.1. The reactive power reference has been calculated initially from (7.3), from which the q component of the positive sequence current reference ($I_{q_ref}^+$) is obtained.

$$Q_{ref} = \begin{cases} Q_{max} & \text{if } v \leq v_{p1} \\ Q_{max} + \frac{Q_{p2} - Q_{max}}{v_{p2} - v_{p1}}(v - v_{p1}) & \text{if } v_{p1} < v < v_{p2} \\ 0 & \text{if } v_{p2} < v < v_{nom} \end{cases} \quad (7.3)$$

where, v_{p1} is the voltage at P_1 , v_{p2} is the voltage at P_2 and v_{nom} is the nominal voltage.

When the positive sequence voltage drops below 0.92 p.u. the DG will deliver the reactive power at full capacity. When it is above 0.98 p.u., there is no reactive power support from the DG and when the positive sequence voltage is between 0.92 p.u and 0.98 p.u., the reactive power reference is calculated from (7.3).

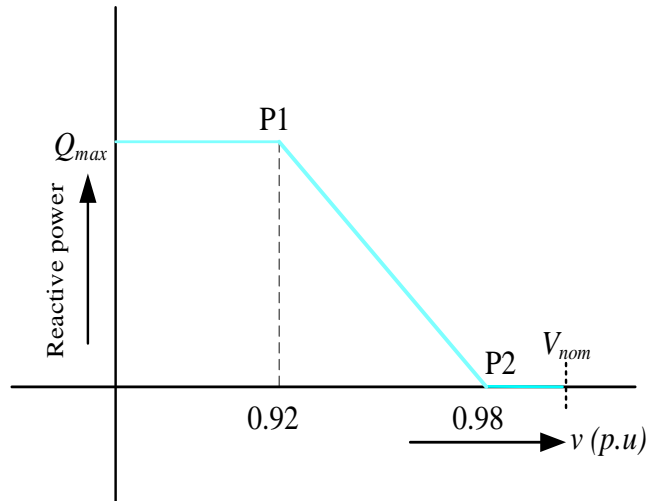


Fig. 7.1. Reactive power requirement to support the positive sequence voltage.

7.2.3. Unbalance Voltage Compensation

The negative sequence current consumed by the unbalanced loads that are connected to load buses will flow through the line admittance and makes the load buses to experience voltage distortion. Due to the voltage distortion, the voltage quality deteriorates causing problems to the electrical equipment which are sensitive to the voltage quality. If the DGs are able to deliver the negative sequence quantities, the voltage unbalance at the load buses can be compensated. Therefore, by supplying the proper amount of negative sequence quantities from the DGs, the load buses negative sequence voltage can be regulated. This requires the power flow to be calculated. A benchmark low voltage microgrid network [103] as shown in Fig. 6.4 has been considered to demonstrate the compensation scheme. The load flow has to be calculated for this purpose and the negative sequence equivalent network for the considered test system is required. The simplified negative sequence equivalent network at bus k is shown in Fig.7.2 in which it is assumed that bus k is a DG connected bus. From Fig.7.2, by using the nodal analysis, the expression for the negative sequence current at node k can be derive as shown in (7.4)

$$I_k^- - Y_{jk}^- (V_j^- - V_k^-) - Y_{kl}^- (V_l^- - V_k^-) + (V_{Gk}^- - V_k^-) Y_{Gk}^- = 0 \quad (7.4)$$

where $I_k^- = i_k^{d-} + j i_k^{q-}$.

Equation (7.4) can be generalized and rewritten as (7.5).

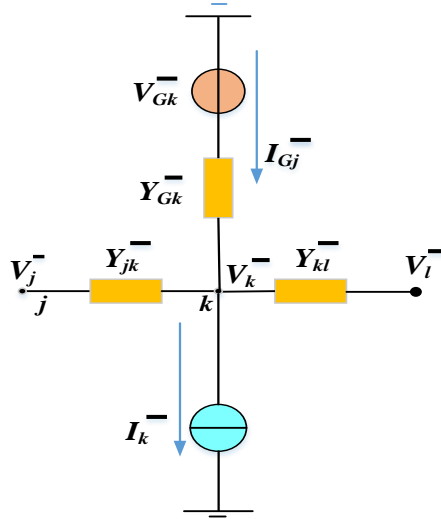


Fig. 7.2. Negative sequence equivalent of bus k .

$$V_{Gk}^- Y_{Gk}^- - I_k^- = V_k^- (Y_{Gk}^- + \sum_{k=1}^n Y_{jk}^-) - \sum_{\substack{j=1 \\ j \neq k}}^n V_j^- Y_{jk}^- \quad (7.5)$$

When there is no DG connected to bus k , V_{Gk}^- and Y_{Gk}^- will become zero and n indicates number of buses. Based on (7.5) for n number of buses, n number of linear equations can be formulated with n number of unknowns (V_1^- , V_2^- , ..., V_n^-). From (7.5) it can be observed that the negative sequence DG voltages (V_{G1}^- , V_{G2}^- , ..., V_{Gn}^-) and negative sequence bus voltages (V_1^- , V_2^- , ..., V_n^-) are related to each other. Therefore, the negative sequence bus voltage can be controlled by adjusting the DG negative sequence voltage. Hence, by controlling the negative sequence voltage, the VUF at each load bus can be reduced below a certain level so that the voltage quality can be maintained at the load buses. By knowing the positive sequence voltage at the load buses, VUF can be calculated as shown in (7.6) which has been considered as one objective function.

$$f_1 = VUF = \sum_{k=1}^n \frac{V_k^-}{V_k^+} \times 100 \quad (7.6)$$

7.2.4. DG Current Limitation

To compensate the voltage unbalance, in addition to the positive sequence quantities the DGs in the microgrid will start to supply the negative sequence quantities. It may cause the overall current of the DG to rise above the safety limit of the DG. The studies indicate that the inverter can operate safely till the overall current of DG is 1.2 p.u of the rated current [105]. Since the DG consists of the semiconductor devices, it has to be operated below the safety limit

of the DG output current. Therefore, the control technique in this study makes sure that the DG current is less than the safety limit of the DG. The total injected current of the DG into the grid can be calculated from (7.7).

$$\vec{I}_{abc} = \vec{I}_{abc}^+ + \vec{I}_{abc}^- \quad (7.7)$$

The positive sequence component of the DG current is the summation of the d and q components as shown below.

$$\vec{I}_{abc}^+ = (I_d^+ + j \cdot I_q^-) \cdot e^{-j \cdot \theta} \quad (7.8)$$

$$|\vec{I}_{abc}^+|^2 = (I_d^+)^2 + (I_q^-)^2 \quad (7.9)$$

With the knowledge of the bus voltage, negative sequence DG voltage and line admittance, the negative sequence component of the DG current can be obtained. The negative sequence component of the DG current for the DG connected to the bus k can be determined from (7.10).

$$I_{Gk}^- = (V_{Gk}^- - V_k^-) \cdot Y_{Gk}^- \quad (7.10)$$

By reverse Park's transformation, the negative sequence component of the current can be obtained from (7.11).

$$\vec{I}_{abc}^- = \begin{bmatrix} \cos(-\theta) & -\sin(-\theta) & 1 \\ \cos(-\theta - \frac{2\pi}{3}) & \sin(-\theta - \frac{2\pi}{3}) & 1 \\ \sin(-\theta - \frac{2\pi}{3}) & \sin(-\theta + \frac{2\pi}{3}) & 1 \end{bmatrix} \cdot [I_{Gd}^- \ I_{Gq}^- \ I_{G0}^-]^T \quad (7.11)$$

From (7.11) the required amount of the negative sequence component of the DG current can be obtained. But in order to maintain the DG safety limit, it may be possible that the DG is not being able to provide that much amount of the negative sequence current since it is already supplying required amount of positive sequence current. Therefore, after delivering the required amount of positive sequence current, the available capacity of the DG can be obtained from (7.12 - 7.14).

$$I_{abc}^{limit\ 2} \geq |\vec{I}_{abc}^-|^2 \quad (7.12)$$

$$|\vec{I}_{abc}^+|^2 + |\vec{I}_{abc}^-|^2 \leq I_{abc}^{limit\ 2} \quad (7.13)$$

$$\left| I_{abc}^- \right|^2 \leq I_{abc}^{limit\ 2} - \left| I_{abc}^+ \right|^2 \quad (7.14)$$

Equation (7.14) gives the allowable amount of the negative sequence component of the DG current at which the DG operates safely. Hence, (7.14) determines the limit for the negative sequence DG current. Therefore, the DG negative sequence current obtained from (7.11) has to be less than or equal to the allowable limit. To achieve this, in this study another objective function as shown in (7.15) has been formulated.

$$f_2 = \left| I_{abc}^- \right|^2 - \left| I_{abc_available}^- \right|^2 \quad (7.15)$$

To solve both the objective functions as given in (7.6) and (7.15), an optimization approach is required. To minimize the VUF and DG phase currents, optimized references are essential for the DGs to properly supply the compensating quantities. Hence, the optimization problem corresponding to f_1 and f_2 can be developed considering the weight coefficients as shown in (7.16).

$$f = w_1 * f_1 + w_2 * f_2 \quad (7.16)$$

where, w_1 and w_2 are the weight functions, w_2 has been given higher priority so that the output phase currents of the DG always stay well within the desired safety limit. To solve the optimization problem stated in (7.16), Artificial cooperative search (ACS) algorithm has been used in this study. The behaviour of the natural species like butterflies, honey bees and bird species is the inspiration behind the development of the ACS algorithm. DG negative sequence voltages are considered as design variables (V_{G1}^- , V_{G2}^- , ..., V_{Gn}^-) and VUF as constraint. The overall optimization problem can be given as shown in equation (7.17). The optimization algorithm will give the optimized values of negative sequence DG voltages to minimize the VUF along with the optimized positive sequence DG reference currents.

$$F = \begin{cases} \text{Minimise}(f) \\ VUF < VUF^{lmt} \end{cases} \quad (7.17)$$

7.3. Proposed Multi-Objective Control Strategy

To achieve the control objectives as mentioned in the above section, the multi-objective control strategy has been implemented in this study. The control strategy is aimed to supply the reactive power through the positive sequence quantities in order to support the positive sequence

voltage and secondly it is aimed to minimise the voltage unbalance as much as possible by injecting the negative sequence quantities with efficient balance between the active power production and current limitation. To implement these objectives simultaneously in the microgrid test system consisting of several DGs, the proposed control strategy has been developed in two stages viz. local control and central control, where the central control coordinates with the local control.

7.3.1. Local Control

The microgrid test system consists of different IIDGs connected at different buses viz. DG_j , DG_m , DG_l and DG_n . The local control is the control which controls the DGs individually. The main task of the local control is to monitor each DG individually, track and control the positive sequence DG currents (I_d^+, I_q^+) locally and update it after getting feedback from the central control. Secondly it will receive the references for the reactive power support (Q_{ref}) and active power production ($I_{d_ref}^+$) from the central control and tracks the d and q components (I_d^+, I_q^+) of the positive sequence current which will be fed to the grid side inverter.

7.3.2. Central Control

The central control (CC) operates globally in the microgrid and it coordinates with all the DGs. The CC tracks the positive sequence bus voltages ($V_1^+, V_2^+, \dots, V_n^+$), negative sequence load currents ($I_1^-, I_2^-, \dots, I_n^-$) at each bus and the DG positive sequence currents. Initially, CC detects the voltage sag and depending on the voltage sag CC classifies the scenario. In this study two scenario classifications are considered which are 1). Active power prioritization during small voltage sag at the PCC. In this scenario, the first priority is given to the active power production of the DG and the DG will get the reference current to deliver the maximum active power. The next priority has been given to the positive sequence voltage support and finally remaining capacity of the DG, if any, is utilized for unbalance voltage compensation. 2). Positive sequence voltage support prioritization during large voltage sag at the PCC. In this scenario, the first priority is to provide the reactive power to support the voltage magnitude. The DG starts to supply the maximum amount of the reactive power, then the unbalance compensation and finally the remaining capacity is used for the active power injection.

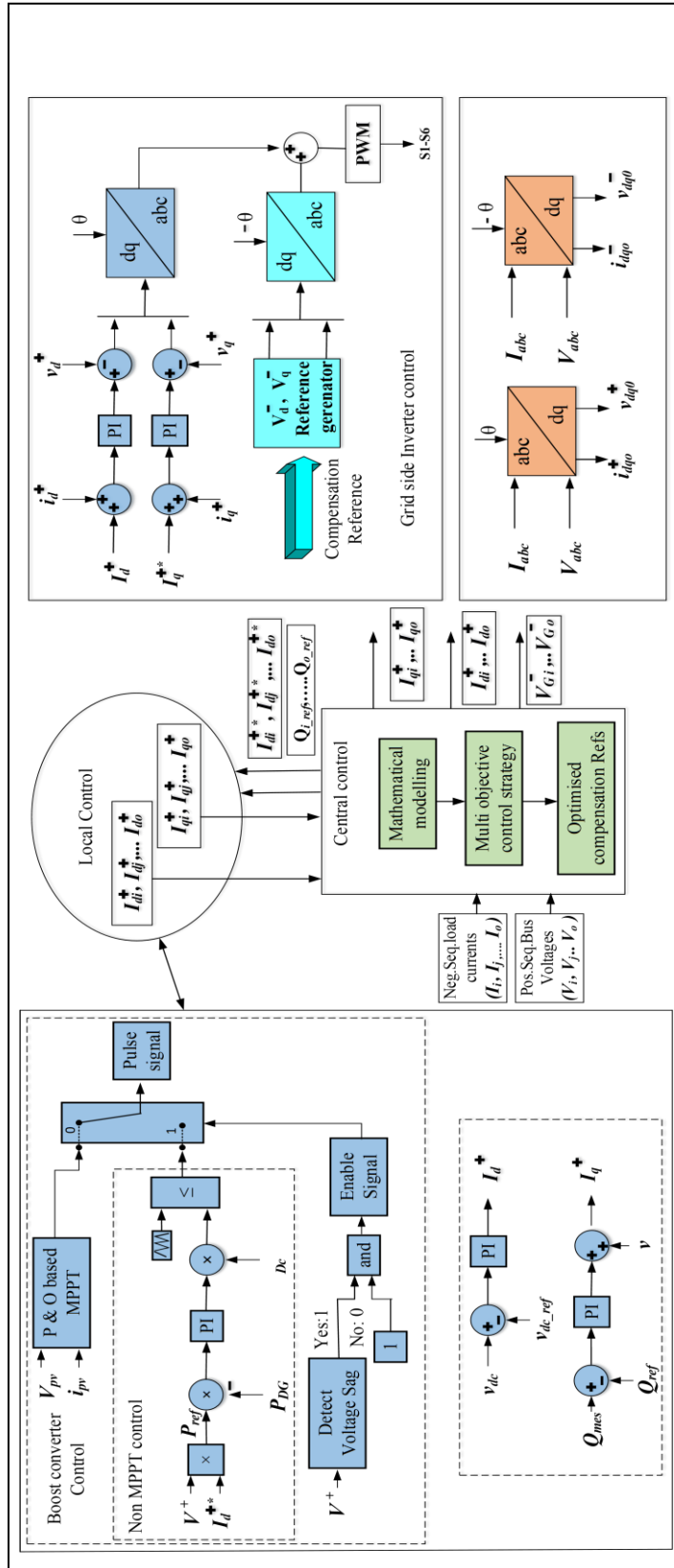


Fig. 7.3. Overall control structure of the proposed scheme.

7.3.3. Application of the Proposed Multi-Objective Control Strategy

Initially the control system detects the voltage sag and the scenario classification is performed depending on the positive sequence voltage. The control strategy follows the following steps:

- 1) For scenario 1: The active power injection of the DG is prioritized in this scenario. Therefore, the initial reference current for active power ($I_{d_ref}^+$) which injects the maximum amount of active power into the grid will remain same. Then to support the positive sequence voltage, the required reactive power from each DG will be calculated depending on the voltage level as given in (7.3). These references are initially fed to the local control and it tracks I_d^+ and I_q^+ values. Then the optimization problem which is mentioned in (7.17) is solved using the ACS algorithm.
- 2) For scenario 2: In this scenario, since the voltage sag is more, the DGs prioritize to deliver the full capacity of reactive power and therefore, the initial $I_{d_ref}^+$ will be fed into the control system. In this scenario it is assumed that the second priority is given to the voltage unbalance compensation. To achieve that, voltage unbalance constraint has been included in the optimization problem as given in (7.19). Here, the DG is delivering maximum amount of reactive power, providing unbalance compensation in addition to the active power production. Therefore, it may be possible that the DG overall current will exceed its limit. In this case the control technique has to sacrifice the active power production so that the DG can accomplish other objectives. For this the active power current reference ($I_{d_ref}^+$) will be updated accordingly as given in (7.20).

$$Q_{ref} = Q_{max} \quad (7.18)$$

$$VUF \leq VUF^{lim} \quad (7.19)$$

$$I_{d_ref}^+ = I_{d_ref}^+ \pm \Delta I_d^+ \quad (7.20)$$

where, ΔI_d^+ is considered as 10% of the initial current reference and the optimization algorithm will update $I_{d_ref}^+$ which results in active power curtailment until the DG currents reach the safety limits. The positive sign is considered during the restoration of the active power and the negative sign is considered during active power curtailment.

- 3) Next, the optimized values of the positive sequence DG current references and DG negative sequence voltage references are fed to the DG inverter control as shown in

Fig.7.3.

- 4) Finally, the voltage reference signal which is a combination of positive and negative sequence voltages as shown in (7.21) is fed to the power converter with the help of PWM.

$$\begin{bmatrix} V_a \\ V_b \\ V_c \end{bmatrix} = \begin{bmatrix} V_a^+ \\ V_b^+ \\ V_c^+ \end{bmatrix} + \begin{bmatrix} V_a^- \\ V_b^- \\ V_c^- \end{bmatrix} \quad (7.21)$$

7.4. Simulation Results

To evaluate the performance of the proposed flexible multi-objective control strategy, the simulation is carried out for the test model shown in Fig. 6.4 in MATLAB/ Simulink environment. The three phase three wire low voltage test system have four DGs which are connected at j , m , l and n buses and seven three phase loads. The rated capacities of the DGs that are connected to the buses j, m, n and o are 10kW, 10kW, 3kW and 5kW respectively. The power electronic interfaces (i.e. three phase three leg inverters) are utilized to connect all the DGs to the microgrid. The rated voltage of the test system is considered as 400V and the frequency is 50Hz. The DG tie line admittances, feeder tie line admittances and the delta connected three phase loads at each load bus are given in Table 7.1. To create the unbalance, several single phase loads are connected in the microgrid at different time intervals. The optimization algorithm runs for every 0.2s and the obtained optimal references are given to the DGs. Different case studies are carried out to evaluate the robustness of the proposed control strategy.

7.4.1. Case 1: During Small Voltage Sag

The performance of the proposed method is assessed during small voltage sag in this case study. In addition to the balanced delta connected three phase loads, the single phase loads are connected at different buses. The single phase loads (50Ω , 45Ω and 143Ω) are connected to the two phases of the three phase balanced loads at the load buses j , m and i at 2s, 3s and 4s. All the DGs in the microgrid are producing maximum active power and the load buses experience increment in the negative sequence voltage because of the presence of the single phase loads which makes the VUF to rise at each load bus as shown in Fig 7.4. Moreover, the positive sequence voltage at the DG terminals are also reduced due to the extra burden of the single phase loads. The positive sequence voltage at the terminals of DG_j , DG_m , DG_l and DG_n after 4s is observed as 0.978 p.u, 0.976 p.u, 0.973 p.u and 0.974 p.u respectively. At 4.5s the control strategy is started and the positive sequence voltages at all the DG terminals are above 0.92 p.u. Therefore, the control strategy works in scenario 1 mode. Fig 7.5 illustrates that even after 4.5s

all the DGs continue to deliver the active power at full capacity. Also, as shown in Fig. 7.6 and tabulated in Table 7.3 the positive sequence voltages at the terminals of each DG rise near to the nominal voltage since the DGs are supplying the reactive power. VUF has been reduced at each bus at 4.5s as shown in Fig. 7.4 and Table 7.2 since all the DGs are producing the compensating currents. At 5s another single phase load of 75Ω has been added to bus n and all the DGs receive the updated references. The reactive power support has been adjusted as per the new references and the positive sequence voltages at the terminals of the DGs which are connected to the load buses j, m, i and n are tabulated in Table 7.3. The reactive power support from each DG is shown in Fig. 7.7. Here, since the active power is prioritized, the DGs are producing full active power and to maintain the DG phase currents within the safety limits, the control has to sacrifice the voltage unbalance compensation since the DG currents are already operating near to the safety limit as shown in Fig 7.8. Therefore, as given in Fig. 7.4 and Table 7.2, the VUF has been increased slightly at each load bus after 5s

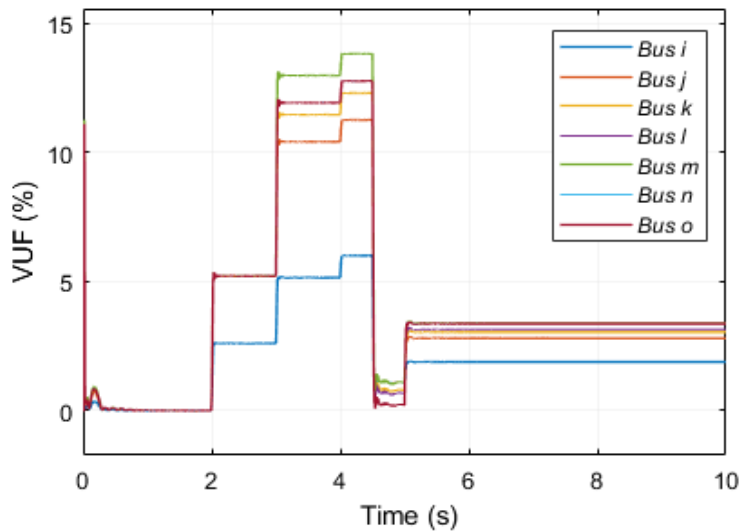


Fig. 7.4.VUF at each load bus in case 1.

Table 7.1. Feeder line data and three phase load data

Tie lines	Conductance (S)	Susceptance (S)	Bus	Load (Ω)
Between i & j	0.1269	0.6379	i	588.2
Between j & k	0.3032	1.7148	j	1425.6
Between k & l	0.4683	3.9230	k	588.2
Between l & m	0.0332	1.7148	l	588.2
Between l & n	0.3032	1.7148	m	588.2
Between n & o	0.3032	1.7148	n	588.2
DG's	0.3032	1.7148	o	588.2

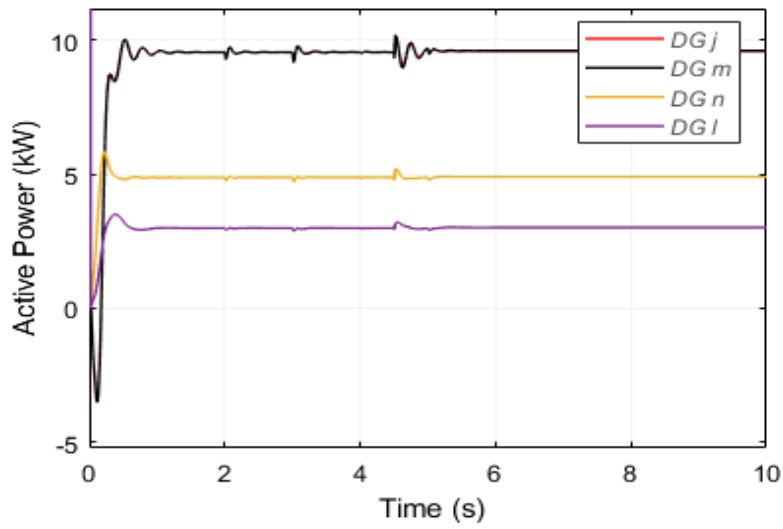


Fig. 7.5. Active power output of the DGs in case 1.

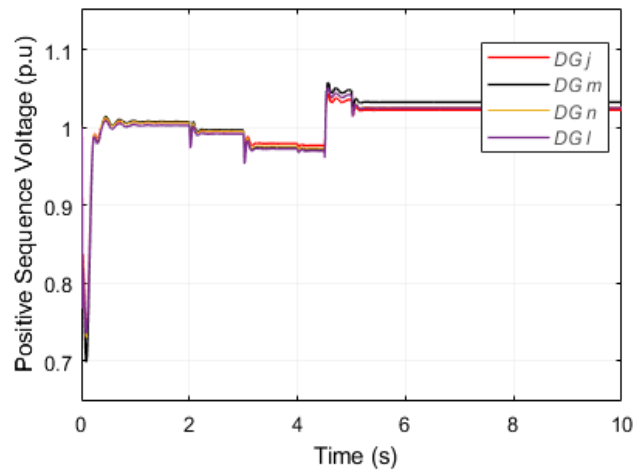


Fig. 7.6. Positive sequence voltages at the terminals of the DGs in case 1.

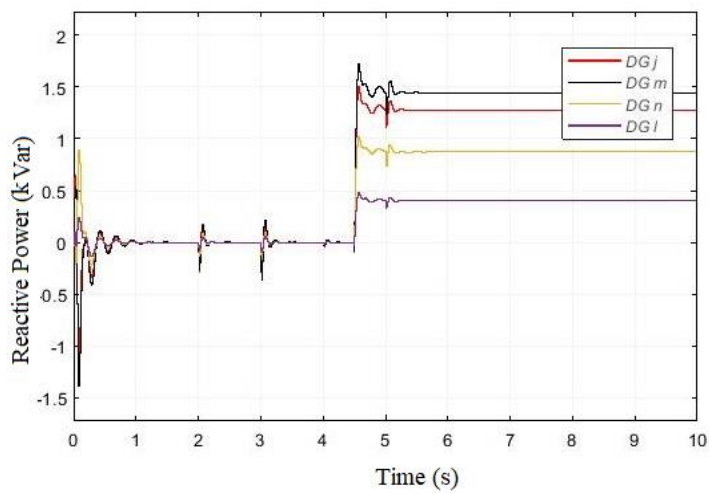


Fig. 7.7. Reactive power output of the DGs in case 1.

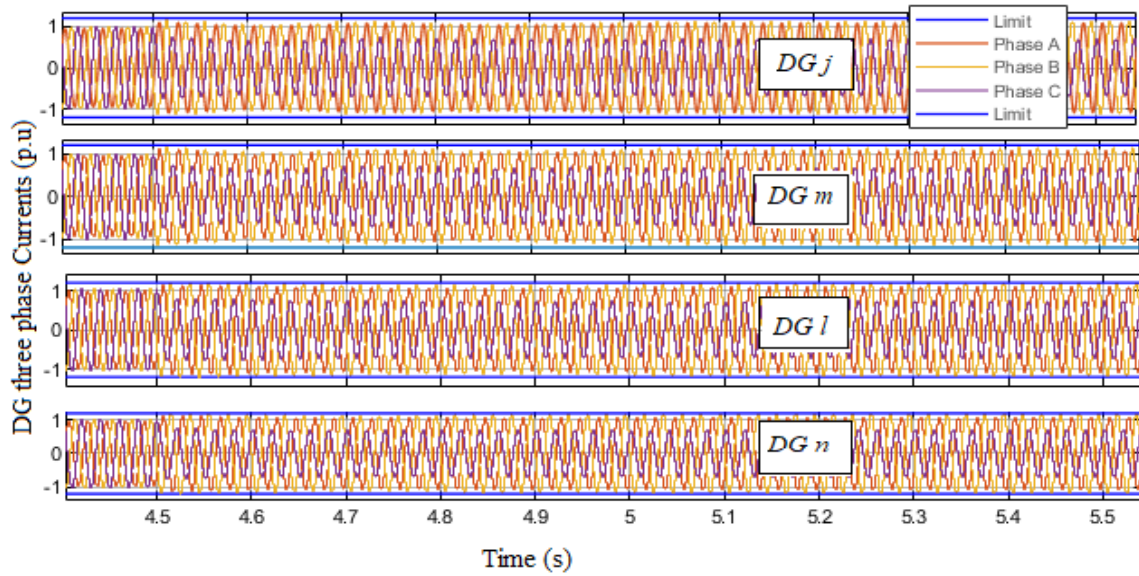


Fig. 7.8. Three phase DG currents in case 1.

7.4.2. Case 2: During Moderate Voltage Sag

The voltage sag is created in this study by connecting the various single phase loads during different time intervals at different load buses. A 50Ω , 25Ω , 50Ω , 60Ω , 35Ω and 75Ω single phase loads are connected to the load buses i , j , k , l , m and n respectively from 2s to 5s. The positive sequence voltages at the terminals of the DGs which are connected to the load buses j , m , i and n after 5s are observed as 0.91 p.u, 0.88 p.u, 0.89p.u and 0.88 p.u respectively and the maximum voltage unbalance at the load buses observed as 32.5%. Here, in this case the PCC voltages of the DGs are less than the 0.92 p.u. and therefore, priority has been given to the supply of the reactive power. The unbalance compensation is prioritized by adding the constraint that VUF at each bus should be less than 10%. The compensation control strategy is started at 5.5s and all the DGs are injecting the maximum amount of reactive power. Hence, the positive sequence voltages at the DG terminals are raised as tabulated in Table 7.3 which can also be observed from Fig. 7.9. Fig. 7.10 shows that the VUF is reduced to below 10% at 5.5s at all the load buses. Since all the DGs are supplying the reactive power at full capacity and also the majority of the DG capacity is utilized for the unbalance compensation, the DGs had to curtail the production of the active power to maintain the DG phase currents within the limits. From Fig. 7.11 it is visible that the active power is curtailed at 5.5s and the reactive power injected by the DGs is shown in Fig. 7.12. The DG currents are within the safety limit as given in Fig.7.13. To test the robustness of the proposed control strategy it is assumed that at 6.5s the single phase loads which are connected to the load buses m and n are removed. The central control sends the

updated references to each DG and it can be seen that the positive sequence voltages at the terminals of the DGs have been raised above 1 p.u after 6.5s as shown in Fig 7.9. Since two unbalanced loads are removed, the DGs have extra capacity and therefore, the active power injection of the DGs is enhanced after 7s as shown in the Fig. 7.11. Again, another single phase load at bus k is removed at 7s and the control technique updates the references to the DGs. It can be seen from the results that the DGs are able to support the positive sequence voltage and unbalance compensation fully and also the active power injection of the DGs is restored to full capacity. The detailed VUF at each load bus during each step has been tabulated in Table 7.2. The DG phase currents are shown in Fig.7.13 and it can be observed that all the phase currents are well within the safety limit.

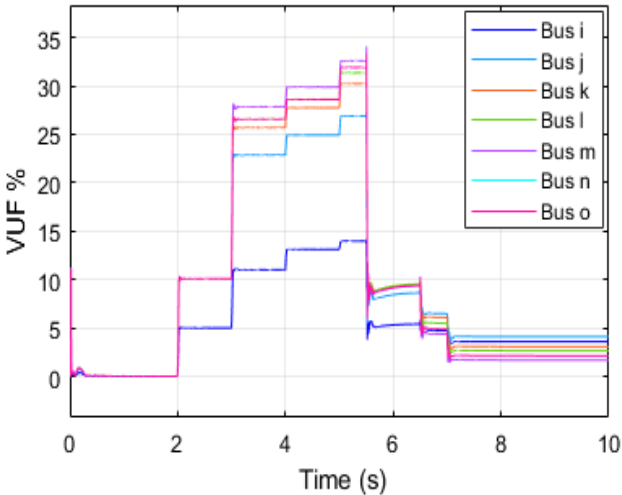


Fig. 7.9. Positive sequence voltages at the terminals of the DGs for case 2.

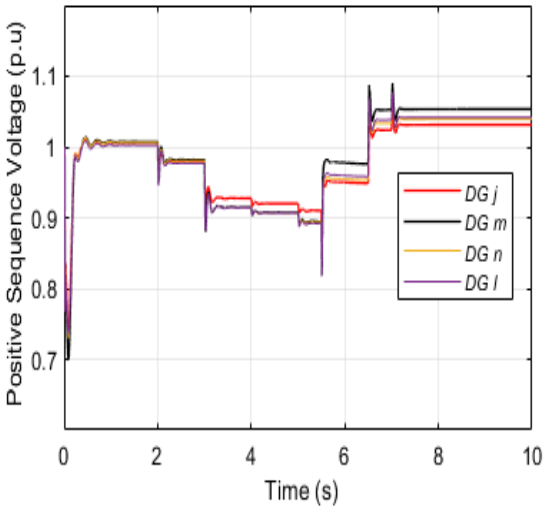


Fig. 7.10. VUF at each load bus in case 2.

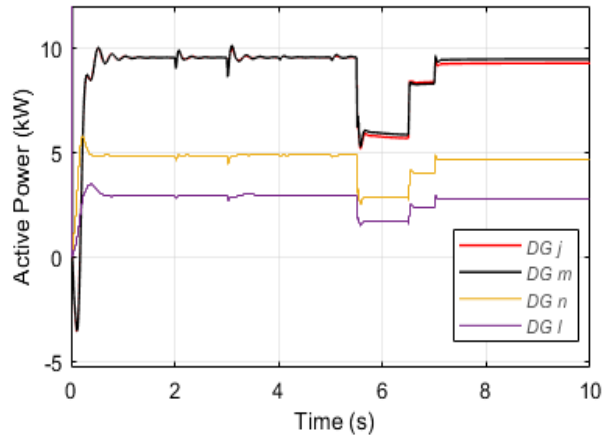


Fig. 7.11. Active power output of the DGs in case 2.

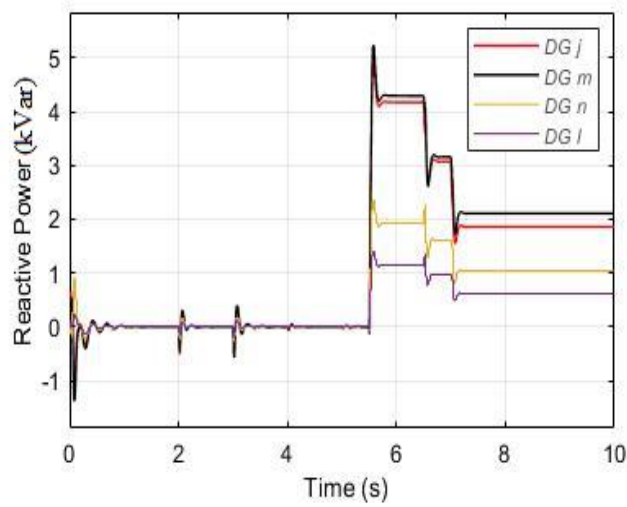


Fig. 7.12. Reactive power output of the DGs in case 2.

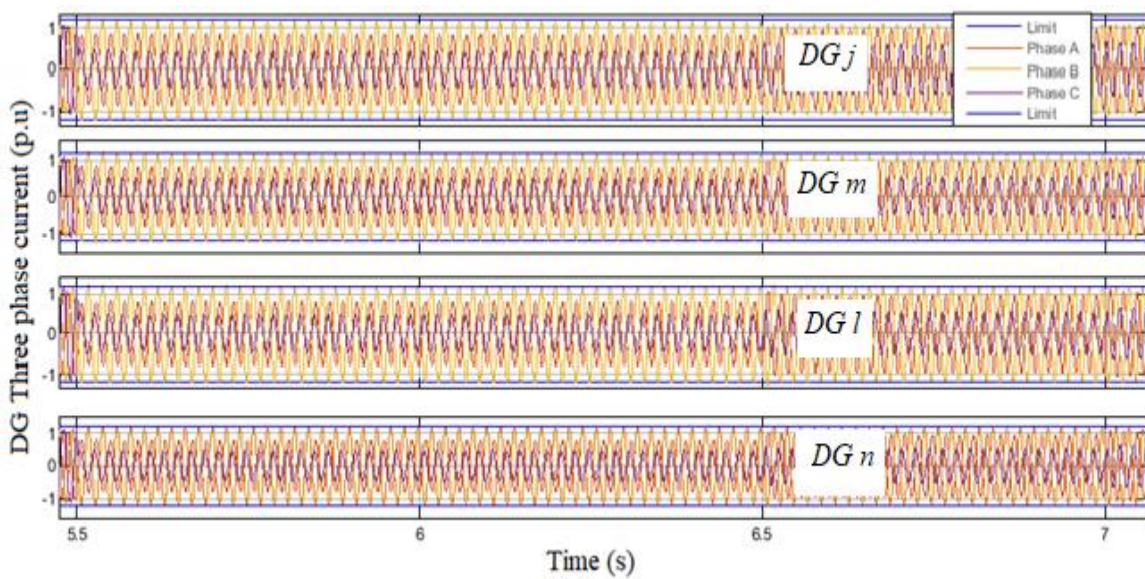


Fig. 7.13. Three phase DG currents in case 2.

7.4.3. Case 3: Under Grid Imbalance

The proposed control strategy has been evaluated under grid imbalance to ensure its effectiveness. An unsymmetrical fault has been created at 2s near to the grid to create the grid imbalance as a result of which VUF at the grid becomes 24% and it is observed that the positive sequence voltage at the DG connected buses are dropped below 0.9 p.u. The control strategy is started at 3.5s and all the DGs start injecting reactive power. It can be observed from Table 7.3 that the positive sequence voltage of each DG has been raised to near the nominal voltage. The reactive power sharing of each DG is shown in Fig. 7.14. Simultaneously, as shown in the Fig. 7.15, the VUF at each load bus is reduced after 3.5s since all the DGs start to supply the negative sequence quantities. Since the DGs are prioritized to inject the reactive power at full capacity and unbalance compensation, the active power injection of the DGs has been curtailed as shown in Fig. 7.16 to operate the DG under safety mode. In this case the fault persists till 10s. To validate the real time application of the proposed approach, this case study has been implemented in OPAL-RT with RT lab version 19.3.0.228 and RTS OP5600 chassis. The observed grid voltage in DSO from OPAL-RT is shown in Fig. 7.17, from which it can be observed that due to fault, the grid voltage remains imbalanced (till 3.5s) as during this time no compensation is provided and after the DGs start the compensation, the imbalance is reduced. All the phase currents of the DGs are maintained within the safety limit. The positive sequence voltage in DSO under this case study is presented in Fig. 7.18.

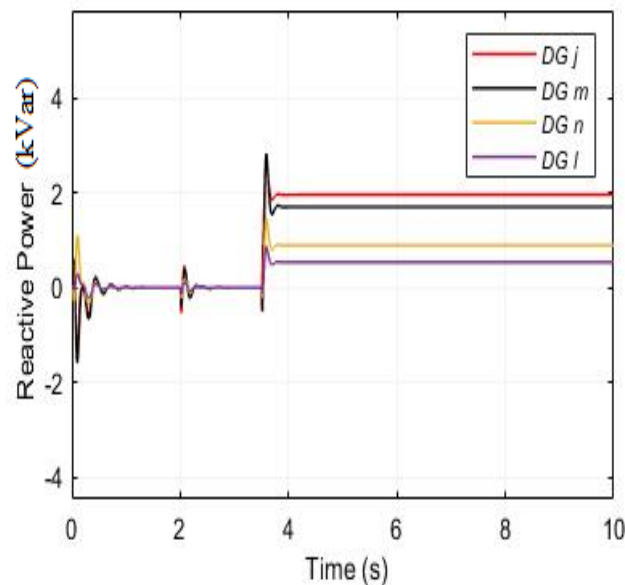


Fig. 7.14. Reactive power output of the DGs under case 3.

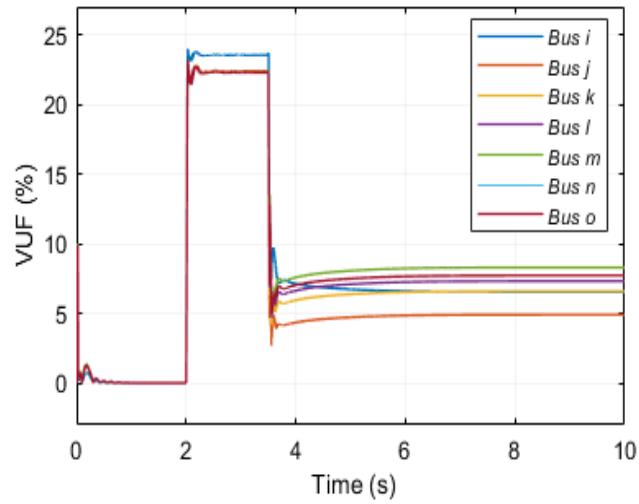


Fig. 7.15. VUF at each load bus in case 3.

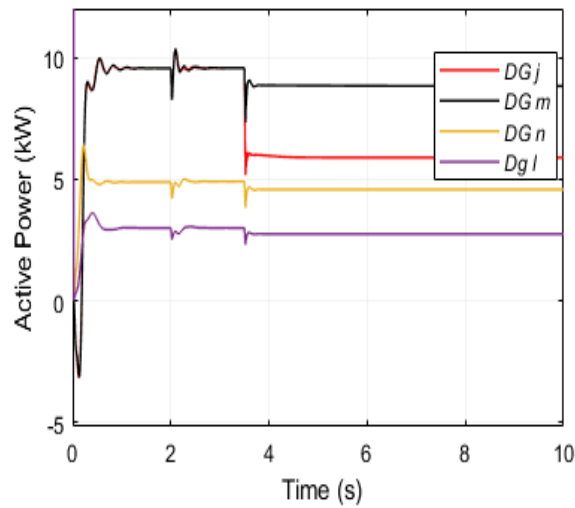


Fig. 7.16. Active power output of the DGs under case 3.

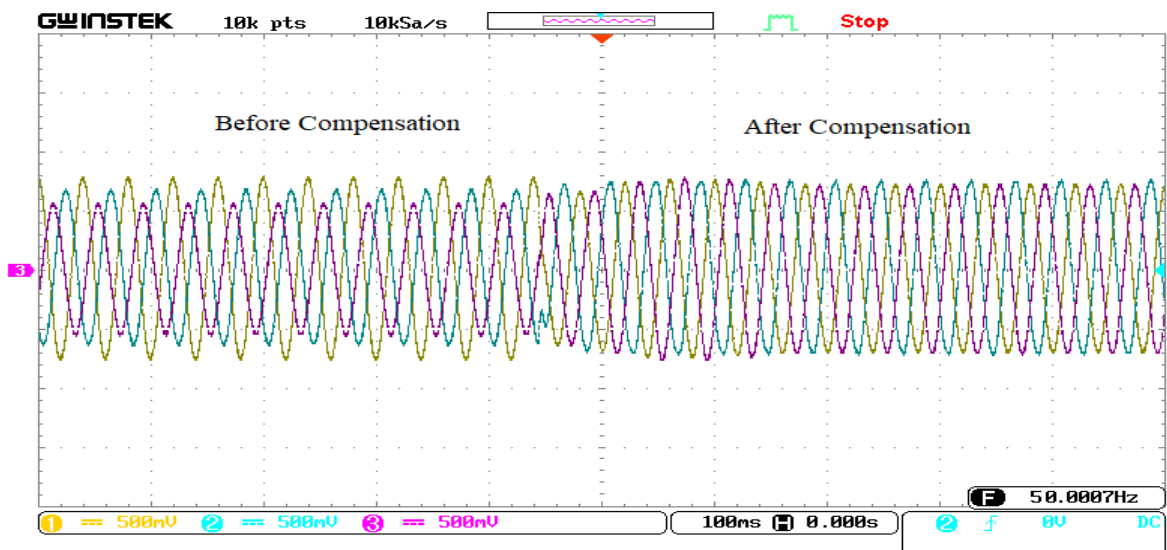


Fig. 7.17. Three phase grid voltages from RTDS under case 3.

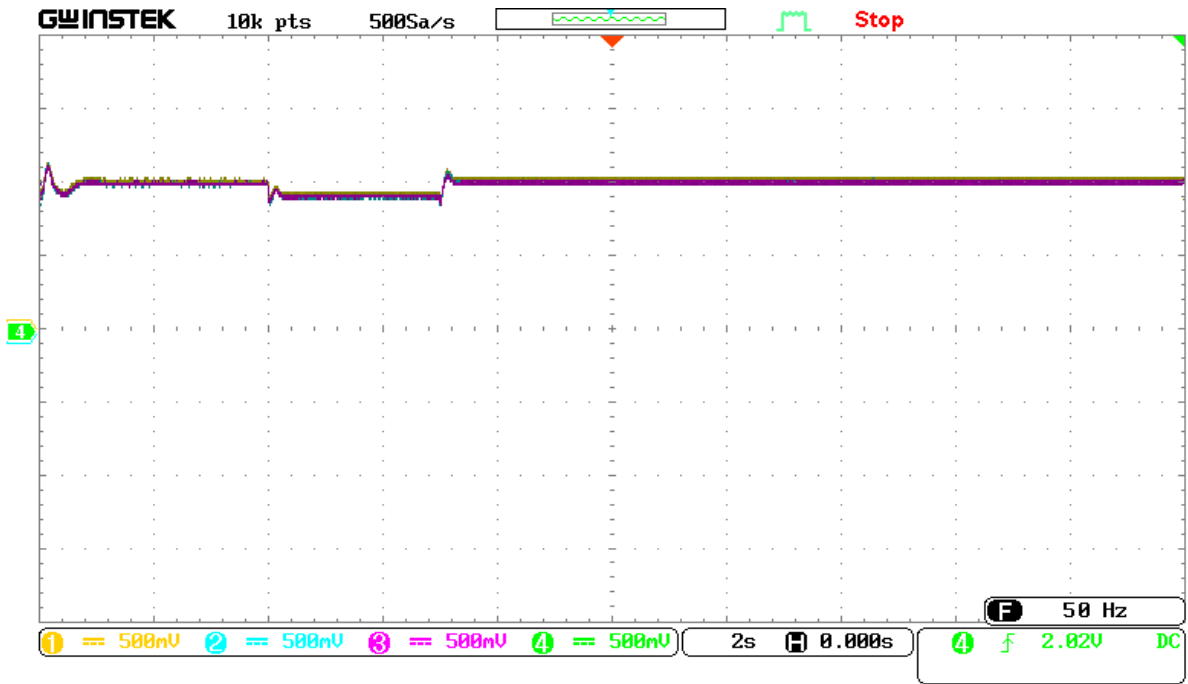


Fig. 7.18. Positive sequence voltage at the terminals of the DGs in case 3 from RTDS.

Table 7.2. VUF at the buses

Load Buses	Case 1		Case 2			Case 3	Case 4	Case 5
	VUF (%)		VUF (%)			VUF (%)	VUF (%)	VUF (%)
	After 4.5s	After 5s	After 5.5s	After 6.5s	After 7s	After 3.5s	After 4.5s	After 4.5s
<i>i</i>	1.1	1.8	5.2	4.7	3.5	6.6	1.7	2.7
<i>j</i>	1.1	2.7	8.5	6.4	4	4.9	2.3	4.4
<i>k</i>	0.8	3.1	9.4	6	3	6.6	2.7	4.9
<i>l</i>	0.7	3.2	9.4	5.5	2.5	7.4	2.8	5
<i>m</i>	1.1	3.4	9.2	4.3	1.6	8.3	4	6.1
<i>n</i>	0.3	3.38	9.2	4.9	2.1	7.6	2.4	4.6
<i>o</i>	0.3	3.38	9.2	4.9	2.1	7.6	2.4	4.6

Table 7.3. Positive sequence voltages (V^+) at the terminals of the DGs

DGs	Case 1		Case 2			Case 3	Case 4	Case 5
	V^+ (p.u)		V^+ (p.u)			V^+ (p.u)	V^+ (p.u)	V^+ (p.u)
	After 4.5s	After 5s	After 5.5s	After 6.5s	After 7s	After 3.5s	After 4.5s	After 4.5s
DG_j	1.03	1.021	0.98	1.03	1.031	0.982	1.018	1.017
DG_m	1.045	1.031	0.98	1.05	1.05	1.002	1.014	1.013
DG_n	1.04	1.026	0.965	1.04	1.041	0.994	1.017	1.016
DG_i	1.04	1.025	0.96	1.038	1.039	0.994	1.018	1.017

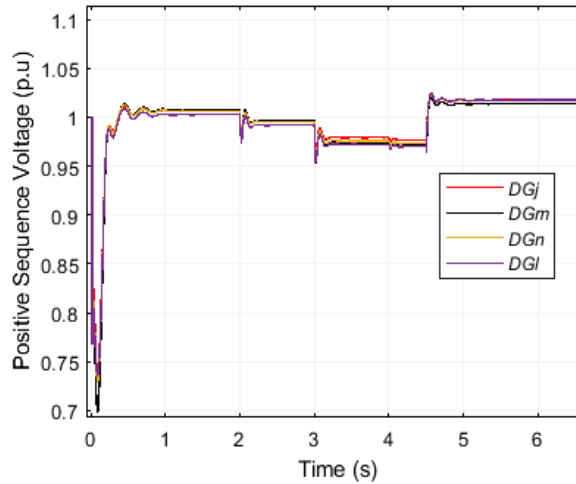


Fig. 7.19. Positive sequence voltage of DG terminals in case 4.

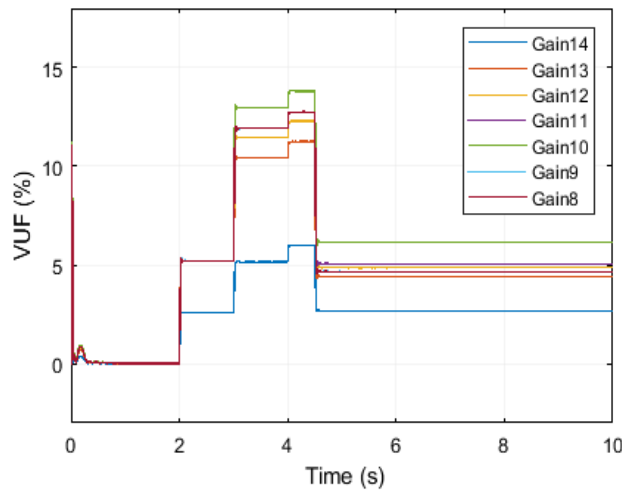


Fig. 7.20. VUF at each load bus in case 4.

7.4.4. Case 4: DG Unavailability

In this case study the proposed control strategy is tested under the condition of DG unavailability. It is assumed that DG_m cannot participate in the compensation control. Initially, the central control gets the signal from the local control about the unavailability of the DG and the control system considers the remaining DGs for the compensation control. The loads are considered same as in case 1 till 4s and at 4.5s the compensation control has been initiated. From Table 7.3, it is evident that the positive sequence voltages at terminals of the DGs have been raised near to the nominal voltage. Here, it is noteworthy to mention that even though DG_m is not supplying any reactive power, the positive sequence voltage at this particular bus is also raised near to the nominal voltage since all the other three DGs are supplying sufficient reactive power which affects the voltage at the terminals of DG_m as shown in Fig. 7.19. Further, the VUF

at each load bus is tabulated in Table 7.2 and also shown in Fig. 7.20. From Table 7.2 it is revealed that the VUF at every load bus is slightly higher compared to the VUF in case 1 because in this case the compensation is done only by the three DGs since only three DGs are available for compensation. All the DGs in this case study are delivering the maximum amount of active power and also it is observed that the compensating DGs output current in all phases is well within the safety limit.

7.4.5. Case 5: Communication Failure

The communication between the local control and the central control plays an important role in the control strategy. It is possible that there might be a communication problem between the local control and the central control and to illustrate this scenario in this case study it is assumed that initially all the DGs are available for the compensation control. The central control sends the optimal references to all the four DGs, but due to the communication failure DG_m could not receive the optimal references. The single phase loads are considered as same as case 1 till 4s. At 4.5s the control strategy started to work and three DGs participated in the compensation process and one DG only supplying the active power since it did not receive the references. In Table 7.2 the VUF information at each load bus is tabulated which is also shown in Fig.7.21. It can be seen that VUF is more at the load buses compared to case 4 because in this case only three DGs are participated in the compensation control even though the central control sent the references for all the four DGs. The positive sequence voltage at the DG terminals is well supported up to the nominal voltage as shown in the Fig. 7.22.

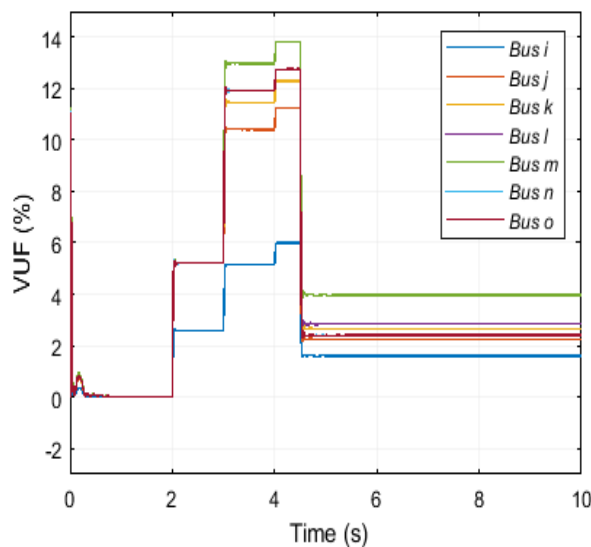


Fig. 7.21.VUF at each load bus in case 5.

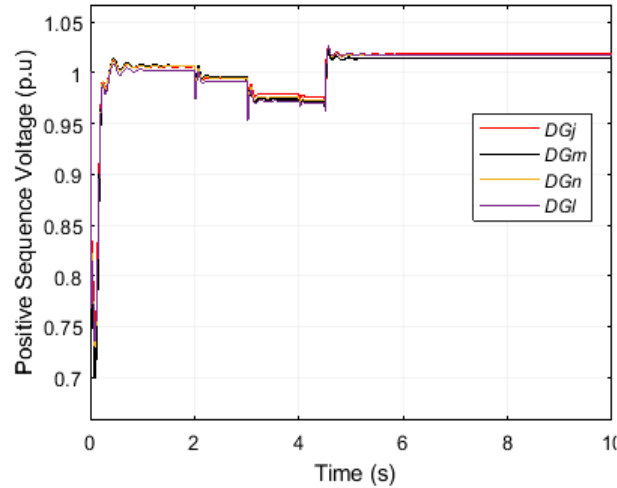


Fig. 7.22. Positive sequence voltage at the terminals of the DGs in case 5.

7.5. Comparative Assessment

To highlight the robustness of the proposed approach, comparative study has been conducted with the recently proposed methods in the literature. In this study, a flexible multi-objective control strategy for the IIDG based microgrid is implemented which can support the positive sequence voltage at the DG terminals, provides unbalance voltage compensation and maximize the active power whereas in [108] and [104] only the unbalance voltage compensation has been considered. In the proposed approach the positive sequence voltage has been supported near to the nominal voltage during voltage sags. In this study, the developed method is able to compensate moderate voltage sags whereas in [104] only small voltage sags have been mitigated. The method proposed in [104] injects constant amount of active power and therefore, these approaches cannot adjust the active power injection depending on the requirement whereas the proposed method is able to prioritize and curtail the active power production of the DGs depending on the situation. Moreover, the unbalance compensation control in the proposed method does not depend on the type of the unbalance and it works satisfactorily during grid imbalances which has not been considered in [104] and [108]. The proposed method only utilizes the local data of the measured voltage and current for the control strategy whereas ref. [108] requires data from multiple agents and from multiple microgrids which increases the chances of malfunctions. The communication between the microgrids plays an important role in the control strategy. The failure of communication link which may cause severe disturbance in the system performance has not been considered in [108] whereas the authors in the proposed method investigated the effect of communication link failure on the performance of the algorithm and obtained satisfactory results.

7.6. Conclusion

This work presents a flexible multi-objective control strategy for microgrid to simultaneously support the positive sequence voltage and compensate the voltage unbalance at the load buses. By supplying the reactive power from the DGs the proposed approach is able to support the positive sequence voltage at all PCC near to the nominal voltage and it is also capable of compensating the voltage unbalance at the load buses as much as possible maintaining the DG phase currents within the safety limit. Moreover, the control strategy used in this study is able to prioritize the active power injection when the voltage is near to its nominal value and adjusts the negative and positive sequence components to mitigate voltage sag and voltage unbalance. The grid operator can maintain customized voltage profile at different load buses using this flexible control strategy. The robustness of the proposed technique is tested during the grid imbalances and other diverse conditions. The simulation results show that the performance of the proposed approach is satisfactory. The test results from the hardware-in-the-loop environment establish that the scheme is suitable for execution in real time.

CHAPTER 8

Conclusions

8.1. Conclusions

The rapid enhancement of the load demand and the depletion of the fossil fuels increase the dependency on the renewable based power generation. The intermittent and variable nature of the RE sources make the consistency of power generation vulnerable. Therefore, individually these RE sources are not able to serve the load effectively. Hence, two or more RE sources are grouped together to form a microgrid to deliver more reliable power supply to the load. By integrating the microgrid system to the utility grid, the stability of the microgrid increases because the utility grid acts as a backup. The modelling of these hybrid systems is complicated because of the varying nature of the renewable. Hence, a proper algorithm is essential to select the accurate optimal sizes of the DGs in a microgrid system.

The probability density functions are well known for characterizing the stochastic nature of the renewables. Different PDFs are tested to characterize the stochastic nature of the renewables and based on the analysis Weibull PDF and Normal PDF are used in this study. A multi- objective artificial cooperative search algorithm is developed to solve the conflicting objectives in this study to obtain the optimal microgrid system. Later a typical monthly based probabilistic power dispatch strategy is implemented to achieve the reliable and cost effective grid connected microgrid system. The obtained results proved that the proposed method performs better compared to the standard deterministic method.

Secondly, the fault detection in the microgrid is complex especially in the presence of the IIDGs because the fault currents of the IIDGs are very small. Therefore, conventional protection schemes are incapable to protect the IIDG based microgrid. In this study a novel fault detection scheme is developed based on the phase change in the positive sequence current. The proposed method detects all types of faults and does not depend on the fault resistances. Moreover, the algorithm is tested under practical scenarios such as different load power factors in each case and the performance of the algorithm is satisfactory.

The identification of the islanding of the DGs is more important in the microgrid system, failure of such incidents causes severe problems. In this work a new islanding technique is proposed based on the Lissajous figure. The Lissajous figure is drawn between the voltage and

current signals at each breaker and based on the change in the area of the Lissajous figure the islanding has been detected. The proposed algorithm shows satisfactory results under different microgrid islanding conditions and also it is able to differentiate the islanding and other transient conditions. The proposed method shows satisfactory results in HIL testing and therefore, it is suitable for real time applications.

Finally, the presence of unbalanced loads in the microgrid creates several voltage quality issues such as positive sequence voltage drop, unbalanced voltage, etc. In the first stage pareto optimization based voltage unbalance compensation is developed for the multi-bus microgrid, where the voltage quality at each load bus can be customized according to the requirement. The proposed control technique is able to reduce the voltage unbalance factor as per the requirement at every load bus without violating the DG phase current limits. Different case studies are performed under diverse conditions and the performance of the proposed method is satisfactory. Later a two stage multi-objective control strategy is developed to handle the multiple objectives (positive sequence voltage support, unbalance voltage compensation, flexible active power control and DG phase current limitation) simultaneously. The proposed control strategy is able to prioritize the objectives based on the requirement and also able to adjust the compensation references. Hence, the over current problem is avoided in the DGs. The method is tested under diverse operating conditions and verified in HIL testing platform. The results indicate that the performance of the proposed technique is satisfactory.

8.2. Future Scope

In recent years, the consumers and the industries are moving towards electric vehicles (EVs). This mass penetration of the EVs means that it requires more power from the utilities in order to manage the load demand. Moreover, it requires tremendous amount of infrastructure related to the charging stations for the EVs. Therefore, now the pressure is on the utilities and developers to handle the power consumption caused by this rapid enhancement in the EVs. Hence, to handle this challenge, instead of totally relying on the utilities, the EV drivers have to go for the alternative sources such as renewable based microgrids to charge their batteries. As a future scope of this research new control strategies will be developed to provide the EV charging stations in the microgrid and also to tackle the power quality issues raised because of the penetration of the EV charging stations.

Moreover, smart grids nowadays have become prone to cyber-attacks which adversely affect its security and reliability. To ensure cyber-security, bad data detection and elimination is essential in the protection algorithms. In future cyber-security can be considered to develop the protection algorithms such as fault detection and islanding detection for the microgrid.

LIST OF FIGURES

Figure Number	Figure caption	Page Number
2.1	Grid Integrated Hybrid System	22
2.2	Predicted and Observed Solar Irradiance Distribution	23
2.3	Predicted and Observed Wind Speed Distribution	26
2.4	Flowchart for Operational Strategy	37
2.5	Flowchart for Application of MOACS for Optimal HRES System Design	40
2.6	Optimal Pareto Front for Scenario I	44
2.7	Optimal Pareto Front obtained for Scenario II	45
2.8	Distribution of Obtained C-Metrics for Scenario I by Box – Plot	49
2.9	Distribution of Obtained C-Metrics for Scenario II by Box-Plot	49
2.10	Box-Plot of Average Sp-Metric for Scenario I	49
2.11	Box-Plot of Average Sp-Metric for Scenario II	50
3.1	Optimal Pareto Front with MOACS for Scenario I	60
3.2	Optimal Pareto Front with MOACS for Scenario II	61
3.3	Convergence Characteristics with WSA in Both Scenarios	62
4.1	DG Voltage and Current Phasors (a) Voltage Coefficient Above 90%. (b) Voltage Coefficient between 50%-90%. (c) Voltage Coefficient Below 50%.	67
4.2	Grid Connected Microgrid Simplified Model	68
4.3	Positive Sequence Network When F1 Fault Occur in the Microgrid	69
4.4	Positive Sequence Current Phasors for Both DG Voltages > 0.9 (A) Bus A (B) Bus B (C) Bus C	71
4.5	Flowchart for Fault Detection in Microgrid for Both DG Voltages > 0.9	72

4.6	Positive Sequence Current Phasors for Both DG Voltages < 0.9	
	(a) Bus A	73
	(b) Bus B	
	(c) Bus C.	
4.7	Flowchart for Fault Detection in the Microgrid for Both DG Voltages < 0.9	74
4.8	Flowchart for Fault Detection in the Microgrid for One DG Voltage > 0.9 and Another DG Voltage < 0.9	75
5.1	Example of Lissajous Figure: (A) Voltage Signal, (B) Current Signal, (C) Lissajous Figure Corresponding to Voltage and Current Signal	87
5.2	Microgrid Test System	89
5.3	Proposed Islanding Detection Algorithm	89
5.4	Otsu Thresholding Analysis for PV	91
5.5	Lissajous Figures When Islanding Occurs At Different DGs:	92
	(A) Lissajous Figure at CB1	
	(B) Lissajous Figure at CB2	
	(C) Lissajous Figure at CB3	
5.6	<i>SI</i> Values When Islanding Occurs at Different DGs:	92
	(A) <i>SI</i> at CB1, (B) <i>SI</i> at CB2, (C) <i>SI</i> at CB3.	
5.7	<i>SI</i> Values under Multiple Islanding Condition:	93
	(A) <i>SI</i> at CB1, (B) <i>SI</i> at CB2, (C) <i>SI</i> at CB3	
5.8	Analysis of <i>SI</i> under NDZ Region:	94
	(A) <i>SI</i> at CB1, (B) <i>SI</i> at CB2, (C) <i>SI</i> at CB3	
5.9	Performance of the Proposed Algorithm under UL1741 Test Conditions:	95
	(A) <i>SI</i> at CB1, (B) <i>SI</i> at CB2, (C) <i>SI</i> at CB3	
5.10	Performance of <i>SI</i> Under Different Q_f :	96
	(A) <i>SI</i> at CB1, (B) <i>SI</i> at CB2, (C) <i>SI</i> at CB3	
5.11	Behavior of <i>SI</i> during Load Switching:	97
	(A) <i>SI</i> at CB1, (B) <i>SI</i> at CB2, (C) <i>SI</i> at CB3	
5.12	Lissajous Figure under Faults: (A) Lissajous Figure at CB1 (B) Lissajous Figure at CB2: (C) Lissajous Figure at CB3	98
5.13	Behaviour of <i>SI</i> under Different Types of Faults:	99
	(A) <i>SI</i> at CB1, (B) <i>SI</i> at CB2, (C) <i>SI</i> at CB3.	
5.14	Performance of the Proposed Approach under Sensing Errors:	99
	(A) Lissajous Curve at CB3 in Case 1	

	(B) Behavior of SI at CB3 in Case 1	
	(C) Lissajous Curve at CB1 in Case 2	
	(D) Behavior of SI at CB3 in Case 2	
5.15	HIL Testing Results of Islanding at CB1 under UL1741:	100
	(A) Measured Current Signal, (B) Measured Voltage Signal	
	(C) Lissajous Figure, (D) Similarity Index	
6.1	Proposed Control Scheme	108
6.2	Reactive Power Requirement	109
6.3	Overall Optimization Procedure	114
6.4	Low Voltage Microgrid Test System	116
6.5	Simplified Negative Sequence Network of the Test System	116
6.6	(A). VUF at Different Buses for Case (i).	119
	(B). Negative Sequence Bus Voltages at Different Buses for Case (i).	
6.7	(A). Positive Sequence Voltage at DG Terminals for Case (i)	120
	(B). Active Power Output at DG Terminals for Case (i).	120
6.8	(A). Three Phase DG Output Currents for Case (i)	120
	(B). Bus Voltages Before and After Compensation for Case (i)	121
6.9	Optimal Pareto Front	121
6.10	(A). Figure Simulation of Real Time Digital Simulator	122
	(B). OPAL RT Overall Set Up	123
6.11	Three Phase Load Bus Voltage at Bus I from RTDS for Case (ii)	123
6.12	VUF at Different Load Buses from RTDS for Case (ii)	124
6.13	(A). Three Phase DG Currents of DGs for Case (V)	125
	(B). Active Power Output Of DGs for Case (V).	126
6.14	(A). Three Phase Currents of the DGs for Case (Vii)	127
	(B). Active Power Output of the DGs for Case (Vii).	127
6.15	Convergence Characteristic of Objective Function with ACS	129
6.16	Negative Sequence Bus Voltages	131
6.17	DG _j Phase Currents	132
6.18	Convergence Characteristics with ACS Algorithm	132
7.1	Reactive Power Requirement to Support the Positive Sequence Voltage	138
7.2	Negative Sequence Equivalent of Bus K	139
7.3	Overall Control Structure of the Proposed Scheme	143
7.4	VUF at Each Load Bus in Case 1	146

7.5	Active Power Output of the DGs in Case 1	147
7.6	Positive Sequence Voltages at the Terminals of the DGs in Case 1	147
7.7	Reactive Power Output of the DGs in Case 1	147
7.8	Three Phase DG Currents in Case 1	148
7.9	Positive Sequence Voltages at the Terminals of the DGs in Case 2	149
7.10	VUF at Each Load Bus in Case 2	149
7.11	Active Power Output of the DGs in Case 2	150
7.12	Reactive Power Output of the DGs in Case 2	150
7.13	Three Phase DG Currents in Case 2	150
7.14	Reactive Power Output of the DGs under Case 3	151
7.15	VUF at Each Load Bus in Case 3	152
7.16	Active Power Output of the DGs under Case 3	152
7.17	Three Phase Grid Voltages from RTDS under Case 3	152
7.18	Positive Sequence Voltage at the Terminals of the DGs in Case 3 From RTDS	153
7.19	Positive Sequence Voltage of DG Terminals in Case 4	154
7.20	VUF at Each Load Bus in Case 4	154
7.21	VUF at Each Load Bus in Case 5	155
7.22	Positive Sequence Voltage at the Terminals of the DGs in Case 5	156

LIST OF TABLES

Table Number	Table caption	Page Number
2.1	Statistical Errors for Different Distribution Functions for Solar Irradiance	23
2.2	Solar Data Parameters from January to June	24
2.3	Solar Data Parameters from July to December	25
2.4	Statistical Errors for Different Distribution Functions for Wind Speeds	27
2.5	Wind Data Parameter from January to June	27
2.6	Wind Data Parameter from July to December	28
2.7	Load Data Parameters from January to June	30
2.8	Load Data Parameters from July to December	30
2.9	Component Specifications	43
2.10	Optimal sizes of the Hybrid System	46
2.11	ALCC of Hybrid System designed using MOACS pertaining to S - II	46
2.12	Energy Balance for Hybrid System	47
2.13	C-metric Results	50
2.14	Sp-metric Results	50
3.1	Obtained Optimal Sizes of the Proposed System	61
4.1	Phase Change of Positive Sequence Feeder Currents when both DG Voltages >0.9 (Load Pfs- Unity).	77
4.2	Phase Change of Positive Sequence Feeder Currents when both DG Voltages >0.9 (LD1-1 Pf, LD2- 0.95 Pf, LD3-0.9 Pf.	77
4.3	Phase Change of Positive Sequence Feeder Currents when both DG Voltages >0.9 (LD1-0.85 Pf, LD2-0.95 Pf, LD3-0.9 Pf)	78
4.4	Phase Change of Positive Sequence Feeder Currents when both DG Voltages <0.9 (Load Pf's- Unity)	79
4.5	Phase Change of Positive Sequence Feeder Currents when both DG Voltages <0.9 (LD1-1 Pf, LD2-0.95 Pf, LD3-0.9 Pf)	79
4.6	Phase Change of Positive Sequence Feeder Currents when both DG Voltages <0.9 (LD1-0.85 Pf, LD2-0.95 Pf, LD3-0.9 Pf)	79

4.7	Phase Change of Positive Sequence Feeder Currents when One DG Voltage <0.9 and other DG voltage >0.9 (load pfs- unity)	80
4.8	Phase Change of Positive Sequence Feeder Currents when One DG Voltage <0.9 and Other DG Voltage >0.9 (LD1-1 Pf, LD2- 0.95 Pf, LD3-0.9 Pf)	80
4.9	Phase Change of Positive Sequence Feeder Currents when One DG Voltage <0.9 and Other DG Voltage >0.9 (LD1-0.85 Pf, LD2- 0.95 Pf, LD3-0.9 Pf)	81
5.1	Statistical Errors for Different Distribution Functions	91
5.2	Switching and Faults	97
5.3	Comparative Assessment	101
6.1	VUF and Negative Sequence Voltages at Load Buses.	117
6.2	DG Positive Sequence Voltage and DG Current in p.u	118
6.3	Comparative Results of VUF and Negative Sequence Voltages at Load Buses	129
6.4	Comparative Results of DG Positive Sequence Voltage and DG Current	129
7.1	Feeder Line Data and Three Phase Load Data	146
7.2	VUF at the Buses	153
7.3	Positive Sequence Voltages (V^+) at the Terminals of the DGs	153

List of Publications

A. Journal

Published

- I. **Y. Pavankumar**, R. Kollu, and S. Debnath, “Multi-objective optimization of photovoltaic/ wind/ biomass/ battery-based grid-integrated hybrid renewable energy system,” *IET Renewable Power Generation*, Pp. 1528-1541, March 2021, DOI: 10.1049/rpg2.12131.
- II. **Y. Pavankumar**, S. Debnath and S. Paul, “Microgrid fault detection technique using phase change of positive sequence current,” *International Journal of Modelling and Simulation*, Volume 43, Issue 3, Pp. 171-184, 2023, DOI: 10.1080/02286203.2022.2059613.
- III. **Y. Pavankumar**, S. Debnath, and S. Paul, “Multi-objective pareto optimal unbalance voltage compensation in the microgrid,” *Electric Power Systems Research*, 217 (2023) 109104, DOI: 10.1016/j.epsr.2022.109104.
- IV. **Y. Pavankumar**, S. Debnath, and S. Paul, “A New Lissajous-Based Technique for Islanding Detection in Microgrid,” *IEEE Transactions on Smart Grid*, DOI: 10.1109/TSG.2023.3322435.

Communicated

- Y. Pavankumar**, S. Debnath, and S. Paul, “An optimization based flexible multi-objective control strategy for grid integrated microgrid system,” *Electrical Engineering*, Springer.

B. Conference

- I. **Y. Pavankumar**, R. Kollu, S. Debnath, and S. Paul, “A multi objective approach for optimal design of solar/ wind/ biomass/ battery-based grid connected microgrid system,” *2022 International Conference on Intelligent Controller and Computing for Smart Power (ICICCSP), Hyderabad, India, 2022, pp. 1-6, doi: 10.1109/ICICCSP53532.2022.9862483.*
- II. **Y. Pavankumar**, S. Debnath, and S. Paul, “Optimization based voltage unbalance compensation in the microgrid,” *2023 9th International Conference on Electrical Energy Systems (ICEES), Chennai, India, 2023, pp. 630-634, doi: 10.1109/ICEES57979.2023.10110127.*

NOMENCLATURE

f_{pv}	Derating Factor
ff	Fill Factor
V_{oc}	Open Circuit Voltage
I_{sc}	Short Circuit Current
K_i, K_v	Temperature Coefficients of Current and Voltage
K^t, C^t	Shape and Scale Parameters
V_r, V_{ci}, V_{co}	Rated, Cut-in, and Cut-out Velocities
η_{mppt}	Mppt Factor
CV_{bm}	Biomass Calorific Value
μ	Expectation or Mean
C_{bio}, C_{inv}	Total Annualised Cost of Biomass Gasifier and Power Inverter
σ^2	Variance
C_{bat}	Nominal Battery Capacity (Ah)
Δt	Time Step (Equal to 1)
Sdr	Self-Discharge Rate
η_c	Efficiency Factor
SOC	State of Charge
$P_l(l_{st}^t)$	Probability of Load Demand of A Given State During any Time Frame 't'
S_{stc}	Irradiance at STC (Standard Test Condition)
$P_t^{supplied}$	Power Supplied to the Load by the Grid Integrated HRES in Time Frame 't'
C_x^{asg}, C_x^{arp}	Annualised Salvage Cost and Replacement Cost of A Particular Component.
C_x^{rp}	Replacement Cost of A Particular Component
$P_{gp}(t)$	Power Purchased from Grid in Time Frame 't'
$P_{gs}(t)$	Power Pumped into the Grid in Time Frame 't'
N_x	Number of Units of A Particular Component
P_t^{need}	Power Required by the Load in Time Frame 't'
η_{re}, η_{inv}	Rectifier and Inverter Efficiencies.
N_s, N_v, N_l	Total Number of Solar Irradiance States, Wind Speed States, and Load States
a, b, I_{10}	Working Condition Parameters of the Battery
m	Number of Objectives

N_{bio}	Number of Biomass Gasifiers
N_{pv}, N_w	Number of PV Modules and Wind Turbines
f, i	Inflation and Interest Rate
C_g^p	Unit Cost Price of Purchased Energy From Grid
C_g^s	Unit Cost Price of Sold Energy to Grid
n	Planning Period or Total Life Time of the Project
Nb_{se}	Number of Series Connected Batteries
Nb_{st}	Number of Shunt Paths
t	Time Segment
st	State
$P_{bat_d_max}(t)$	Maximum Power Delivered by Battery Bank in Time Frame 't'
P_{bio}	Power Generated by Biomass Gasifier.
t_w	Biomass Gasifier Working Hours Per Annum
t_{bio}	Biomass Gasifier Working Hours Per Day
p_{rw}	Rated Power of Wind Turbine
C_{gs}	Total Cost of Energy Sold to the Grid
C_{gp}	Total Cost of Energy Purchased From the Grid
C_{pv}, C_{wt}, C_b	Total Annualized Cost of Entire PV Panels, Wind Turbines and Batteries
T_{stc}	PV Module Temperature at STC
$S_{st}^t, V_{st}^t, I_{st}^t$	Solar Irradiance, Wind Speed and Load Demand in St^{th} State for A Given Time Frame 't'
C_x^{acap}, C_x^{am}	Annualized Capital Cost and Maintenance Cost of A Particular Component
C_x^{asg}	Present Value of Salvage Cost of A Component
σ	Standard Deviation
P_{dump}	Dump Power
C_x^m	Total Maintenance Cost of Single Unit
$I_{bat}(t)$	Charging Current Of Battery in Time Fame 't'
V_{bat}	Terminal Voltage of the Battery
$P_{bat_c_max}(t)$	Maximum Power can be Stored in the Battery in a Time Frame 't'
d	Mean of All d_i
P_{ref}	Reference Value of Active Power
Q_{ref}	Reference Value of Reactive Power
I_{max}	Maximum Reference Current
R_F	Fault Resistance
I_d	Active Fault Current Output
$\Delta \dot{V}_F$	Fault Point Positive Additional Source
I_q	Reactive Fault Current Output

$V_{d,f}$	Positive Sequence Fault Voltage Of DG
V_d	D-Axis Voltage at the GCP
$Z_{L1}-Z_{L3},$ Z_{AF}, Z_{FB}, Z_S	Equivalent Positive Sequence Feeder Impedances
DG_1, DG_2	Distributed Generators
$Load1-$ $Load3$	Loads
L_1-L_8	Feeders
A_1-A_4, B_1- $B_3, C_1-C_3,$	Circuit Breakers
t_1, t_2	Threshold Values of Phase Angles
\emptyset	Phase Difference Between V_{dgf} and V_{DG}
φ	Phase Difference Between $V_{DG.F}$ and I_{dgf}
$\Delta \dot{V}_A - \Delta \dot{V}_c$	Fault Components of Positive Sequence Bus Voltages
U_n	Voltage Coefficient
V_n	Rated Voltage
V_{DG}, I_{DG}	Phasors of Pre Fault Voltage and Currents of DGs
$V_{DG,f}, I_{DG,f}$	Phasors of Post Fault Voltage and Currents of DGs
$I_{A2} - I_{A4},$ $I_{B2} - I_{B3}$ $I_{C2} - I_{C3}$	Positive Sequence Pre Fault Feeder Currents
$I_{A2,f} - I_{A4,f}$ $I_{B2,f} - I_{B3,f}$ $I_{C2,f} - I_{C3,f}$	Positive Sequence Post Fault Feeder Currents
I_r	Rated Current
$\dot{V}_A - \dot{V}_c$	Positive Sequence Bus Voltages
θ	Phase Difference Between $I_{DG.F}$ and I_{DG}
$\Delta \dot{I}_1, \Delta \dot{I}_2$	Fault Current Components of DG1 and DG2
$\Delta \dot{I}_{A1} - \Delta \dot{I}_{A3},$ $\Delta \dot{I}_{C1} - \Delta \dot{I}_{C3},$ $\Delta \dot{I}_{B1} - \Delta \dot{I}_{B3}.$	Fault Components of Positive Sequence Currents at Bus A, Bus B and Bus C
st	represents the present state
$st+1$	represents the upcoming state
$st-1$	represents the previous state

REFERENCES

- [1] Mehdi Foumani, Kate Smith-Miles.: ‘The impact of various carbon reduction policies on green flowshop scheduling, *Applied Energy*,2019,249,Pages 300-315.
- [2] P.Suhane., S. Rangnekar., A. Mittal., et al.: ‘Sizing and performance analysis of standalone wind-photovoltaic based hybrid energy system using ant colony optimisation,*IET Renewable Power generation*, 2016, 10, (7), pp. 964972.
- [3] R.Belfkira., Lu Zhang., G. Barakat.: ‘Optimal sizing stu-dy of hybrid wind/PV/diesel power generation unit, *Solar Energy*, 2011, 85, (1), pp .100110.
- [4] D. Abbes., A. Martinez., G. Champenois.: ‘Eco-design optimisation of an autonomous hybrid wind-photovoltaic system with battery storage, *IET Renewable Power Generation*, 2012, 6, (5), pp. 358-371.
- [5] Masoud Sharafi., Tarek Y., EL Mekkawy.: ‘Multi-objective optimal design of hybrid renewable energy systems using PSO-simulation based approach, *Renewable Energy*,2014, 68, Pages 67-79.
- [6] P. Balamurugan., S. Ashok., T. L Jose.: ‘ Optimal operation of Biomass/Wind/PV Hybrid Energy System for Rural Areas, *International Journal of Green Energy*,2009, 6, (1), pp.104116.
- [7] A. Kyritsis., D.Voglitsis., N. Papanikolaou., et al.: ‘Evolution of PV systems in Greece and review of applicable solutions for higher penetration levels, *Renewable Energy* , 2017, 109, pages 487-499.
- [8] J. Cao., W.Du., H.Wang., et al.: ‘Optimal Sizing and control Strategies for Hybrid Storage sytem, as Limited by Grid Frequency Deviations, *IEEE Transactions on Power Systems*, 2018, 33, (5), pp.54865495.
- [9] S.Thapa.,R. Karki.: ‘Reliability benefit of energy storage in wind integrated power system operation, *IET Genera- tion, Transmission& Distribution*, 2016, 10, (3), pp. 807-814.
- [10] M. Khalid., A.V. Savkin.: ‘ A model predictive control approach to the problem of wind power smoothing with controlled battery storage, *Renewable Energy*, 2010, 35, (7), pp.1520-1526.
- [11] Palo Alto., CA., U.S. Department of Energy.: ‘wind applications for benefit-cost assessment, in EPRI-.’Handbook Supplement of Energy Storage for Grid Connected Wind Generation Applications’ (Washington, DC: 2004), pp.3-9.

- [12] M. Xu., L. Wu., H. Liu., et al.: ‘Multi-objective optimal scheduling strategy for wind power, PV and pumped storage plant in VSC-HVDC grid, *The Journal of Engineering*, 2019, 1, (16), pp.3017-3021.
- [13] K.Basaran., N. S.Cetin., S. Borekci.: ‘Energy management for on-grid and off-grid wind/PV and battery hybrid systems, *IET Renewable Power Generation*, 2017, 11, (5),pp. 642-649.
- [14] K.S.El-Bidairi., H.D.Nguyen., et al.: ‘Multi objective intelligent Energy Management Optimization for Grid connected Microgrids, Palermo, 2018,pp 1-6.
- [15] U.B.Tayab., F. Yang.: ‘Energy Management System for a Grid-Connected Microgrid With PV and Battery Energy Storage system, *Australian & New Zealand Control Conference (ANZCC)*, Melbourne, VIC, 2018, pp.141-144.
- [16] A. Elgammal., M. El-Naggar.: ‘Energy management in smart grids for the integration of hybrid wind-PV-FC- battery renewable energy resources using multi-objective objective Particle Swarm Optimization, *The Journal of Engineering*, 2018, 11, pp.18061806-1816.
- [17] S.Singhand., S.C.Kaushik.: ‘Optimal sizing of grid integrated hybrid PV-biomass energy system using artificial bee colony algorithm, *IET Renewable Power Generation*, 2016, 10, (5), pp. 642-650.
- [18] U.Akram., M. Khalid., S. Shafiq.: ‘Optimal sizing of a wind/solar/battery hybrid grid-connected microgrid system, *IET Renewable Power Generation*, 2017,12, (1), pp. 72-80.
- [19] H.g. Yang., L Lu., W Zhou.: ‘A novel optimization sizing model for hybrid solar-wind power generation system, *Solar Energy*, 2007, 81,(1), pp. 7684.
- [20] Janardhan., Kavali.,Srivastava., et al.: ‘Hybrid PV And Biomass System For Rural Electrification, *International Journal of ChemTech Research*, 2013, 5, pp.802-810.
- [21] K. Ravindra., R. SrinivasaRao, et al.: ‘Wind distribution analysis incorporating Artificial Bee Colony Algorithm, *International Conference on Advances in Power Conversion and Energy Technologies (APCET)*, 2012,pp.1-6.
- [22] Kollu,R., Rayapudi, S.R., et al.: ‘ Mixture probability distribution functions to model wind speed, *Int J Energy Environ Eng*, 2012, **3**, (27), pp.2251-6832-3-27.
- [23] D. Villanueva., J. L. Pazos., A. Feijoo.: ‘Probabilistic Load Flow Including Wind Power Generation, *IEEE Transactions on Power Systems*, 2011, 26, (3), pp. 1659-1667.
- [24] Tina, G., Gagliano, S., Raiti, S.: ‘Hybrid solar/ wind power system probabilistic modelling for long-term performance assessment, *Solar energy*, 2006, 80,(5), pp.578-588.

- [25] Juan M., Lujano-Rojas., et al.: ‘probabilistic modelling and analysis of standalone hybrid power systems, *Energy*, 2013, 63, pp. 19-27.
- [26] G M Tina., S Gagliano.: ‘ Probabilistic modelling of hybrid solar/wind power system with solar tracking system, *Renewable Energy*, 2011, 36, (6), pp. 1719-1727.
- [27] Hong xing Yang, Wei Zhou, Lin Lu, Zhaohong Fang. : ‘Optimal sizing method for stand-alone hybrid solar–wind system with LPSP technology by using genetic algorithm, *Solar Energy*, 2008, 82(4), pp. 354-367.
- [28] Carlos Eduardo Camargo Nogueira, Magno Luiz Vidotto, et al.: ‘Sizing and simulation of a photovoltaic-wind energy system using batteries, applied for a small rural property located in the south of Brazil, *Renewable and Sustainable Energy Reviews*, 2014, 29, pp. 151-157.
- [29] Zitzler., Eckart, Kalyanmoy Deb., Lothar Thiele.: ‘Comparison of multi objective evolutionary algorithms: Empirical results, *Evolutionary computation* , 2000, pp. 173-195.
- [30] Nekooei., Komai., et al.: ‘An improved multi-objective harrmony search for optimal placement of DGs in distribution systems, *IEEE Trans on smart grid*, 2013, 4, (1), pp. 557-567.
- [31] B. J. Brearley and R. R. Prabu. A review on issues and approaches for microgrid protection. *Renew. Sustain. Energy Rev.*, vol. 67;2017. pp. 988–997.
- [32] D. A. Gadanayak. Protection algorithms of microgrids with inverter interfaced distributed generation units—A review. *Electr. Power Syst. Res.*, vol. 192, no. November 2020, p. 106986.
- [33] P. Dondi, D. Bayoumi, C. Haederli, D. Julian, and M. Suter. Network integration of distributed power generation. *J. Power Sources*, vol. 106; 2002. no. 1–2, pp. 1–9.
- [34] J. O. C. P. Pinto and M. Moreto. Protection strategy for fault detection in inverter-dominated low voltage AC microgrid. *Electr. Power Syst. Res.*, vol. 190, no. July 2020, p. 106572.
- [35] P. Mahat, Z. Chen, B. Bak-Jensen, and C. L. Bak. A simple adaptive overcurrent protection of distribution systems with distributed generation. *IEEE Trans. Smart Grid*, vol. 2; 2011. no. 3, pp. 428–437.
- [36] I. Chilvers, N. Jenkins, and P. Crossley. Distance relaying of 11 kV circuits to increase the installed capacity of distributed generation. *IEE Proc. - Gener. Transm. Distrib.*, vol. 152;

2005. no. 1, p. 40.

- [37] M. Petit, X. Le Pivert, and L. Garcia-Santander. Directional relays without voltage sensors for distribution networks with distributed generation: Use of symmetrical components. *Electr. Power Syst. Res.*, vol. 80; 2010. no. 10, pp. 1222–1228.
- [38] N. K. Sharma and S. R. Samantaray. Assessment of PMU-based wide-area angle criterion for fault detection in microgrid. *IET Gener. Transm. Distrib.*, vol. 13; 2019. no. 19, pp. 4301–4310.
- [39] M. Dewadasa, A. Ghosh, and G. Ledwich. Protection of microgrids using differential relays. *2011 21st Australas. Univ. Power Eng. Conf. AUPEC 2011*, pp. 9–14.
- [40] S. Kar and S. R. Samantaray. Time-frequency transform-based differential scheme for microgrid protection. *IET Gener. Transm. Distrib.*, vol. 8; 2014. no. 2, pp. 310–320.
- [41] S. R. Samantaray, G. Joos, and I. Kamwa. Differential energy based microgrid protection against fault conditions. *2012 IEEE PES Innov. Smart Grid Technol. ISGT 2012*, pp. 1–7.
- [42] R. Escudero, J. Noel, J. Elizondo, and J. Kirtley. Microgrid fault detection based on wavelet transformation and Park ' s vector approach . *Electr. Power Syst. Res.*, vol. 152; 2017. pp. 401–410.
- [43] J. J. Q. Yu, Y. Hou, A. Y. S. Lam, and V. O. K. Li. Intelligent fault detection scheme for microgrids with wavelet-based deep neural networks. *IEEE Trans. Smart Grid*, vol. 10; 2019.no. 2, pp. 1694–1703.
- [44] Y. Alper and G. Bayrak. A real-time UWT-based intelligent fault detection method for PV-based microgrids. vol. 177, no. September 2018. doi: 10.1016/j.epr.2019.105984.
- [45] T. Gush *et al.* Fault detection and location in a microgrid using mathematical morphology and recursive least square methods. *Int. J. Electr. Power Energy Syst.*, vol. 102; 2018. no. May, pp. 324–331.
- [46] M. M. A. Mahfouz and M. A. H. El-Sayed. Fault detection scheme based on feeder buses impedance angles discriminator in smart microgrid. *Sustain. Energy, Grids Networks*, vol. 23; 2020. p. 100379.
- [47] B. Chatterjee and S. Debnath. A new protection scheme for transmission lines utilizing positive sequence fault components. *Electr. Power Syst. Res.*, vol. 190; 2021. no. September 2020, p. 106847.
- [48] H. Gao and P. A. Crossley. Design and evaluation of a directional algorithm for transmission-line protection based on positive-sequence fault components. *IEE Proc. -*

Gener. Transm. Distrib., vol. 153; 2006. no. 6, p. 711.

- [49] A. K. Pradhan, A. Routray, and S. Madhan Gudipalli. Fault direction estimation in radial distribution system using phase change in sequence current. *IEEE Trans. Power Deliv.*, vol. 22; 2007 no. 4, pp. 2065–2071.
- [50] P. Jena and A. K. Pradhan. Directional relaying during single-pole tripping using phase change in negative-sequence current. *IEEE Trans. Power Deliv.*, vol. 28; 2013 no. 3, pp. 1548–1557.
- [51] Z. Shuai, C. Shen, X. Yin, X. Liu, and Z. J. Shen. Fault Analysis of Inverter-Interfaced Distributed Generators with Different Control Schemes. *IEEE Trans. Power Deliv.*, vol. 33; 2018. no. 3, pp. 1223–1235.
- [52] W. M. Guo, L. H. Mu, and X. Zhang. Fault Models of Inverter-Interfaced Distributed Generators Within a Low-Voltage Microgrid. *IEEE Trans. Power Deliv.*, vol. 32; 2017. no. 1, pp. 453–461.
- [53] A. Camacho, M. Castilla, J. Miret, A. Borrell, and L. G. De Vicuña. Active and reactive power strategies with peak current limitation for distributed generation inverters during unbalanced grid faults. *IEEE Trans. Ind. Electron.*, vol. 62; 2015. no. 3, pp. 1515–1525.
- [54] H. D. Tafti *et al.* Low-voltage ride-through capability of photovoltaic grid-connected neutral-point-clamped inverters with active/reactive power injection. *IET Renew. Power Gener.*, vol. 11; 2017. no. 8, pp. 1182–119
- [55] F. Zhang and L. Mu,. A Fault Detection Method of Microgrids with Grid-Connected Inverter Interfaced Distributed Generators Based on the PQ Control Strategy. *IEEE Trans. Smart Grid*, Sep. 2018.
- [56] IEEE Std 1547, *IEEE Standard for Interconnection and Interoperability of Distributed Energy Resources with Associated Electric Power Systems Interfaces*. 2018.
- [57] S. L. Works, “protection against loss of utility grid supply for a dispersed storage and generation unit,” *IEEE Transactions on Power Delivery*, Vol. 8, No. 3, July 1993,” vol. 8, no. 3, pp. 948–954, 1993.
- [58] A. M. Massoud, K. H. Ahmed, S. J. Finney, and B. W. Williams, “Harmonic distortion-based island detection technique for inverter-based distributed generation,” *IET Renew. Power Gener.*, vol. 3, no. 4, pp. 493–507, 2009, doi: 10.1049/iet-rpg.2008.0101.
- [59] W. Xu, G. Zhang, C. Li, W. Wang, G. Wang, and J. Kliber, “A power line signaling based technique for anti-islanding protection of distributed generators - Part I: Scheme and analysis,” *IEEE Trans. Power Deliv.*, vol. 22, no. 3, pp. 1758–1766, 2007, doi: 10.1109/TPWRD.2007.899618.

- [60] H. Samet, F. Hashemi, and T. Ghanbari, "Islanding detection method for inverter-based distributed generation with negligible non-detection zone using energy of rate of change of voltage phase angle," *IET Gener. Transm. Distrib.*, vol. 9, no. 15, pp. 2337–2350, 2015, doi: 10.1049/iet-gtd.2015.0638.
- [61] H. Khosravi, H. Samet, and M. Tajdinian, "Robust Islanding Detection in Microgrids Employing Rate of Change of Kinetic Energy over Reactive Power," *IEEE Trans. Smart Grid*, vol. 13, no. 1, pp. 505–515, 2022, doi: 10.1109/TSG.2021.3119644.
- [62] P. Kumar, V. Kumar, and B. Tyagi, "Islanding detection for reconfigurable microgrid with RES," *IET Gener. Transm. Distrib.*, vol. 15, no. 7, pp. 1187–1202, 2021, doi: 10.1049/gtd.12095.
- [63] H. Muda and P. Jena, "Rate of change of superimposed negative sequence impedance based islanding detection technique for distributed generations," *IET Gener. Transm. Distrib.*, vol. 10, no. 13, pp. 3170–3182, 2016, doi: 10.1049/iet-gtd.2015.1229.
- [64] R. Nale, M. Biswal, and N. Kishor, "A passive communication based islanding detection technique for AC microgrid," *Int. J. Electr. Power Energy Syst.*, vol. 137, no. September 2021, p. 107657, 2022, doi: 10.1016/j.ijepes.2021.107657.
- [65] M. W. Altaf, M. T. Arif, S. Saha, S. N. Islam, M. E. Haque, and A. M. T. Oo, "Effective ROCOF Based Islanding Detection Technique for Different Types of Microgrid," *Conf. Rec. - IAS Annu. Meet. (IEEE Ind. Appl. Soc.)*, vol. 2021-Octob, no. 2, pp. 1809–1821, 2021, doi: 10.1109/IAS48185.2021.9677270.
- [66] P. Gupta, R. S. Bhatia, and D. K. Jain, "Active ROCOF Relay for Islanding Detection," *IEEE Trans. Power Deliv.*, vol. 32, no. 1, pp. 420–429, 2017, doi: 10.1109/TPWRD.2016.2540723.
- [67] R. Zamani, M. E. Hamedani-Golshan, H. H. Alhelou, P. Siano, and H. R. Pota, "Islanding detection of synchronous distributed generator based on the active and reactive power control loops," *Energies*, vol. 11, no. 10, 2018, doi: 10.3390/en1102819.
- [68] P. Gupta, R. S. Bhatia, and D. K. Jain, "Average absolute frequency deviation value based active islanding detection technique," *IEEE Trans. Smart Grid*, vol. 6, no. 1, pp. 26–35, 2015, doi: 10.1109/TSG.2014.2337751.
- [69] T. Z. Bei, "Accurate active islanding detection method for grid-tied inverters in distributed generation," *IET Renew. Power Gener.*, vol. 11, no. 13, pp. 1633–1639, 2017, doi: 10.1049/iet-rpg.2017.0080.
- [70] D. Voglitsis, F. Valsamas, N. Rigogiannis, and N. Papanikolaou, "On the injection of

sub/inter-harmonic current components for active anti-islanding purposes,” *Energies*, vol. 11, no. 9, 2018, doi: 10.3390/en11092183.

- [71] A. Rostami, A. Jalilian, S. Zabihi, J. Olamaei, and E. Pouresmaeil, “Islanding Detection of Distributed Generation Based on Parallel Inductive Impedance Switching,” *IEEE Syst. J.*, vol. 14, no. 1, pp. 813–823, 2020, doi: 10.1109/JSYST.2019.2923289.
- [72] P. K. Ray, N. Kishor, and S. R. Mohanty, “Islanding and power quality disturbance detection in grid-connected hybrid power system using wavelet and S-transform,” *IEEE Trans. Smart Grid*, vol. 3, no. 3, pp. 1082–1094, 2012, doi: 10.1109/TSG.2012.2197642.
- [73] A. Samui and S. R. Samantaray, “Wavelet singular entropy-based islanding detection in distributed generation,” *IEEE Trans. Power Deliv.*, vol. 28, no. 1, pp. 411–418, 2013, doi: 10.1109/TPWRD.2012.2220987.
- [74] S. Alshareef, S. Talwar, and W. G. Morsi, “A new approach based on wavelet design and machine learning for islanding detection of distributed generation,” *IEEE Trans. Smart Grid*, vol. 5, no. 4, pp. 1575–1583, 2014, doi: 10.1109/TSG.2013.2296598.
- [75] H. Khosravi, H. Samet, and M. Tajdinian, “Empirical mode decomposition based algorithm for islanding detection in micro-grids,” *Electr. Power Syst. Res.*, vol. 201, no. September, p. 107542, 2021, doi: 10.1016/j.epsr.2021.107542.
- [76] B. K. Chaitanya and A. Yadav, “Hilbert-huang transform based islanding detection scheme for Distributed generation,” *8th IEEE Power India Int. Conf. PIICON 2018*, Jul. 2018, doi: 10.1109/POWERI.2018.8704444.
- [77] D. Mlakic, H. R. Baghaee, and S. Nikolovski, “A Novel ANFIS-Based Islanding Detection for Inverter-Interfaced Microgrids,” *IEEE Trans. Smart Grid*, vol. 10, no. 4, pp. 4411–4424, 2019, doi: 10.1109/TSG.2018.2859360.
- [78] S. R. Samantaray, B. C. Babu, and P. K. Dash, “Probabilistic neural network based islanding detection in distributed generation,” *Electr. Power Components Syst.*, vol. 39, no. 3, pp. 191–203, 2011, doi: 10.1080/15325008.2010.526986.
- [79] P. Kumar, V. Kumar, and B. Tyagi, “A Novel Islanding Detection Technique Based on Event Index Value for Reconfigurable Microgrid,” *IEEE Trans. Ind. Appl.*, vol. 57, no. 4, pp. 3451–3462, 2021, doi: 10.1109/TIA.2021.3079384.
- [80] R. Bakhshi-Jafarabadi, J. Sadeh, and M. Popov, “Maximum power point tracking injection method for islanding detection of grid-connected photovoltaic systems in microgrid,” *IEEE Trans. Power Deliv.*, vol. 36, no. 1, pp. 168–179, 2021, doi: 10.1109/TPWRD.2020.2976739.

- [81] M. Tajdinian, H. Khosravi, H. Samet, and Z. M. Ali, "Islanding Detection Scheme Using Potential Energy Function Based Criterion," *Electr. Power Syst. Res.*, vol. 209, no. September 2021, p. 108047, 2022, doi: 10.1016/j.epsr.2022.108047.
- [82] Z. S. Chafi, H. Afrakhte, and A. Borghetti, "µPMU-based islanding detection method in power distribution systems," *Int. J. Electr. Power Energy Syst.*, vol. 151, no. February, p. 109102, 2023, doi: 10.1016/j.ijepes.2023.109102.
- [83] B. Patel, "A new technique for detection and classification of faults during power swing," *Electr. Power Syst. Res.*, vol. 175, no. June, p. 105920, 2019, doi: 10.1016/j.epsr.2019.105920.
- [84] Y. W. Li and J. He, "Distribution system harmonic compensation methods: An overview of DG-interfacing inverters," *IEEE Ind. Electron. Mag.* vol. 8, no. 4, pp. 18–31, 2014.
- [85] M. H. Andishgar, M. Gholipour, and R. Hooshmand, "Improved secondary control for optimal unbalance compensation in islanded microgrids with parallel DGs," *Electr. Power Energy Syst.*, vol. 116, no. April 2019, p. 105535, 2020, doi: 10.1016/j.ijepes.2019.105535.
- [86] S. Hoseinnia, M. Akhbari, M. Hamzeh, and J. M. Guerrero, "A control scheme for voltage unbalance compensation in an islanded microgrid," *Electr. Power Syst. Res.*, vol. 177, no. August 2019, p. 106016, 2021, doi: 10.1016/j.epsr.2019.106016.
- [87] A. M. Stanisavljević and V. A. Katić, "Magnitude of Voltage Sags Prediction Based on the Harmonic Footprint for Application in DG Control System," *IEEE Trans. Ind. Electron.*, vol. 66, no. 11, pp. 8902–8912, 2019.
- [88] D. Li, M. Song, J. Hu, Y. Luo, X. Xiao, and K. Yang, "Improved series active power filter with fundamental and harmonic magnetic flux hybrid compensation," *IET Power Electron.*, vol. 11, no. 6, pp. 1038–1045, 2018, doi: 10.1049/iet-pel.2017.0765.
- [89] K. Senthilnathan and I. Annapoorani, "Implementation of unified power quality conditioner (UPQC) based on current source converters for distribution grid and performance monitoring through labview simulation interface toolkit server: A cyber physical model," *IET Gener. Transm. Distrib.*, vol. 10, no. 11, pp. 2622–2630, 2016, doi: 10.1049/iet-gtd.2015.1040.
- [90] A. F. Cupertino, J. V. M. Farias, H. A. Pereira, S. I. Seleme, and R. Teodorescu, "Comparison of DSCC and SDBC modular multilevel converters for STATCOM application during negative sequence compensation," *IEEE Trans. Ind. Electron.*, vol. 66, no. 3, pp. 2302–2312, 2019.
- [91] V. P. Suppioni and A. P. Grilo, "Unbalance compensation control in microgrids based on the unbalance profile," *Electr. Power Syst. Res.*, vol. 196, no. April, p. 107199, 2021.

- [92] X. Su, M. A. S. Masoum, and P. Wolfs, “Comprehensive optimal photovoltaic inverter control strategy in unbalanced three-phase four-wire low voltage distribution networks,” *IET Genr. Transm. Distrib.* vol. 8, no.11. March, pp. 1848–1859, 2014, doi: 10.1049/iet-gtd.2013.0841.
- [93] M. Savaghebi, S. Member, A. Jalilian, J. C. Vasquez, J. M. Guerrero, and S. Member, “Autonomous voltage unbalance compensation in an islanded droop-controlled microgrid,” *IEEE Trans. Ind. Electron.*, vol. 60, no. 4, pp. 1390–1402, 2013.
- [94] M. Savaghebi, S. Member, A. Jalilian, J. C. Vasquez, J. M. Guerrero, and S. Member, “Secondary control for voltage quality enhancement in microgrids,” *IEEE Trans. Smart Grid*, vol. 3, no. 4, pp. 1893–1902, 2012.
- [95] J. Lu, B. Zhang, X. Hou, and J. M. Guerrero, “A Distributed Control Strategy for Unbalanced Voltage Compensation in Islanded AC Microgrids Without Continuous Communication,” *IEEE Trans. Ind. Electron.*, vol. 0046, no. c, 2022, doi: 10.1109/TIE.2022.3169841.
- [96] M. S. Golsorkhi, D. J. Hill, and M. Baharizadeh, “A Secondary Control Method for Voltage Unbalance Compensation and Accurate Load Sharing in Networked Microgrids,” *IEEE Trans. Smart Grid*, vol. 12, no. 4, pp. 2822–2833, 2021, doi: 10.1109/TSG.2021.3062404.
- [97] J. Li *et al.*, “Coordinated Current and Voltage Unbalance Mitigation in Networked Microgrids With Aggregated PV Systems,” *IEEE Trans. Power Syst.*, vol. 1, pp. 1–4, 2022, doi: 10.1109/tpwrs.2022.3210770.
- [98] A. Borrell, M. Velasco, M. Castilla, J. Miret, and R. Guzman, “Collaborative Voltage Unbalance Compensation in Islanded AC Microgrids With Grid-Forming Inverters,” *IEEE Trans. Power Electron.*, vol. 37, no. 9, pp. 10499–10513, 2022, doi: 10.1109/TPEL.2022.3169830.
- [99] X. Wang *et al.*, “Optimal voltage regulation for distribution networks with multi-microgrids,” *Applied Energy*, vol. 210. pp. 1027–1036, 2018, doi: 10.1016/j.apenergy.2017.08.113.
- [100] Y. Peng, Z. Shuai, J. M. Guerrero, Y. Li, A. Luo, and Z. J. Shen, “Performance improvement of the unbalanced voltage compensation in islanded microgrid based on small-signal analysis,” *IEEE Trans. Ind. Electron.*, vol. 67, no. 7, pp. 5531–5542, 2020, doi: 10.1109/TIE.2019.2934021.
- [101] D. I. Brandao, W. M. Ferreira, A. M. S. Alonso, E. Tedeschi, and F. P. Marafao, “Optimal Multiobjective Control of Low-Voltage AC Microgrids: Power Flow Regulation and

Compensation of Reactive Power and Unbalance,” *IEEE Trans. Smart Grid*, vol. 11, no. 2, pp. 1239–1252, 2020, doi: 10.1109/TSG.2019.2933790.

- [102] Y. Han, P. Shen, X. Zhao, and J. M. Guerrero, “An enhanced power sharing scheme for voltage unbalance and harmonics compensation in an islanded ac microgrid,” *IEEE Trans. Energy conversion*, vol. 31, no. 3, pp. 1037–1050, 2016.
- [103] L. Meng, and J. M. Guerrero, “Optimization for customized power quality service in multibus microgrids,” *IEEE Trans. Ind. Electron.* vol. 64, no. 11, pp. 8767–8777, 2017.
- [104] M. M. Ghahderijani, A. Camacho, C. Moreira, M. Castilla, and L. G. De Vicuña, “Imbalance-voltage mitigation in an inverter-based distributed generation system using a minimum current-based control strategy,” *IEEE Trans. Power Delivery*. vol. 35, no. 3, pp. 1399–1409, 2020.
- [105] L. Ji, J. Shi, Q. Hong, Y. Fu, and X. Chang, “A multi-objective control strategy for three phase grid-connected inverter during unbalanced voltage sag,” *IEEE Trans. Power Delivery* .vol. 36, no. 4, pp. 2490–2500, 2021.
- [106] L. Meng, F. Tang, M. Savaghebi, J. C. Vasquez, J. M. Guerrero, and S. Member, “Tertiary control of voltage unbalance compensation for optimal power quality in islanded microgrids,” *IEEE Trans. Energy conversion*, vol. 29, no. 4, pp. 802–815, 2014.
- [107] Á. Borrell, M. Velasco, M. Castilla, J. Miret and R. Guzmán, "Collaborative Voltage Unbalance Compensation in Islanded AC Microgrids With Grid-Forming Inverters," in *IEEE Transactions on Power Electronics*, vol. 37, no. 9, pp. 10499-10513, Sept. 2022.
- [108] Xiaoxue Wang, Chengshan Wang, Tao Xu, Lingxu Guo, Peng Li, Li Yu, He Meng, “Optimal voltage regulation for distribution networks with multi-microgrids,” *Applied Energy*, Volume 210, 2018, Pages 1027-1036.
- [109] M. M. Shabestary and Y. A. R. I. Mohamed, “An Analytical Method to Obtain Maximum Allowable Grid Support by Using Grid-Connected Converters,” *IEEE Trans. Sustain. Energy*, vol. 7, no. 4, pp. 1558–1571, 2016.
- [110] X. Guo, W. Liu, and Z. Lu, “Flexible Power Regulation and Current-Limited Control of the Grid-Connected Inverter under Unbalanced Grid Voltage Faults,” *IEEE Trans. Ind. Electron.*, vol. 64, no. 9, pp. 7425–7432, 2017.
- [111] M. M. Shabestary and Y. A. R. I. Mohamed, “Advanced Voltage Support and Active Power Flow Control in Grid-Connected Converters under Unbalanced Conditions,” *IEEE Trans. Power Electron.*, vol. 33, no. 2, pp. 1855–1864, Feb. 2018.
- [112] M. M. Shabestary and Y. A. R. I. Mohamed, “Asymmetrical Ride-Through and Grid

Support in Converter-Interfaced DG Units under Unbalanced Conditions,” *IEEE Trans. Ind. Electron.*, vol. 66, no. 2, pp. 1130–1141, 2019.

- [113] X. Du, Y. Wu, S. Gu, H. M. Tai, P. Sun, and Y. Ji, “Power oscillation analysis and control of three-phase grid-connected voltage source converters under unbalanced grid faults,” *IET Power Electron.*, vol. 9, no. 11, pp. 2162–2173, 2016.
- [114] M. Mirhosseini, J. Pou, and V. G. Agelidis, “Individual phase current control with the capability to avoid overvoltage in grid-connected photovoltaic power plants under unbalanced voltage sags,” *IEEE Trans. Power Electron.*, vol. 30, no. 10, pp. 5346–5351, 2015.
- [115] W. Jiang, Y. Wang, H. Hang, Z. Zheng, and L. Wang, “Coordinated instantaneous active power control for PWM rectifier under grid voltage dips considering the limitation of phase current,” *Zhongguo Dianji Gongcheng Xuebao/Proceedings Chinese Soc. Electr. Eng.*, vol. 36, no. 22, pp. 6220–6230, 2016.
- [116] L. Chen *et al.*, “Pareto optimal allocation of resistive-type fault current limiters in active distribution networks with inverter-interfaced and synchronous distributed generators,” *Energy Sci. Eng.*, vol. 7, no. 6, pp. 2554–2571, 2019, doi: 10.1002/ese3.443.
- [117] Ministry of New and Renewable energy, Government of India’ <http://niwe.res.in:8080/niwewradata>, accessed on 20thmarch 2020.
- [118] Jinko-Mono-72-cells-300-320W solar panel parameters’ <https://amazingsolar.com.au/wpcontent/uploads/2019/02/Jinko-Mono-72-cells-300-320W.pdf>, accessed 20 march 2020.

APPENDIX

Address to the Examiner's Comments

Comment 1: In Chapter 2, explain briefly the equation and terminologies involved in equation 2.3.

Response: Equation 2.3, and terminologies involved in the equation has been explained as follows:

As shown in equation 2.3, each hour is divided into N_s number of states, i.e. from state 1 to state N_s , where N_s is the highest state number. Each state will have the probability of the average solar irradiance and the overall probability can be obtained from the probabilities of the all states in that particular hour ' t '. Hence, during any particular time frame or any particular hour ' t ', for a given state, the solar irradiance probability can be expressed as (2.3). Here, st represents the present state, $st+1$ represents the upcoming state and $st-1$ represents the previous state. The terminologies of equation 2.3 have been added in the nomenclature.

Comment 2: In Fig. 2.6 of Chapter 2. the x-axis title of optimal pareto front is missing. Correct the figure with proper labeling.

Response: The label of the x- axis of Fig. 2.6 has been corrected in the thesis.

Comment 3: In Chapter 4 how were the fault resistances determined for different fault points within the microgrid? What factors were taken into account when selecting these resistance values?

Response: In chapter 4, different fault resistances are considered for different fault locations in the microgrid. The fault resistance has been varied widely which results in different DG voltage coefficients. The DGs present in the microgrid are having the LVRT capability, where the DG injects 2% reactive current for every 1% voltage drop when the DG voltage coefficient is between 0.5 p.u to 0.9 p.u and when the DG voltage coefficient is below 0.5 p.u it injects maximum amount of the reactive current to support the PCC voltage. The test system considered in this study consists of two IIDGs. Therefore, three different scenarios can be formed viz. both the DG voltages are above 0.9 p.u., both the DG voltages are below 0.9 p.u. and one DG voltage is above 0.9 p.u. and another DG voltage is below 0.9 p.u. Therefore, to test the proposed fault detection technique under these conditions, in the first case the fault

resistances are considered in such a way that both the DG voltages remain above 0.9 p.u. In the second case the fault resistances are considered in such a way that both the DG voltages are below 0.9 p.u. and in the third case the fault resistances are considered in such a way that one DG voltage is above 0.9 p.u. and another DG voltage is below 0.9 p.u.

Comment 4: In Chapter 5. in the validation through hardware in loop testing, what were the key parameters or metrics used to assess the performance of the proposed method in real time applications?

Response: With the evolution of power system network caused by increased diffusion of distributed energy sources, it is necessary to validate any proposed technique before deployment. Hardware-in-the-Loop (HIL) simulation is an alternative to traditional testing method and it has become the standard for testing complex systems around the globe. In other words, HIL simulator can accurately reproduce the plant and its dynamics. OPAL-RT consists of a real-time simulator including HIL testing which creates the real time environment. The simulation is executed in the real time simulator which works with physical clock and allows the simulator to duplicate the real hardware. OPAL-RT considers real time issues such as noise and randomness of events which do not exist in simulation-only system. Moreover, in conventional simulation-only system, the objective is to obtain the results as fast as possible and the time required to compute all the functional blocks and equations representing a system during that particular time step may be longer or shorter depending upon the computational power of the system and model complexity. In real time simulation, the accuracy of the computation depends on the length of the time used to produce the results in addition to the system dynamics. The time required to accurately produce the internal variables and outputs is same as that of its physical counterpart. Thus it permits the RTDS to perform all the necessary operations relevant to real time applications.

Therefore, the proposed method has been tested in HIL environment. The voltage and current waveforms are observed through the digital oscilloscope and the similarity index has been calculated from the data collected from the oscilloscope. It is observed that for any given islanding condition, the obtained results from the HIL testing have matched with the simulation results. Hence, it can be concluded that the proposed method can be implementable in real time applications.

Comment 5: In Chapter 6, can you elaborate on the simulation results comparing the proposed algorithm with another optimization algorithm?

Response: The results obtained with the proposed algorithm using MOACS has been compared with the results obtained with Artificial Cooperative Search (ACS) algorithm in section 6.5 of Chapter 6.

The results obtained from the proposed optimization algorithm have been compared with the results obtained from Artificial cooperative search (ACS) algorithm using single objective function. The negative sequence voltage limit at each load bus is considered as one constraint and the DG maximum phase current is considered as another constraint. The objective function is considered as

$$\text{Objective function} = \sum_{k=1}^n (1 - V_k^d)$$

where, $V_k^d = V_k^+ - V_k^-$

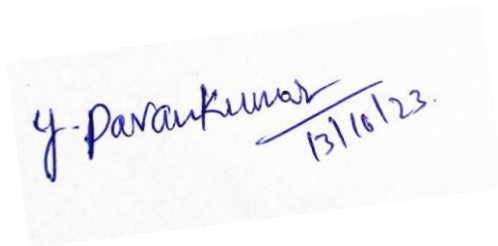
To visualize the performance of the optimization technique with ACS algorithm, same loads have been considered as in case (i). The convergence characteristic of the optimization problem with ACS algorithm is given in Fig. 6.15. The results obtained from the optimization technique with ACS algorithm are tabulated in Table 6.3 and Table 6.4. From Table 6.3 it can be observed that the negative sequence voltages at each load bus obtained from the proposed MOACS algorithm is less than 3.5V whereas, the negative sequence voltage at every load bus obtained with ACS algorithm is greater than 3.45V. Also, it can be seen that at every load bus the VUF is less than 0.9 with the proposed algorithm and the VUF at every load bus is greater than 0.9 with ACS algorithm. On the other hand, Table 6.4 reveals that the positive sequence voltage at the PCC of each DG obtained with the proposed algorithm is slightly higher than the positive sequence DG voltage obtained with the ACS algorithm. The maximum phase currents of the DGs obtained from ACS approach are higher than that obtained from the proposed optimization technique. Therefore, from the comparative results it can be seen that the proposed approach with MOACS is more effective and reliable.

Comment 6: In Chapter 7. how does the control strategy adjust positive and negative sequence components to mitigate voltage sag and voltage unbalance? Can you discuss the mechanism or algorithm used for adjustment and how it contributes to improvement of power system parameters?

Response: The proposed control strategy consists of local control and central control systems. The central control system monitors local control and exchanges the information and sends the control signals to the local control of the DG. The DG control consists of positive sequence current control and negative sequence current control. Initially all the DGs will operate under

normal condition, where the DG will inject the active power and hence each DG will send the positive sequence d-axis current reference ($I_{d_ref}^+$) to the central control. After the compensation mechanism starts, the central control will calculate the optimal references for negative sequence components $I_{d_ref}^-$, $I_{q_ref}^-$ (d and q-axis), the positive sequence q-axis current reference $I_{q_ref}^+$ and sends to the local control. The control mechanism priorities the scenarios depending on the requirements. When the voltage unbalance compensation has been given the priority, the central control gives the maximum negative sequence current references and it will curtail the active power output of the DG by reducing the positive sequence DG current references to maintain the DG operation under the safety limit. Similarly, when the voltage support is prioritised, the control mechanism gives the maximum positive sequence q axis current reference to inject the maximum amount of reactive power. In this case the voltage unbalance compensation will be compromised if the overall DG current is exceeding the safety limits. Therefore, the proposed control mechanism can control both the positive sequence components and negative sequence components of the DG to enhance the microgrid operation.

The control mechanism implemented in this study has been explained in the section 7.3.3. of the thesis.



y. Parankumar
13/10/23.